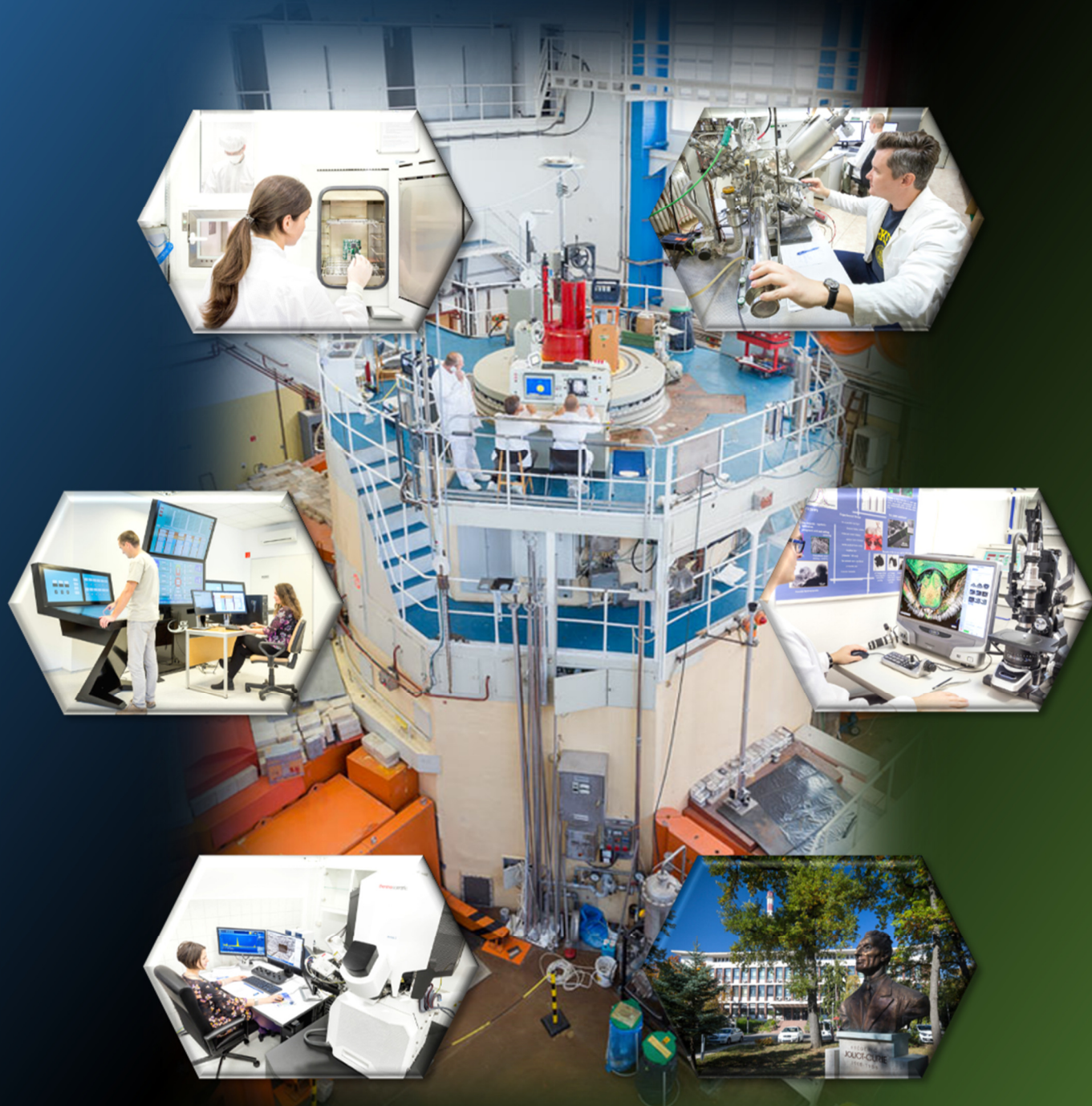


# HUNGARIAN ACADEMY OF SCIENCES CENTRE FOR ENERGY RESEARCH



PROGRESS REPORT ON RESEARCH ACTIVITIES

2018

HUNGARIAN ACADEMY OF SCIENCES  
CENTRE FOR ENERGY RESEARCH

29-33 KONKOLY-THEGE MIKLÓS ÚT

1121 BUDAPEST, HUNGARY

PROGRESS REPORT  
ON RESEARCH ACTIVITIES  
IN 2018

## DEAR READER,

Welcome to the 2018 yearbook published by the MTA Centre for Energy Research (MTA EK), summarizing the scientific results of its three institutions and highlights in 2018. This booklet provides a summary of the research personnel and equipment of departments and research groups working in the Centre.

The year 2018 was average in terms of awarded grants and new opportunities. The National Nuclear Research Programme was successfully terminated with a large amount of new research results. On the 26<sup>th</sup> of March a new test laboratory was inaugurated for space research in the framework of news conference at the campus of our Research Centre. The laboratory was built according to the European Cooperation for Space Standardization and will provide a comprehensive ground for testing space products such as electronics or other parts of space crafts.

In the field of renewable energies important discoveries were published in the prestigious Nature Chemistry journal on cheap catalysts (MoS<sub>2</sub>) for hydrogen production and in the Nature Energy on bio-ethanol produced from cellulose with fully integrated process to the existing fuel refinery factories. In the field of nuclear energy, a compact training simulator was developed for nuclear reactors, using the in-house developed simulation engine software and touch screens. Beside this, a significantly modernized environment monitoring system was designed and built for the Paks Nuclear Power Plant to replace the old system.

The Budapest Neutron Centre (BNC) became a member of the League of advanced European Neutron Sources on the 12<sup>th</sup> of September. This organization will work on the promotion of the neutron based scientific research and the harmonized open science environment including the open data idea. The BNC researchers continue their work in various EU funded projects such as IPERION, E-RIHS, BrightnESS and CHANDA. The Centre is involved in the preparation of the European Spallation Source project aimed at constructing the new neutron source facility in Sweden. Member countries are invited to contribute on an *in-kind* basis, and the expenditures of the participating institutions in Hungary are compensated from the membership fee of the country.

*Ákos Horváth*  
*Director General*  
*horvath.akos@energia.mta.hu*

# CONTENTS

Dear Reader,.....	2
Contents .....	3
Mission Statement of MTA Centre for Energy Research.....	7
Scientific Advisory Board of the MTA Centre for Energy Research.....	7
Organization Structure of the MTA Centre for Energy Research .....	8
Quality Management .....	9
Budapest Research Reactor .....	10
Environmental Protection Service.....	12
<b>I. EU OR NKFH SUPPORTED RESEARCH ACTIVITIES.....</b>	<b>13</b>
Hungarian Nuclear Research Program.....	14
The ALLEGRO Project.....	15
Zirconium Materials Science Studies.....	16
Severe Accident Experiments with Nitrogen Injection.....	19
Normal Operation Calculations to Validate the Creep Model of the Code FUROM.....	20
Investigation of the Axial Profile of Hydrogen-to-Zirconium Mass and Atomic Ratios by Neutron-Based Methods in Zr Fuel Cladding Tubes.....	21
Irradiation of Functional Materials .....	22
Material Property Databases and Handbooks for the DEMO Fusion Reactor.....	23
Advances in the ATLAS+ Project.....	24
Nondestructive Evaluation (NDE) System for the Inspection of Operation-Induced Material Degradation in Nuclear Power Plants – NOMAD.....	25
CORTEX – Core Monitoring Techniques and Experimental Validation and Demonstration.....	26
Strengthening Nuclear Security by Participating in HORIZON-2020 Projects.....	27
Uncertainties of Atmospheric Dispersion Calculations .....	31
Detector Development for the European Spallation Source .....	32
Engineering and Neutronic Design of an Experimental Cave for the European Spallation Source.....	33
Concrete Activation Study for the European Spallation Source .....	34
Transnational Access Within the EC H2020 IPERION CH Project .....	35
Cold Neutron Moderator Development and Cold Source Upgrade Project at Budapest Research Reactor.....	36
Participation in the Activities of the Multidisciplinary European Low Dose Initiative.....	37
<b>II. RESEARCH AND DEVELOPMENT RELATED TO NUCLEAR POWER PLANTS.....</b>	<b>38</b>
Preparation of the FUROM 2.2 Code Version.....	39
Development of Advanced Methodologies and Models for Future Structural Integrity Calculations.....	40
Start-up and Transient Calculations in TRANSURANUS Fuel Behaviour Modelling Code .....	44
Introduction of New Fuel Types to Thermal Power Plants: International Methods for Post-Irradiation Examination of Light Water Reactor Fuel Assemblies .....	45
Modelling the Breakaway Oxidation of the Russian E110 Cladding.....	46
Activities of MTA EK as Main Consultant of Paks NPP .....	47
Multi-physics: Coupling of Reactor Physics and Fuel Behaviour Algorithms of the Hot Channel Analysis .....	48
Investigation of the Reactor Heat Transfer Function between the Cold and the Hot leg of the Primary Circuit.....	49
Development of Interaction Techniques for a Virtual Control Room .....	50
Development of an Examination Technique to Analyse Silver Deposits (Silver Measurement on the By-pass System of the Paks Nuclear Power Plant).....	51
Working Fluids .....	52

Development of Codes for Analysing Reactivity Transients of the VVER-1200 Reactor.....	53
Testing and Qualification of Cladding Samples for ALLEGRO Fuel.....	54
ALLEGRO Core Design.....	55
Simulation of a Station Blackout Transient and Special Topics of Group Constant Generation for the ALLEGRO.....	56
Reactivity Analysis of the Modified Supercritical VVER-SCP Reactor Concept.....	57
Investigation of Thermal Insulation of Experimental Assembly of ALLEGRO Reactor.....	58
Sensitivity Study of Decay Heat Removal Blower Pressure Loss in ALLEGRO Reactor.....	59
Complementary Experiments for High Temperature Irradiated Samples.....	60
<b>III. NUCLEAR SECURITY AND DOSIMETRY.....</b>	<b>61</b>
Quantitative In-field Analysis of UO <sub>2</sub> Samples for Determination Impurities Using Portable LIBS System.....	62
Determining the Irradiation History of Spent Nuclear Fuel Using Gamma Spectrometry (2 <sup>nd</sup> year).....	63
Improvements on Measurement Techniques for Solid State Nuclear Track Detectors.....	64
Analysis of the Measurement Results of the Environmental Radiological Monitoring System of the KFKI Campus.....	65
Development of Measurement Methods for Determining Internal Dose.....	67
Establishing the Methodology of Level 3 Probabilistic Safety Assessment.....	68
Study of the Radiation Field in the Upper Atmosphere.....	70
Modelling the Transport of Radionuclides in Surface Water: Part 4.....	71
Development of the System for Evaluating the Radiation Situation – Developing the Database.....	72
Space Dosimetry for Human Spaceflight and Biosatellite Research.....	73
TRITEL Instrument On Board the ESEO Satellite.....	74
Dose Distribution Inside the International Space Station-3D / DOSIS 3D.....	75
Research&Development Activities in Space Weather.....	76
Preparation for Experimental Studies of Radiation Response at the Cellular Level.....	78
Research on the Biophysical Effects of Low Doses of Ionising Radiation.....	79
Rapid Separation of Actinides from Human Urine, Soil and Sediment Matrices by Extraction Chromatography.....	80
<b>IV. ENERGY AND ENVIRONMENTAL STUDIES.....</b>	<b>82</b>
Testing of MoS <sub>2-x</sub> O <sub>x</sub> 2D Surfaces in Electrocatalytic Water Splitting.....	83
Understanding of the Dry Reforming Reaction for the Development of Novel Catalysts.....	84
Effect of Preparation and Support of Au-based Catalysts on Selective Oxidation of Alcohols.....	86
Biomass Content Determination of Biofuels by <sup>14</sup> C Liquid Scintillation Counter (LSC) Method.....	88
SOD-like Activity and Cytotoxicity Assessment of New Antioxidant Systems.....	89
Long-term Prospects and Development Opportunities of the Domestic Electricity and Heat Supply.....	91
Effects of Heterogeneity in Power-Grid Network Models.....	93
Conditioning and Final Disposal of High-Level Radioactive Waste.....	94
Characterization of Atmospheric Aerosol Particles Having an Energy Generation Origin.....	95
Strategic Research Group for the Challenges of Renewable Energy Based Systems.....	96
Reduction-oxidation Equilibria in Boda Claystone Minerals Determined from Fe <sup>3+</sup> /Fe <sup>2+</sup> Ratios.....	97
Preparation and Characterization of Nanoparticle Systems Developed for Plant Nutrition Experiments.....	98
Exploring the Impact of Nanoparticles on Productivity, Metal Uptake and Iron Metabolism of Plants.....	99
The Effect of Chemical Composition of Concrete on its Long-term Performance in Irradiated Environment.....	100
Preparation and Characterization of Efficient Supported Nanodispersed Gold Catalysts.....	101
Applicability Evaluation of Advanced Oxidation Process for Elimination of Neurophysiological Activity Antidepressant Fluoxetine.....	103
Assessment of Antibacterial Activity, Toxicity and Biodegradability of Products in the Course of Radiolysis Induced Decomposition of Sulphonamides.....	104

Synthesis of Cellulose Derivative/Clay Composite Superabsorbents by Gamma-irradiation.....	105
<b>V. NUCLEAR ANALYSIS AND CHEMISTRY .....</b>	<b>106</b>
Coordinated Research Project on Photonuclear Data and Photon Strength Functions.....	107
Stability of All-inorganic Perovskite Nanocrystals .....	108
Structural Characterisation and Biocompatibility of Phosphate Based Glasses for Biomedical Application .....	109
Applications of Nuclear Analytical Techniques.....	110
Development of Nuclear Analytical Techniques, Nuclear Data Measurements & Dissemination Activities.....	112
Valency States of Iron as Probed by Mössbauer Spectroscopy.....	114
Radiography and Tomography at BRR .....	115
Preparation and Studies of Polysaccharide Derivative-based Nanostructures.....	116
<b>VI. RESEARCH AND DEVELOPMENT IN INSTITUTE OF TECHNICAL PHYSICS AND MATERIAL SCIENCES.....</b>	<b>117</b>
A New Generation Electron Microscope for the Open Laboratory of the Hungarian Materials Science .....	118
Single-atom Catalysts Based on Doped MoS <sub>2</sub> Single Layers for Efficient Hydrogen Evolution .....	121
Direct-indirect Bandgap and Semiconductor-metal Transitions in MoS <sub>2</sub> Single-layers at Moderate Strain .....	123
Measuring the Edge States of Pt <sub>2</sub> HgSe <sub>3</sub> , a Room Temperature Two-dimensional Topological Insulator Candidate.....	125
Highly Ordered Grain Boundaries in CVD MoSe <sub>2</sub> Single Layers.....	127
Mechanical Strain puts a Twist on Dirac Fermions in Graphene.....	128
Dynamic Strain in Gold Nanoparticle Supported Graphene Induced by Focused Laser Irradiation .....	130
Optical Vapour Sensing on Single Wing Scales and on Whole Wings of the <i>Albulina metallica</i> Butterfly .....	132
Optical Spectroscopy of Individual Nanoscale Objects.....	134
Non-destructive Evaluation System for the Inspection of Operation-Induced Material Degradation in Nuclear Power Plants .....	136
Contact Angle Measurements with $r$ - $\theta$ type Capillary Bridges .....	138
In Situ Monitoring of ZrO <sub>2</sub> Surfaces During Oxidation .....	140
Multilayers for Tuneable Resonance in Ellipsometric Biosensors .....	141
Sustainable Autonomous System for Nitrites/Nitrates and Heavy Metals Monitoring of Natural Water Sources .....	142
Diffusion and Reaction Kinetics Governing Surface Blistering in RF Sputtered a-Si <sub>x</sub> Ge <sub>1-x</sub> :H Thin Films .....	143
Makyoh Topography .....	144
Refractive Index Variation of Magnetron-Sputtered a-Si <sub>1-x</sub> Ge <sub>x</sub> by “One-Sample Concept” Combinatory.....	145
KoFAH - Advanced Functional Materials for Autonomous Sensor Networks.....	146
Investigation of Memristive Structures .....	151
Large-angle Dual Scattering Contribution in the Medium Energy Ion Scattering Spectra of Thin Gold Layers and Gold Nanoparticles.....	153
ECSEL JU “POSITION-II project, “Towards Next Generation of Smart Catheters and Implants” .....	155
Low Power Combustible-type Nanosensors for Gas Detection in Harsh Environment.....	156
Biomechanical Tissue Characterization by Force Sensitive Smart Laparoscope of Robin Heart Surgical Robot .....	158
Polymer Microfluidic Systems for Medical Diagnostics .....	160
Finite Element Modelling and Simulation in the Development of MEMS and Microfluidics Devices.....	162
Polimer Based Optical Waveguides for Biomedical Applications .....	163
Cell and Particle Manipulation and Screening in Microfluidic Systems.....	164
Solid State Nanopore and Nanocapillar Based Bioanalytical Systems.....	166
Surface-Enhanced Raman Scattering Active Periodic 3D Structure for Trapping and High Sensitive Molecular Analysis of Particles or Cells .....	167
Intelligent Wound Patch for Online Monitoring Wound Healing Processes - WoundER.....	169
Investigation of Metal (Ni) Induced Lateral Crystallization of Amorphous Si Thin Films at Low Temperature .....	170

Design of Corrosion Resistive SiC Nano-layers .....	171
Highly Safe GaN Metal-Oxide-Semiconductor Transistor Switch.....	172
In situ TEM and Ex situ Heating Experiments on $\kappa$ -Ga <sub>2</sub> O <sub>3</sub> .....	174
The Influence of Bath Additives on the Thermal Stability of Nanocrystalline Ni Films Processed by Electrodeposition .....	175
Structure and Mechanical Properties of Hard and Tough WBC Layers – Possible Industrial Application .....	176
New Type Functional Alloy Films .....	177
TEM Study of Copper Silicides.....	179
The Influence of Artificial Aging on the Microstructure of an Al-Zn-Mg-Zr Alloy Processed by Equal Channel Angular Pressing.....	180
Wear Mechanism of Spark Plasma Sintered Multiwall Carbon Nanotubes Reinforced Zirconia Composites Under Dry Sliding Conditions .....	182
Examination of Milled Hexagonal Boron Nitride Addition on Sintered Si <sub>3</sub> N <sub>4</sub> -BN Ceramic Composites.....	183
CO <sub>2</sub> Reforming of Methane by Ni-In/SiO <sub>2</sub> Catalyst with no Coke Formation.....	184
Thinning of TEM Samples (Know-how).....	185
Micro-combinatorial Analysis of Concentration Dependent Properties of Binary Films .....	186
Development and Characterization of Multi-element Doped Hydroxyapatite Coatings on Metallic Implant Materials.....	188
Ceramic Dispersed Austenitic Strengthened Steels .....	189
New Approaches in the Development of Hypoallergenic Implant Material in Orthopaedics: Steps to Personalised Medicine .....	190
Graphene-ceramic Composites for Tribological Application in Aqueous Environments .....	191
Bacteria Repellent Layer Made of Flagellin .....	192
Kinetics and Structure of Self-assembled Flagellin Monolayers on Hydrophobic Surfaces in the Presence of Hofmeister Salts: Experimental Measurement of the Protein Interfacial Tension at the Nanometer Scale.....	193
Interaction of Positively Charged Gold Nanoparticles With Cancer Cells Monitored by an In Situ Label-free Optical Biosensor and Transmission Electron Microscopy .....	194
High-resolution Adhesion Kinetics of EGCG-exposed Tumor Cells on Biomimetic Interfaces: Comparative Monitoring of Cell Viability Using Label-free Biosensor and Classic End-point Assays.....	195
Label-free Optical Biosensor for Real-time Monitoring the Cytotoxicity of Xenobiotics: A Proof of Principle Study on Glyphosate.....	196
Integrin Targeting of Glyphosate and its Cell Adhesion Modulation Effects on Osteoblastic MC3T3-E1 Cells Revealed by Label-free Optical Biosensing .....	197
<i>In situ</i> Viscoelastic Properties and Chain Conformations of Heavily Hydrated Carboxymethyl Dextran Layers: A Comparative Study Using OWLS and QCM-I Chips Coated With Waveguide Material .....	198
Competition and Partnership Between Conformity and Payoff-based Imitations in Social Dilemmas .....	199
Griffiths Phases in Infinite-dimensional, Non-hierarchical Modular Networks.....	201
Correlation Analysis of Jointly Propagating Genetic and Musical Characteristics of Modern and Ancient Populations in Eurasia and America – A Simultaneous Quest for Ancient Human Populations and Their Musical Parent Languages .....	202
ABBREVIATIONS .....	203

## MISSION STATEMENT OF MTA CENTRE FOR ENERGY RESEARCH

- Research and development in the field of nuclear science and technology for facilitating the adoption and the safe use of nuclear technology in Hungary.
- To participate in international research effort aiming at the establishing a new generation of nuclear power plants and closing the fuel cycle.
- Maintaining and improving competence in nuclear science and technology, especially in the field of nuclear safety, security, health physics, nuclear and isotope chemistry.
- To guarantee the safe operation of Budapest Research Reactor (BRR), and to ensure the open access of the research facilities around the reactor.
- Research activities to improve nuclear analytical and imaging methods and their applications for energy and materials science.
- To perform studies in the field of environmental physics related to energy generation, renewable energies, energy storage and their impact on public health, and on environmental safety.
- Research and development in the field of low carbon energy technologies and of energy saving in industrial technologies.
- Interdisciplinary research on complex functional materials and nanometer-scale structures, exploration of physical, chemical, and biological principles, their exploitation in integrated micro- and nanosystems, and in the development of characterization techniques.
- Dissemination of the results in international programs, education and industrial research and development.

## SCIENTIFIC ADVISORY BOARD OF THE MTA CENTRE FOR ENERGY RESEARCH

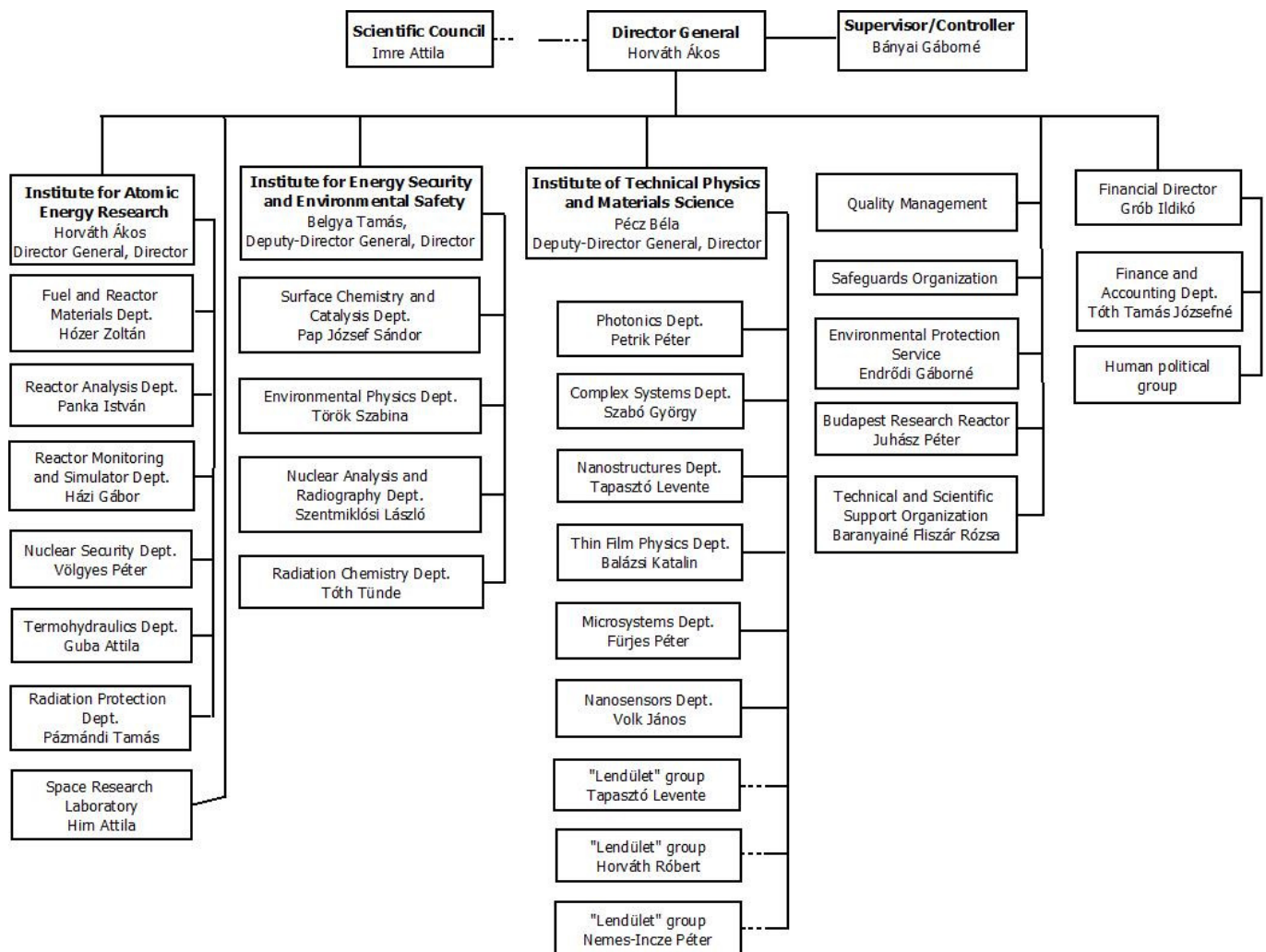
The Board consists of five Hungarian and two foreign leading scientists. The last meeting of the board took place in Budapest, on the 11<sup>th</sup> of April 2018. The management of EK presents usually an overview of the R & D activities in the previous year as well as figures about financial data, analyses of human resources and the dissemination of the research results. The R&D plans for the coming year and for the near future are also presented.

The Board members usually comment the presentations and ask questions. The French member of the Board offered help in the nuclear waste management topic and supported the continuation of this research. The German member of the Board pointed out that Siemens and other big companies have their own research bases. He supported our good contacts with small and medium enterprises. He was very satisfied to learn about the development of Institute for Energy Security and Environmental Safety's "artificial leaf" results and asked why we did not patent it. The general opinion of the board was that Hungarian researchers were not socialized in making patents. It was also commented that if we patent a discovery we should initiate a start-up as well. One of the Hungarian member of the Board mentioned that the integration of Institute of Technical Physics and Materials Science did not cause problems, which is very satisfactory result of the joining process. The Board acknowledged that the internal research cooperation increases and provides successful results, which positively effects the mood.

### Members of the Board:

- Prof. Dr. László Keviczky (Chair), MTA Institute for Computer Techniques and Automation
- Dr. Hervé Bernard (Deputy Chair), Centre French Alternative Energies and Atomic Energy Commission (CEA)
- Dr. Maximilian Fleischer, Head of Department of Corporate Technology, Siemens AG
- Prof. Dr. Ádám Kiss, Eötvös Loránd University
- Dr. Zoltán Homonnay, Head of Laboratory of Nuclear Chemistry, Eötvös Loránd University
- Mr. István Hamvas, Director General, Paks Nuclear Power Plant
- Dr. József Rónaky, Scientific Advisor, Hungarian Atomic Energy Authority

# ORGANIZATION STRUCTURE OF THE MTA CENTRE FOR ENERGY RESEARCH



# QUALITY MANAGEMENT

In order to achieve the highest quality of research, development, design, condition monitoring and valuation, engineering, contracting and managing in design, production, implementation and inspection, the Research Centre’s quality management system has continuously been upgraded by the recommendations of ISO 9001 standard since 1994. Reviewing our QM system by integral audits and management reviews, evaluating improvement opportunities, maintaining project documentation, infrastructure, supporting communication, ensuring the competence of workers the management improves the Centre’s QM system. For the new organization structure, our Quality Policy has been renewed. Many new employees induced a need to upgrade our QM tuition practice. We organised the work and fire safety educations. Our QM system has been certified by Hungarian Standards Institution, IQNet, MVM Paks NPP and MVM Paks II NPP. The last one gives concrete certifications for special topics; up to now three of them were awarded, one of these documents is shown below.



Certifications by Hungarian Standards Institution, IQNet, and MVM Paks NPP and MVM Paks NPP II

## BUDAPEST RESEARCH REACTOR

One of the most important strategic large scale research facilities in Hungary is the Budapest Research Reactor (BRR). It serves the needs of an extensive and diverse scientific community by supporting R&D opportunities, helping innovation and providing a strong foundation for training and education.



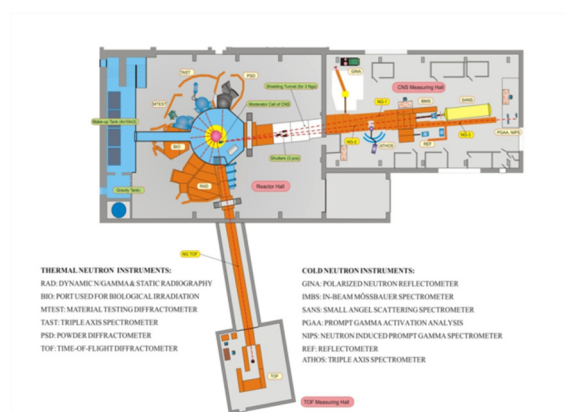
*Bird's eye view of the Budapest Research Reactor*

BRR is a VVR-type reactor that uses light water as moderator and cooling fluid. The power of the reactor is 10 MW provided by low enrichment uranium fuel, and its main purposes – as established during the feasibility/functionality study – are radioisotope production, production of thermal and cold neutron beams for research and applications in all areas, development of new functional materials and neutron activation analysis.

The core is designed to have about 10-11 reactor cycles per year, each having a time-span of 10 days. We are committed to long-term safety and responsible operations, taking care of the wastes from the spent fuel coming from the reactor. Besides the temporary spent fuel storage pool, we also operate a long-term spent fuel storage building for the physical and environmental separation between the reactor and the spent fuel storage.



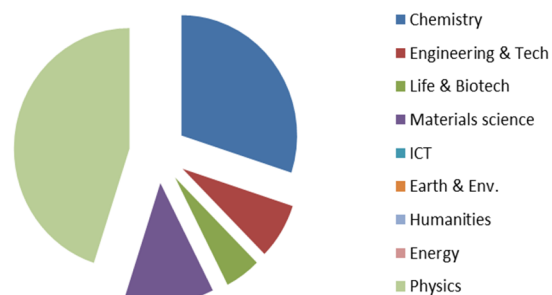
*Top view of the research reactor*



*Layout of the BRR's facilities*

The reactor hosts three kinds of activities: the research activities utilizing neutron beams, production of radioisotopes for industrial and research purposes, and providing national and international training. We are proud of our innovative flagship research topics, which are carried out by a network of neutron beam stations, including beam-lines of thermal neutrons, experiments on powder and residual stress diffractometry, radiography, biological irradiations and beam-lines of cold neutrons for experiments on small angle neutron scattering, reflectometry, prompt gamma activation analysis and nuclear data measurements. In accordance with recent worldwide trends, we are open to establishing new industrial relations and supporting innovation. The BRR's experimental facilities are open for science based on excellence for researcher all over the world. We aim to increase our competence in special topics, to implement new technologies and develop new materials, to promote and exploit our R&D capacity at the national and regional/international level. During the past years the BRR hosted several international schools on various technical and research topics, special trainings in the field of reactor physics, reactor operation, nuclear measurement techniques, and safety and environmental issues.

### BNC: Experiments per scientific field



The BRR is used by groups of different scientific communities from medical, environmental, material, archaeological, nuclear sciences and industry, as well as several Hungarian Universities. Neutron beams are uniquely suited to study the structure and dynamics of materials at the atomic level. The Budapest Neutron Centre (BNC) coordinates the scientific utilization of the research reactor. Some of main research topics currently are:

- neutron scattering, used to examine changes of sample properties under different conditions such as variations in vacuum or pressure, high and low temperature, magnetic field, modelling real-world conditions.
- using prompt and delayed neutron activation analysis, it is possible to measure the concentration of elements in ppm and ppb levels even for small samples. Atoms of a sample become radioactive by exposure to neutrons from the reactor. They decay of gamma-rays characteristic for each element that can be detected by suitable detectors
- neutron activation is also used to produce different radioisotopes, widely used in industry and medicine. For example, Y-90 microspheres to treat liver cancer are produced by bombarding Y-89 with neutrons, which captures them.
- testing reactor materials; materials are subjected to intense neutron irradiation which causes radiation damage of their crystalline structure. For instance, some steels become brittle. Thus the so called high-entropy alloys resisting embrittlement are to be used in nuclear reactors.
- production of radioisotopes for different applications such as medicine, sterilization and industrial use.
- applied research using neutron beams to produce images. Dynamic neutron radiography of cooling system of refrigerator or visualization of fuel burn in engine system of a car, and tomography of different materials and items.

The BNC provides researchers with 15 neutron-specific instruments; 13 of them are installed directly on the horizontal beam ports of the reactor or to the thermal and cold neutron guides, while the other 2 are placed at the vertical irradiation channels. The instruments are supported by a variety of sample environments and data analysis and visualization capabilities.

The BNC provides access to the international neutron user community through a peer-review system. Local scientists assist researchers and industrial users to find the appropriate neutron techniques that meet their research needs. The various neutron scattering instruments in BNC cater to a large number of users from Europe and have grown in strength and stature over the years.

BNC is a member of the League of advanced European Neutron Sources and CERIC-ERIC, and partner in recent EU Framework Programme projects (NMI3-II, CHANDA, IPERION, SINE2020, ESS-BrighnESS, E-RIHS).

BNC is strongly committed to the training of future professionals inland and all over the world in co-operation with the International Atomic Energy Agency. We cooperate with Hungarian universities (Budapest University of Technology and Economics, Eötvös Loránd University (ELTE), Pannon University, ...), BNC accommodates students for laboratory practice to study nuclear-based techniques. A specialized course was developed for geology students of ELTE to introduce nuclear analytical techniques into their education. BNC organizes the Central European Training School on Neutron Scattering annually, to train young scientists for neutron physics and to attract new users. The school provides insight into neutron scattering, element analysis and imaging techniques and their applications to study the structure and dynamics of condensed matter.

The Budapest Research Reactor is open to the public. Members of the local communities and high school and university students are invited to visit regularly and learn more about the amazing nuclear science possibilities available at BRR.



*Research staff of the Budapest Research Reactor facilities in the operator's room*

## ENVIRONMENTAL PROTECTION SERVICE

According to the law, during the use of nuclear energy not only the release of radioactive substances into the air and water, but also the radioactive contamination of the air and the water environment should be checked. The latter task is carried out in the territory of KFKI Campus by the MTA EK Environmental Protection Service (EPS).

In 2018, EPS performed its work on the basis of the renewed Environmental Policy, which accurately reflects the frequency and characteristics of the measurements in the whole 27.4 hectares of KFKI Campus. These studies include monitoring of airborne gamma radiation, atmospheric fallout, gamma spectrometric and total beta activity test of air aerosol particles. They continuously develop their sampling and instrumentation equipment in order to ensure the continuous high quality of their work.



*Mobil laboratory*

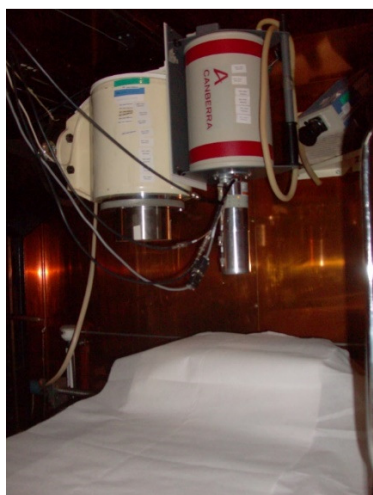


*Dry-Wet fallout sampler*



*Environment controlling gamma probe*

Other tasks include determining the exposure of site workers due to site exposure. In addition to the official, obligatory test, the employees' external exposure to workplace radiation is controlled by their own thermoluminescent dosimeters (TLDs), while possible internal radiation exposure is controlled by so-called whole body examination. EPS constantly develops these measuring systems, and upgrade them so that they can perform the tests as accurately as possible. Thus, in 2018, the whole body detector and bed motion electronics were renovated and the measuring system was supplemented with an irradiation instrument to ensure the quality of TLD tests.



*In-vivo whole body counter*



*RADOS Irradiator*

A detailed report of the work of the Service carried out in 2018 can be found on the MTA EK website.

Gáborné, Endródi  
Head of Service  
endrodi.gaborne@energia.mta.hu



## I. EU OR NKFIH SUPPORTED RESEARCH ACTIVITIES



**CERIC**

Central European  
Research Infrastructure  
Consortium

# HUNGARIAN NUCLEAR RESEARCH PROGRAM

Árpád Farkas

## Objective

The Hungarian Nuclear Research Program (2014-2018) is a research and development project funded by the National Research, Development and Innovation Office (NKFIH, project identifier: VKSZ\_14-1-2015-0021; homepage: vkszk14.kfki.hu). The participants of the consortium project are: Centre for Energy Research, Hungarian Academy of Sciences (MTA EK, as



Figure 1: Research reactor building

coordinator), Budapest University of Technology and Economics (BME), Hungarian Academy of Sciences Institute for Nuclear Research (MTA Atomki), National Public Health Centre (NNK) and Nuclear Safety Research Institute Ltd (NUBIKI). The main objective of the project is to conduct high level research on the technologies supporting the long-term and safe use of atomic energy and to maintain and extend the Hungarian nuclear professional knowledge. One of the main efforts of the project is oriented towards providing the technical and scientific background for the safe operation of the existing reactor blocks of the Paks Nuclear Power Plant (NPP) and preparing for the installation of the new reactors. State-of-the-art research on the safe disposal of spent fuel and development of novel approaches to study different aspects of new generation reactors are also organic parts of the project. Elaboration of the mid-term strategic plans of the Hungarian nuclear research infrastructure is also in focus within this complex research program.

## Results

In the last year of the project, significant progress was achieved in each of the three main task groups, namely: (i) experimental nuclear physics; (ii) simulation of reactor processes; and (iii) nuclear waste management and research on new generation nuclear power plants. Among the most important research results in the field of characterization of new reactor materials it is worth noting that the cladding of the first (15-15Ti) and second (SiC<sub>t</sub>/SiC) ALLEGRO reactor zone is stable in a high temperature He atmosphere even in the presence of impurities. Both mixed oxide (MOX) and uranium dioxide (UOX) fuel types may be appropriate for use. The most important achievement in the field of structural integrity analysis was the development of an optical method able to track the geometrical evolution of the fuel samples during the experiments. In 2018 important code development has been carried out. All the elements of the VVER-1200 reactor code system have been developed and validated. A Multiphysics-type reactor analysis system was developed by linking the physical models with the fuel-behaviour algorithms. A complex Computational Fluid Dynamics (CFD) analysis has demonstrated that in the case of mixed fuel the thermal shield can provide appropriate protection of the MOX subassemblies even assuming a significantly lowered coolant flow rate. Another important result of the new code developments was the extension of FUROM-FBR fuel-behaviour analysis code to the case of sodium and lead cooled fast reactors. In the field of the sampling and analysis of beta- and gamma-active isotopes, new methods for the characterization of <sup>3</sup>H, <sup>14</sup>C, <sup>36</sup>Cl, <sup>79</sup>Se, <sup>99</sup>Tc, <sup>107</sup>Pd, <sup>108m</sup>Ag and <sup>129</sup>I nuclides dispersed in the fluid waste of Paks NPP have been developed. Important mechanisms of action of the low dose radiations at cellular level have been described. In addition, progress in identification and quantification of Deoxyribonucleic Acid (DNA) damages (deletions) has been made.



Figure 2: Research reactor

## Remaining work

The project has finished in 2018.

## Related publications

- [1] B.G. Madas and E.J. Drozsdik: *Effects of mucus thickness and goblet cell hyperplasia on microdosimetric quantities characterizing the bronchial epithelium upon radon exposure*, International Journal of Radiation Biology **94**, 967-974 (2018)
- [2] B. Batki, A. Keresztúri and I. Panka: *Calculation of core safety parameters and uncertainty analyses during unprotected transients for the ALLEGRO and a sodium-cooled fast reactor*, Annals of Nuclear Energy **118**, 260-271 (2018)
- [3] *Strategic Research Agenda of the Sustainable Nuclear Energy Technology Platform for 2019-2022*, in Hungarian. Edited by János Gadó. Available at: [http://faetp.energia.mta.hu/dl/FAETP\\_SKT\\_aktualis.pdf](http://faetp.energia.mta.hu/dl/FAETP_SKT_aktualis.pdf)

# THE ALLEGRO PROJECT

*János Gadó, Ákos Horváth, Zoltán Hózer, Gusztáv Mayer*

## **Objective**

Corresponding to the European initiative on launching research in the field of Generation IV nuclear reactors, the nuclear research institutes of the Visegrad 4 (V4G4) countries and the French CEA started a co-operation on the development of the Gas Cooled Fast Reactor demonstration reactor ALLEGRO in 2010. The final objective of the co-operation is to build up and operate this reactor but the construction has to be preceded by a long period of research and development related to various technological issues and the design of the reactor has to be prepared in several steps. ALLEGRO can start operation not earlier than in 2030.

## **Methods**

The ALLEGRO Project Preparatory Phase was launched by the consortium of the V4G4 in 2015. In the preparatory phase of the ALLEGRO project (2015-2025), the conceptual design will be elaborated and the necessary research-development-qualification tasks will be executed. During the design of ALLEGRO the usual design methods will be applied. First, a pre-conceptual design shall be elaborated using the existing CEA 2009 Design with the necessary additions and modifications by a deadline of about 2020. Design additions and modifications are motivated by the safety concerns related to the CEA 2009 Design. After 2020 the conceptual design will be elaborated (by about 2025) which will be the basis of submitting the construction license application. Elaboration of the detailed design, construction, commissioning and operation will be a task of a new consortium.

## **Results**

In the framework of the ALLEGRO project several basic documents have been created (ALLEGRO Design and Safety Roadmap, ALLEGRO Safety Requirements) and others are gradually actualized (ALLEGRO Design Specifications, ALLEGRO Research and Development Roadmap, ALLEGRO Business Plan, ALLEGRO V4G4 Concept Database). They show the directions of the design works. The Horizon 2020 project VINCO was finished in 2018. It significantly contributed to the ALLEGRO project by benchmarking reactor physical and thermo-hydraulic computational models. Several technical solutions concerning safety related issues have been analysed, like strengthening the guard vessel to reach a higher back-pressure hydrogen injection in loss of coolant accidents.

The Hungarian National Nuclear Research Program (NNKP) was completed in 2019. The program gave the possibility to prepare a lot of studies in line with the ALLEGRO Design and Safety Roadmap. New reports were issued by MTA EK [1-4] (most of them are described in details elsewhere in this Yearbook) and its Hungarian partners NUBIKI and BME NTI.

## **Remaining work**

The finalization of safety relevant solutions requires further studies.

## **Related publications**

- [1] G. Mayer: *Thermohydraulic studies for the ALLEGRO core optimization*, AEMI-2018-206-3.2-01-M0
- [2] I. Farkas, I. T. Farkas, G. Mayer: *Investigation of thermal insulation of experimental subassembly of ALLEGRO reactor*, AEMI-2018-206-3.3-01-M0
- [3] Z. Hózer: *Proposal for ALLEGRO fuel qualification procedure*, MTA EK-FRL-2018-218-1-1-M0
- [4] J. Gadó: *Description of the FUROM-FBR-2 code*, AEMI-2018-206-3.4-01-M0

## ZIRCONIUM MATERIALS SCIENCE STUDIES

Zoltán Hózer<sup>1</sup>, Ildikó Szenthe<sup>1</sup>, Márta Horváth<sup>1</sup>, Ferenc Gillemot<sup>1</sup>, Erzsébet Perez-Feró<sup>1</sup>, Tamás Novotny<sup>1</sup>, Zsolt Kerner<sup>1</sup>, Nóra Vér<sup>1</sup>, Márton Király<sup>1</sup>, Richárd Nagy<sup>1</sup>, Attila Nagy<sup>1</sup>, Ádám Almási<sup>1</sup>, Péter Szabó<sup>1</sup>, Katalin Gméling<sup>1</sup>, Tímea Kocsis<sup>1</sup>, Róbert Farkas<sup>1</sup>, Levente Illés<sup>1</sup>, Anna Pintér Csordás<sup>1</sup>, Katalin Balázsi<sup>1</sup>, Csaba Balázsi<sup>1</sup>, Zsolt Endre Horváth<sup>1</sup>, Noémi Szász<sup>1</sup>, Zsolt Fogarassy<sup>1</sup>, Mária Dobosy<sup>1</sup>, Dániel Antók<sup>1</sup>, Levente Tatár<sup>1</sup>, József Cselovszki<sup>1</sup>, Valér Gottlasz<sup>1</sup>, Gábor Baranyai<sup>1</sup>, Martin Steinbrück<sup>2</sup>, Ulrike Stegmaier<sup>2</sup>, Péter Sipos<sup>3</sup>, Máté Szabó<sup>3</sup>

<sup>1</sup>MTA EK, <sup>2</sup>Karlsruhe Institute of Technology (KIT), <sup>3</sup>MTA CSFK

### Objective

In the second year of the project several experiments were performed in order to simulate those phenomena that can have an effect on the properties of Zr cladding in a nuclear reactor. The examination of the tested samples aimed at identification of microstructural changes. The main objective of the numerical modelling was the detailed analysis of cladding behaviour during mechanical tests.

### Methods

The following experimental techniques and numerical methods were applied according to the detailed project plan in 2018:

- The irradiation of 186 Zr samples was continued in the Budapest Research Reactor for two more irradiation cycles.
- High pressure corrosion phenomena were investigated in autoclaves at 270 °C and 300 °C simulating the reactor core inlet and outlet conditions with five different coolant compositions. The treatments lasted up to 112 days. The mass gain of samples was determined on the basis of weight measurements.
- A new device (ELEMENTRAC® OH-p type analyser) was used to determine the absorbed hydrogen content in the Zr samples.
- Four-point bending tests, mandrel tests, axial and tangential tensile tests and ring compression tests were applied using a tensile test machine.
- Neutron activation analysis, profilometry, metallography, microhardness measurement, SEM, TEM and XRD techniques were applied for the examination of the as-received and pre-treated Zr samples.
- High temperature furnaces and thermogravimeter were used to investigate the behaviour of Zr samples during oxidation. The burst of cladding tubes was recorded by high speed camera (Fig. 1). Cladding creep due to high internal pressure at high temperature was investigated with pre-hydrided Zr tubes.

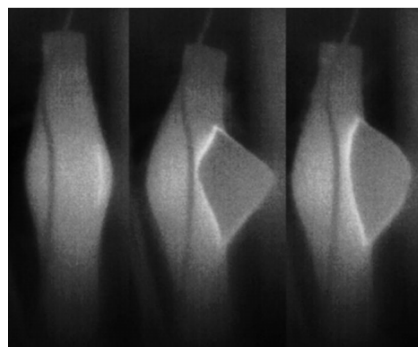


Figure 1: Cladding burst at high temperature recorded by high speed camera

- Finite element numerical models were applied for the simulation of mandrel tests with pre-hydrided samples. The effect of H content was taken into account in the modified Young modulus, which was specified as input data for the calculation.



Figure 2: Shape of experimental (left) and simulated (right) cladding specimen after mandrel test



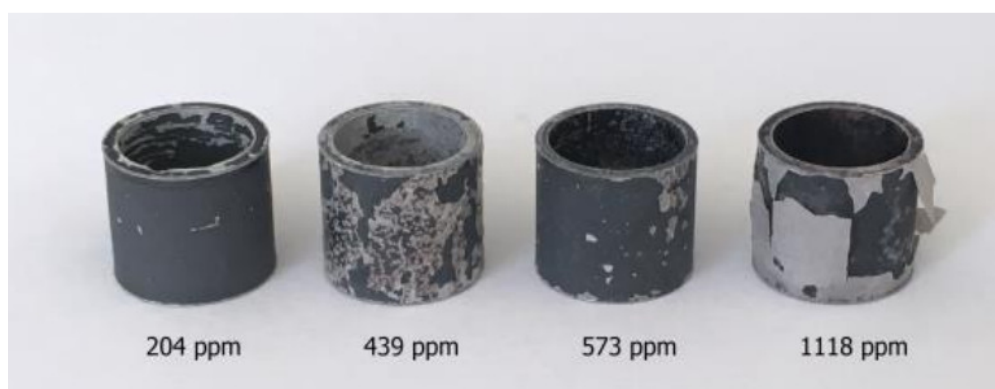


Figure 5: View of electrolytically pre-hydrided E110 samples after oxidation in steam at 1200 S for 690 s

### Remaining work

Further measurements, examinations and calculations will be carried out according to the Zirconium Materials Science Studies project plan.

### Related publications

- [1] I. Szenthe, M. Horváth, F. Gillemot: *Irradiation of Zr alloys in the Budapest Research Reactor*, MTA EK-FRL-2018-229-1-1-M0, in Hungarian (2018)
- [2] E. Perez-Feró, T. Novotny, Zs. Kerner: *Corrosion of Zr claddings II.*, MTA EK-FRL-2018-230-1-1-M0, in Hungarian (2018)
- [3] E. Perez-Feró, T. Novotny: *Hydrogen content measurements with hot extraction method*, MTA EK-FRL-2018-230-1-2-M0, in Hungarian (2018)
- [4] M. Horváth, E. Perez-Feró, T. Novotny, Z. Hózer, P. Szabó: *Ring compression and four-point bending tests with pre-treated Zr samples*, MTA EK-FRL-2018-231-1-1-M0, in Hungarian (2018)
- [5] M. Horváth, Z. Hózer, P. Szabó: *Tensile tests with pre-treated Zr samples*, MTA EK-FRL-2018-231-1-2-M0, in Hungarian (2018)
- [6] K. Gméling, T. Kocsis, M. Horváth, M. Dobosy, M. Király, R. Nagy, R. Farkas, Á. Almási, Z. Hózer: *Neutron activation analytic, profilometric and metallographic examination of Zr samples*, MTA EK-FRL-2018-231-1-3-M0, in Hungarian (2018)
- [7] A. Pintér Csordás, L. Illés: *SEM investigation of oxidised and hydrided Zr samples, Part I.*, MTA EK-FRL-2018-231-1-5-M0, in Hungarian (2018)
- [8] A. Pintér Csordás, L. Illés: *SEM investigation of oxidised and hydrided Zr samples, Part II.*, MTA EK-FRL-2018-231-1-6-M0, in Hungarian (2018)
- [9] K. Balázsi, Cs. Balázsi, L. Illés, Zs. Horváth, N. Szász, Zs. Fogarassy: *SEM, TEM and XRD examination of as-received and oxidised Zr alloys*, MTA EK-FRL-2018-231-1-7-M0, in Hungarian (2018)
- [10] M. Horváth, M. Dobosy, E. Perez-Feró, T. Novotny, Z. Hózer: *Microhardness measurements of Zr samples in their original state and after high temperature treatments in inert atmosphere*, MTA EK-FRL-2018-231-1-5-M0, in Hungarian (2018)
- [11] E. Perez-Feró, T. Novotny: *Oxidation of Zr cladding in steam at atmospheric pressure, Part II.*, MTA EK-FRL-2018-232-1-1-M0, in Hungarian (2018)
- [12] N. Vér, E. Perez-Feró, T. Novotny, M. Steinbrück, U. Stegmaier: *Oxidation kinetics measurements of zirconium alloys in steam and air atmospheres*, MTA EK-FRL-2018-233-1-1-M0
- [13] M. Király, R. Nagy, P. Szabó, Á. Almási: *Burst and oxidation cladding tubes at high temperatures*, MTA EK-FRL-2018-234-1-3-M0, in Hungarian (2018)
- [14] M. Király, R. Nagy, N. Vér: *Cladding creep due to high internal pressure at high temperatures*, MTA EK-FRL-2018-234-2-1-M0, in Hungarian (2018)
- [15] M. Király, M. Horváth, T. Novotny, E. Perez-Feró, N. Vér: *Mandrel test with chemically pre-treated Zr samples*, MTA EK-FRL-2018-234-1-1-M0, in Hungarian (2018)
- [16] R. Nagy, D. Antók, M. Király, L. Tatár: *Finite element simulation of mandrel tests with pre-hydrided samples*, MTA EK-FRL-2018-236-1-1-M0, in Hungarian (2018)
- [17] E. Perez-Feró, T. Novotny, J. Cselovszki, V. Gottlasz, A. Nagy, G. Baranyai: *Zr cladding oxidation in high pressure steam*, MTA EK-FRL-2018-232-1-2-M0, in Hungarian (2018)
- [18] A. Pintér-Csordás, M. Szabó, P. Sipos, M. Király: *Micro XRD and SEM analyses of oxidised and hydrogenated Zr samples*, MTA EK-FRL-2018-234-1-4-M0, in Hungarian (2018)

# SEVERE ACCIDENT EXPERIMENTS WITH NITROGEN INJECTION

*Imre Nagy, Nóra Vér, Róbert Farkas, Márta Horváth, Zoltán Hózer, Péter Szabó, Gergely Szabó*

## Objective

The presence of nitrogen in the atmosphere during a severe reactor accident can influence the core degradation process. The main objective of the present work was the demonstration of the effect of nitrogen on the zirconium cladding oxidation phenomena at high temperatures in two different scenarios.

## Methods

The integral experiments were carried out in the CODEX facility with electrically heated fuel rods. The cladding materials were Russian E110 alloys produced by different technologies. ZrO<sub>2</sub> pellets with 7.65 mm diameter were used inside of the rods and two tungsten heaters were applied. The rods in the bundle were fixed by three spacer grids made of Zr1%Nb alloy. The bundle was placed into a hexagonal shroud. The shroud material was Zr2.5%Nb alloy. The inlet junction was located at 20 mm and the outlet junction at 1020 mm elevation. The upper head of the test section was cooled by a water loop. The bundle was heated by DC power supply units.

## Results

Two experiments were successfully performed.

The CODEX-AIT-3 experiment simulated a bottom-head failure scenario with penetration of air into the reactor core. The duration of air ingress phase was 1 hour and the maximum cladding temperature was slightly above 1600 °C. The analysis of the outlet gas composition showed that during the air ingress phase steam and oxygen starvation conditions were established. The partial consumption of nitrogen indicated the formation of nitrides. The temperature profile significantly changed during the air ingress phase: the maximum temperature moved from the upper section to the middle of bundle due to the intense chemical interactions in the less oxidized central part. The post-test examination showed that the rods were covered by significant amount of nitrides (Figure 1). This structure indicated that oxygen starvation took place in the last phase of the test. The presence of nitrides on the oxide- $\alpha$  layer interface shows that the Zr cladding was strongly concerned by air oxidation before oxygen starvation took place

In the CODEX-NITRO experiment a loss of coolant accident was simulated with injection of nitrogen from hydroaccumulators. The maximum temperature exceeded 1700 °C and the bundle suffered severe degradation. The presence of nitrogen accelerated the steam-zirconium chemical reaction. Due to the low steam flowrate steam starvation took place and it resulted in intense steam-nitrogen reaction.

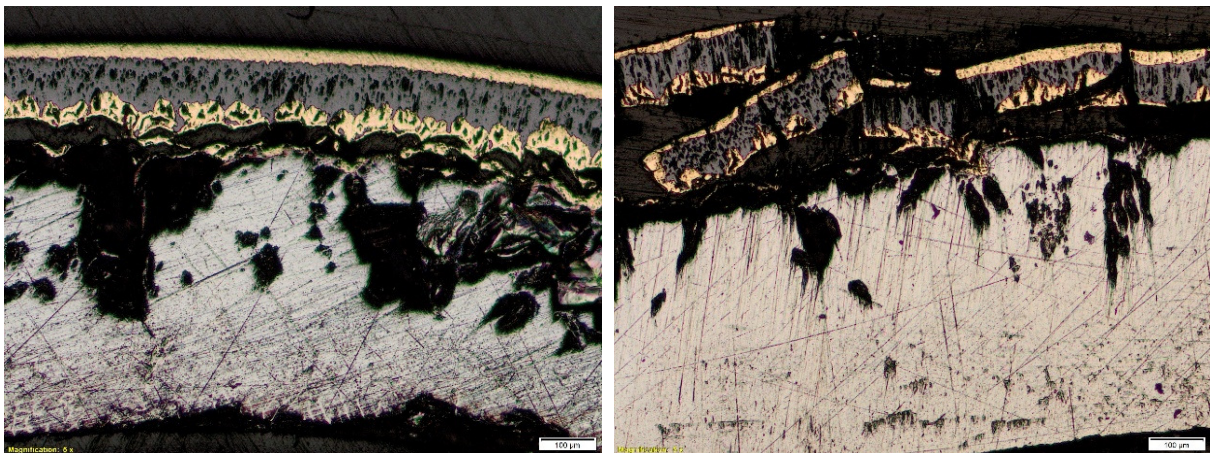


Figure 1: Optical microscopy pictures of CODEX-AIT-3 bundle at 550 mm

## Remaining work

Post-test examination of the bundles will be completed.

## Related publications

- [1] I. Nagy, R. Farkas, N. Vér, Z. Hózer, P. Szabó, G. Szabó: *The CODEX-NITRO integral severe accident experiment*, MTA EK-FRL-2018-235-1-1-M0, in Hungarian (2018)
- [2] I. Nagy, N. Vér, R. Farkas, M. Horváth, Z. Hózer, P. Szabó, M. Steinbrück, J. Stuckert, M. Grosse: *CODEX-AIT-3 experimental data report*, MTA EK-FRL-2018-448-1-1-M0, in Hungarian (2018)
- [3] N. Vér, I. Nagy, R. Farkas, M. Horváth, P. Szabó, Z. Hózer: *The CODEX-AIT-3 integral air ingress experiment*, 24th International QUENCH Workshop, KIT Karlsruhe, 13-15 November 2018

# NORMAL OPERATION CALCULATIONS TO VALIDATE THE CREEP MODEL OF THE CODE FUROM

*Katalin Kulacsy*

## Objective

Cladding creep plays an important role in nuclear fuel behaviour, as, together with fuel densification and swelling, it determines the size of the pellet-cladding gap while the gap is open, and relieves cladding stresses when the gap is closed. Creep depends on many factors, the most important ones being stress, temperature and fast neutron flux both instantaneously and integrated over time.

In order to validate a fuel behaviour code, the creep model has to be assessed, preferably using separate effect tests. The creep model of the code FUROM-2.1.1 has been validated against data from several experiments, both integral and separate effect ones. The present work extended this validation using creep data measured on pressurised samples irradiated in the Russian research reactor BOR-60 at different pressures, temperatures and fast neutron fluxes. The samples were over-pressurised, therefore the cladding crept outwards. This situation arises in commercial reactors when the rod internal pressure exceeds the system pressure or when the pellet-cladding gap is closed and the rating increases, in the latter case the expanding pellet exerts the pressure on the cladding.

The work was supported by the National Research, Development and Innovation Fund of Hungary (contract number: NVKP\_16-1-2016-0014).

## Methods

The samples were 16 and 65 cm long sections of fuel cladding pressurised and sealed, irradiated in different locations in the reactor for different time periods. The test matrix consisted of a systematic combination of several pressure (hoop stress), fast neutron flux, temperature and irradiation time values. The radius of the samples was measured after irradiation.

During irradiation the cladding undergoes thermal expansion, elastic deformation, irradiation growth and creep. All these phenomena were taken into account in the simulations, together with the deformations caused by them. The thickness of the cladding is of special interest, since true stress is approximately inversely proportional to it, so its decrease due to outward creep has a positive feed-back effect.

## Results

The calculation results showed that the creep model implemented in the code FUROM-2.1.1 yields too large deformations. For certain samples some data (irradiation temperature or final hoop stress) were not given as a single value but as an interval. In these cases, we could use the lowest temperature for the simulation and the largest measured hoop strain, but even with these settings the calculated creep was too fast (Fig. 1). The red dots correspond to samples where so much creep was calculated that the cladding thickness decreased significantly and due to positive feed-back the cladding ruptured which did not occur in any of the experiments. However, all tendencies (dependence of creep on time, stress, flux and temperature) were reproduced well by the simulations.

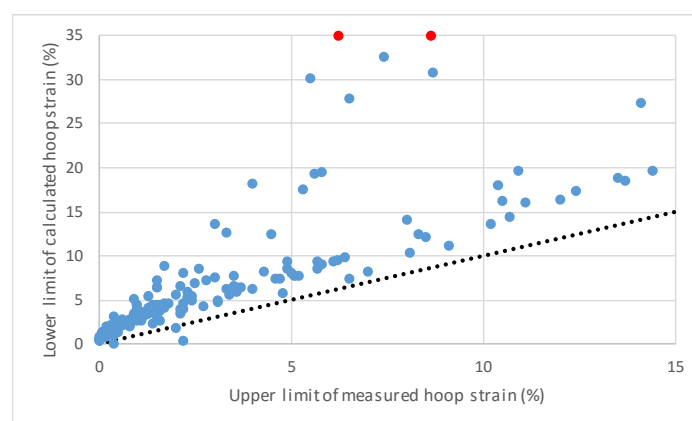


Figure 1: Hoop strains calculated at the lower limit of the given temperature ranges vs. maxima of the measured hoop strain ranges

The implementation of a new creep model into the code FUROM is under consideration.

## Remaining work

The work has been finished.

## Related publication

- [1] K. Kulacsy: *Zirconium Material Science Research: Numerical Modelling of Normal Operation States – Part 1*, MTA EK FRL-2018-238-1-1-M1, in Hungarian (2018)

# INVESTIGATION OF THE AXIAL PROFILE OF HYDROGEN-TO-ZIRCONIUM MASS AND ATOMIC RATIOS BY NEUTRON-BASED METHODS IN ZR FUEL CLADDING TUBES

Zoltán Kis, Boglárka Maróti, László Szentmiklósi

## Objective

To determine the H-to-Zr ratio along the longitudinal axis of fuel cladding tubes following high temperature burst and oxidation of the currently used (E110) and the newly developed (E110G) types of Zr cladding tubes designed for NPPs.

## Methods

Prompt gamma-ray neutron activation analysis and neutron imaging are well applicable techniques, as they detect hydrogen in zirconium matrix effectively. They offer direct and specific determination of the hydrogen content. The position-sensitive prompt gamma-ray neutron activation imaging (PGAI) driven by neutron radiography (NR) has been applied to fulfil this task. Localizing the irradiated volume to a smaller part of the sample yields spatially resolved compositional information. The localization could be carried out by positioning the sample in the collimated neutron beam with the help of a motorized sample stage and imaging. Two times seven tubes (from CODEX-LOCA-200 and CODEX-LOCA-E4 experiments, respectively) were measured at the NIPS-NORMA facility. Altogether around 29 gamma spectra were taken for each cladding tube with 5 mm increments. The obtained elemental composition data characterize the bulk composition of the irradiated volumes. The evaluation is based on the precise determination of pairs of prompt-gamma peaks originating from the two elements. The characteristic peaks used for the calculation were at 2223 keV and at 935 keV for H and Zr, respectively.

## Results

The axial profiles of the H/Zr mass/atomic ratios obtained can be categorized into three groups in both LOCA experiments (Fig. 1.a). In LOCA-200 (Fig. 1.b) in the first group, there are cladding tubes (E110G: No. 1, 3, 5 and E110: No. 6) with no visible deformation, and the values fluctuate around 80 – 100 ppm showing no clear peaks. In the second group, the cladding tubes (No. 2, 4) have a visible burst, and the values show a clear peak (1200 – 1600 ppm) around the opening. The H-profile, however, does not show the usual two-peaks shape. In the third group, the cladding tube (No. 7) has a visible burst with two smaller openings, and the values show three smaller clear peaks (100 – 250 ppm), a pattern not seen before. In LOCA-E4 (Fig. 1.c) in the first group, there are cladding tubes (E110G, No. 1, 3 and 5) with visible deformation and a smaller opening after the burst; and the highest values fluctuate around 400 – 500 ppm showing clear peaks. In the second group, the cladding tubes (E110, No. 2, 4 and 6) have a large visible burst and fracture, and the values show the highest concentration of hydrogen (6000 – 7000 ppm) in a wide section around the opening. The H-profile, however, shows the two-peaks shape only for tube No.4, while for tubes No.2 and No.6 rather smooth profiles were measured. In the third group, where the maximum burst pressure was applied, the cladding tube (E110G, No. 7) has a visible burst with one larger opening, and the values show a smaller clear peak (1600 – 1800 ppm) at it. This categorization could help to better understand the processes if the experimental history of these tubes would be related to the hydrogen profiles.

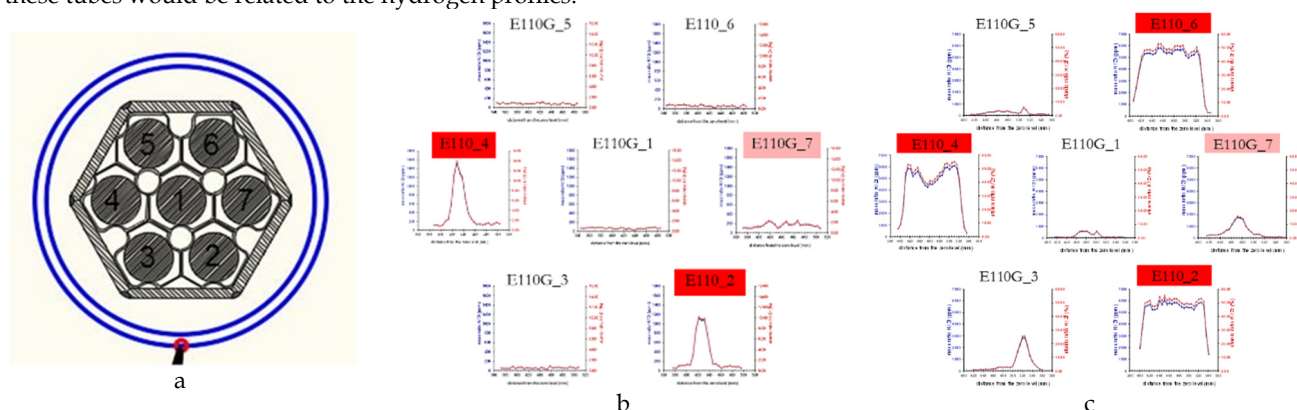


Figure 1: (a) The geometrical arrangement of the cladding tubes in the CODEX-LOCA-200 and -E4 experiments. (b) and (c) The longitudinal profiles of the H/Zr mass ratios (blue line) and the atomic ratios (red line) in CODEX-LOCA-200 (b) and -E4 (c) experiments, respectively. The red labels mark the tubes whose hydrogen profile have clear peak(s).

## Remaining work

The project was finished as planned.

## Related publication

- [1] Z. Hózer, I. Nagy, A. Vimi, M. Kunstár, P. Szabó, T. Novotny, E. Perez-Feró, Z. Kis, L. Szentmiklósi, M. Horváth, A. Pintér Csordás, E. Barsy, K. Kulacsy, M. Grosse: *High-Temperature Secondary Hydriding Experiments with E110 and E110G Cladding*, in: R.J. Comstock, A.T. Motta (Eds.), *Zircon. Nucl. Ind. 18th Int. Symp. ASTM STP1597* (2018)

# IRRADIATION OF FUNCTIONAL MATERIALS

*Ildikó Szenthe, Ferenc Gillemot*

## Objective

Functional materials are the common name of the safety related, but not structural, materials built into the primary system of the future fusion devices. Typical functional materials are the optical elements, cables etc. The EUROfusion WP-MAT program has a subproject to test the ageing under irradiation of the functional materials. Optical elements (e.g. lenses) are planned to be used in the instrumentation system of the future DEMO reactor. Gamma and neutron irradiation may cause degradation of the optical properties. The decrease of the wave transmission factor is the main interest. The task is shared between the Spanish CIEMAT (Centre for Energy, Environment and Technology, Madrid) and the MTA EK.

## Methods

CIEMAT selected and provided 65 samples: different silica grades, spinels, yttrium-aluminium-garnet (YAG), sapphire, diamond, alumina, BaF<sub>2</sub>, CaF<sub>2</sub>, ZnS and coated versions of these types of materials. The task of MTA EK was to irradiate these samples in the Budapest Research Reactor. The irradiation requirements were 0,1 dpa, 0,2 dpa, 0,4 dpa, and 1 dpa fast neutron fluences, calculated with the cross section data of the Eurofer steel. The requested irradiation temperature was 250±10 °C. Two irradiations were performed in 2017 and 2018 in the BAGIRA temperature controlled irradiation rig. The irradiation rig can accommodate 6 different target holders. The target holders are 21\*25\*65 mm size aluminium blocks. Holes are drilled in the target holders for the specimens (see figure 1). During irradiation the target holders are heated by the radiation and temperature controlled by the flow rate of helium-nitrogen gas mixture inside the rig. The helium is a 10x better heat conductor than the nitrogen. The temperature of every target holder is measured by thermocouples, and auxiliary electrical heating is used to eliminate the temperature differences among them. Every target holder includes a set of dosimetry foils to measure the actual fluence. The irradiation time to reach the required 1 dpa fluence was estimated to be 2400 hours.

The design of the target holders was a very difficult task due to the unusually large number of very thin and fragile specimens. A further difficulty was to manipulate the irradiated (radioactive) samples. A few of them remained below the allowed activity level, but some others became highly radioactive.

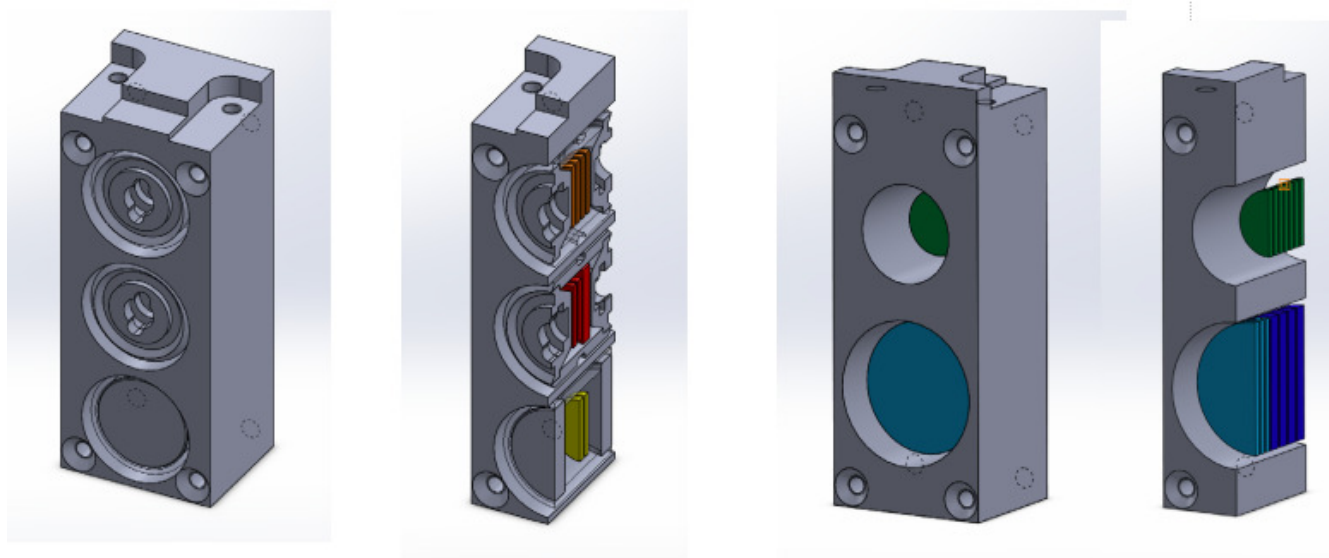


Figure 1. Design of the different target holders

## Results

In 2017 and 2018 the irradiations up 0.4 dpa were finished, and the target holders were withdrawn from the reactor and opened. Since some samples became too radioactive, the 1 dpa irradiation was interrupted and after a sample selection it was continued.

The samples irradiated up to 0,4 dpa have been prepared for transport to CIEMAT. The treatment of the samples required a lot of development to be able to manipulate the very fragile radioactive materials.

## Remaining work

As was mentioned above the completion of the 1 dpa irradiation has been delayed, and will be finished in April, 2019. In 2019 two transports will be organized to carry the samples to CIEMAT. The optical testing of the irradiated samples will be the task of 2019-2020. Also, in 2019 the dosimetry foils will be evaluated and the final irradiation report should be prepared.

# MATERIAL PROPERTY DATABASES AND HANDBOOKS FOR THE DEMO FUSION REACTOR

Ferenc Gillemot, Ildikó Szenthe, Márta Horváth

## Objective

DEMO will be the first fusion reactor producing electricity. The design of it has been started. In support of the design work there is a research and development project, "EDDI WP-MAT", initiated by the EUROfusion Project. One part of the project develops the rules for determining the dimensions of the structural elements, and the other part collects the available data for the materials that will be used in DEMO. Among such materials are the low activity ferrite-martensitic steel of Eurofer, and the functional materials. The functional materials are the dielectric (e.g. cable insulation) materials and the optical materials. Optical materials are the lenses and windows planned for use in DEMO instrumentation and in the heating system. These windows are used to transfer all types of electromagnetic waves (e.g. light, infrared, microwaves etc.). The data provided by research laboratories are first typed into the database, then evaluated and the relevant ones are included into the Material Properties Handbook (MPH). The task of our institute is to plan and elaborate the structure of the databases and the MPH, collect the data, and finally provide and edit the MPH.

## Methods

The first step is to determine the database structure. In some cases, there are ready or semi ready databases (e.g. for Eurofer). In other cases, the database structure should be extended. Several types of data will be collected: production information, mechanical properties (e.g. yield strength, fracture toughness etc.), physical properties (heat conduction, density, etc.), chemical composition, optical properties, dielectric properties etc. Where the material ageing is important, the aged properties determine the lifetime of the structure. Generally, 25-30 properties are considered, depending on the material type and its use (e.g. optical properties are not relevant for structural steels, and the elongation is not considered as a property in case of optical elements). The collected data are evaluated and included into the MPH. First the data base structure (the relevant properties) is determined and after that average and lower bound curves are elaborated for the designers. The properties are separately provided for the as-received-new and service-aged materials. Typical aging damages are the radiation effects, thermal ageing, fatigue, creep etc. In some safety related cases, the data are given in both figures and tables (e.g. Eurofer), in other cases only diagrams are used. Figure 1 shows some examples from the Eurofer and the functional materials handbooks.

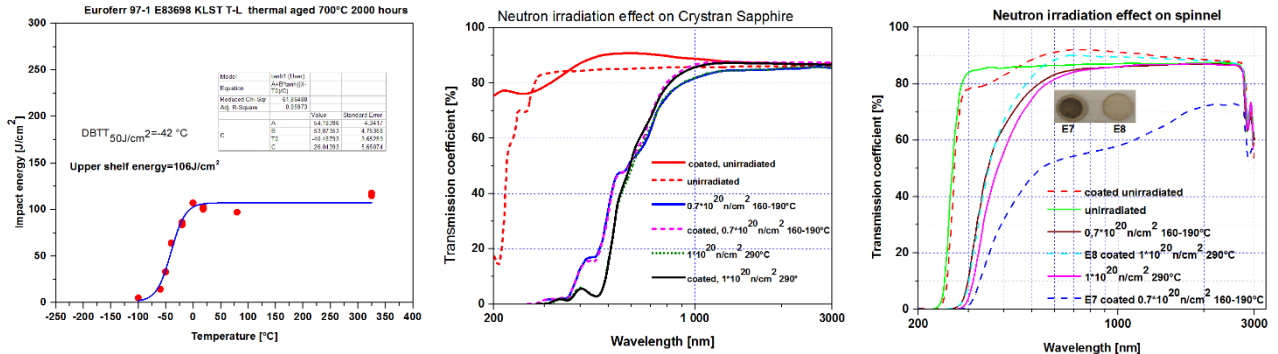


Figure 1. a. Impact energy diagram of Eurofer steel, b. Neutron irradiation effects on Sapphire, c. Neutron irradiation effect on Spinel

## Results

Presently, the most recent version of the Eurofer MPH is finished and the structure of the Functional Materials MPH is set and available. A large amount of data is already available in the Functional Materials MPH.

## Remaining work

The preparation of the databases and MPH-s is a continuing work. Some new data are already available for the existing volumes, and new volumes are planned (tungsten alloys, CuCrZr alloy).

## Related publication

- [1] E. Gaganidze, F. Gillemot, I. Szenthe, M. Gorley, M. Rieth, E. Diegele: *Development of EUROFER97 database and material property handbook*, Fusion Engineering and Design, **135: A**, 9-14 (2018)

# ADVANCES IN THE ATLAS+ PROJECT

*Levente Tatár*

## Objective

An important part of the MTA EK participation in the ATLAS+ (Advanced Structural Integrity Assessment Tools for Safe Long Term Operation) project is a “medium” range experiment consisting of experimental study of crack propagation in an 1:5 mockup (MU) of the VVER-440 main feedwater nozzle [1]. This experiment, along with suitable FEM (Finite Element Method) models will increase the validity of the simulations. The experiment will be carried out in close cooperation with BZN (Bay Zoltán Nonprofit Ltd. for Applied Research).

## Methods

The basic concept briefly: An extension arm will be welded to the VVER-440 mockup. A notch will be manufactured in the MU by EDM (Electrical Discharge Machining) followed by fatigue precracking. The final experiment aims at crack propagation by applying force to the extension arm. During experiment forces and displacements will be measured.

In the preparatory phase several problems have been identified, leading to important changes of the experimental setup. Most important changes are:

- The originally considered pipe-type arm can't carry enough bending moment, so a solid arm will be used.
- Pulling instead of pushing is more advantageous, thus the former will be used.
- It has been revealed that due to the fact that large deflections may occur during the experiments, large lateral forces will develop. The testing machine is not designed to withstand large lateral forces, therefore they have to be limited. To handle this problem, many different constructive solutions have been designed. After preselection two candidate solutions remained: MTA EK solution with guiding pins and BZN solution with oriented pulling bar. (See Figure 1.) Finally, BZN solution has been adopted.
- As there is a large uncertainty regarding material properties at the location of crack front it has been decided that a part from the original MU will be cut by EDM and will be used for additional material testing (see cutaway on Figure 1, b).

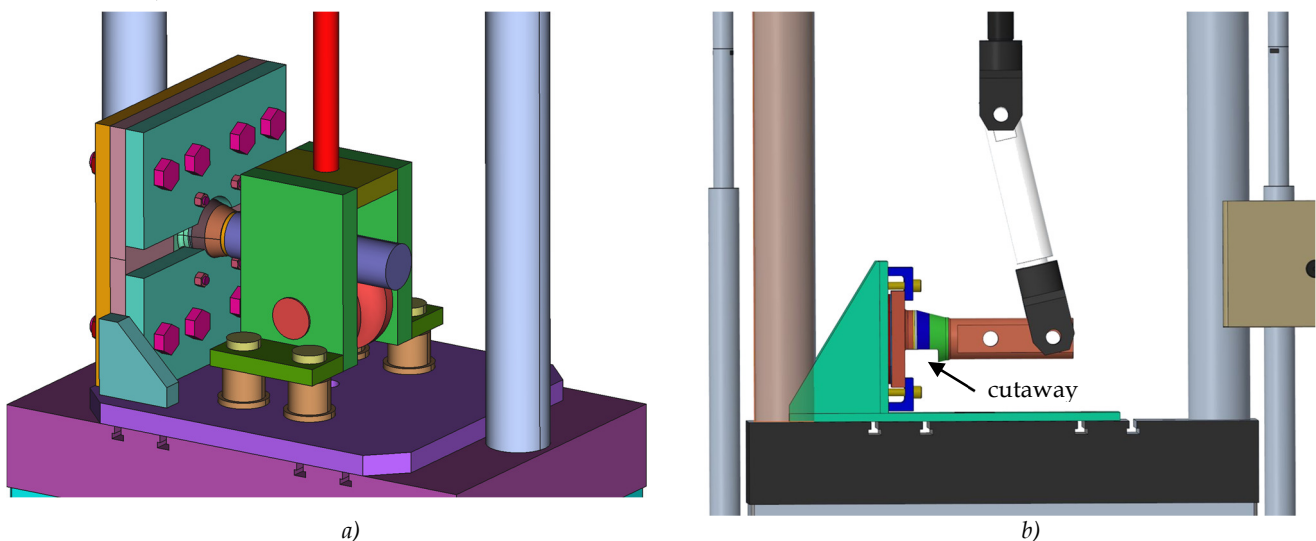


Figure 1: Candidate solutions: a) MTA EK solution with guiding pins, b) BZN solution with oriented pulling bar

## Results

Both analytical and finite element solutions have been used to design the experiment. A large amount of work has been done for designing the supporting structure. Weak points of the structure have been identified, modifications have been considered. However, there are large uncertainties regarding maximum force and maximum deflection so the design has to be based on a “worst case” scenario.

## Remaining work

Due to the large uncertainties besides the main MU from the STYLE (EU FP7) project two other MUs will be tested, too. Thus the test setup can be checked before performing tests on real reactor steel. The workpieces from which these MUs will be manufactured have been machined, they will be welded with the same electrodes and process as the original STYLE MU.

As these experiments are in preparatory phase, the main results of the experiments are still ahead.

## Related publication

- [1] L. Tatár: *EK Progress in the ATLAS+ Project*. MTA EK progress report 2017 (2018)

# NONDESTRUCTIVE EVALUATION (NDE) SYSTEM FOR THE INSPECTION OF OPERATION-INDUCED MATERIAL DEGRADATION IN NUCLEAR POWER PLANTS – NOMAD

*Ildikó Szenthe, Ferenc Gillemot, Antal Gasparics, Gábor Vértesy*

## Objective

NOMAD EU project focuses on the non-destructive investigations of RPV (Reactor Pressure Vessel) steels to better assess their integrity for lifetime management. The primary goals of NOMAD are:

- development and calibration of an NDE (Non Destructive Evaluation) tool for the in-situ inspection of clad RPV material, which can have microstructure heterogeneities,
- validation of the surveillance programs with respect to the actual vessel under LTO (Long Term Operation) conditions.

In order to reach these goals, multiple NDE methods will be applied to multiple scales of samples in neutron irradiated condition: micromagnetic, electrical, ultrasound and acoustic emission methods. The results will be compared and combined in order to define a hybrid approach and finally demonstrate it in a modular way.

## Methods

Within MTA EK a specially designed tool with a sensing yoke is applied for measurement of families of minor loops of the magnetic circuit differential permeability (MAT = Magnetic Adaptive Testing). The magnetizing coil is fed by a triangular waveform current with step-wise increasing amplitudes and with a fixed slope magnitude in all the triangles. The voltage signal in the pick-up coil is proportional to the differential permeability of the magnetic circuit. During the evaluation large sets of so-called magnetic descriptors from the measured data are delivered. The optimal descriptor as an output is selected by careful correlation analysis.

## Results

A lot of experimental results were performed on Charpy impact tester and on block type specimens which were aged by thermal treatments. The team evaluated the results of the heat treatment study for A508Cl.2 and 15kH2NMFA reactor steel materials to ensure benchmark for the future measurements. The influence of heat treatment was unambiguously demonstrated by this method.

Influence of neutron irradiation was also studied. An example obtained on Charpy specimens made of 22NiMoCr37 material can be seen in Figure 1.

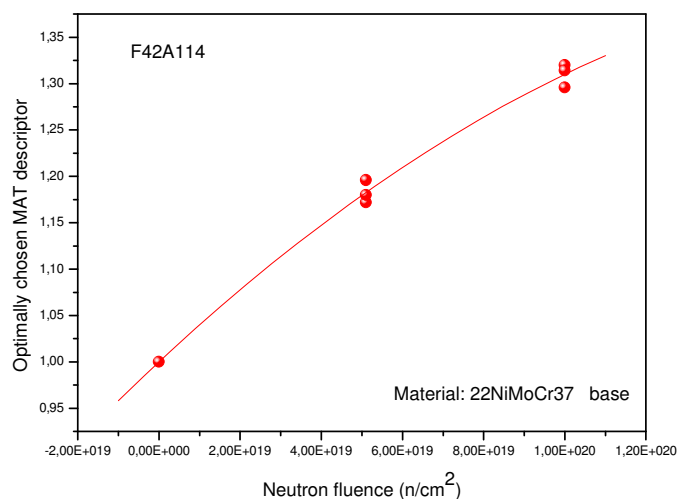


Figure 1: Optimally selected MAT descriptor as the function of the neutron fluence. Monotonous correlation had been got with the degree of irradiation, the scattering was ~5%, while the difference between the samples irradiated by  $5.1 \times 10^{19} \text{ n/cm}^2$  and  $1 \times 10^{20} \text{ n/cm}^2$  achieved 13% and 30%.

## Remaining work

During the future measurements the hysteresis loops of the differently degraded samples will be compared and evaluation of loops will result in a large number of parameters, some of them characterizing the material degradation. This gives us a good chance, the measurement and evaluation will provide reliable data about material degradation.

# CORTEX – CORE MONITORING TECHNIQUES AND EXPERIMENTAL VALIDATION AND DEMONSTRATION

*Sándor Kiss and Sándor Lipcsei*

## **Objective**

The CORTEX project is a four-year long, wide contribution between 19 institutes, universities and companies of 11 countries in several working packages. The consortium was strategically structured around the required core expertise from all the necessary actors of the nuclear industry, both within Europe and outside. The project aims at developing an innovative core monitoring technique that allows detecting anomalies in nuclear reactors, such as excessive vibrations of core internals, flow blockage, coolant inlet perturbations, etc. The technique will be based on primarily using the inherent fluctuations in neutron flux recorded by in-core and ex-core instrumentation, from which the anomalies will be differentiated depending on their type, location and characteristics. The method is non-intrusive and does not require any external perturbation of the system. The project will result in a deepened understanding of the physical processes involved. This will allow utilities to detect operational problems at a very early stage and to take proper actions before such problems have any adverse effect on plant safety and reliability.

## **Methods**

We are participating in Working Package 4 (Application and demonstration of the developed modelling tools and signal processing) focusing on VVER-440 techniques against plant data measured at Paks NPP.

## **Results**

For the project purposes longer and more frequent measurements were made than the regular ones at all four VVER-440/213 units of Paks NPP. Moreover, these measurements were virtually continuous for a whole fuel cycle at Unit 2 in order to choose periods as still as possible for the steady state measurements: one from the beginning, one from the middle and one from the end of the fuel cycle. The reactor instrumentation, relevant properties of the primary loop, the measurement system as well as the measurements and the reactor parameters are extensively described in deliverable D4.3 (Document describing all validation data), while the measurements are made available in the project repository. Additionally, we have coordinated the gathering of the contributions from the work package partners for deliverable D4.3 and edited it.

VVER-440 core data were assembled and provided for deliverable D4.2 (Core data for steady state calculations), additionally core loading data were also made available for the dates of the chosen noise data measurements. Since cross section data were not available due to legal restrictions, we will execute the core calculation code provided by the Technical University of Valencia.

## **Remaining work**

The project finishes in 2021.

## **Acknowledgement**

The research leading to these results has received funding from the Euratom research and training programme 2014-2018 under grant agreement No 754316.

# STRENGTHENING NUCLEAR SECURITY BY PARTICIPATING IN HORIZON-2020 PROJECTS

*András Kovács, Péter Völgyesi*

## Objective

In order to strengthen nuclear security in Hungary and worldwide, the Nuclear Security Department of MTA EK got involved in three different Horizon-2020 EU projects. The aim of the **C-BORD** („effective Container inspection at BORDER control points”) project (2015-2018) was to develop, improve and test new comprehensive and cost-effective detection methods for higher efficiency Non-Intrusive Inspection (NII) of freight containers to be applied both at sea ports and at land border crossing points to disclose the illegal trade of e.g. cigarette, drugs, arms and radioactive and nuclear materials. Five different detection methods have been developed and tested at two sea ports (Rotterdam and Gdansk) and at a land border crossing place (BCP) at the Hungarian-Serbian border in Röszke.

The objective of the **INSIDER** project (2017-2021) is to improve decommissioning and dismantling (D&D) of nuclear facilities with medium and high radioactivity levels and/or other constrained environments from complex non-standard facilities, with regard to waste production. Thus, the project aims at improving the management of waste from nuclear sites developing and validating an improved integrated methodology of characterization based on different new statistical processing and modelling, coupled with present (and adapted) analytical and measurement methods, with respect to sustainability and economic objectives. The specific task of MTA EK in the frame of WP 5 – as the task leader of WP 5.3 – is to participate at in situ and on site initial characterizations, mapping of contaminated areas, determination of hot spots and sludge tank and hot cell measurements.

The third project is the 2nd phase of **ITRAP-10+** („Illicit Trafficking Radiation Assessment Program, 2017-2019”) with the primary aim to build testing and performance assessment capacity within EU member states to improve international standardization and detection capabilities. During the project JRC provided portable spectroscopic radiation portal monitors (SRPM), handheld Radionuclide Identification Device (RID) and personal radiation dosimeters (PRD) for American National Standards Institute (ANSI) based tests for five test laboratories including MTA EK. At the end of the project the results of the measurements and the intercomparison will be discussed and analysed.

## Methods

In the **C-BORD** project an advanced X-ray scanning system (developed by Smiths Detection), a set of relocatable and mobile radiation portal monitors (RPM, developed by Symetrica Ltd. and Commissariat à l'Énergie Atomique et aux Énergies Alternatives (CEA)) and a new design of gas phase detectors (developed at the University of Manchester and Bonn-Sieg-Rhein University) were tested at Röszke land border crossing place (Figure 1).



Figure 1: Sniffer device (left) and in operation at Röszke BCP (right)

The next generation cargo **X-ray system** has been designed to improve both the accuracy and the material classification capabilities (high energy material discrimination of X-ray images). The new HCVM-T X-ray scanner, included in the trailer, is capable of operating both in portal and in mobile modes (Figure 2). These X-ray screening systems are designed to optimize security checks at ports, airports and border crossings. These systems are used to inspect entire trucks (cabin included), containers and smaller vehicles even for threats such as explosives, narcotics, weapons of mass destruction (WMDs), contraband, as well as for manifest verification, reducing the need for manual inspection. When equipped with the automatic radioactive material detection (ARDTM) (optional), the HCVM-T simultaneously carries out both the X-ray inspection and an analysis to detect the presence of radioactive gamma and/or neutron materials within the container or vehicle. The trailer is equipped with an electrical engine that effectuates independent forward and backward motion. The HCVM-T series systems use a range of accelerators from 4 MeV to 6 MeV, allowing steel penetration ranging from 280 mm to 320 mm, while providing a high throughput of up to 25 trucks per hour in scan mode and up to 150 trucks per hour in pass through mode, with up to 4 system operators in the cabin.



Figure 2: The HCVM-T X-ray scanning system with built-in RPMs in operation at Rösske pass through mode (left) and mobile mode (right)

The **current version of RPMs** is a new generation of passive neutron and gamma detection systems used both in mobile and relocatable arrangements (Figure 3), designed to detect radioactive and nuclear materials. The main aim of the passive technology development is to achieve better sensitivity and improved isotope identification. The new design is capable of determining the category of the radioactive material and its position in the cargo. During the field validation exercises two types of RPM systems, integrated with a HCVM-T X-ray system (Figure 1), were tested by using various radioactive and Naturally-occurring Radioactive Materials (NORM) (e.g. fertilizers). Besides this SRPM system, similar gamma and neutron detectors were located in a passenger car and were used during the field exercise to test both mock-up containers and commercial trucks.



Figure 3: Relocatable (left) and mobile detector modules (right, in a passenger car) of Symetrica under test at Rösske

The **INSIDER** project started during the last quarter of 2017. MTA EK’s first task was the identification of European companies’ methodologies for radiological characterization of nuclear installations undergoing decommissioning and gathering information about instruments and methodologies in use for radiological characterization of contaminated sites and structures in constrained environment (high temperature and/or humidity, dose rate, etc.). The experimental work started in Q3 2018. In the frame of an INSIDER based international intercomparison exercise the gamma spectrometry experts of MTA EK carried out waste characterization measurements at the partly decommissioned zone, i.e. at the concrete wall of the biological shielding of the BR-3 type research reactor of SCK-CEN in Mol, Belgium. The high resolution gamma spectra were taken with Canberra GL2020 HPGGe detector. Dose rate and total gamma measurements were also performed at the sampling locations using Berthold LB-124, Thermo Scientific RadEye B20-ER and LaBr<sub>3</sub> instruments (Figure 4).

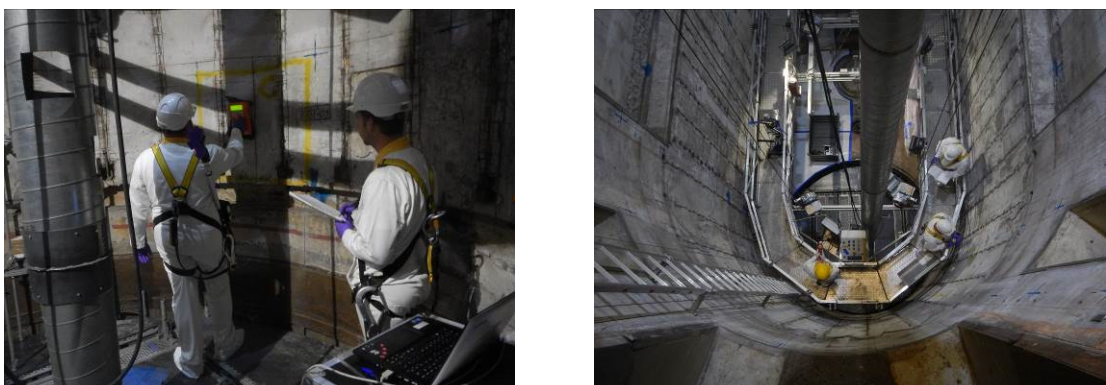


Figure 4: In situ measurements at SCK CEN reactor pool under decommissioning

Concerning the ITRAP+10 project, the testing of the radiation detectors SRPM, a RID and an PRD (Figure 5) was performed at the Testing Laboratory of MTA EK according to the relevant international standards (e.g. ANS I4243) using the required gamma and neutron radiation sources (Special Nuclear Materials (SNM), NORM, medical and industrial isotopes). The Testing Laboratory consists of two rooms, both equipped for different types of testing applications (Figure 6 and 7).

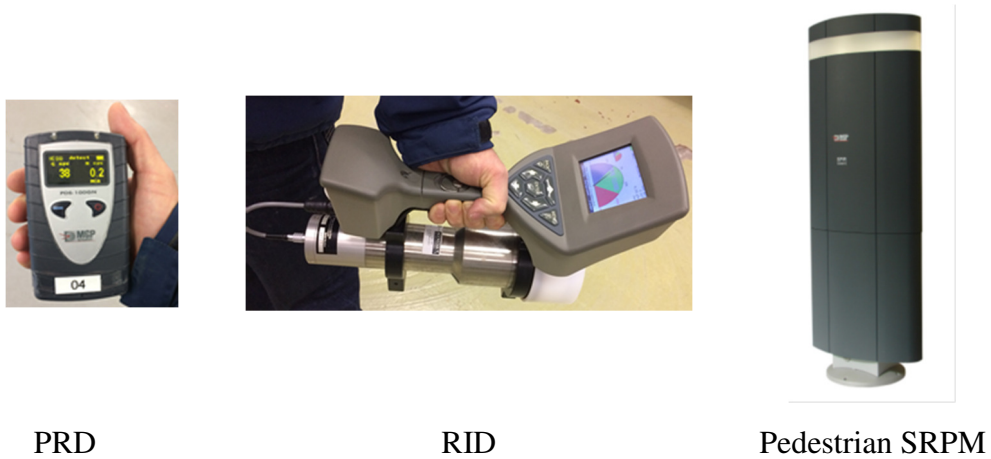


Figure 5: Three categories of instruments taking part in the round robin exercise

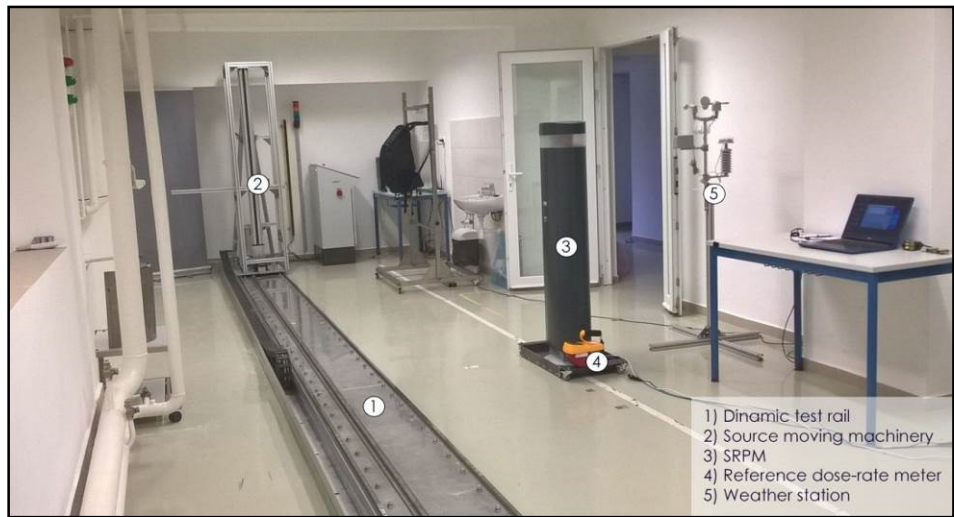


Figure 6: Dynamic test bed facility at MTA EK with the SRPM detector under test



Figure 7: Static test bed facility at MTA EK with the PRD detector under test

**Results**

1. As a conclusion of the C-BORD field validation exercise at Rösztke it was found that the next generation cargo X-ray system of SmithsD with improved accuracy (of the X-ray images) and material classification capabilities (high energy material discrimination) has come up to the expectations. Similar conclusions were drawn with respect to the high level

performance of the Symetrica designed mobile, portable, built-in and fixed portable monitors. The CEA designed fixed radiation portal monitor has also shown good performance. Only the gas phase detection technology was evaluated as promising but needing further development.

The idea of combining detection technologies to maximize effectiveness and efficiency was achieved by developing the common user interface, which allows better allocation of human resources and also facilitates to shorten the time of the customs inspections. This is with no doubt one of the biggest benefits of the C-BORD project.

It was also concluded, that customs organizations need more technology support for the control of non-commercial traffic and private vehicles.

2. In the frame of the **INSIDER** project high resolution gamma spectrometry measurements have been performed by MTA EK to characterize the concrete shielding of the decommissioned reactor zone. The high resolution HPGe gamma spectrometry measurements revealed the presence of  $^{154}\text{Eu}$  and  $^{60}\text{Co}$  as main components and  $^{152}\text{Eu}$ ,  $^{137}\text{Cs}$  and  $^{133}\text{Ba}$  as minor components in the samples. Dose rate and total gamma measurements were also performed at the sampling locations. The evaluation of the measurements as well as the comparison of the data measured by the other participants are in progress.
3. Summarizing the main results of **ITRAP+10** project it was concluded, that most of the planned tests could be performed at the MTA EK Detector Testing Laboratory, though some modifications had to be made on the testing facility itself, or the test methods, in order to meet the test requirements on a satisfactory level.

### *Remaining work*

1. The **C-BORD** project has been completed and finished in 2018. Further continuation of the work, maybe in the frame of another international project, is under review and investigation.
2. The **INSIDER** project is continued according to the present programme and milestones. Waste characterization measurements by MTA EK will also be performed at another partly decommissioned research reactor in Ispra, JRC.
3. The final report of the **ITRAP+10** project is under preparation and the project will be completed and finished with a final evaluation meeting in 2019.

# UNCERTAINTIES OF ATMOSPHERIC DISPERSION CALCULATIONS

*Csilla Rudas, Péter Szántó, Tamás Pázmándi*

## Objective

The objective of the CONFIDENCE research project is to understand, reduce and cope with the uncertainty of meteorological and radiological data and their further propagation in decision support systems, including atmospheric dispersion, dose estimation, food-chain modelling and countermeasure simulation models. Work package 1 (WP1) is focused on modelling of uncertainties during the emergency phase, from meteorological and source term inputs, and applied to atmospheric dispersion calculations and dose estimations.

## Methods

In the second year of the 3-year long EU H2020 project, the input and model parameters used in the atmospheric dispersion calculations were selected based on the uncertainty evaluation done in the previous year. First, a simple deterministic calculation was performed by all participants testing the use of meteorological data and producing the results in a common form. After the simulation programs were tested, the calculations for the Borssele case study (a hypothetical radioactive release from the Borssele nuclear power plant) were carried out. In this release scenario the source term and meteorological uncertainties were investigated. The source term uncertainties included time to release (24 h +/- 6 h, equally distributed), the effective release height (50 m +/- 50 m, equally distributed) and the released activity (factor 1/3 to 3). The meteorological uncertainties were considered with meteorological ensemble data provided by the Harmonie-AROME model with a horizontal resolution of about 2.5 km and a temporal resolution of one hour. The time-span of the data was 72 hours and the domain was 300 km x 300 km.

## Results

The results of the participants are shown on maps of probability of threshold exceedance, based on an ensemble of simulations and corresponding to the probability that a given zone is contaminated above a given level. The reference levels in this project were:

- 10 kBq/m<sup>2</sup> deposition for Cs-137 and I-131;
- 10 mSv effective dose for 1-year old child;
- 10 mSv inhalation thyroid dose for 1-year old child.

Based on these thresholds, useful outputs for decision making are the maximum distance and surface area affected by the threshold exceedance and associated uncertainties. The probability maps of threshold exceedance for deposition of Cs-137 are shown in Fig.1 for three participants. In this figure, the variability between the results given by the participants is clear. The pattern induced by scavenging, showing “hot spots” of deposition, is clearer in Participant #2 and Participant #3 maps, while the results of Participant #1 show a more continuous plume.

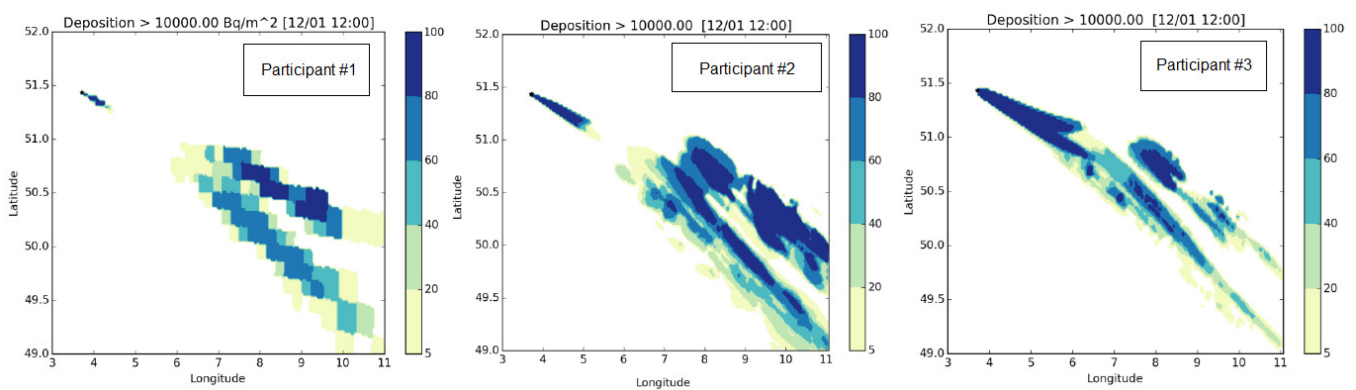


Figure 2: Probability maps of a threshold exceedance of 10 kBq/m<sup>2</sup> for Cs-137 deposition, for a number of discrete bands of percentiles, for several participants [1]

## Remaining work

Further calculations will be conducted for the Western Norway and Fukushima release cases, as well as an additional Borssele simulation focusing on a different meteorological situation with higher uncertainties. Recommendations will be made for the use of uncertainty analysis and propagation with an ensemble approach in an operational context. In the last year of the project, the results of all the simulations will be evaluated and the findings will be presented in deliverable documents and at a dissemination workshop.

## Related publication

- [1] H. De Vries, G. Geertsema, I. Korsakissok, R. Périllat, R. Scheele, J. Tomas: *Published sets of probability maps of threshold exceedance for scenarios*, CONCERT CONFIDENCE Report D9.4 (2019)

# DETECTOR DEVELOPMENT FOR THE EUROPEAN SPALLATION SOURCE

*Eszter Dian, Milán Klausz, Péter Zagyvai*

## Objective

The European Spallation Source (ESS) aspires to be the brightest neutron source of the world, which requires joint and organised efforts of the neutronic community, as well as research and development in fields like neutron instrumentation, especially detector development, in order to meet the potential of the ESS. In addition, the recent  $^3\text{He}$ -shortage necessitates the development of new,  $^3\text{He}$ -replacement neutron detectors where it is reasonably achievable. As part of this effort, the investigation and development of two, novel solid  $^{10}\text{B}_4\text{C}$ -converter-based, Ar/ $\text{CO}_2$ -filled detectors were planned; for the off-the-shelf BCS (Boron Coated Straws) detector, and for the Multi-Grid detector, jointly developed by the ESS and the ILL (Institut Laue-Langevin).

## Methods

Thanks to the recent development of neutron simulation tools, detailed and realistic GEANT4-based Monte Carlo simulation studies were performed for both detectors. A comprehensive study of the BCS was presented, investigating various aspects of the detector performance, e.g. efficiency, activation, absorption and the impact of scattering on the measured signal. This detector has already been selected for one of the Small Angle Neutron Scattering (SANS) instruments of the ESS, for which the exceptional flux of the ESS challenges the count-rate capability of the detector. Therefore, the BCS detector was also modelled under realistic operating conditions of the ESS SANS instruments.

A similar model was built for the Multi-Grid detector as well, which will serve the chopper spectrometers of the ESS. These instruments, since they are based on inelastic neutron scattering, are particularly background-sensitive, and a large Signal-to-Background Ratio (SBR) is a key requirement for them. For this reason, sources of intrinsic scattered neutron background for the Multi-Grid detector were determined and studied separately, and for the first time, thermal neutron scattering background sources were modelled in a detailed simulation of detector response. Based on the results obtained, optimisation of the internal detector shielding was started in order to increase the SBR via background-suppression.

## Results

For the BCS detector, the detection efficiency was determined for representative incident neutron energies in multiple detector-system setups, and recommendations are made for a multi-panel design. The absorption and activation of the structural materials are found to be sufficiently low, as well as the scattering effects for SANS applications. The simulations revealed the limitations the detector choice is subjected to and provided valuable input for the decision-making process of the final detector design.

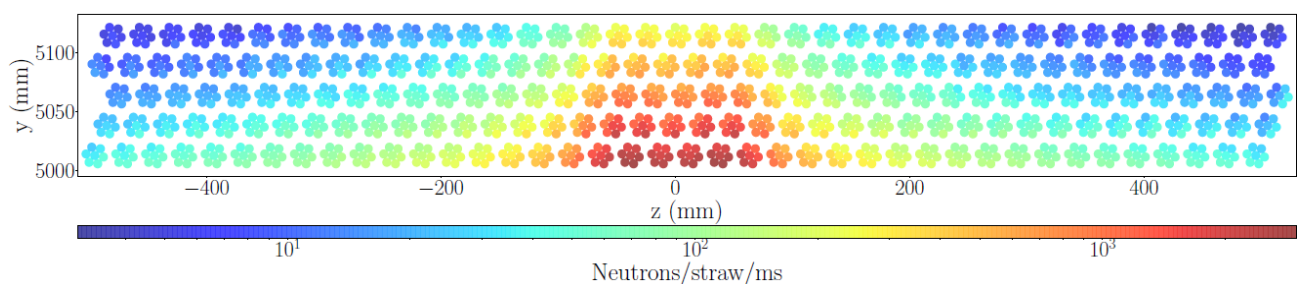


Figure 1: Peak incident rate per BCS straw for realistic worst-case scenario for SANS instruments at ESS

The Multi-Grid detector model was validated against measured data from previous detector tests, being part of the overall validation of the used simulation framework. The comparison of the impact of scattering on different detector and instrument components emphasised the importance of the intrinsic detector background, providing input for further design optimisation for background suppression.

## Remaining work

The detector count rate study is a three-year project. Specific simulations are going to be performed for the BIFROST instrument of the ESS in the remaining one year.

## Related publications

- [1] K. Kanaki, M. Klausz, T. Kittelmann, G. Albani, E. Perelli Cippo, A. Jackson, S. Jaksch, T. Nielsen, P. Zagyvai, R. Hall-Wilton, *Detector rates for the Small Angle Neutron Scattering instruments at the European Spallation Source*, Journal of Instrumentation (JINST) **13**, P07016 (2018) [doi: 10.1088/1748-0221/13/07/P07016](https://doi.org/10.1088/1748-0221/13/07/P07016)
- [2] E. Dian, K. Kanaki, G. Ehlers, R.J. Hall-Wilton, A. Khaplanov, T. Kittelmann and P. Zagyvai, *Scattered neutron background in thermal neutron detectors*, Nuclear Inst. and Methods in Physics Research, A **902**, 173–183 (2018) [doi: 10.1016/j.nima.2018.04.055](https://doi.org/10.1016/j.nima.2018.04.055)

# ENGINEERING AND NEUTRONIC DESIGN OF AN EXPERIMENTAL CAVE FOR THE EUROPEAN SPALLATION SOURCE

*Szabina Török, Péter Zagyvai, Milán Klausz, Viktória Sugár*

## Objective

The focus in this part of the project is to find engineering solutions of Neutron Macromolecular Diffraction (NMX) Experimental Cave, which is to be built as part of the European Spallation Source (ESS) in Lund, Sweden. The experimental cave provides biological shielding to personnel standing outside its walls while the neutron shutters allow the beam inside the cave. The cave also provides a reduction of background radiation reaching the detectors inside the cave.

## Methods

Based on a complex requirement system provided by the ESS, the cave has to comply with numerous requirements like radiology, stability, functional as well as manufacturing and transport related constraints. This year, the main objective of the project was to present the mechanical design of the system and to demonstrate its capability to fulfil the requirements and comply with the engineering constraints. The compliance will have to be proved by a complex 3D model, multiple radiology Monte Carlo N-particle Transport Code (MCNP) simulations and structural engineer's statement.

## Results

The existing model is a result of development, where the model had gone through several versions before reaching current design (Figure 1). The cave walls and roof are a reinforced concrete structure assembled from premanufactured units of 90 cm thickness. This bulk is necessary to protect the users from radiation emerging in the cave.

Concerning the layout, the basic shape is an 'L', which is designed to contain a labyrinth to protect the entrance door which is located in front of the labyrinth. It can be accessed from a separate landing structure equipped with lift for pallets and stairs. There are two separate concrete beams to support the robot rails which are designed to bear the loads of the robots moving the detectors inside the cave.

The chicane of the walls and slabs are needed to comply with the neutronic design requirements of chicane geometry and overlapping of elements. The roof is constructed of two layers, both are supported by the walls. The floor cable inlets are also designed as chicanes. They are situated under the first row of wall units connecting to the floor. The cables are then bended upstream, for which the floor slabs of the cave have openings next to the wall. The floor slabs next to these openings are not exceeding 1,5 tons thus the internal crane can be used for moving them if re-cabling is necessary.

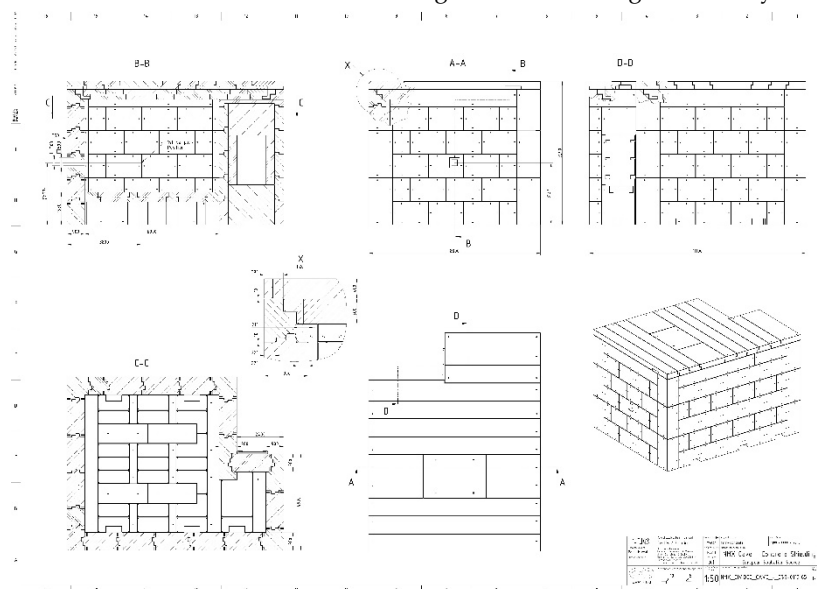


Figure 1: Representative networks of cluster 1 and 2

## Remaining work

The project is to be continued with the detailed design of the cave.

## Related publication

- [1] V. Sugár, Sz. Török, P. Zagyvai, G. Náfrádi, G. Aprigliano: *Experimental Cave Design for Neutron Diffraction at a High Brilliance Source*. The 8<sup>th</sup> International Conference on Charged and Neutral Particles Channeling Phenomena 2018, Ischia

# CONCRETE ACTIVATION STUDY FOR THE EUROPEAN SPALLATION SOURCE

*Eszter Dian, Katalin Gméling, Dávid Hajdú, Péter Zagyoai*

## Objective

The European Spallation Source (ESS) aspires to be the brightest neutron source of the world, which requires joint and organised efforts of the neutronic community, as well as research and development in additional fields like radiation shielding.

A new PE-B4C-concrete (polyethylene, boron-carbide) has been developed as part of the SINE2020 project, to improve the neutron absorption effect of concrete for neutron energies below 10 MeV, where iron has resonances in the cross section. It is essential to know the activation of the shielding material, like the concrete and metal components, considering both short-term effects on personnel during the operation phase, and long-term effects in the decommissioning of the ESS facility. Two other types of concrete samples were irradiated along with the PE-B4C samples: the “reference” concrete - a standard concrete from which the PE-B4C version was developed, - and the “Skanska” concrete. The double aim of the current study is to compare the neutron activation properties of the new PE-B4C-concrete to those of the reference concrete, and to determine the impact of the trace elements on the generated activity and recommend concrete compositions for conservative Monte Carlo activity simulations, that involve relevant trace elements in addition to the nominal composition, provided by the manufacturer.

## Methods

For the shielding activation study, typical shielding concrete samples were irradiated in the fast and the rotating vertical irradiation channels of the Budapest Research Reactor for neutron activation analysis (NAA). The gamma-rays emitted by the samples were then measured with an HPGe detector, from which their activity and composition was determined. The chemical composition of the samples was also determined with X-ray fluorescence (XRF) and prompt gamma activation analysis (PGAA). The measured activities were compared to the results of Monte Carlo N-Particle Transport Code (MCNP) activation simulations based on the measured and nominal concrete composition data, respectively.

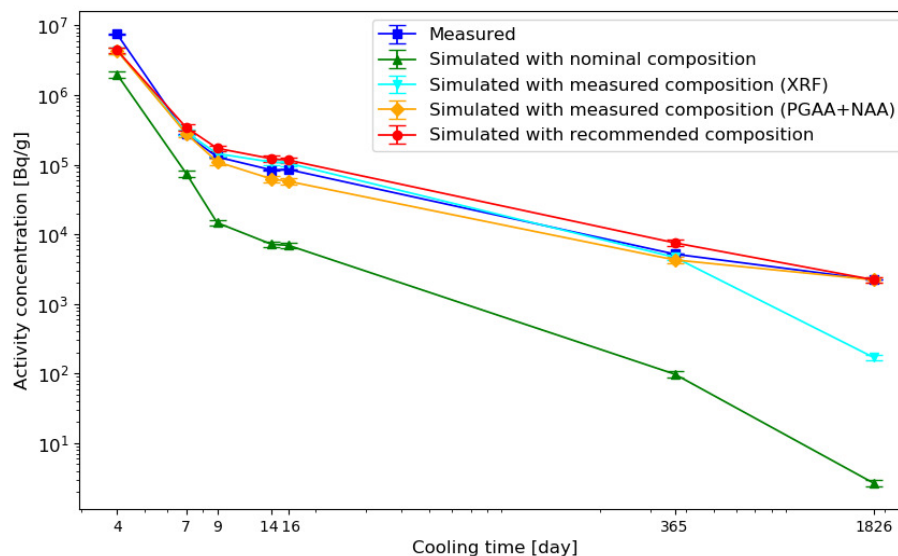


Figure 1: Measured and simulated total activity concentration in PE-B4C-concrete with nominal (provided by the manufacturer) and measured (PGAA NAA and XRF) initial compositions

## Results

The activation experiment confirmed that the newly developed PE-B4C-concrete is not activated as much as the initial reference concrete, but the study also revealed the importance of trace elements in terms of activation. A recommended, effective composition was developed for more detailed and conservative MCNP simulations, of the three studied concrete samples.

## Remaining work

A summarising publication is in progress on the impact of concrete trace elements in neutron-generated activity.

## Related publication

- [1] E. Dian et al: *Preparation for activation measurements of concrete and PE-B4C-concrete to be applied for shielding at the European Spallation Source*, J. Phys.: Conf. Ser. **1021**, 012050 (2018)

# TRANSNATIONAL ACCESS WITHIN THE EC H2020 IPERION CH PROJECT

Zsolt Kasztovszky<sup>1</sup>, László Szentmiklósi<sup>1</sup>, Zoltán Kis<sup>1</sup>, Ildikó Harsányi<sup>1</sup>, Adél Len<sup>1,2</sup>, Katalin Bajnok<sup>2</sup>, György Káli<sup>2</sup>, Imre Kovács<sup>2</sup>, Zoltán Szőkefalvi-Nagy<sup>2</sup>, László Rosta<sup>2</sup>, Veronika Szilágyi<sup>1</sup>

<sup>1</sup>Centre for Energy Research, <sup>2</sup>Wigner Research Centre for Physics

## Objective

Within the IPERION CH H2020 project, transnational access is offered for experts of Heritage science to use the instruments of the Budapest Neutron Centre. In the short term experiments available there, compositional and structural data are obtained non-destructively, and information regarding provenance, condition, and genuineness of the objects are obtained.

## Methods

Prompt Gamma Activation Analysis (PGAA), Prompt Gamma Activation Imaging (PGAI), Neutron Activation Analysis (NAA), Neutron Radiography (RAD), Time of Flight Neutron Diffraction (TOF-ND), Small Angle Neutron Scattering (SANS) and complementary Proton Induced X-ray Emission (PIXE) measurements can be applied for.

## Results

In 2018, 14 experimental proposals have been completed. Four experiments were done to determine the chemical composition of historical glass from Roman, Byzantine and Medieval ages, in order to identify the producing workshops. Four proposals aimed to study the composition (PGAA) and the microstructure (RAD) of Neolithic and Renaissance pottery. One proposal aimed to characterize the production techniques of Bronze Age belts; one dealt with Celtic coins, and two were about the provenance of chipped stone raw materials, such as flint and obsidian. One proposal was submitted to study the salt absorption properties of various porous building materials.

**Highlight: Analysis of Celtic silver coins from Slovenia - Žiga Šmit, Faculty of Math. and Physics, University of Ljubljana**

Celts started to mint iron coins by the 2nd c. BC, following the Greek nominal coinage system. Beside tetradrachms, many small coins were in circulation, which are frequent finds in the eastern Alps. Prior analyses showed that the silver content for two important sites, Magdalensberg (Austria) and Celje (Slovenia) differ. 74 coins were measured with PIXE and PGAA. Kernel density estimates (KDE) from PGAA show that, contrary to the PIXE results, the coins contain varying proportions of silver, between 50 and 90 m%. The difference between the PGAA and the PIXE results has to do with the fact that the PIXE method only samples the surface material, while the PGAA method samples the whole volume of the object. For a few coins, in-beam NAA was made to determine the gold content at the trace level. The silver content distribution, obtained by PGAA is double-peaked and dominated by two coin types, with rosette and with horse motifs. One peak corresponds to coins with a base-silver core of about 50 m% Ag, while the other contains silver of about 80 m% Ag. The two different types exhibit similar silver purity distributions, which reflects two different recipes of making silver alloy formulas.



Figure 1: A set of silver coins at the NIPS-NORMA station

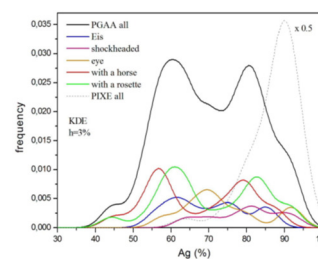


Figure 2: Silver content in all coins and in particular types – PGAA vs. PIXE data

## Related publications

- [1] B. Constantinescu, D. Cristea-Stan, Z. Szőkefalvi-Nagy, I. Kovács, I. Harsányi, Zs. Kasztovszky: *PIXE and PGAA – Complementary methods for studies on ancient glass artefacts (from Byzantine, late medieval to modern Murano glass)*, Nuclear Instruments and Methods in Physics Research B **417**, 105 (2018)
- [2] N. Zacharias, M. Kaparou, A. Oikonomou, Zs. Kasztovszky: *Mycenaean glass from the Argolid, Peloponnese, Greece: A technological and provenance study*, Microchemical Journal **141**, 404 (2018).
- [3] M.I. Dias, Zs. Kasztovszky, M.I. Prudêncio, I. Harsányi, I. Kovács, Z. Szőkefalvi-Nagy, J. Mihály, G. Káli, A.C. Valera, A.L. Rodrigues: *Investigating beads from Chalcolithic funerary cremation contexts of Perdigões, Portugal*, Journal of Archaeological Science: Reports **20** 434 (2018)
- [4] D. Di Martino, E. Perelli Cippo, W. Kockelmann, A. Scherillo, T. Minniti, R. Lorenzi, M. Malagodi, C. Merlo, T. Rovetta, G.V. Fichera, M. Albano, Zs. Kasztovszky, I. Harsányi, G. Gorini: *A multidisciplinary non-destructive study of ancient pipe organ fragments*, Materials Characterisation, **148**, 317 (2019)
- [5] Ž. Šmit, B. Maróti, Zs. Kasztovszky, A. Šemrov, P. Kos: *Analysis of Celtic small silver coins from Slovenia by PIXE and PGAA. Poster presentation, 16th Internal Conference on Particle-Induced X-ray Emission. 24-29 March 2019, Lisbon, Portugal*

# COLD NEUTRON MODERATOR DEVELOPMENT AND COLD SOURCE UPGRADE PROJECT AT BUDAPEST RESEARCH REACTOR

*József Janik, László Rosta*

## Objective

The European Spallation Source AB has developed the novel concept of so-called low dimensional neutron moderators. Monte Carlo Simulations have shown that this concept can improve the performance of the facility (measured in moderator brightness) by a factor of two to five in comparison to conventional volume moderator designs. On the one hand, our objective in joining this activity was to contribute to moderator developments based on the experimental possibilities of the liquid hydrogen moderator operating at BRR; and on the other hand, to design a new vessel for the BRR (Budapest Research Reactor) cold neutron source (CNS) and also to prepare the manufacturing plans for the complex up-grade of this CNS.

## Methods

This activity was a part of the H2020 BrightnESS project and ran on several lines. The first step was to perform a reactor simulation on BRR including the CNS. MCMPX (Monte Carlo Method particle extended) was used to calculate the neutron and gamma field of the core, and then the calculation was extended to the moderator cell. The shape of the moderator cell was optimized by iterating for the best neutron brightness at the vessel exit and these results were used as input for the thermal-hydraulics investigations. Throughout the calculations, it was considered that the cell should be filled by para-hydrogen at as high as possible ratio with respect to ortho-hydrogen.

Our experimental approach was to measure the para-hydrogen content in the currently used CNS cell. For this case, the CNS should have run without reactor-on power, since the ortho-para equilibrium below 30K° starts shifting toward the para-hydrogen state and it will fill the cell. This process is labelled as precooling. The result of this regime modification was that the level of neutron brightness was increased as it was measured by SANS (Small-angle Neutron Scattering).

## Results

Results of the simulations:

1. The optimization has shown that a low dimension type bare moderator cell has a two times higher neutron brightness than the existing cylindrical volume moderator vessel. The parameters of the low dimension type bare moderator cell were varied in the following range: radius 10-25 mm, length 90-180 mm. The moderator cell is filled with pure para-hydrogen during the optimization.
2. The applicability of a pre-moderator material was also studied. Using light- and heavy water as material of a pre-moderator could increase the neutron brightness for a low dimension moderator bare cell by 6-8 %.

The low dimension type bare moderator cell is very sensitive to the type of filling material. The high level of para-hydrogen purity in the low dimension type moderator cell must be maintained for all periods of the reactor cycle. Otherwise the neutron brightness decreases below the level which can be reached by the thick moderator. When the para-hydrogen ratio is less than 90% the thick moderator cell has better neutron properties.

Results of the measurements:

A series of pin-hole camera time-of-flight measurements were carried out to understand the possible improvement of our current brightness with the neutron moderator cell, so we can modify the ortho-para hydrogen ratio in the moderator cell. Although the measurements were not fully convincing about the geometrical effect of the low dimensional moderation (non-adequate geometry), the positive outcome was that we found a new working regime for the operation with a considerable gain in flux from the current CNS.

Plans for manufacture:

The design of a low dimensional moderator cell was elaborated and the optimal manufacturing technology is being developed. We found two methods: one is the 3D metal printing; the other is the electron beam welding. Both methods are under test.

## Remaining work

A new test equipment is being considered at the reactor hall. We are going to use this experimental bench for testing the new moderator cell. It requires, however a careful redesigning of the biological shielding of fifth and fourth channels in the reactor hall.

## Related publications

- [1] J. Füzi, V. Heirich, Z. László, A. Len, J. Orbán, L. Rosta, J. Janik: *Compact equipment for neutron source imaging*, VII UCANS conference, San Carlos de Bariloche, Argentina, (2018)
- [2] L. Rosta, M. Rogante: *Neutrons for materials research*, Proc. 7th Int. Conf. "Mechanical Technologies and Structural Materials" MTSM 2017, Split, Croatia, 21-22 Sept. 2017, S. Jozić, B. Lela, Eds., Croatian Society for Mechanical Technologies Split, Croatia (2017) italic, Editor (2018)

# PARTICIPATION IN THE ACTIVITIES OF THE MULTIDISCIPLINARY EUROPEAN LOW DOSE INITIATIVE

*Balázs Madas*

## **Objective**

MELODI (Multidisciplinary European Low Dose Initiative) is a European radiation protection research platform with a focus on research on health risks after exposure to low-dose ionising radiation. MTA EK is one of its members since 2013. A major activity of MELODI is the establishment and updating of a long term (>20 years) Strategic Research Agenda (SRA) for research on low dose risk for radiation protection in Europe. The SRA is intended to guide the priorities for national and European research programmes and the preparation of competitive calls at European level.

In October 2017, the European Commission indicated its intention to open a EURATOM call that includes radiation protection. The proposed work programme included topics NFRP-2018-8 for research and NFRP-2018-9 for review of previous activities. NFRP-2018-8 specifically indicated that a 'Gap analysis' will be required for each proposal. Therefore, the preparation of a gap analysis was a specific objective for 2018.

## **Methods**

A dedicated working group (WG) for the development of the SRA has been formed in 2014 with one member from MTA EK. Since then, the WG regularly updates the SRA based on new findings and newly identified research needs. The WG meets once or twice a year. Since 2016, the European Radiation Protection Week series has been providing input and an open forum for discussions on the MELODI SRA. In 2018, a series of dedicated Workshops on different topics was also launched.

For the gap analysis, the WG reviewed relevant EURATOM research undertaken in Framework Programmes 6 and 7 (FP6, FP7) and Horizon 2020 (H2020) identifying their relevance to the six key areas of research identified in the MELODI SRA and roadmap: (1) To explore the shape of the dose-response relationship for radiation-induced health effects; (2) To understand the potential impact of individual susceptibility on radiation-induced health effects; (3) To identify, develop and validate biomarkers for exposure, early and late effects for cancer or/and non-cancer diseases; (4) To explore and define the role of epigenetic modifications in radiation-induced health effects; (5) To explore the roles of specific target cells for radiation-induced late developing health effects; (6) To understand the health effects of inhomogeneous dose distributions, radiation quality and internal emitters.

## **Results**

A three-day-long MELODI Workshop on Individual Radiosensitivity and Radiosusceptibility was held in Malta in March. Sessions were organized in three topics: Clinical and epidemiological observations, Mechanisms involved in radiation sensitivity, Screening systems. On the last day, there were synthesis sessions in order to prepare position papers in each topic. The 3<sup>rd</sup> European Radiation Protection Week was held in Croatia in October. On the first day, a plenary session was devoted to presenting the results of the workshop on individual sensitivity. MTA EK was strongly involved in the session entitled "Understanding the health effects of inhomogeneous dose distributions, radiation quality and internal emitters (incl. Space)" as one of the co-chairs and one of the presenters had come from MTA EK.

The review of relevant EURATOM research surveyed the identification of gaps that were considered as potential areas for research under NFRP-2018-8 call. A mature reflection and identification of knowledge gaps would require results of all projects to be available; this has not been possible in all cases as some projects have not come to completion yet. There have been many projects supported under FP6, FP7 and H2020 that address issues highlighted by MELODI as key areas requiring research to improve low dose and low dose rate radiation health risk assessment. All funded projects align with one or more of MELODI's key areas as identified in the SRA and roadmap. All have contributed to advancement of the field and building the scientific evidence base for low-dose/dose-rate risk assessment. All diseases/health effects of actual and potential relevance to low dose risk (cancer, circulatory disease, cognitive effects and cataract) have been considered and a shift in emphasis amongst funded projects towards the non-cancer diseases could be seen. While all projects have made progress in building the evidence base, there remain areas where additional work could be beneficial; these are considered in the gaps described in the MELODI Statement 2018. The WG anticipated that its gap analysis was going to be of benefit to those applying to the calls. The gap analysis was presented in different meetings including the European Radiation Research 2018 conference held in Pécs [1].

## **Remaining work**

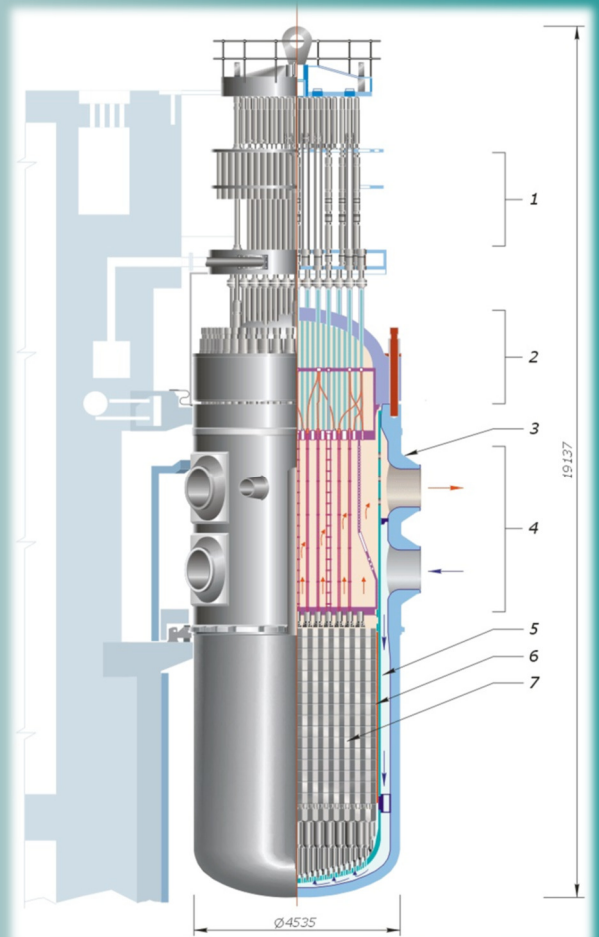
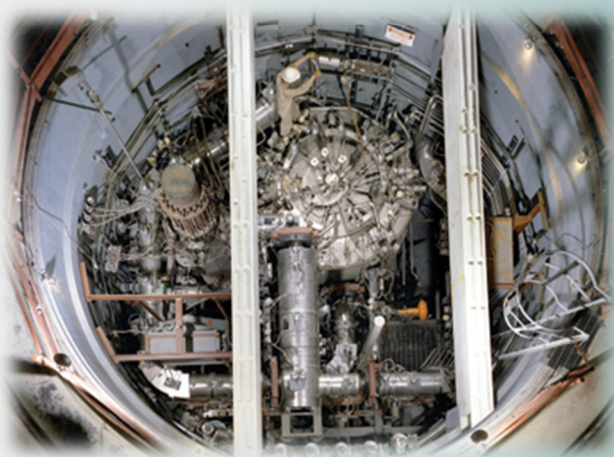
A revision of the SRA is due in 2019. Manuscripts of the position papers on individual sensitivity are to be finalized in early 2019. MELODI Workshops on non-cancer effects (2019) and on the effects of inhomogeneous exposures (2020) have to be prepared. The latter will be held in Hungary with strong involvement of MTA EK.

## **Related publication**

- [1] B. G. Madas, A. Auvinen, E. Cardis, M. Durante, M. Harms-Ringdahl, J. R. Jourdain, et al.: *Research prioritisation in MELODI*, European Radiation Research, Pécs, Hungary, 21-25 August, 2018 p. 115 (2018)



## II. RESEARCH AND DEVELOPMENT RELATED TO NUCLEAR POWER PLANTS



# PREPARATION OF THE FUROM 2.2 CODE VERSION

*János Gadó, Ágnes Griger, Katalin Kulacsy*

## **Objective**

The FUROM code had been developed in the institute about 20 years ago for the analysis of fuel behaviour in VVER-440 reactors. It was further improved using up-to-date results of measurements and state-of-the-art models. As a consequence, several official versions were released over the years. Now the version FUROM 2.2 is under preparation. The aim is to refine the modelling of fuel swelling, densification and other phenomena, to make it possible to apply the code for VVER-1200 calculations and also to perform minor corrections. The new official version FUROM 2.2 will be issued by September 2019.

The work is financed by MVM Paks NPP Co.

## **Methods**

New models are selected based on extensive review of the literature and the available experimental data. Then they are built in and tested. Bug fixes constitute an important part of the work as well. Special attention is given to increase the transparency of the code for future programmers. The code documentation (model description, programmers' guide and users' guide) will be upgraded and the validation will be repeated.

## **Results**

In 2018 the modelling of fuel swelling was studied. The new code version allows for using a conservative and a best estimate dependence of swelling on fuel burn-up, and a more detailed model that takes into account the swelling of the pellet matrix due to solid fission products is also made available. New densification models were also introduced. One of them is based on the temperature dependence of densification rather than on the burn-up dependence. A new model has been introduced to describe the growth of UO<sub>2</sub> grains. The model of high temperature recrystallization has been corrected. The code results with the various models will be compared to experiments in 2019. Furthermore, the calculation of VVER-1200 fuel was also made possible, though certain correlations have still to be established using reactor physics codes.

The calculation speed was basically improved in connection with avoiding the repetitive calculation of power and burn-up distributions in the pellet. Various solutions were applied to decrease the memory need of the code and to introduce mnemonic technical simplifications.

A summary description of the FUROM code was published [1].

## **Remaining work**

Further model improvements have to be finalized. Validation of the code has to be performed. The new documentation has to be prepared.

## **Related publication**

- [1] J. Gadó, Á. Griger, A. Kulacsy: *The fuel behaviour code FUROM and its high burn-up simulation capabilities*, Nuclear Engineering and Design **327**, 274-285 (2018)

# DEVELOPMENT OF ADVANCED METHODOLOGIES AND MODELS FOR FUTURE STRUCTURAL INTEGRITY CALCULATIONS

*Tamás Fekete, Dániel Antók, Levente Tatár*

## Objective

The final objective of the research program is to develop a unified, coherent analysis methodology and also advanced models for future nonlinear SI calculations of various safety relevant systems of Nuclear Power Plant (NPP) units.

The main research directions of the program are formulated as follows:

- Large deformation models for analyses of engineering structures;
- Complex constitutive models for future engineering SI problems;
- Advanced assessment methods for evaluations of material tests;
- Long-time ageing of RPV structural materials.

For details see the EK Annual Report 2017, page 33. Methods

In the theoretical part of the project, a material model development – based on a systematic theoretical study – is being conducted in order to elaborate a state-of-the art theoretical and simulation method that seems promising for applications in future industrial SI projects. In the modelling part, numerical models are being developed for special research problems first. These models will be further developed for industrial applications.

## Results

The main goal during the theoretical part of the project was the elaboration of a complex material model that is able to describe plasticity and damage in a coupled fashion. Large deformation plasticity theory is used to model the effects of geometrical nonlinearities. Plastic-damage material behaviour is modelled in many instances by the Gurson–Tvergaard–Needleman (GTN) material model. The GTN model is based on the hypothesis that the impairment caused by void nucleation and growth in a metal may be macroscopically described by extending the von Mises plasticity theory using one scalar damage variable. Despite the fact that when using the GTN model one is able to follow the weakening of elastic-plastic metallic materials on a qualitative level, the model has some weaknesses. Among these, and one of the most problematic, is the overly simplistic model used for the description of damage evolution. Based on lessons learned from earlier numerical works and extensive literature studies, the GTN model has been redesigned. The new model is called the modified GTN model below. The central part of the modified GTN model, the plastic potential, is of the form:

$$\Phi(T, \sigma_m, d, f) = \frac{\sigma_v^2(T)}{\sigma_m^2} + 2q_1 \cdot d \cosh\left(q_2 \frac{\text{tr}(T)}{2\sigma_m}\right) - (1 + (q_1 \cdot d)^2) = 0$$

where  $T$  represents the Cauchy stress tensor, and  $\sigma_v$  designates the local, equivalent von Mises stress. The yield stress of the matrix material is designated by  $\sigma_m$ ,  $d$  denotes the mesoscopic damage variable, and  $f$  represents the microscopic – or equivalently called microlocal – damage variable in the matrix material. The parameter  $q_1$  is called the damage-mechanical coupling parameter, and  $q_2$  is called the triaxiality parameter, and has the same form as in the original GTN model. Originally,  $q_1$  and  $q_2$  were introduced by Tvergaard to improve the behaviour of the model for larger values of  $f$ . Here,  $q_1$  plays a slightly modified role compared to that in the original model, while  $q_2$  has the same form and meaning as in the original GTN model. The evolution equation for the mesoscopic damage variable  $d$  is formulated in this model according to the theory of weakly nonlocal –diffusive– internal variables in the internal variable approach of irreversible thermodynamics, as follows:

$$\dot{d} + a\nabla \cdot (b\nabla d + c\nabla \dot{d}) = \dot{f}$$

where  $\dot{\phantom{x}}$  denotes time derivation. The source term for the mesoscopic damage evolution is the evolution rate of the microlocal damage variable ( $\dot{f}$ ), which is composed of the sum of microlocal damage growth associated (1) with plastic strain rate in the matrix  $\dot{f}_{mat}$ ; (2) with a number ( $i$ ) of smaller, transient accelerations? of damage, – each of them causing faster, but not final, catastrophic weakening in the material at around distinct critical values of  $\varepsilon_p$  (designated as  $\varepsilon_{crit}$ ) – called  $\dot{f}_{crit}^i$ ; and (3) with the jump-like acceleration of microlocal damage, – at  $\varepsilon_{crit}^{final}$  – called  $\dot{f}_{final}$ , causing the final, fast stability loss of the material:

$$\dot{f} = \dot{f}_{mat} + \sum_i \dot{f}_{trans}^i + \dot{f}_{final} = \overbrace{(1-f) \cdot \text{tr}(\dot{\varepsilon}_p)}^{mat} + \sum_i \overbrace{A(\varepsilon_{crit}^i) \cdot \dot{\varepsilon}_m}^{trans} + \overbrace{B(\varepsilon_{crit}^{final}) \cdot \dot{\varepsilon}_m}^{final}$$

where  $\varepsilon_p$  designates the plastic strain tensor, and  $\varepsilon_m$  denotes the equivalent plastic strain as follows:

$$\dot{\varepsilon}_m = \sqrt{\frac{2}{3} \varepsilon_p : \varepsilon_p}, \varepsilon_m = \int_0^t \dot{\varepsilon}_m d\tau$$

It is assumed that during a transient acceleration of microlocal damage, the kinetics of the phenomenon may be characterized with a normal distribution around  $\varepsilon_{crit}$ ; therefore,  $A(\varepsilon_{crit})$  is defined as:

$$A(\varepsilon_{crit}^i) = \frac{f_n^i}{\sqrt{2\pi(s_n^i)^2}} \cdot \exp\left(-\frac{(\varepsilon_m - \varepsilon_{crit}^i)^2}{2(s_n^i)^2}\right)$$

where  $\epsilon_{crit}^i$  denotes the critical value of  $\epsilon_m$  at the  $i$ -th critical step,  $s_n^i$  means the standard deviation of  $\epsilon_m$  around  $\epsilon_{crit}^i$  and  $f_n^i$  designates the weight factor (which describes the influence of the process on the microlocal damage evolution rate). It is assumed in the description of the final failure that the jump-like acceleration of the microlocal damage may be characterized with a three parameter Weibull distribution around  $\epsilon_{crit}^{final}$ ; therefore,  $B(\epsilon_{crit}^{final})$  is defined as:

$$B(\epsilon_{crit}^{final}) = \frac{\alpha \cdot f_n^{final}}{(s_n^{final})^\alpha} \cdot (\epsilon_m - \epsilon_{crit}^{final})^\alpha \exp\left(\frac{-(\epsilon_m - \epsilon_{crit}^{final})^\alpha}{2(s_n^{final})^\alpha}\right)$$

where  $\epsilon_{crit}^{final}$  denotes the critical value of  $\epsilon_m$  at final failure,  $s_n^{final}$  is the scale parameter,  $\alpha$  is the shape parameter of the distribution, and  $f_n^{final}$  designates the weight factor (which describes the influence of the process on the microlocal damage rate). According to preliminary calculations for the evolution of the mesoscopic damage variable  $d$ , the modified GTN model will be able to simulate the ‘multi-stage’ character of load carrying capacity attenuation, observed on many materials, including structural steels. Based on the results, a typical example showing the nature of the evolution of the mesoscopic damage variable  $d$  during steady, extremely slow stretching is depicted in Fig. 1. The material model will be incorporated into user defined subroutines available in the MSC Marc FEM system.

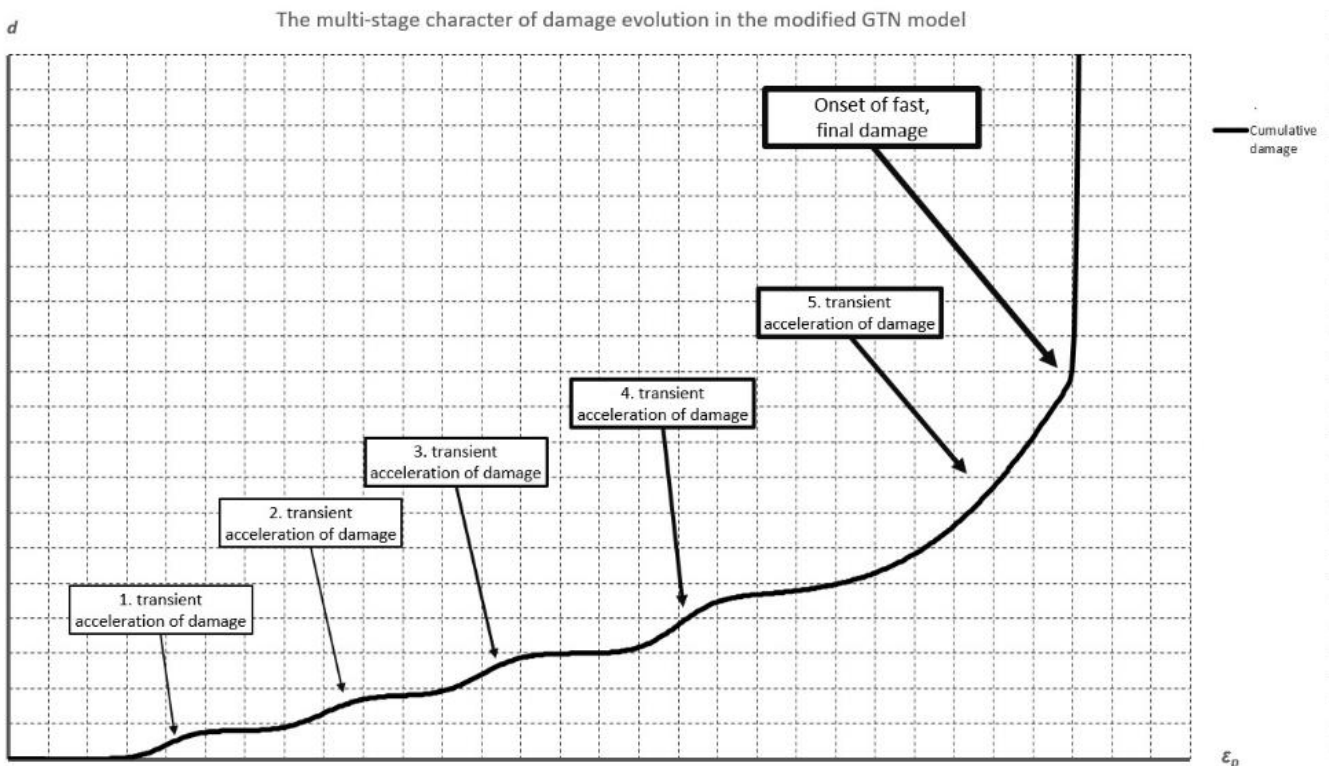


Figure 1: The multi-stage character of damage evolution, according to the modified GTN model

In the modelling part of the project, the calculation methodology that simulates the ballooning tests of fuel cladding tubes has been further developed based on a geometrically and materially nonlinear formulation of the problem. Thermomechanics, employing large deformation plasticity, was used to model the effects of geometrical and material nonlinearities that are present in the system during calculations. The temperature dependent plastic flow curves of structural materials have been developed from tensile test results, performed at many temperatures. Numerical calculations were performed using the MSC Marc FEM code. During the process, a parametric study was conducted to assess the influence of material inhomogeneities on the test results, because – based on theoretical considerations – it was expected that material inhomogeneities can have strong effects on the final state, more specifically on the geometry and on the stress-strain state of the test piece.

The 3D finite element models of the ballooning specimens have been tested. The final shapes of some specimens are shown on Fig. 2. The simulations have been performed on a geometrically perfect tube model, with an assumed flat material inhomogeneity (see Fig. 3. a). The calculation results for the total equivalent plastic strain at the last calculated time step are presented in Fig 3. (b). It can easily be seen that the geometrical shape of the specimen evolves into a pronounced asymmetric 3D structure, which is very similar to the shape of the tested specimens. The calculated results for the temperature distribution can be seen on Fig. 4. (a), while the results for the equivalent von Mises stress distribution at the last calculated time step are presented in Fig 4. (b).

Based on the improved theoretical and numerical results, it can be stated that the more complex models provide a deeper understanding of the events occurring during the material tests, as well as contributing to the development of more advanced models for future SI calculations of fuel cladding tubes.



Figure 2: Fuel cladding tube pieces after the ballooning tests

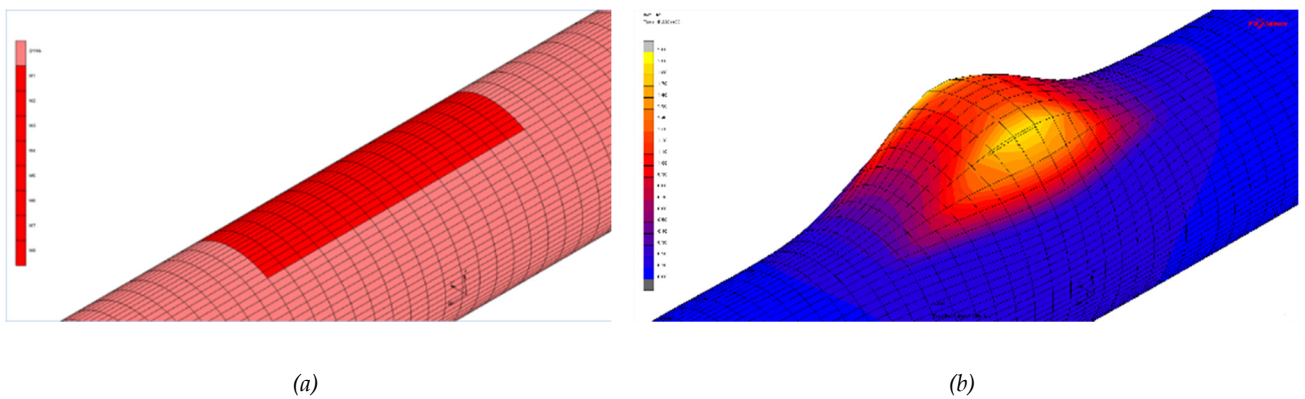


Figure 3: FEM model of a tube piece with flat initial material inhomogeneity distribution (a), final results –shape and equivalent plastic strain field– of the ballooning simulation (b)

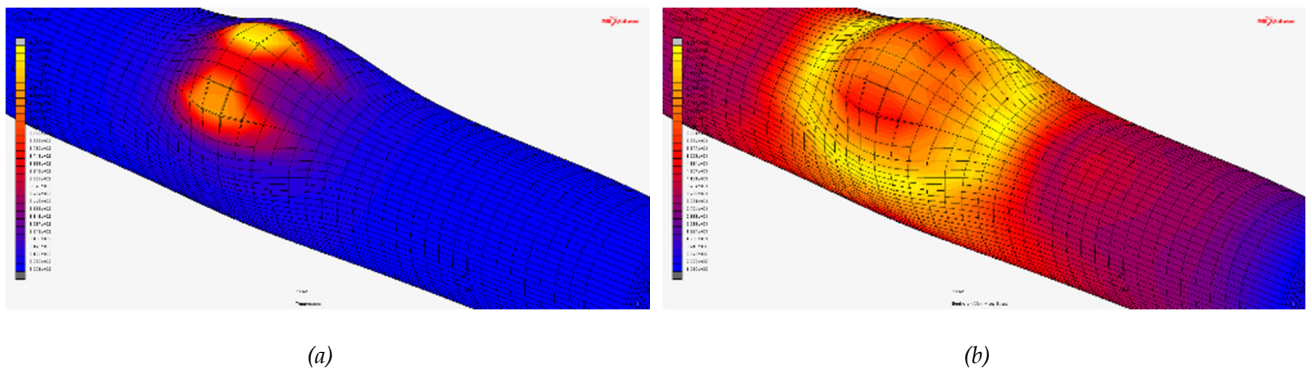


Figure 4: Final FEM model results for the ballooning simulation of a tube piece: temperature field at the final stage (a), and equivalent von Mises stress field (b)

The parameters of a given material model can be determined by adequate measurement procedures. A measurement procedure consists of the necessary observations and their evaluation using the very same material model. During SI calculations, the behaviour of a structure will be examined with its more complex geometrical model which is dependent on the material model of the relevant phenomena occurring in the structure during its operation. The key point for reliable calculation results is that the same material model needs to be applied to the structure model as well as to the material model used to evaluate the material tests, to meet the essential requirement that ‘*the theory and the experiments need to be harmonized*’. Nowadays, very simple material models are used in standard measurement evaluation procedures, but cannot be used to determine the parameters of complex material models. Advanced assessment methods for the evaluations of material tests have been developed therefore, in order to ensure that the appropriate theoretical framework is used when estimating the parameters of a material model. 3D numerical models have been developed for the evaluation of three-point bend fracture mechanics tests (see Fig. 5. a), using the MSC Marc FEM system. In parallel with the theoretical and numerical work, an optical data acquisition and data evaluation system has been developed and tested, with the aim of supporting the measurement evaluation process with more detailed and accurate geometrical data. A representative picture of a specimen during a three-

point bending test is presented in Fig. 5 (b). Combining the high-performance, computing assisted, measurement simulations with more accurate geometrical data registered during the tests, paves the way to extract more reliable data from the measurement procedures for future industrial calculations in the near or mid future.

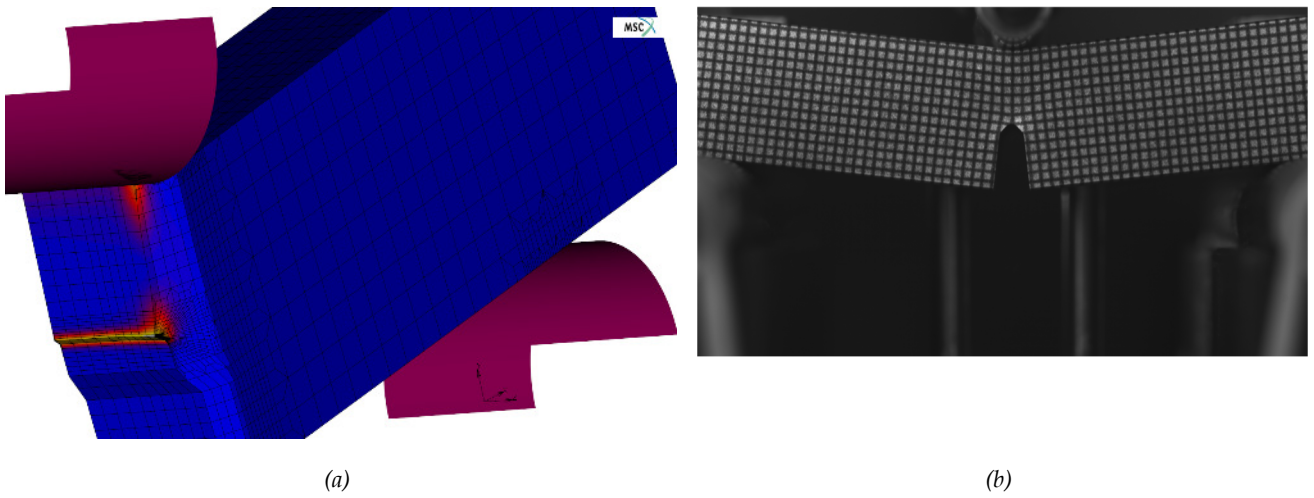


Figure 5: 3D FEM model of a three-point bend fracture mechanics specimen (a), a photo made of a three-point bend fracture mechanics specimen during the measuring process (b)

# START-UP AND TRANSIENT CALCULATIONS IN TRANSURANUS FUEL BEHAVIOUR MODELLING CODE

*Eszter Kozsda-Barsy, Katalin Kulacsy*

## Objective

During start-up of the 30th cycle of Unit 4 of the Paks NPP a short and steep increase in power occurred. The Hungarian Atomic Energy Authority commissioned MTA EK to conduct an independent study of this event.

## Methods

Due to the swelling of the pellet, the gap between the cladding and the fuel decreases with increasing burnup, and once it disappears PCMI (pellet-cladding mechanical interaction) occurs. During PCMI the cladding experiences stress, especially during power ramps. Meanwhile fission products cause corrosion on the surface of the cladding. The effect of stress along with corrosion may lead to stress-corrosion cracking (SCC) and crack propagation which may lead to fuel rod failure and coolant contamination. For this reason, an upper limit (SCC limit) is imposed to tangential stresses. Further quantities relevant to cladding integrity are yield stress, ultimate tensile strength and the limit of 0.5% plastic strain.

We made simulations concerning the behaviour of a VVER-440 fuel rod at 0.8 MW<sub>e</sub>/min and 1 MW<sub>e</sub>/min ramp rates with the use of the TRANSURANUS fuel behaviour modelling code and studied the effect of the power spike on the cladding. We also simulated a worst-case scenario with a significantly larger spike.

After creating input time series, we ran 12 simulations and analysed the data. The evaluation of the results was based on the limits that determine the maximum allowed stresses in the cladding during safe operation.

## Results

The results of the simulations performed concerning the spike were compared to these limits (Fig. 1-2), and none of the limits was found to have been exceeded.

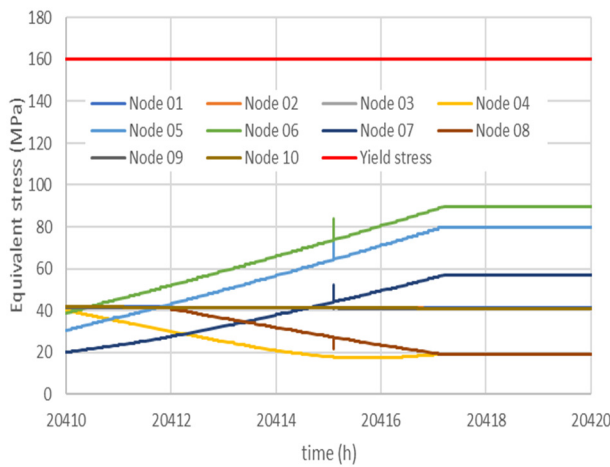


Figure 1: Effect of spike (t= 20415 h) on equivalent stress during start-up (the axial nodes of the rod are colour-coded, and the yield stress is red) in case of Sim. No. 5\*

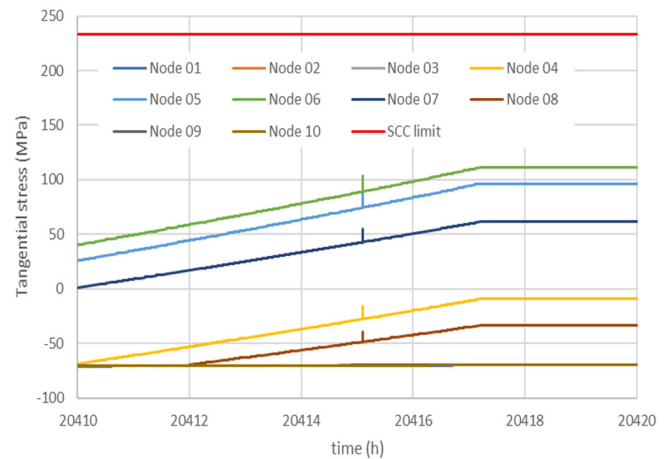


Figure 2: Effect of spike (t= 20415 h) on tangential stress during start-up (the axial nodes of the rod are colour-coded, and the SCC limit is red) in case of Sim. No. 5\*

\*Simulation 5: 0.8 MW<sub>e</sub>/min ramp rate, actual power spike

The lines of the axial nodes 1, 2, 3, 9 and 10 are overlapping on this scale.

## Remaining work

The project was finished as planned.

# INTRODUCTION OF NEW FUEL TYPES TO THERMAL POWER PLANTS: INTERNATIONAL METHODS FOR POST-IRRADIATION EXAMINATION OF LIGHT WATER REACTOR FUEL ASSEMBLIES

*Emese Slonszki*

## **Objective**

To maintain and improve the reliability of fuel assemblies and fuel elements, it is necessary to investigate and evaluate the effect of loads in the reactor on the behaviour of fuel assemblies. Therefore, we need to examine and analyse both the irradiated fuel assemblies and the individual fuel rods. This work aims to show the methods and equipment used for testing of non-leaking Light Water Reactor (LWR) spent fuel assemblies.

## **Methods**

Part of the methods used for post irradiation examinations, such as burnup determination or geometry measurements, can be performed under power plant conditions. In the hot cells, after appropriate sample preparation, further extensive tests can be carried out, including non-destructive and destructive procedures. In this work we summarized these methods.

## **Results**

Visual and dimensional inspections of spent fuel assemblies (FA) can be carried out even in the reactor pool. FA length, bowing and twist can be measured.

Hot cells non-destructive testing includes visual inspection (surface condition), profilometry (length, diameter, diametric and axial deformation, bow, quality), eddy current measurement (cladding integrity), interferometry (oxide thickness), gamma scanning and tomography (burnup).

Several destructive tests were also presented, like fission gas analysis (volume and composition), various microscopic techniques (pellet and cladding microstructural characterization), hot vacuum extraction and differential scanning calorimetry (hydrogen and deuterium content). In addition, techniques which are used to determine the chemical, mechanical and physical properties of the cladding were presented, like ion beam techniques as well as hardness, tensile, fracture toughness, fatigue testing and finally oxygen/metal ratio and thermal diffusivity measurements.

Spent fuels and fuel assemblies can extensively be characterized by the presented pool-side and hot cell post irradiation examination (PIE) techniques. These techniques are constantly being developed. All this contribute to the fact that the establishment and operation of a hot cell is very useful when introducing new fuel elements. This makes it possible to check and verify their safe operation.

## **Remaining work**

This project has been completed.

## **Related publication**

- [1] E. Slonszki: *Introduction of new fuel types to thermal power plants: International methods for post irradiation examination of LWR fuel assemblies*, MTA EK-FRL-2018-292-1-1-M0, in Hungarian (2018)

# MODELLING THE BREAKAWAY OXIDATION OF THE RUSSIAN E110 CLADDING

*Katalin Kulacsy*

## Objective

The cladding of the fuel pins currently used at Paks NPP is manufactured from a mixture of zirconium made by the electrolytic and the iodide reduction methods. During a loss-of-coolant accident (LOCA), the high-temperature steam oxidises the cladding. Outside the temperature range of 800-1050 °C, the oxide layer is compact and inhibits further oxidation even for long oxidation periods, but within this range it repeatedly cracks and spalls off, exposing fresh metal to the steam, which results in an accelerated, so-called breakaway oxidation characteristic of this specific alloy. Traditional parabolic oxidation kinetics correlations based on diffusion through an ever thickening compact oxide layer cannot describe this phenomenon as it results in linear kinetics, therefore a new model had to be developed. The work was supported by Paks NPP.

## Methods

The basic concept was to describe oxide spalling in such a way that at a given weight gain a certain constant surface fraction of the oxide exfoliates from the metal, and the fresh metal surface oxidises as the as-manufactured cladding. Exfoliation affects identically all parts of the surface: those that have not suffered spalling yet and those that have already suffered one or even several spalling events.

First a model was developed to describe the hydrogen production during breakaway oxidation. The model takes into account the oxidation of the metal, the partial absorption of the hydrogen produced in the process and the periodic exfoliation of a certain surface fraction of the oxide, resetting the oxidation kinetics to the initial rate characteristic of the fresh metallic surface, as described above. The parameters of the model were fitted using the results of high-temperature steam oxidation experiments carried out at MTA EK on E110 cladding in the breakaway regime, that featured a TCD (thermal conductivity detector) to measure the amount of released hydrogen on-line, in addition to measuring the weight gain at the end of the oxidation period.

Then the parameters of the model (the temperature-dependent weight gain threshold where spalling occurs and the exfoliating surface fraction) were determined using hydrogen production and weight gain measurements.

Finally, for very long term oxidation a linear kinetics correlation was fitted to the curve resulting from the detailed model.

## Results

The measured integral TCD signals were well reproduced, which justified the basic concepts of the model (Fig. 1). The downward spikes are due to increased hydrogen absorption of the fresh metal surfaces in the simulation, but they do not affect the integral results.

The agreement between the measured and calculated weight gains was good, considering the large scatter of the measured data (Fig. 2).

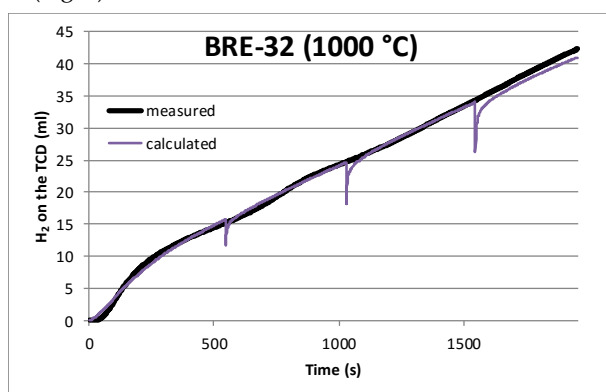


Figure 1: Measured and calculated integral TCD signal for sample BRE-32 oxidised at 1000 °C

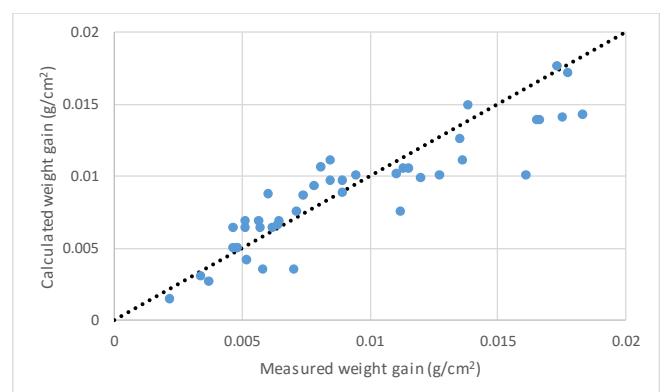


Figure 2: Measured and calculated weight gains (900-1050 °C)

Moreover, the sum of the individual parabolic oxidation kinetics yielded a near linear function, in accordance with experimental findings.

## Remaining work

The work has been finished. Journal publication of the model is planned.

## Related publication

[1] K. Kulacsy: *Modelling break-away oxidation*, MTA EK-FRL-2018-721-01-01-M0, in Hungarian (2018)

# ACTIVITIES OF MTA EK AS MAIN CONSULTANT OF PAKS NPP

*Katalin Kulacsy*

## **Objective**

MTA EK, together with NUBIKI (Nuclear Safety Research Institute), has been the main consultant of Paks Nuclear Power Plant (NPP) for over a decade. The main consultant supports the NPP in solving safety-related technical issues and helping with strategic planning. The work is done by the most experienced and highly qualified members of the staff on the basis of yearly work plans. In 2018 MTA EK undertook the following separate tasks, done by different groups of experts:

- determination of the eye lens dose for photon radiation
- analysis of the organic material content of secondary circuit deposits
- outlining the future of structural integrity (SI)
- assessment of the on-line hydrogen measurement method in the primary circuits.

## **Methods**

Each task required a different method, which can be summarized as follows.

In order to determine the eye lens dose, a survey of the national and international requirements, best practices and of different dosimeters applied was given. Calculations were made to justify the usability of whole-body dosimeters to determine the eye lens dose, taking into account the limitations of this solution.

Six samples were taken from different parts of the secondary circuit of Paks NPP and analysed by means of scanning electron microscopy, organic carbon analysis, dissolution tests, high-performance liquid chromatography with mass spectrometry and gas chromatography with mass spectrometry.

The future of SI was outlined based on literature survey and in-house method development.

The sources, importance and typical quantities of hydrogen in the primary circuit were reviewed on the basis of literature. The manual and on-line measurement techniques were assessed in terms of accuracy and calibration.

## **Results**

The individual results of the tasks were the following.

The eye lens dose could be determined using whole-body dosimeters in the typical radiation fields present in Paks NPP, except for certain special cases where the dosimeter has to be worn near the eye.

The secondary circuit deposits did not contain any inorganic carbon compounds. The morphology and composition of the samples were similar, they consisted mainly of iron and oxygen. The main organic compound was the octadecylamine used as anti-corrosion coating during shut-down periods.

The outline of the future of SI presented past and present best practices and wide-spread and innovative problem solving methods, including the role and description of material aging in the assessment of the technically allowable lifetime of a structure. Modelling the effect of inhomogeneities was identified as the most important imminent task in the field.

The on-line measurement of the hydrogen concentration has a good accuracy but is not properly calibrated. A new calibration method was proposed, together with a new scheme for hydrazine feeding and alternative control procedures.

## **Remaining work**

The 2018 tasks were finished.

## **Related publications**

- [1] S. Deme, T. Pázmándi, P. Szántó: *Determination of the eye-lens dose for photon radiation*, MTA EK TFO-2018-751-04-01-M0, in Hungarian (2018)
- [2] T. Tóth, T. Fekete, K. Kovács, Sz. Papné Góger: *Analysis of the organic material content of secondary circuit deposits*, MTA EK TFO-2018-751-05-01-M0, in Hungarian (2018)
- [3] T. Fekete: *The future of structural integrity*, MTA EK TFO-2018-751-06-01-M0, in Hungarian (2018)
- [4] Zs. Kerner: *Assessment of the on-line measurement of the hydrogen content in the primary circuit*, MTA EK-SZV-2018-751-01-M0, in Hungarian (2018)

# MULTI-PHYSICS: COUPLING OF REACTOR PHYSICS AND FUEL BEHAVIOUR ALGORITHMS OF THE HOT CHANNEL ANALYSIS

*András Keresztúri*

## Objective

In the transient phase of a fast reactivity event, the heat transfer process in the hot-channel fuel pin is influenced to a great extent by the burnup and the profile of the relative power inside of the pellet. However, these characteristics are determined during the long term burnup process, in which the resonance self-shielding of the *reactor physics model* plays an important role. On the other hand, the resonance self-shielding is significantly temperature-dependent, and the distribution of this parameter depends on the heat transfer process, which itself is influenced by the gap size and the fission gas release. The latter parameters are outputs of the *fuel behaviour modelling*. Consequently, online coupled stationary-reactor physics and fuel behaviour algorithms must be applied to model the above mentioned complex phenomena correctly. However, the present practice is to separate the mentioned disciplines in an approximate manner. The goal of the present study was to quantify the effect caused by this approximation.

## Methods

The main characteristics of the two algorithm types are as follows. Concerning the reactor physics, the hot fuel pin surrounded by a whole fuel assembly is modelled by using the first flight collision probability method. The hot fuel pin is subdivided into 16 cylindrical layers with equal-sized volumes. 35 thermal and 35 epithermal energy groups were used for modelling the whole assembly with the exception of the hot channel where 10 000 energy groups were used in order to model the resonance self-shielding more precisely and correctly. Concerning the fuel behaviour, the following effects were taken into account: fission gas release, densification and swelling due to the burnup, heat transfer and expansion effects, elastic and inelastic geometrical changes including the creep of the cladding, closure of the gap, and pellet-cladding mechanical interaction.

## Results

The differences between the correct combined algorithm and the approximation using separate methodologies are in the range of the uncertainties of the separated algorithms. As an example, see the figure below where the burnup-dependent average fuel temperatures are presented.

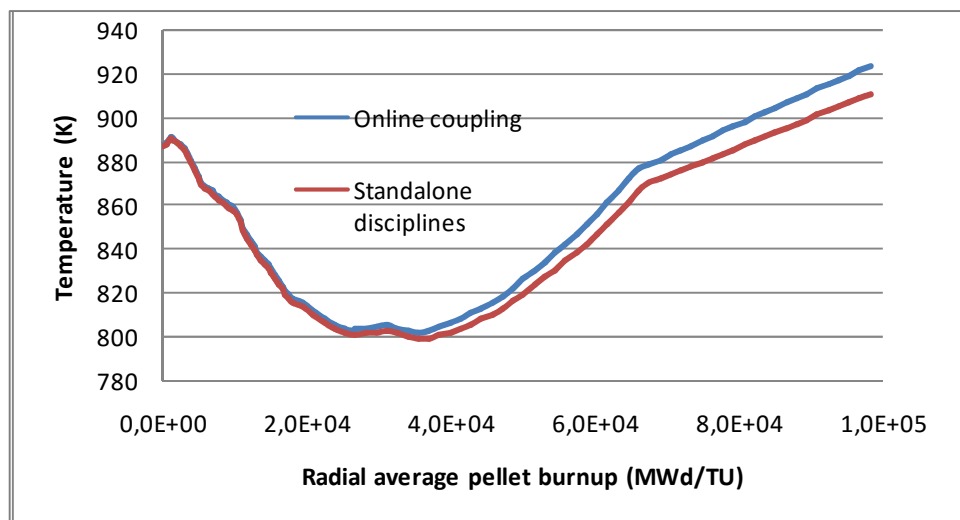


Figure 1: Radial average pellet temperature

## Remaining work

There is no remaining work.

## Related publication

- [1] A. Keresztúri: *On line coupling of reactor physics and fuel behaviour algorithms*, (VKSZ\_14-1-2015-0021 / MTA-EK-RAL-2016-212), in Hungarian (2018)

# INVESTIGATION OF THE REACTOR HEAT TRANSFER FUNCTION BETWEEN THE COLD AND THE HOT LEG OF THE PRIMARY CIRCUIT

*Sándor Kiss, Sándor Lipcsei*

## Objective

In the steady state condition of the reactor, temperature inhomogeneities travelling together with the primary coolant pass through the reactor core and induce reactivity fluctuations generating small perturbations of the reactor power. This change of the power is moderated by the negative feedback of the Moderator Temperature Coefficient of the reactivity and the Doppler effect. This variation of the energy production reacts on the coolant temperature and so on the negative feedback. Additionally, due to circulation of the coolant, the perturbations arisen in the primary loop pass through the reactor core and the steam generators several times before their attenuation (more details in [1]). In this way, the perturbations passing through the core are fed back with a delay of the circulation period of the primary coolant with a significant attenuation. The complexity of these effects causes difficulties in the determination of the heat transfer properties of the primary loop.

## Methods

In this research the propagation mechanism of the temperature fluctuations was investigated above 0.1 Hz using the measured hot and cold leg temperature signals of the primary loops of a VVER-440 reactor and an estimation method of the heat transfer functions of the coolant passing through the steam generators and the reactor core has been provided based on the measured temperature data.

In order to carry out this investigation some of our previous works are invoked. The investigation requires the knowledge of circulation period of the primary coolant and the transit times of the coolant between the thermocouples in the primary loops [2], the transfer properties of the steam generators [3], as well as the source and the propagation of the temperature perturbations and the proportions of the perturbation components [1]. To achieve this overall evaluation an average primary loop model was also created [1], [2], [4].

## Results

An estimation of the reactor heat transfer function between the cold and the hot leg of the primary circuit was provided (see Figure 1), which was enabled by the finding that the ratio of the auto power spectral density functions of temperature noise of the reactor and the steam generators can be well approximated with the ratio of the spectra of the hot leg and the cold leg temperature noise. It was found that the effect of the control system and the power feedback cannot be neglected up to 0.2 Hz for VVER-440 reactors. The transfer properties of the steam generator were estimated using temperature noise measurements as well. For more detail see [5].

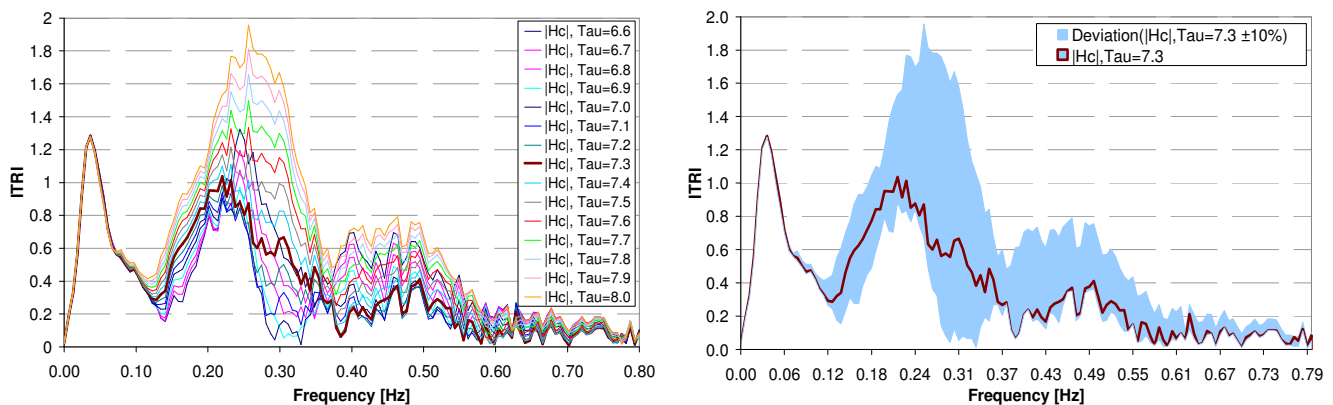


Figure 1: Frequency response of the reactor heat transfer function at 10% accuracy of the transit time

## Related publications

- [1] S. Kiss and S. Lipcsei: *Analysis of propagating temperature perturbations in the primary circuit of PWRs*, Annals of Nuclear Energy **85**, 1167-1174 (2015)
- [2] S. Kiss and S. Lipcsei: *Measurement of average circulation period of temperature fluctuations in the coolant of VVER-440 reactors' primary circuit*, Progress in Nuclear Energy **71**, 188-194 (2014)
- [3] S. Kiss and S. Lipcsei: *Effect of the steam generator on temperature fluctuations of the primary circuit coolant in VVER-440 reactors*, Ann. Nucl. Energy **72**, 166-172 (2014)
- [4] S. Kiss, S. Lipcsei and J. Végh: *Monitoring MTC using cold leg thermocouple and background neutron detector noise signals in a VVER-440 reactor during a whole fuel cycle*, Annals of Nuclear Energy **37**, 827-834 (2010)
- [5] S. Kiss and S. Lipcsei: *Investigation of the reactor heat transfer function between the cold and the hot leg of the primary circuit*, Annals of Nuclear Energy **124**, 327-334 (2019)

# DEVELOPMENT OF INTERACTION TECHNIQUES FOR A VIRTUAL CONTROL ROOM

*B. Katalin Szabó*

## **Objective**

The objective was to implement gesture-driven and control-panel-driven navigation in the virtual model of a huge control room of a power plant, in an immersive virtual reality application, and the handling of collisions in the model.

## **Methods**

Hardware and software tools used: Leap Motion hand movement sensor, Oculus Rift headset, 64-bit Windows 10 operating system, Blender Game Engine (version 2.76b), OpenHMD package with python-rift extension. The Leap Motion device drives a self-developed rigged hand model which reproduces the appearance and the movement of the real hands with acceptable accuracy.

First a finger-operated virtual control panel was built into the model, the buttons on it corresponded to translational and rotational movements, as if the user was controlling a wheelchair. However, this input method did not prove accurate enough, there were misses while hitting the buttons next to each other. (This is affected by how good the light conditions are, as the accuracy of the Leap Motion sensor is very sensitive to light conditions in the room.) Therefore, this line was abandoned and gesture-driven interaction ("natural interaction") was introduced, where the navigation is solely controlled by the movements, gestures of the user's hands, without any physical or virtual input tool other than the hand movement sensor.

While there are various examples of gesture-driven interaction in the literature, there is no generally usable sure-fire method. Solutions are always specific to the actual applications.

For our application, the user's actions which had to be handled were divided into 3 categories:

- navigation, i.e. "walking", "moving around" in the control room, going from one spot to the other
- head rotation, i.e. the turning of the head to look at various objects
- interaction with pushbuttons and switches (this involves collision detection)

In our case, for the navigation, four degrees of freedom (out of the possible six) seemed to be adequate: translational movement along all 3 coordinate axes and rotation around the vertical axis.

## **Results**

For the navigation, two clearly separable input modes have been introduced:

- Translational mode: the user is able to move along the 3 coordinate axes. This is possible when only the left hand is within the detection range of the Leap Motion, the right hand is out of sight. The user moves his/her hand along 1, 2 or 3 coordinate axis/axes, and the view moves with it. The most important direction is along the horizontal axis. As the user sometimes has to travel large distances, acceleration has been implemented. This mode ends when the user puts his/her right hand into and/or pulls his/her left hand out of Leap Motion's "sight". When the user's left hand is clenched into a fist, the movement of the hand does not result in the movement of the view - this sub-mode is necessary to make it possible for the user to return the hand into the field of detection ("sight") of the sensor.
- Rotational mode: the user is able to rotate the view around the vertical axis, by rotating his/her hand. This mode is in effect only when the right hand is within the detection range of the Leap Motion and the left hand is out of sight.

The interaction mode - to be implemented - is in effect when both hands are visible and can interact with buttons and switches. Additionally, to use the already implemented head rotation input is possible all the time. Unlike the rotational mode described above, it may occur around all 3 axes, and it affects only the user's view, not the position or orientation of the hand within the control room.

## **Remaining work**

Implement interaction mode (handling collisions). Test the various interaction modes rigorously.

# DEVELOPMENT OF AN EXAMINATION TECHNIQUE TO ANALYSE SILVER DEPOSITS (SILVER MEASUREMENT ON THE BY-PASS SYSTEM OF THE PAKS NUCLEAR POWER PLANT)

*István Almási, Gergely Dósa, Zoltán Hlavathy, Zsolt Kerner, Péter Kirchknopf, András Kocsonya, Katalin Zsuzsanna Szabó, Péter Völgyesi*

## Objective

A measurement method was developed to determine the surface activity concentration of  $\text{Ag}^{110\text{m}}$  on the tubes of the by-pass system by in situ gamma-spectrometry, to map the spatial distribution and to study the temporal changes of  $\text{Ag}^{110\text{m}}$ . During the project several locations of the by-pass system were measured and the dose rates were determined. The other aim of the project was to determine the physical-chemical processes responsible for the  $\text{Ag}^{110\text{m}}$  transport.

## Methods

Altogether 70 points were analysed by in-situ gamma-ray spectrometers and dose rate meters during the reparation period of each reactor blocks. Eight 1-week long measurement campaigns were carried out in the 3-years long project. Additionally, few weeks long gamma spectrometry measurements were also performed on a given point in order to carry out time series analysis. A calibration methodology ('tube-model') was also developed at MTA EK to determine the surface activity concentration of  $\text{Ag}^{110\text{m}}$  (Figure 1).

## Results

By evaluating more than 500 measurements, the dose rate and  $\text{Ag}^{110\text{m}}$  activity concentration maps were completed for the 4 reactor blocks in a 3-years long period. The results enabled us to compare the amount and distribution of  $\text{Ag}^{110\text{m}}$  in the different reactor blocks and also the  $\text{Ag}^{110\text{m}}$  variation each year in the block studied. Significant portion of the gamma dose rate is originating from the  $\text{Ag}^{110\text{m}}$  nuclide. Based on our study it was possible to identify hot spots with higher activity concentration and gamma dose rate values as well as the main parameters influencing the  $\text{Ag}^{110\text{m}}$  transport. The temperature, pH and redox potential were revealed as main parameters influencing the solution/deposition processes of  $\text{Ag}^{110\text{m}}$ .

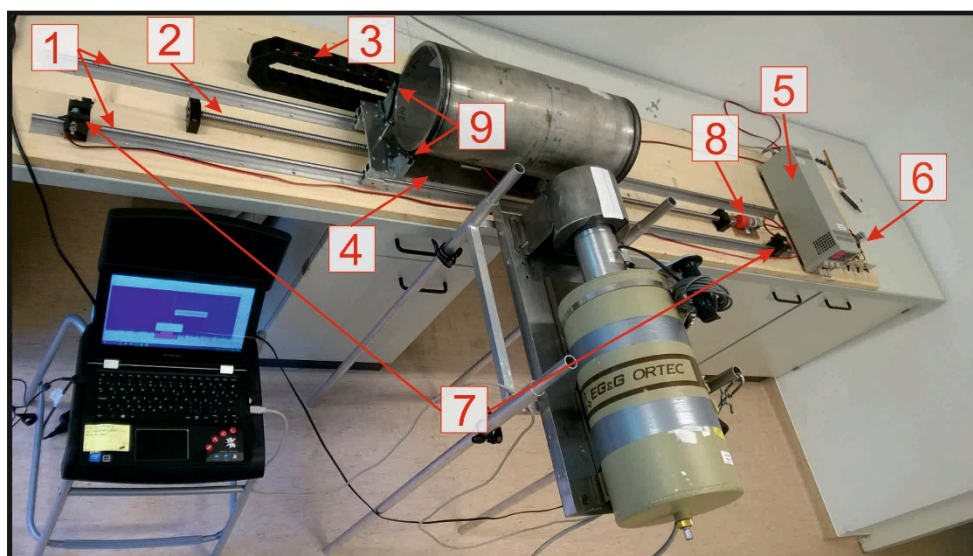


Figure 1: Calibration model to determine the surface activity concentration of the by-pass system tubes developed at MTA EK  
Components of the model: 1: guide rail, 2: bowl screw, 3: energy chain, 4: moving panel, 5: power supply, 6: control unit, 7: reversing trigger, 8: electro-motor, 9: bearing

## Remaining work

The project has been finished in 2018.

# WORKING FLUIDS

*Attila R. Imre*

## **Objective**

One of the major issues for sustainable development of electricity production is to use low-temperature heat sources (60-200 °C) like thermal solar, geothermal, biomass or waste heat. Conventional water-based thermodynamic cycles are not suitable in this temperature range or operate with low efficiency, therefore other working fluids need to be applied. These fluids are usually organic ones with low boiling point, where the given temperatures are sufficient to produce organic vapour with pressure high enough to drive generators. One of the thermodynamic cycles used for this purpose is the Organic Rankine Cycle (ORC), using organic material instead of water as working fluid. In this study, we are trying to determine how to choose the thermodynamically best working fluid for a given heat source. Elementary steps (adiabatic expansion/compression and isobaric heating/cooling) of fluids were also studied.

## **Methods**

Analytical method, special computer codes and some commercial codes and databases (ThermoC, NIST Webbook, Cycle-Tempo) were used for the calculations.

## **Results**

Organic Rankine Cycle (ORC) uses organic working fluids to reach higher thermal efficiency for low-temperature heat sources. New working fluids are usually found by a trial and error procedure testing chemically similar materials. This procedure is quite risky, considering the possibility of excluding the optimal working fluid; therefore a new method has been developed. A novel classification has been proposed [1] to help in choosing the most suitable working fluid for a given heat source (with given upper temperature). Theoretical considerations show that the most important factors in the classification are the interconnected isochoric heat capacity and the degree of freedom of the given molecule [2]. Based on these results, some simple rules can be given to choose potentially optimal working fluids not only for ORC processes but also for the Trilateral Flash Cycles (TFC) where vapour is produced by dropping the pressure, instead of heating [3]. A database for ORC liquids has been prepared and will be published soon.

For both of the aforementioned cycles (ORC and TFC) adiabatic expansion/compression and isobaric heating/cooling are very important parts, therefore the better understanding of these processes are crucial. Adiabatic, isobaric and the similarly important isenthalpic processes were investigated under unusual circumstances. For isobaric heating/cooling a thermodynamically interesting novel process was found, where heat can be transferred to/from a body, while the associated thermal expansion or contraction happens with zero work [4]. In another study, adiabatic isenthalpic pressure drops were studied to model pressure changes during LOCA (Loss of Coolant Accidents) in Supercritical Water Cooled Reactors (SCWR) [5]. In connection with this study, relative location of adiabatic lines and the so-called Widom-lines (representing anomalous properties in the supercritical region) were calculated for several materials, including water [6]. Similar adiabatic and isochoric pressure drops were studied in deeply metastable water, demonstrating the need of a quintic (5<sup>th</sup> degree) volume component in the equation of state of metastable water [7].

## **Remaining work**

A well-usable method will be developed next year to help engineers to find the proper working fluid for the available heat source. Also, related theoretical studies will be continued.

## **Related publications**

- [1] G. Györke, U. K. Deiters, A. Groniewsky, I. Lassu, A. R. Imre: *Novel Classification of Pure Working Fluids for Organic Rankine Cycle*, Energy **145**: 288-300 (2018)
- [2] A. Groniewsky, A. R. Imre: *Prediction of the ORC working fluid's temperature-entropy saturation boundary using Redlich-Kwong equation of state*, Entropy **20**: 93 (2018)
- [3] A. R. Imre, A. Groniewsky: *Various ways of adiabatic expansion in Organic Rankine Cycle (ORC) and in Trilateral Flash Cycle (TFC)*, Zeitschrift für Physikalische Chemie, in press, DOI: <https://doi.org/10.1515/zpch-2018-1292>
- [4] A. R. Imre, K. W. Wojciechowski, G. Györke, A. Groniewsky, J. W. Narojczyk: *Pressure-volume work for metastable liquid and solid at zero pressure*, Entropy **20(5)**: 338 (2018)
- [5] G. Györke, A. R. Imre: *Physical-chemical background of the potential phase transitions during Loss of Coolant Accidents in the supercritical water loops of various Generation IV nuclear reactor types*, Periodica Polytechnica Chemical Engineering, **63**: 12770 (2019)
- [6] A. R. Imre, A. Groniewsky, G. Györke, A. Katona, D. Velmóvszki: *Anomalous properties of some fluids – with high relevance in energy engineering – in their pseudo-critical (Widom) region*, Periodica Polytechnica Chemical Engineering, **63**: 12905 (2019)
- [7] A. R. Imre, A. Groniewsky, G. Györke: *Description of the metastable liquid region with quintic and quasi-quintic equation of states*, Interfacial Phenomena and Heat Transfer, **5**: 173-185 (2017) (back-dated, real publication year 2018)

# DEVELOPMENT OF CODES FOR ANALYSING REACTIVITY TRANSIENTS OF THE VVER-1200 REACTOR

György Hegyi, András Keresztúri, Csaba Maráczy, István Panka, István Trosztel

## Objective

The general objective of the project is the development of the elements of a code system for the alternative solution of core design and safety analysis of the new Paks units. This year, the specific aim was the development of codes for analysing reactivity transients of the VVER-1200 reactor.

## Methods

VVER-1200 specific upgrading and input generation for the following codes:

- KARATE quasi-stationary neutronic-thermohydraulic code system
- KIKO3D reactor dynamics code
- ATHLET system thermohydraulics code
- KIKO3D-ATHLET coupled reactor dynamics - system thermohydraulics code
- TRABCO code for checking the fulfilment of hot-channel acceptance criteria.

## Results

The above codes have already been successfully applied in the case of VVER-440 reactors. Unlike VVER-440 reactors, in the VVER-1200 fuel assemblies the control rod cluster type reactivity regulation is used. It made necessary to integrate our methods for solving a number of benchmarks related to the VVER-1000 reactor which is the predecessor of the new Paks units. We have upgraded and tested the programme required for the analysis of reactivity transients of the VVER-1200 reactor.

Figure 1, as an example, illustrates the nodalisation of the VVER-1200 primary loop in the ATHLET model.

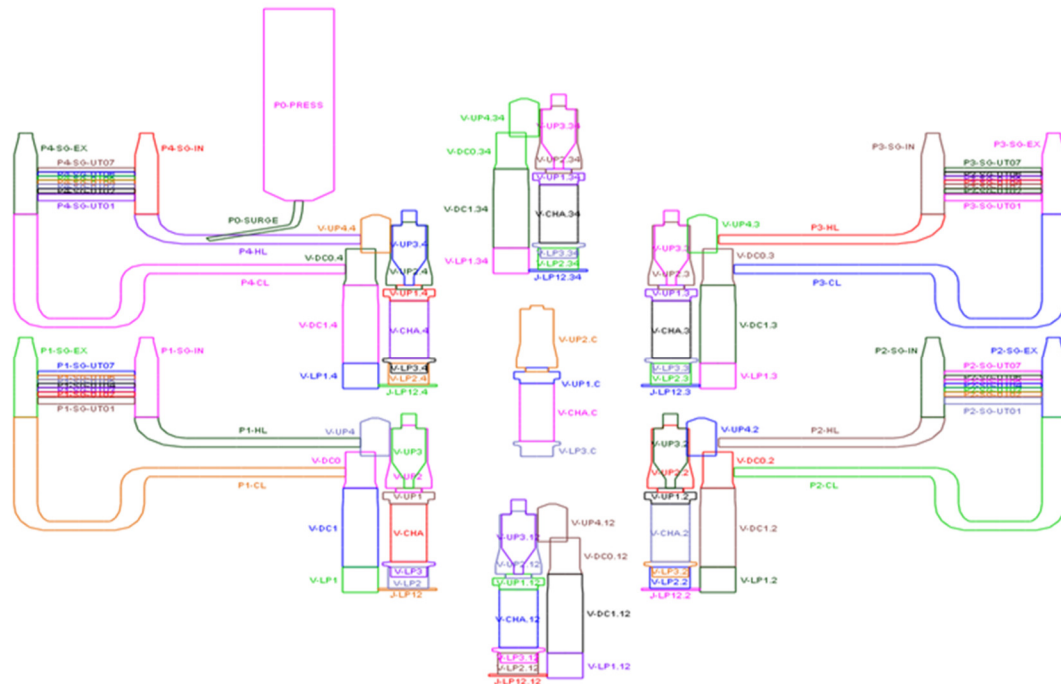


Figure 1: Nodalisation of the VVER-1200 primary loop in the ATHLET model

## Remaining work

This project has been completed.

## Related publication

- [1] E. Temesvári, Á. Brolly, Gy. Hegyi, G. Hordósy and Cs. Maráczy: *Verification of an Indigenous Code System for Calculation of VVER-1200 (AES-2006) Reactor*, PHYSOR 2018, Cancun, Mexico, April 22-26

# TESTING AND QUALIFICATION OF CLADDING SAMPLES FOR ALLEGRO FUEL

Zoltán Hózer, Péter Szabó, Tamás Novotny, Erzsébet Perez-Feró,  
Márton Király, Anna Pintér Csordás, Levente Illés, Marc Schyns (SCK·CEN),  
Rémi Delville (SCK·CEN), Daejong Kim (KAERI), Weon-Ju Kim (KAERI)

## Objective

The main objective of the development of ALLEGRO gas-cooled fast reactor is the demonstration of operability of a fast neutron reactor with gas coolant. The first (start-up) core of ALLEGRO will be built with MOX or UOX fuel in 15-15Ti stainless steel (SS) cladding. The second core of ALLEGRO will use carbide fuel - (UPu)C or UC - in SiC cladding. In order to support the introduction of these cladding materials a qualification procedure is needed and representative experiments have to be carried out.

## Methods

Qualification procedures have been proposed for the start-up and refractory ALLEGRO fuel on the basis of technology readiness level (TRL) approach.

The 15-15Ti cladding tube samples (provided by SCK·CEN) were tested in high temperature (1000 °C) helium with different impurities (methane, hydrogen, nitrogen). The load bearing capabilities of pre-treated 15-15Ti and Duplex and Triplex type SiCf/SiC samples (manufactured by KAERI (Korean Atomic Research Institute)) were tested in ring compression tests. Isothermal high temperature burst tests have been performed with 15-15Ti claddings using internal pressurization. Scanning electron microscopy was applied to analyse the microstructure of the cladding samples.

## Results

The basic steps of qualification procedure were identified. Using the currently available information, the further needs were specified which include experimental activities, design work, development of numerical models, technology developments, establishment of fuel fabrication capabilities, irradiation in research reactors and post-irradiation examination of fuel.

The high temperature treatment of 15-15Ti cladding samples showed considerable mass increase only in case of methane impurity, due to its decomposition. In pure helium atmosphere the uptake was negligible. The load bearing capabilities of pre-treated 15-15Ti samples decreased in comparison with the as-received material. The treatment in methane resulted in brittle failure of the sample, while the other samples remained ductile. The ballooning tests proved that the 15-15Ti cladding tubes can keep their integrity at high temperatures. The failure pressure of samples tested at 960-1000 °C was above 18 MPa.

The ring compression tests indicated that the compression resistance of Triplex type SiCf/SiC cladding is much better than the Duplex ones'. The thermal pre-treatment of samples in helium with different impurities did not significantly influence the mechanical properties of cladding tubes.

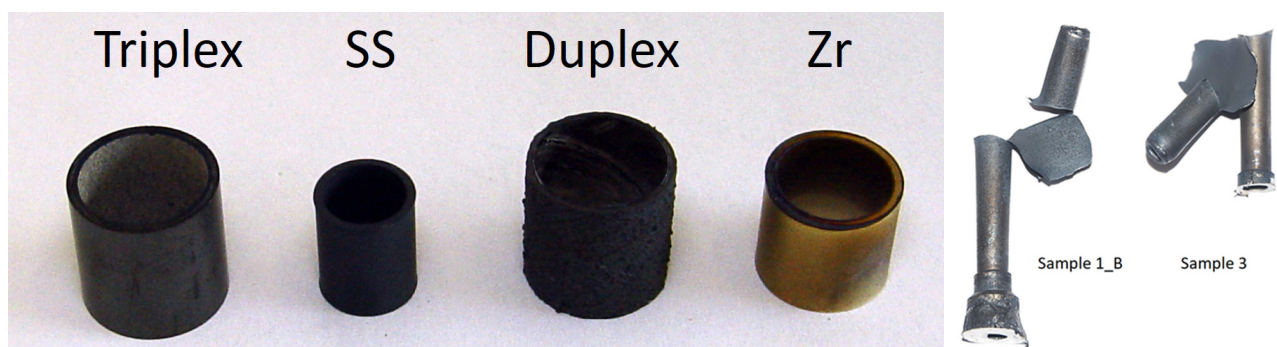


Figure 1: View of ring specimens after high temperature treatment in helium-nitrogen atmosphere (left) and state of the 15-15Ti cladding tubes after burst (right)

## Remaining work

The planned work has been completed.

## Related publications

- [1] Z. Hózer, P. Szabó, T. Novotny, E. Perez-Feró, M. Király, A. Pintér Csordás, L. Illés, M. Schyns, R. Delville: *Testing of 15-15Ti cladding for ALLEGRO gas-cooled fast reactor conditions*, MTA EK-FRL-2018-219-1-1-M0
- [2] Z. Hózer, T. Novotny, E. Perez-Feró, M. Horváth, A. Pintér Csordás, L. Illés, D. Kim, W.-J. Kim: *SEM studies and mechanical testing of SiCf/SiC claddings for ALLEGRO gas-cooled fast reactor*, MTA EK-FRL-2018-219-1-2-M0
- [3] Z. Hózer: *Proposal for ALLEGRO fuel qualification procedure*, MTA EK-FRL-2018-218-1-1-M0

# ALLEGRO CORE DESIGN

*András Keresztúri, Gusztáv Mayer, István Pataki, Bálint Batki*

## Objective

In the recent generic ALLEGRO design status, a concept and the corresponding multi-discipline methodology had to be elaborated for the ALLEGRO core design where the target quantity DPA (Displacement Per Atom) is maximized by keeping the core design safety limits according to the fulfilment of the safety analysis acceptance criteria. The basic free parameters of the core design are the core size (number of fuel assemblies), the maximum allowed stationary power ("nominal power"), the plutonium content of each fuel assembly and the reactivity reserve necessary for the burnup.

## Methods

For the fulfilment of the safety requirements, it was necessary to define and determine a function ("base function") playing essential role in the core design, which is the maximum value of the allowed linear heat rate at normal operation depending on the nominal reactor power. This function must be determined by a set of safety analyses of the most limiting initial event(s) of the Design Basis at the present cooling strategy. Based on earlier studies, the hot duct break was selected as the enveloping initiating event, assuming a single failure of the intact loop. The group constants of the assemblies depending on the plutonium content were determined by using the SERPENT code, while the target and the core design parameters were calculated by the KIKO3DMG code. The careful assembly-wise plutonium profiling was a labour-intensive part of the core design.

It is noted that the starting point of the investigation, namely the "base function" of the linear heat rate, can be changed if the cooling strategy of ALLEGRO is changed in the future, but the multi-discipline methodology elaborated here will still be applicable.

## Results

The applicability of the elaborated concept was demonstrated. A total of 48 CATHARE safety analysis calculations were performed by varying the initial core power and the radial peaking factor. Using the methodology, the original CEA ALLEGRO core was successfully modified by decreasing the maximum linear heat rate but keeping the total power at 75MW in order to fulfil the safety criteria. The new core design fulfils the safety criteria for the peak cladding temperature also in case of the hot duct break transient which is considered as the enveloping initiating event. The radial power peaking factor ( $K_p$ ) was set to the required value by using fuel sub-assemblies with different initial plutonium content and increasing the size of the core, while the reactivity reserve necessary for the burnup could be assured in parallel. The earlier proposal for the power reduction (from 75 MW to 35 MW) indicated 53% reduction in the irradiation capability of the core. In contrast, concerning the irradiation performance, the optimized core presented here proved only 26% worse than the original one but this latter one was not fulfilling the acceptance criteria.

## Remaining work

The target reactivity reserve necessary for the burnup could have been more precisely met if the group constants were interpolated according to the plutonium content. During future long term operation, fuel behaviour investigations may modify the base curve.

## Related publication

- [1] A. Keresztúri, G. Mayer, I. Pataki and B. Batki: *Concept and methodology for the multi-discipline ALLEGRO core design, the demonstration of the applicability of the methodology*, ALLEGRO (VKSZ\_14-1-2015-0021 / MTA-EK-RAL-2016-207), in Hungarian (2018)

# SIMULATION OF A STATION BLACKOUT TRANSIENT AND SPECIAL TOPICS OF GROUP CONSTANT GENERATION FOR THE ALLEGRO

*Bálint Batki, István Pataki, István Panka, András Keresztúri*

## Objective

At the present status of the development of the ALLEGRO reactor, it is crucial to identify those parameters which are hard to calculate or measure precisely and play an essential role during normal operation or transients. One aim of our work was to extend the knowledge about the uncertainties of reactor physics and thermal-hydraulics parameters by performing best estimate plus uncertainty analyses of a protected Station Blackout (SBO) transient. Results calculated by different computer codes were compared to validate our model. Another objective was to prepare reliable homogenised cross-sections for the ALLEGRO; thus three special topics of group constant generation were investigated.

## Methods

Thermal hydraulics analyses were performed using the ATHLET computer code. A simplified reactor core model was created. The inlet mass flow rate and temperature were given as functions of time, which were provided by the VUJE (Slovak Engineering Company in the field of Power Generation) and calculated using the RELAP5 code. The performed uncertainty analyses were based on the GRS (Gesellschaft für Anlagen- und ReaktorSicherheit, Köln, Germany) method. The Serpent Monte Carlo code and the KIKO3DMG (nodal reactor physics calculation code developed in the CER) were applied for the investigation of the group constants. One fuel assembly (1D) and full core models of the ALLEGRO were created. Apart from the calculation of effective multiplication factors ( $k_{eff}$ ), group constants were also generated in the Serpent code.

## Results

It was found that the simplification of the core model in the ATHLET, mostly the neglect of the radial heat transfer from the fuel assembly to the bypass and the structural elements, significantly increases the peak cladding temperature during the Station Blackout (Figure 1). This substantial effect is the result of the more than 250 °C difference between the coolant temperature in the hot channel and the bypass. The peak cladding temperature exceeded the melting point by 6 °C in the case of the more conservative ATHLET simulation. In addition, the sensitivity analyses highlighted that the uncertainty of the decay heat curve has the highest impact on the uncertainty of the peak cladding temperature. It should be mentioned, that a 3D core model is needed to accurately investigate this transient, but it is beyond the scope of this study [1].

Regarding the group constant generation topics, a novel finding is that  $k_{eff}$  values from the Serpent and the 1D KIKO3DMG are not correlated (Figure 2). The standard deviations of the  $k_{eff}$  from the two codes are approximately the same. These perceptions will be useful when we want to calculate the standard deviation of reactivity differences between the two codes. It was also seen that reactivity effects calculated using the KIKO3DMG code are within the statistical uncertainties of the Serpent result in the case of the 1D model. Finally, we show that the outermost ring of the shielding assemblies is negligible during full core simulations, which decreases the necessary calculation time of the KIKO3DMG by 20%.

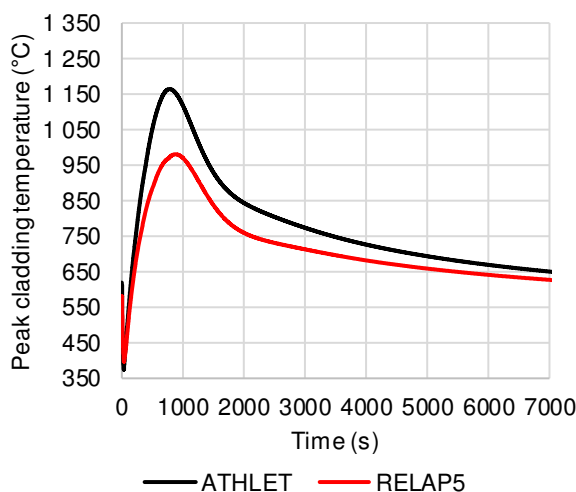


Figure 1: Peak clad temperature during SBO [1]

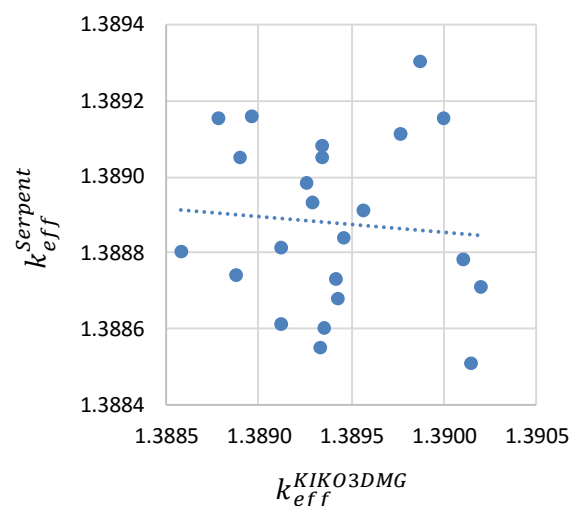


Figure 2: Correlation between the Serpent and KIKO3DMG  $k_{eff}$ s

## Remaining work

There is no remaining work.

## Related publication

- [1] B. Batki, B. Kvizda, A. Keresztúri and I. Panka: *Uncertainty analyses of transients on the ALLEGRO reactor*, Best Estimate Plus Uncertainty International Conference (2018)

# REACTIVITY ANALYSIS OF THE MODIFIED SUPERCRITICAL VVER-SCP REACTOR CONCEPT

*György Hegyi, Gábor Hordósy, Csaba Maráczy*

## Objective

The single circuit, supercritical pressure GEN-IV VVER reactor (VVER-SCP) enables the use of a higher efficiency thermodynamic cycle, and is promising from the aspects of its closed fuel cycle and that it allows final disposal of the weapon grade plutonium stockpile. As there was no detailed information available in the literature on the flow paths of water in the reactor vessel, we have used the conclusions of the European High Performance Light Water Reactor (HPLWR) project on the flow scheme. The equilibrium fuel cycle of the modified VVER-SCP was developed last year. The analysis of several reactivity coefficients and the capability of safe shutdown of VVER-SCP were intended to be investigated in this year of research.

## Methods

We have used the deterministic KARATE code system to calculate the VVER-SCP core behaviour. For cases, which were beyond the scope of KARATE, the MCNP Monte Carlo code was applied.

## Results

We have found that the subcriticality of the reactor cannot be assured in a cold state. The problem can be solved e.g. by using  $^{10}\text{B}$  enriched  $\text{B}_4\text{C}$  absorber instead of the currently assumed natural isotopic boron composition. The fuel temperature reactivity coefficients are similar for the VVER-SCP and VVER-440 reactors, but the water temperature reactivity coefficients are much weaker in the VVER-SCP reactor. Fuel assembly neutron transport calculations with the MULTICELL neutron transport code were performed over a wide range of water densities. The values of the infinite multiplication factor for two burnup values are shown in Figure 1.

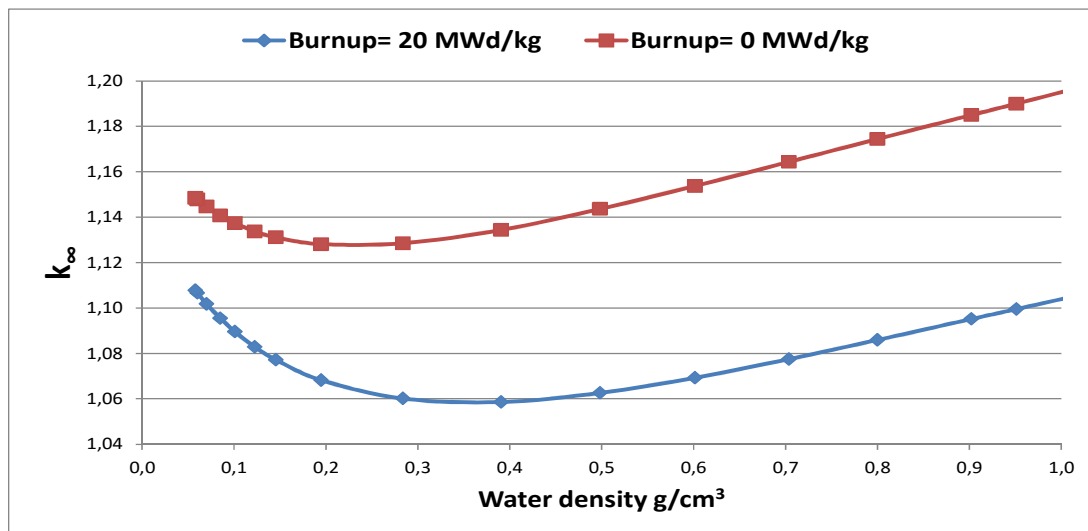


Figure 1: Infinite multiplication factors as a function of water density for two burnup values of a VVER-SCP fuel assembly

The average water density in the nominal state of VVER-SCP is approximately  $0.28 \text{ g/cm}^3$ . At this density, the infinite multiplication factor hardly changes as a function of water density, which supports the extremely low absolute value of the water temperature reactivity coefficient.

The evaluation of the void coefficient was performed with the MCNP code by calculating the multiplication factor of the end-of-cycle state with nominal water density and vacuum. According to the calculations, the void coefficient is positive, so the reactivity increases with the loss of cooling water. To solve the problem, the use of a solid moderator, e.g. zirconium hydride is possible.

## Remaining work

This project has been completed.

# INVESTIGATION OF THERMAL INSULATION OF EXPERIMENTAL ASSEMBLY OF ALLEGRO REACTOR

*István Farkas, István Tamásné Farkas, Attila Guba, Gusztáv Mayer*

## Objective

To test the new ceramic fuel in ALLEGRO reactor a few experimental assemblies will be loaded into the first mixed oxide (MOX) or uranium dioxide (UOX) core. These new experimental assemblies will have ceramic claddings and pellets which are able to operate at working temperature of Gas-Cooled Fast Reactor (GFR). This high temperature exceeds the safety limits of working conditions of the stainless steel MOX assemblies, consequently they have to be protected from the elevated temperature of experimental ceramic assemblies in the "mixed core". In order to ensure thermal insulation between the two types of assemblies a thermal shield around the ceramic assemblies is planned. It consists of two parts: a thermal barrier which contains static helium and a cooling channel where helium flows bypassing the heated part of assembly. In this work we studied the effectiveness of the thermal insulation for different bypass flow rates in the cooling channel that can help to create the final design of experimental assemblies.

## Methods

In the current work we created a 3D thermo-hydraulic model of the experimental assembly, containing the thermal shield and a part of fuel rod bundle. The final numerical model – which was used in this study as the basis of our calculations – was selected by sensitivity studies. We used realistic axial heat power distribution of fuel rods and the effect of convective and radiative heat transfer was also taken into account. Our primary aim was to determine the minimal bypass mass flow rate at which the thermal shield effectively insulates the experimental assembly from the neighbouring MOX assemblies. To ensure that the steel MOX assemblies are not heated by the ceramic ones we applied an adiabatic boundary condition on the outer surface of the assembly shroud. In this conservative case all the heat produced by the experimental assembly remains inside. If the surface temperature of the shroud of the experimental shield remains below the temperature of the neighbouring MOX assembly shrouds, then the experimental assembly would not heat the MOX assemblies. In our study we simplified this criterion using maximal temperature of modelled shroud surface and the average outlet temperature of the MOX assembly. The computational domain and its corresponding boundary conditions are shown in Figure 1 (left).

## Results

The effect of the reduced bypass mass flow rate was studied by performing seven FLUENT code simulations from 100% to 1% relative flow rates. The results show that the maximum outlet temperature stays below the average outlet temperature of the MOX assembly [803 K] down to at least 5% relative bypass mass-flow rate as it can be seen in Figure 1 (right). Consequently, there is no positive heat transport towards the MOX assemblies and the thermal shield can work effectively when the relative bypass mass-flow rate is higher than 5%.

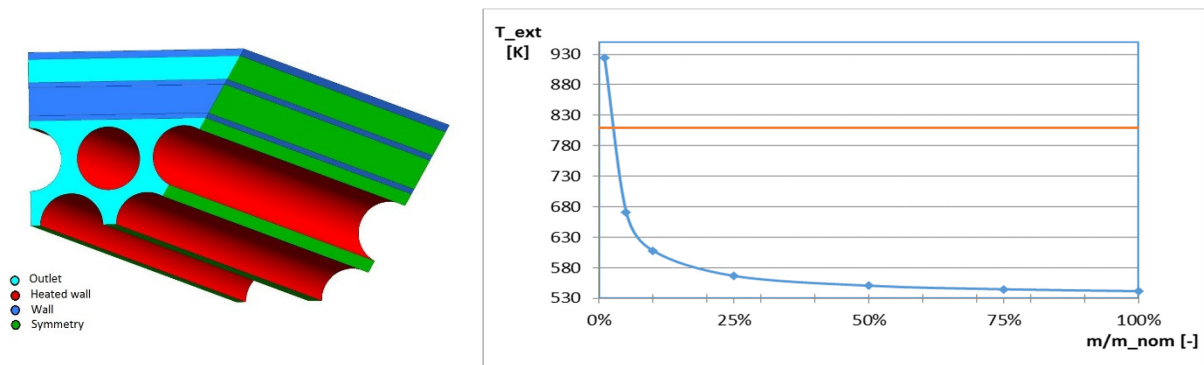


Figure 1: (Left) The computational domain. (Right) The outer wall temperature of the computational domain at different bypass flow rates.

## Related publication

- [1] I. Farkas, I. T. Farkas, A. Guba, G. Mayer: *ALLEGRO kísérleti fűtőelemköteg hőárnyékolásának CFD vizsgálata*, XVII. MNT Nukleáris Technikai Szimpózium, November 29-30. (2018)

# SENSITIVITY STUDY OF DECAY HEAT REMOVAL BLOWER PRESSURE LOSS IN ALLEGRO REACTOR

*Gusztáv Mayer, Attila Guba*

## Objective

The nonrotating blower blades may bring about significant pressure loss in the decay heat removal (DHR) loop of ALLEGRO reactor, which hinders natural circulation. The higher is the pressure loss coefficient of the DHR blower blades, the worse core cooling is available during natural circulation in case of total station blackout (SBO) initiating event. On the other hand, a large core bypass develops if a DHR valve is opened inadvertently during normal operation and if the DHR blower is not rotating. In this case the lower DHR blower pressure loss is disadvantageous from core cooling point of view, because significant amount of coolant bypasses the core through the DHR loop in backward direction. This sensitivity study investigates how the pressure loss coefficient of the nonrotating blower influences the peak cladding temperature in the following two cases: 1.) SBO + LOCA (loss of coolant accident) and 2.) inadvertent DHR valve opening. Both cases may lead to insufficient core cooling in accident conditions, which threatens the integrity of the reactor core.

## Methods

In this study the French CATHARE thermohydraulic code is used to assess the sensitivity of the DHR blower pressure loss coefficient in cases of total station blackout combined with LOCA, and inadvertent DHR valve opening. In the former case the break size and the number of operating nitrogen accumulators were varied, while in the latter case the inadvertent opening of 1, 2 and 3 valves were investigated.

## Results

In Table 1 the calculated peak temperatures are depicted. Red colouring shows that the corresponding temperature criterion was exceeded.

Table 1: The calculated PCT values

Pressure loss coefficient (forward direction) ----- >			0.10	1.00	10.00	100.00	1203	
Initiating event	Break size (inch)	Number of nitrogen tanks	Peak Cladding Temperature [°C] (PCT)					PCT Criterion
SBO+LOCA	1	1	815.19	816.62	829.79	931.34	1240.25	1300 °C
SBO+LOCA	1	2	809.13	810.54	823.40	920.29	1113.84	1300 °C
SBO+LOCA	1	3	808.08	809.31	822.16	916.94	1098.14	1300 °C
SBO+LOCA	2	1	912.76	914.18	927.21	1044.08	1312.82	1300 °C
SBO+LOCA	2	2	614.04	612.48	617.87	646.54	1062.32	1300 °C
SBO+LOCA	2	3	595.94	595.94	595.94	601.44	818.26	1300 °C
SBO+LOCA	3	1	1319.06	1318.10	1314.85	1314.73	1315.70	1300 °C
SBO+LOCA	3	2	892.74	892.88	900.18	974.87	1315.59	1300 °C
SBO+LOCA	3	3	755.87	755.36	757.16	774.10	1212.03	1300 °C
Pressure loss coefficient (backward direction) ----- >			0.17	1.71	17.14	171.43	1203	
Initiating event			Peak Cladding Temperature [°C] (PCT)					PCT Criterion
1 DHR valve opening	0	0	674.28	672.19	650.35	618.91	594.26	620 °C
2 DHR valves opening	0	0	792.31	784.89	743.96	663.76	609.82	850 °C
3 DHR valves opening	0	0	929.68	920.67	828.42	711.37	625.81	850 °C

The results showed that if the blower pressure loss coefficient is about 1.0 [1], then the SBO+LOCA event is manageable up to 3 inch break size using at least 2 nitrogen accumulators. On the other hand, (if the pressure loss value is small) in case of inadvertent opening of one or three DHR valves, the calculated PCT values exceeded the corresponding temperature limit.

## Related publication

- [1] G. Mayer, A. Guba: *Role of the Nonrotating Decay Heat Removal Blower Pressure Loss in ALLEGRO Reactor*, NURETH 18, August 18-23, Portland (2019)

# COMPLEMENTARY EXPERIMENTS FOR HIGH TEMPERATURE IRRADIATED SAMPLES

*Levente Tatár*

## Objective

Innovative fission reactor types and fusion devices pose new requirements on the structural materials to be used. Existing materials may be adequate, but their fitness for purpose has to be proven experimentally. New tests have to be carried out for selected “candidate” materials. In the framework of the MATTER EU FP7 project, the most important candidate materials were P91 (ferritic steel) and 316LN (austenitic steel). MTA EK carried out high temperature irradiation experiments in the Bagira3 irradiation rig [1] for these materials. Due to shifting of interest from P91 to 316LN during the MATTER project, strength tests were carried out only on 316LN material. In the current work we complemented the experiments carried out in the framework of the MATTER project by new measurements.

## Methods

The samples made of P91 and 316LN materials had been irradiated together in the Bagira3 irradiation rig. Irradiation conditions were described in [2]. For the 316LN material, in the framework of the MATTER project, Vickers hardness [3] measurements and instrumented Charpy measurements complying with EN 10 045 1 standard [4] had been done. These measurements were complemented by new hardness measurements on thermally aged specimens and instrumented Charpy measurements on unirradiated and thermally aged specimens.

In the framework of the MATTER project, specimens made of P91 steel were only prepared for testing. To complete the work, we performed three-point bending tests on the specimens and Master Curve analysis conforming to the ASTM E-1921 standard [5].

## Results

For the 316LN material, the Vickers hardness has shown no real difference between irradiated, unirradiated and thermally aged specimens. The Charpy impact energy of the unirradiated and thermally aged specimens were above 300 J, so it could not be determined with our existing equipment, but results show a substantial reduction of the Charpy impact energy due to irradiation. For the P91 material, the results of Master Curve analysis are shown in Figure 1.

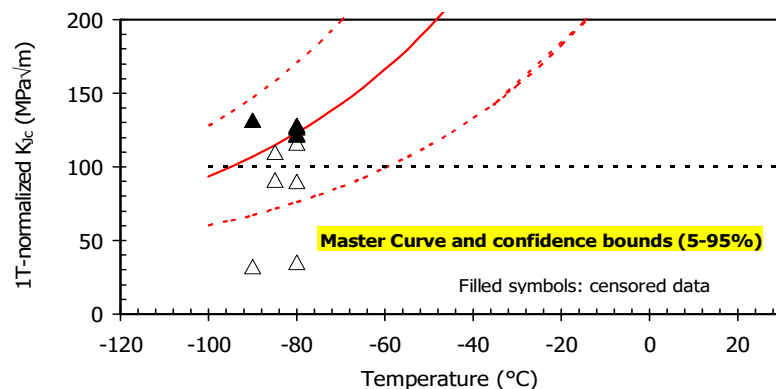


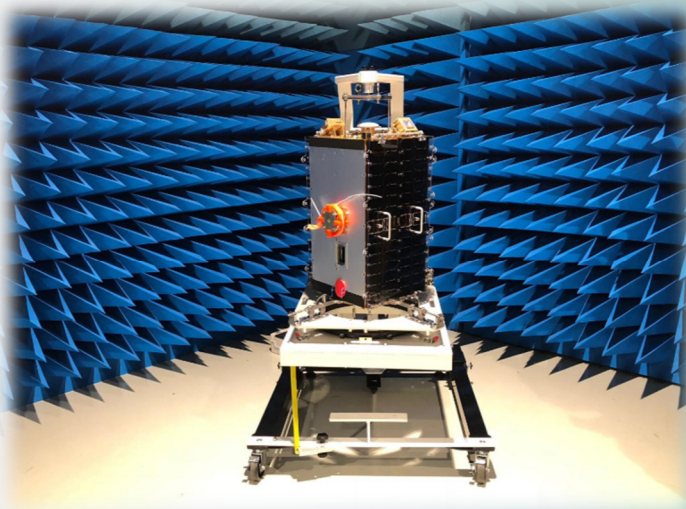
Figure 1: Master Curve results for P91 samples

## Remaining work

This project has been completed.

## Related publications

- [1] R. Székely, Á. Horváth, F. Gillemot, G. Uri, D. Antók, M. Horváth: *New Irradiation Device at the Budapest Research Reactor*, IAEA-TECDOC-CD-1693, Proceedings of the IAEA-Hotlab Technical Meeting Smolenice, Slovakia, 23–27 May 2011, p. 315, IAEA (2013)
- [2] A. Kovács, L. Tatár, F. Gillemot: *Experimental Results on Irradiated Samples in the Framework of MATTER project*, MTA EK progress report 2014 (2015)
- [3] ASTM E92 - 17 “*Standard Test Methods for Vickers Hardness and Knoop Hardness of Metallic Materials*”, ASTM International (2017)
- [4] EN 10 045-1: *Charpy impact test on metallic materials - Part 1: Test method*, European Committee for Standardization (1990)
- [5] ASTM E1921-13a „*Standard Test Method for Determination of Reference Temperature, T<sub>0</sub>, for Ferritic Steels in the Transition Range*”, ASTM International (2017)



### III. NUCLEAR SECURITY AND DOSIMETRY



# QUANTITATIVE IN-FIELD ANALYSIS OF UO<sub>2</sub> SAMPLES FOR DETERMINATION IMPURITIES USING PORTABLE LIBS SYSTEM

Éva Kovács-Széles, Csaba Tóbi

## Objective

As part of the Hungarian Safeguards Support Programme (SP) to the International Atomic Energy Agency, a SP Task (number HUN A2282/17/TND-001) was started in 2017 with the title and topic of "Assessment of Capabilities of Portable LIBS for Impurity Content Determination in Uranium Bearing Materials". This task supports extending the knowledge and providing of experimental data concerning the analytical capabilities of the promising emerging Laser Induced Breakdown Spectroscopy (LIBS) technology for use in the analysis of the purity of nuclear materials which can be used for identification of these materials and their origin for safeguards purposes. This project was the continuation of the task started in 2017.

## Methods

For this task, the portable LIBScan25+ type Laser Induced Breakdown Spectrometer (LIBS) of MTA EK produced by Applied Photonics Ltd. was used. It contains a 50 mJ Nd:YAG laser and an SSD (solid-state drive) specific optical system, closed ablation cells and gas-flushing pressure system. A method for pelleting of UO<sub>2</sub> powder samples was also developed. ~750 kg/cm<sup>2</sup> pressure was the optimal condition to produce pellets with size of 5 mm diameter X 1 mm height, ~ 0.2 g weight. International Atomic Energy Agency rendered 3 reference materials (so-called work standards, measured by other laboratories) for MTA EK to use as calibration standards for the quantitative measurements.

## Results

During this work, calibration curves for several elements were recorded during LIBS measurements. For this purpose, 3 reference materials were analysed in closed ablation chambers. One of the curves for Zn can be seen in Fig. 1. Several analytical performance parameters were also determined for the method, e.g. relative standard deviation: between 10-15% and detection limits: several 10 ppm, depending on the elements. Considering the solid-sample direct method with only 3 standards which has different matrix components, these parameters are satisfying.

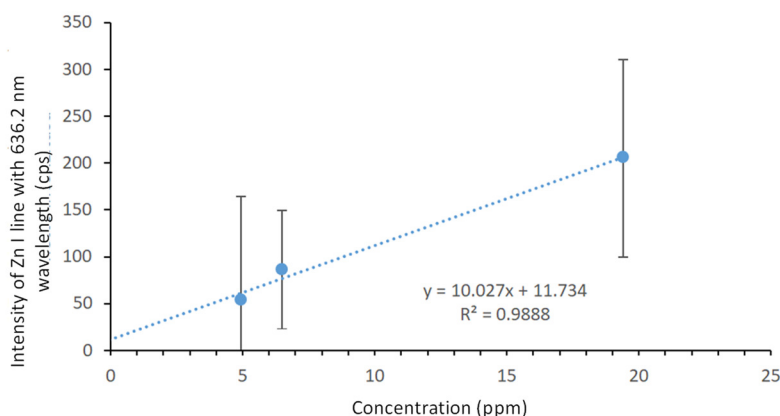


Figure 1: Calibration curve (Zn) for quantitative analysis by portable LIBS system

Using the calibration standards, UO<sub>2</sub> materials available at MTA EK were analysed by LIBScan25+ system as real samples. As Table 1. shows, the measured concentration (determined by ICP-MS) agreed well with reference values.

Table 1: Analysis data of real nuclear samples by LIBS compared with data from ICP-MS measurements

Element	Sample	ICP-MS reference value (ppm)	LIBS results (ppm)
Fe	CMX4-3	643	775
Zn	CMX4-1	28,2	12,2
K	HU1-b	15,1	11,4
Mg	CMX4-3	44,6	44,5

## Remaining work

Next steps of the work will be using real reference material with stable matrix and wide scale of elements, as well as concentrations, to refine the method. CRM-124 material will be transported from the Research Centre JRC Karlsruhe to MTA EK soon. CRM-124 contains 24 elements in 7 different concentrations. Elements are covering the real interest of the International Atomic Energy Agency.

# DETERMINING THE IRRADIATION HISTORY OF SPENT NUCLEAR FUEL USING GAMMA SPECTROMETRY (2<sup>ND</sup> YEAR)

*Péter Kirchknopf, András Kocsonya, István Almási*

## Objective

The Nuclear Security Department regularly measures the gamma spectra of spent fuel at Paks Nuclear Power Plant (NPP). Aside from the  $^{134}\text{Cs}$  and  $^{137}\text{Cs}$  isotopes, which give useful information on the burnup [1], other fission products (e.g.  $^{106}\text{Ru}$ ,  $^{144}\text{Ce}$  and  $^{154}\text{Eu}$ ) were also identified. The objective of this work was to develop a method based on the measured fission product activities that can be used to independently determine the irradiation history of spent fuel.

## Methods

The principle of this technique lies in the production and depletion processes of fission products during in-operation and out-of-operation periods, so the activities of these isotopes depend on the irradiation history of the fuel assembly (e.g. no. of cycles, cycle length). By measuring these activities, some information could be deduced on the assembly history. The gamma measurements were carried out with a coaxial HPGe (High-Purity Germanium) detector. The theoretical activity values for a supposed irradiation history were calculated using the ORIGEN computer code. After this, comparisons were made between the measured and the calculated values. If they agree, the input parameters used in ORIGEN can be accepted as the assembly history. Otherwise modifications to the input need to be made for further calculations. The input parameters include the initial enrichment, the thermal power of the assembly and the duration of in- and out-of-operation times.

## Results

For most nuclides, the difference between the experimental and theoretical activities was less than 25% (Fig. 1), except for  $^{125}\text{Sb}$ , which has a remarkably large discrepancy. The origin of these discrepancies is not yet clear. These results mean that the calculations with ORIGEN may not be accurate for the VVER-440 reactor type. Average correction factors were derived for the examined nuclides to keep the calculated activity ratios (with respect to  $^{137}\text{Cs}$ ) in line with the measurements (Tab. 1).

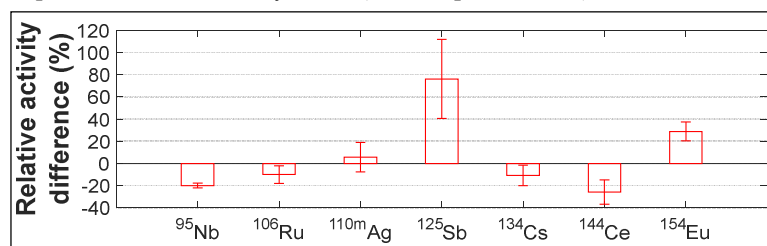


Figure 1: Deviation of the theoretical relative activities calculated with ORIGEN from the measured values

Table 1: Multiplication factors to be used for correcting the activities calculated with ORIGEN

	$^{95}\text{Nb}$	$^{106}\text{Ru}$	$^{110\text{m}}\text{Ag}$	$^{125}\text{Sb}$	$^{134}\text{Cs}$	$^{144}\text{Ce}$	$^{154}\text{Eu}$
<b>Correction factor</b>	1.2501	1.1196	0.9605	0.5912	1.1333	1.3722	0.7795
<b>1<math>\sigma</math> uncertainty (%)</b>	2.8	8.7	12.6	23.1	10.2	14.6	6.7

Activities were computed for several fuel histories with different cycle structures (Fig. 2a) and three thermal power levels (Fig. 2b). The large uncertainties caused by the correction factors, make it difficult to determine the exact assembly history.

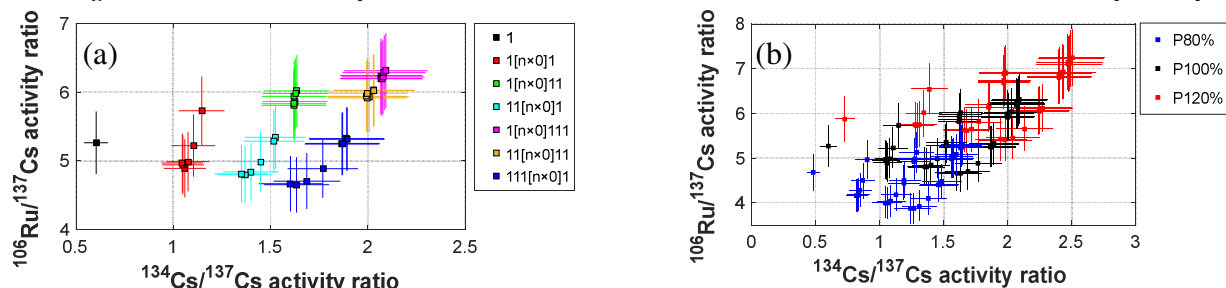


Figure 2: Relative activities for the  $^{134}\text{Cs}$  and  $^{106}\text{Ru}$  nuclide pair for different histories (a) and also for 80, 100 and 120% power levels (b). In the legend of (a), '1' symbolizes one cycle of in-operation time and '[n $\times$ 0]' means n cycle of out-of-operation time

## Remaining work

The work could not be finished entirely as this was the 2<sup>nd</sup> year part of a 4-year project, the 3<sup>rd</sup> year part continues in 2019.

## Related publication

- [1] I. Almási, C.T. Nguyen, Z. Hlavathy, J. Zsigrai, L. Lakosi and P. Nagy: *Burnup monitoring of VVER-440 spent fuel assemblies*, ESARDA Bulletin, No. 50, 41 (2013)

# IMPROVEMENTS ON MEASUREMENT TECHNIQUES FOR SOLID STATE NUCLEAR TRACK DETECTORS

*Julianna Szabó, Andrea Strádi, József Pálfalvi, Attila Hirn, Tamás Pázmándi*

## Objective

This work was aimed to improve the evaluation methods for solid state nuclear track detectors used in various fields, especially in space dosimetry and radon measurements. Besides quickening the measurement also new types of investigations should be introduced as the following of track evolution through multiple sheets of a detector stack or through multiple etching steps.

## Methods

The literature was browsed to find out what types of systems are used by groups involved in space dosimetry. Also the commercially available image analyser systems, usually optimized for radon (or neutron) measurements, were checked.

## Results

It was found that for space dosimetry applications similar systems (optical microscope, digital camera) are used everywhere for imaging and usually home-made image analyser software tools are developed for measurements. The main difference compared to our system is the automatic stage movement and focus control, which enhances the rapidity of the evaluation. Most groups perform the track measurements offline after the automatic image acquisition. This method is quite fast, but as the system is just focused on the detector surface (left image in Fig. 1), measurements can be effectuated only in this plane. For the elliptical tracks, not numbered in Fig. 1, it is enough to determine only the minor and the major axis, these parameters can be measured in fully automatic mode.

However, in space there are born tracks for which, beside the minor and the major axis, the projected length and the depth where the track ends have also to be measured, see the track numbered 1 in Fig. 1. (These are usually the high atomic number and energy - HZE - particles and some short range secondaries, whose contribution to the dose equivalent can be significant). For the measurement of these parameters the focus has to be shifted to the appropriate plane (right image in Fig. 1). Our system is able to perform real time measurements on such tracks examining their three-dimensional geometry in manual mode. The development of automatic methods for these three-dimensional track measurements would be quite complicated, but the automatic stage movement control, which quickens the image acquisition, coming into production.

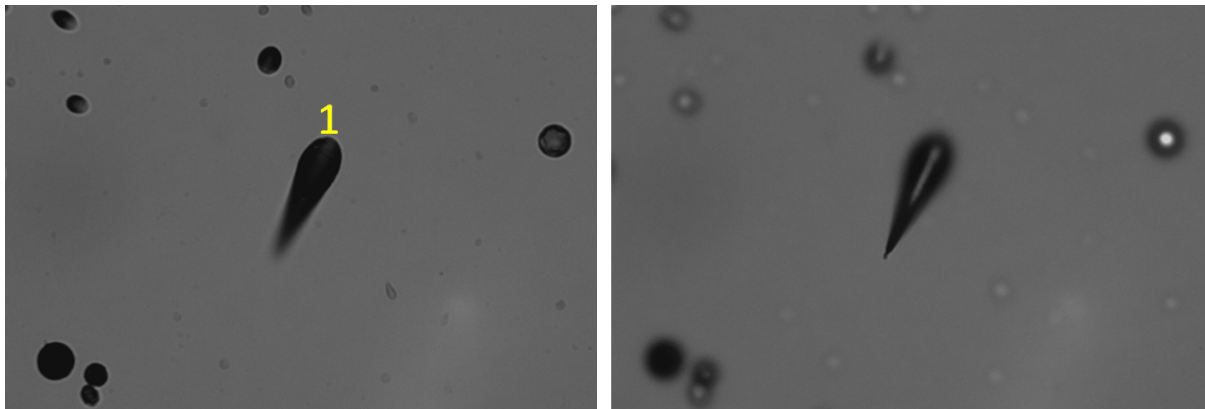


*Fig. 1: Image field from a detector flown onboard the International Space Station*

For radon measurements a fast, fully automatic system would be perfect. Our current system is good in automatic track recognition and with the automatic stage movement control it would be suitable also for these purposes.

## Remaining work

The automatic stage movement control will enable the positioning with high precision. In addition, the examination of long range tracks through multiple sheets of a detector stack and the study of track development over multiple etching steps will also be easier. These are essential in investigations of primary and secondary radiations in space, see [1, 2].

## Related publications

- [1] K.O. Inozemtsev, V.V. Kushin, A. Strádi, I. Ambrožová, S. Kodaira, J. Szabó, R.V. Toloček, V.A. Shurshakov: *Measurement of Different Components of Secondary Radiation onboard International Space Station by Means of Passive Detectors*. *Radiation Protection Dosimetry* **181**:(4), 412-417 (2018) doi: 10.1093/rpd/ncy043
- [2] K.O. Inozemtsev, V.V. Kushin, S. Kodaira, T. Kusumoto, A. Strádi, J. Szabó, I. Ambrožová, R.V. Toloček, V.A. Shurshakov: *Etch Track Detector Methods for the Measurements of Secondary Cosmic Radiation Doses Onboard the International Space Station (poster presentation)*. The 3rd International Symposium on "Physics, Engineering and Technologies for Bio-Medicine", 15 - 17 October 2018, Moscow, Russia.

# ANALYSIS OF THE MEASUREMENT RESULTS OF THE ENVIRONMENTAL RADIOLOGICAL MONITORING SYSTEM OF THE KFKI CAMPUS

*Tamás Pázmándi, István Apáthy, Sándor Deme, Zsuzsa Endrődi, Dorottya Jakab, Andrea Strádi, László Tósaki, Orsolya Várady-Botyánszky*

## Objective

The main objective of this work was to analyse the active dose rate measurement results of the reconstructed gamma radiation monitoring network and compare them with those of passive dose measurements. In addition, integrated analysis of the environmental monitoring related to the occurrence of anthropogenic  $^{106}\text{Ru}$  in various environmental compartments was performed, which helped to validate the accuracy and representativeness of environmental measurements.

## Methods

Part of the work was focused on the assessment of the gamma dose rate data gained during the operation of the reconstructed monitoring network. Correlation analysis was performed between the temporal variation of the measured gamma dose rate values at 17 critical points of the site and meteorological parameters, like precipitation.

The active gamma dose rate measurements were supplemented with passive dose measurements performed by TL dosimeters, which provided time integrated gamma dose rates following monthly readouts. PorTL and Pille dosimeters were installed at 13 points located around the primary nuclear facilities and radioactive material storages on the site. From these 13 points at 9 locations simultaneous measurements were performed with gamma dose rate meters and TL dosimeters, whereas at the remaining 4 locations parallel measurements were carried out with the two types of TL dosimeters. A database of about one year, which was obtained as the outcome of the simultaneous dose measurements, was evaluated.

Experimental characterization of the two types of TL dosimeter materials ( $\text{Al}_2\text{O}_3:\text{C}$  - PorTL;  $\text{CaSO}_4:\text{Dy}$  - Pille) was performed, their properties, as dose response, angular dependence and anomalous fading were investigated. In order to state whether the passive dosimeters are appropriate for environmental area monitoring, we also participated in an intercomparison. 20 Pille dosimeters have been sent to Germany, where some of them were exposed to terrestrial and secondary cosmic radiation for about 6 months, some were irradiated in a primary  $^{137}\text{Cs}$  photon field at two different angles, and a few were stored in an underground laboratory to determine the transport dose.

Anthropogenic  $^{106}\text{Ru}$  has been detected in the environment from late September to early October 2017 by several European environmental radiological monitoring networks - including the monitoring system in the KFKI Campus.  $^{106}\text{Ru}$  activity concentrations in environmental compartments (airborne particulates, deposition, terrestrial indicators) measured by the local monitoring system were evaluated. Potential dose consequences due to the  $^{106}\text{Ru}$  contamination were assessed, considering external exposure from cloudshine and groundshine and internal exposure via inhalation.

## Results

The research resulted the following outcomes:

- The comparative analysis showed -12% average bias between the time integrated gamma dose rates of PorTL and Pille, while both passive dosimeters underestimated the ambient dose rate compared to the active dose rate meters.
- As the result of the experimental characterization, no significant differences were determined between the investigated properties (dose response, angular dependence and anomalous fading) of the TL materials.
- The results of the intercomparison for area photon dosimeters showed below 10% relative bias between the reported and target ambient dose equivalents, which can be considered as an acceptable difference in dosimetry.
- Residence time of the radioactive plume in the atmosphere and temporal variation of the  $^{106}\text{Ru}$  contamination was determined. Results were corrected with account taken of the relation between the sampling duration and the residence time of the radioactive plume, therefore directly comparable results were provided. There was a good agreement between the local results and the reported national and international values. According to the dose assessment, inhalation dose has been found as the main exposure pathway, which predominantly contributed to the total effective dose (150 nSv) in a short-term.
- Integrated analysis of deposition measurements and meteorological data was performed. The calculation indicated that wet deposition mechanism was the dominant contributor to the  $^{106}\text{Ru}$  deposition on the ground surface. In order to enable the separated sampling of wet and dry deposition, a special deposition sampling equipment was designed and manufactured. Separated sampling of wet and dry deposition will be started in 2019.

## Remaining work

In order to identify the potential causes of the differences between the dose values, further investigation is required to determine the energy dependence and thermal fading properties of the used TL dosimeter materials.

## Related publications

- [1] D. Jakab, G. Endrődi, A. Kocsonya, A. Pántya, T. Pázmándi, P. Zagyvai: *Methods, results and dose consequences of  $^{106}\text{Ru}$  detection in the environment in Budapest, Hungary*. Journal of Environmental Radioactivity **192**, 543-550 (2018) <https://doi.org/10.1016/j.jenvrad.2018.08.004>

- [2] D. Jakab, G. Endrődi, S. Kapitány, A. Kocsonya, A. Pántya, T. Pázmándi, P. Zagyvai: *Evaluation of the Hungarian  $^{106}\text{Ru}$  measurement results. XLIII. Annual Meeting on Radiation Protection, April 17-19, 2018, Hajdúszoboszló, Hungary* (oral presentation in Hungarian)
- [3] D. Jakab, G. Endrődi, S. Kapitány, A. Pántya, T. Pázmándi, P. Zagyvai: *Evaluation of the measurement results related to the environmental detection of  $^{106}\text{Ru}$  in the fall of 2017. XVII. Symposium of the Hungarian Nuclear Society, November 29-30, 2018, Szekszárd, Hungary* (oral presentation in Hungarian)

# DEVELOPMENT OF MEASUREMENT METHODS FOR DETERMINING INTERNAL DOSE

*Tamás Pázmándi, Annamária Pántya, Dorottya Jakab, Gáborné Endrődi, Péter Zagyvai*

## Objective

Individual monitoring gives information needed to assess occupational and public exposure by measuring individual body activities, excretion activities or activity of inhaled air.

For the great majority of incorporated radionuclides, the internal dose is estimated in two steps. In the first step the actual activity present in the body is determined by direct or indirect monitoring methods. By direct gamma spectrometric measurements activity in the whole or part of the human body can be determined (in vivo), while by indirect methods the radioactivity of physical and biological (in vitro) samples are assessed. In the second step the value of intake and the associated committed dose can be estimated on the basis of measured data considering necessary assumptions on exposure conditions (time and route of intake, chemical form etc.).

## Methods

During this work, first of all we interpreted the new regulation (487/2015. (XII.30)) and new international recommendations (TECHREC and ICRP OIRs) and the renewed MSZ 62/7 which had been published in the recent years. Based on them, we reviewed the measurement practices applied for in vivo monitoring in MTA EK and then updated or developed measurement specifications for the determination of the internal exposure. The following methods were elaborated: whole body and part of body counting, thyroid measurement, measurement of gamma and beta emitter isotopes in urine, dose estimation. Calibration or quality control of the equipment has been carried out in accordance with the developed measurement procedures. In addition, we took part in several intercomparisons to verify the appropriateness of the methods.

## Results

We presented technical steps for direct and indirect methods of monitoring individuals for occupational intakes of radionuclides. We described the steps needed to measure low- and high-energy photon emitters in the human body and to perform surface contamination check on individuals in order to distinguish between external and internal contamination. The procedure applies to all individuals undergoing in vivo monitoring of potential intakes of photon-emitting radionuclides into the human body at the Whole Body Counter (WBC) Laboratory. We fixed the steps required for equipment calibration, quality control and maintenance in the laboratory. They apply to calibration and regular maintenance of the NaI(Tl) and HPGe detectors used for low- and high-energy photon measurements to assure continuity of in-vivo individual monitoring service. Individual monitoring is extended to parts of body counting as well, namely to lung and thyroid. For this method, we also determined the optimal geometry and performed the necessary measurements, then the steps are summarized in a description. For each measurement the conditions of measurement shall be recorded (counting time, equipment and method used for measurement, limit of detection, name of operator, background count, and calibration). For indirect measurements we determined the measurement techniques and sample preparation method. The gamma emitter nuclides can be determined with HPGe detector in the low background chamber and the activity of soft beta emitter isotopes can be measured with liquid scintillator following an appropriate sample preparation. We have given the measurement instructions for both techniques. We describe the steps involved in the estimation of intakes and assessment of committed doses for workers with demonstrated amount of radionuclides in their bodies and/or excreta.

## Remaining work

This project has been completed.

## Related publications

- [1] A. Pántya, Á. Dálnoki, A. R. Imre, P. Zagyvai, T. Pázmándi: *Tritium internal dose estimation with liquid scintillators*, Applied Radiation and Isotopes **137**, 18-22 (2018)
- [2] A. Pántya, A. Andrási, D. Jakab, T. Pázmándi, P. Zagyvai: *Uncertainty estimation of thyroid activity measurements and its consequences in dose assessment*, 5th European IRPA Congress (2018)
- [3] A. Pántya, T. Pázmándi, D. Jakab: *Uncertainties in analysis of urine samples*, PROCORAD Annual Meeting, Ispra, Italy (June 2018)

# ESTABLISHING THE METHODOLOGY OF LEVEL 3 PROBABILISTIC SAFETY ASSESSMENT

*Tamás Pázmándi, Csilla Rudas, Péter Szántó*

## Objective

In the past decade there has been a growing interest worldwide in the development of a common, standardized Level 3 Probabilistic Safety Assessment (L3PSA) methodology. A couple of international meetings and workshops were organized by the International Atomic Energy Agency (IAEA) to facilitate sharing the knowledge and good practices of L3PSA, documents presenting the state-of-the-art L3PSA practices of the Nuclear Regulatory Commission (NRC) were published and an activity for conducting a comprehensive survey about L3PSA practices was launched by the Organisation for Economic Co-operation and Development (OECD). Currently, there is no Hungarian regulatory requirement for conducting L3PSA analysis. The aim of this work is to evaluate a L3PSA methodology for Hungarian conditions.

## Methods

In this first phase of the work, the most important documents issued by the International Atomic Energy Agency (IAEA), the American Nuclear Authority (NRC) and the American Nuclear Society (ANS) were reviewed. The L3PSA practices in different countries based on the proceedings of the 2012 IAEA Technical Meeting in Vienna and the 2013 Regional Workshop in Warsaw as well as the results of the OECD survey were examined. Available codes which can be used to conduct off-site consequence analysis were evaluated based on the calculation models, the computational capabilities and the necessary input requirements.

## Results

The review of the literature showed that there is no harmonized methodology in the field of L3PSA. The IAEA recommendation for conducting L3PSA analysis issued in 1996 presents a somewhat outdated methodology compared to current practices, in which the explanations and justifications for modelling considerations and omissions are not sufficiently detailed. The preliminary draft of a L3PSA standard issued by the ANS in 2017 defines requirements for the probabilistic analysis of atmospheric radioactive releases, describes the methodology for each calculation step and the appropriate documentation procedures. The requirements are flexible, the modelling decisions are not fixed but can be chosen based on the application of the calculation, thus the standard can widely be used.

The practices of countries that perform L3PSA or conduct research in the field are summarized in Table 1. In Korea and the Netherlands, there are regulatory requirements for L3PSA analysis when applying for a license for establishing, constructing, commissioning, operating or decommissioning nuclear installations. Despite not being legally required to do so, Japan and the USA perform L3PSA calculations to verify the fulfilment of quantitative safety objectives, to improve emergency preparedness and response, to optimize severe accident management strategies and to conduct environmental impact assessments. In Finland and Sweden significant research is underway to assess L3PSA practices, to standardize the calculation methodology, to develop regulatory guidelines and to launch pilot studies. The MACCS software is widely used for L3PSA calculations (in Korea, the USA, the Netherlands and Finland), however, this code is not easily applicable for methods and modelling considerations which differ from the US practices. As a result, some countries are developing or planning to develop their own L3PSA software (OSCAAR - Japan, NUDOS - the Netherlands, LENA - Sweden, ARANO - Finland). Two deterministic codes (COSYMA and RODOS) can be used for limited probabilistic assessments, as they contain statistical analysis tools for considering different weather scenarios or countermeasure strategies.

Table 1: Summary of the international practices of L3PSA

	Regulation	L3PSA calculation	Objective	Software	L3PSA for NNPs
South Korea	yes	yes	Risk Criteria Emergency Planning Zones	MACCS	n.a.
The Netherlands	yes	yes	Risk Criteria	COSYMA NUDOS2 MACCS	Borssele
USA	no	yes	Risk Criteria Environmental Impact Assessment Severe Accident Mitigation Actions	MACCS	Surry, Peach Bottom, Zion, Sequoyah, Grand Gulf
Japan	no	yes	Risk Criteria Emergency Response	OSCAAR	n.a.
Finland	no	yes	Research	ARANO MACCS	no
Sweden	no	interest	Research	LENA	no

***Remaining work***

In the next phase of the work, the Hungarian legal environment and the possibility of introducing L3PSA regulatory criteria will be explored. The resources necessary for conducting L3PSA will be investigated.

***Related publications***

- [1] Cs. Rudas, T. Pázmándi, P. Szántó, A. Bareith, T. Siklóssy: *Establishing a new Level-3 probabilistic safety assessment methodology in Hungary*, PSA-2019 (accepted)
- [2] Cs. Rudas, T. Pázmándi: *Methods of Probabilistic Radiological Consequence Analysis for Hungarian Regulatory Purposes*, HARMO-19 (submitted)

# STUDY OF THE RADIATION FIELD IN THE UPPER ATMOSPHERE

*Balázs Zábori, Attila Hirn*

## **Objective**

The present research focuses on determining the characteristics of the radiation field in the near-Earth region based on measurements performed in space experiments and then, based on these results, aims at giving a detailed description of the radiation field and its dosimetry.

## **Methods**

Measurements had been performed and analysed in the preceding years on board stratospheric balloons and on a sounding rocket. To extend the region of interest around the Earth, a space radiation detector (ESEO-TRITEL) had been developed, manufactured and tested to be operated on board the European Student Earth Orbiter (ESEO) satellite in the frame of a European Space Agency education program. Acceptance tests of the 3D silicon detector ESEO-TRITEL were performed first at payload level. These were followed by integration tests on the payload connected to the ESEO flatsat and by mechanical fit checks to the satellite structure. The final environmental acceptance tests were performed after integration of the satellite, including vibration, thermal-vacuum, and electromagnetic compatibility (EMC) tests.

## **Results**

The integration test campaign of the ESEO-TRITEL protoflight model was successfully completed. The payload passed the final environmental tests and it was ready to be launched into space at the time of the report was written.

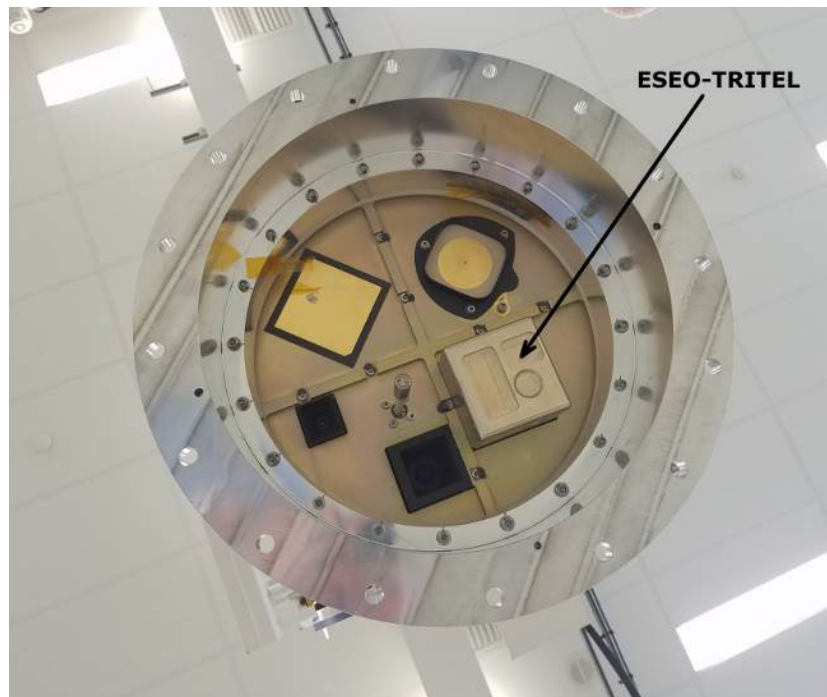


Figure 1: The face of the ESEO satellite pointing into the nadir direction. The section of the ESEO-TRITEL instrument containing the space radiation detectors and therefore protruding from the satellite body is indicated with an arrow in the image.

## **Remaining work**

The project presented is a PhD research work. Scientific analysis of the first set of data from ESEO-TRITEL will be performed next year. PhD thesis work will also be finalized in year 2019.

## **Related publications**

- [1] B. Zábori, A. Hirn, A. Gerecs, A. Pantya, Cs. Rudas, D. Jakab, T. Hurtony: *ESEO-TRITEL experiment to measure the cosmic radiation*, Proc. of 2nd Symposium on Space Educational Activities, April 11-13, 2018, Budapest, Hungary (2018)
- [2] B. Zábori, A. Hirn, J. Eastwood, P. Brown, Ch. Palla, T. Oddy, D. Nolbert, G. Santin, P. Nieminen, G. Marosy: *Space Radiation and Magnetic Field Environment Specification for the RADCUBE Space Weather Related CubeSat Mission*, Proc. 69th International Astronautical Congress, October 1-5, 2018, Bremen, Germany (2018)

# MODELLING THE TRANSPORT OF RADIONUCLIDES IN SURFACE WATER: PART 4

Barbara Brockhauser, Sándor Deme, Tamás Pázmándi, Csilla Rudas, Péter Szántó

## Objective

The objective of the research of modelling the transport of radionuclides in surface water is the development of a dynamic transport model that estimates the environmental radiation resulting from an accidental radioactive emission from the Paks nuclear power plant (NPP). In the last phase of the 4-year project, a software and documentation were developed based on the established aquatic transport model that can determine the consequences of a liquid release from Paks NPP and calculate the dose for different aquatic pathways.

## Methods

The developed aquatic transport model uses local and site specific geological and hydrological data including the local shape of the river's cross-section, the water level dependent flow rate, the flow velocity and also the local sediment data. Sensitivity analyses were conducted to determine the most important input parameters of the program.

## Results

According to the analyses, one of the most important parameters is the river water level as it changes frequently, and has a huge influence on other hydrological parameters. Figure 1 shows the daily change of the water level in 2017 for the Danube at Paks. Analysing the average monthly data for the last 10 years, it can be seen that the highest river stages occur late spring and early summer. The lowest water levels were measured during autumn and winter-time.

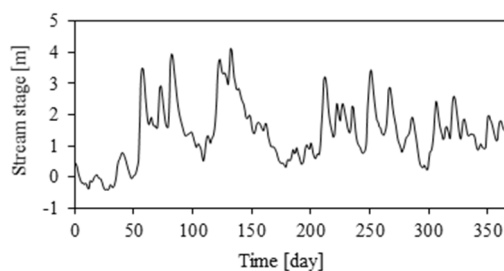


Figure 1: The daily change of the water level at Paks during 2017

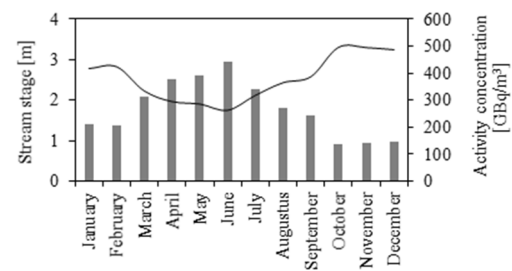


Figure 2: Connection between the calculated activity concentration (line) and the water level (columns)

Further calculations were made with the program to determine a connection between the activity concentration in the water and the water level [1]. In the calculation, the released activity was considered to be  $1E+16$  Bq I-131, and the correlation between the activity concentration and the water level can be seen in Figure 2. It is conspicuous that increase in the water level decreases the activity concentration at shore side. Additional study was conducted to see the behaviour of the lateral mixing of the activity concentration depending on the season. Measurement results suggested that the cross-sectional distributions of the activity concentration are almost the same in the autumn and winter (AW) and also in the spring and summer (SS) time, therefore these seasons can be considered together. The lateral distribution of the activity concentration for autumn-winter and the spring-summer time is shown in Figure 3.

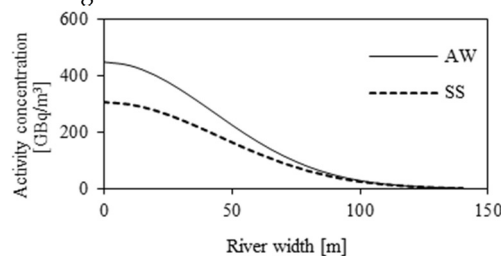


Figure 3: The lateral distribution of the activity concentration for autumn-winter and spring-summer time

The SS time has higher water level, therefore the lateral mixing is better, so the activity concentration at shore side is 1.5 times lower than during AW time. Most of the activity concentration occur in the first 100 m for both cases.

## Remaining work

This project has been completed.

## Related publication

- [1] B. Brockhauser, S. Deme, T. Pázmándi: *Connections between the calculated activity concentration and the water level at Gerjen for liquid release from Paks nuclear power plant*, XVII. MNT Nuclear Technology Symposium, Szekszárd, Hungary (2018)

# DEVELOPMENT OF THE SYSTEM FOR EVALUATING THE RADIATION SITUATION – DEVELOPING THE DATABASE

*Tamás Pázmándi, Péter Szántó*

## Objective

The primary objective of the four-years-long work is to develop a system for the evaluation of the radiation situation in Hungary. The system consists of meteorological and radiological database. The input data for the database are provided by the members of the Hungarian radiological measurement network. The data in the system will be used to provide information on the radiation situation in Hungary. In emergency situations, the system will also be used to estimate the possible sources of the release.

## Methods

The state of the current Hungarian regulatory framework for monitoring systems is fragmented. There are two monitoring systems in Hungary, OKSER (National Environmental Radiation Protection Control System) and OSJER (National Radiation Observation and Control System). They are being overseen by different organizations and institutions. The systems consist of their own stations established by the operating organization, most of stations can be part of both systems. In the already established, long-lasting and satisfactorily operating Hungarian practice, the monitoring of accidental (emergency) and normal (planned) radiation situations is regulated separately and is mostly performed by the same systems but according to different protocols. In order to implement the changes in the regulation, we have designed the database structure for the operation of the data analysis and representation system. The purpose of creating the database is to store the radiological and meteorological data received from the monitoring systems. The requirements towards the database cover the following points:

- content requirements: needs to contain all data from radiological monitoring systems, needs to be able to handle any measurement data generated during a radiological emergency, and needs to be ready to store the results of model calculations for atmospheric dispersion, like the SINAC decision support system used in Hungarian Atomic Energy Authority Centre for Emergency Response, Training and Analysis (OAH CERTA),
- structural requirements: needs to be able to easily filter, render searchable for future representations and analyses, and needs to be easily expandable when the monitoring system develops and changes,
- system requirements: SQL-based IBM DB2 database is recommended to manage the database,
- format and access requirements: needs to be compatible with the requirements of the International Radiological Information Exchange (IRIX) and European Radiological Data Exchange Platform (EURDEP) formats.

## Results

The structure of the system responsible for storing the data is shown in Figure 1. In the current part of the work, the middle element, the database structure was developed.

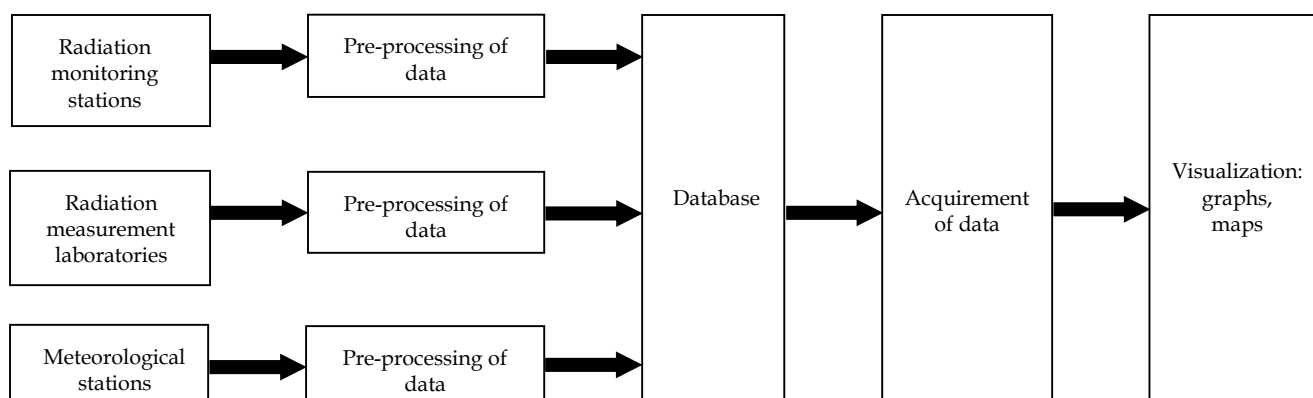


Figure 1: The structure of the system

It has been found that the assessment of the radiation situation in different cases (in normal, accidental and existing radiation situations) should be made by considering the different aspects derived from the given irradiation situation. In any case, the assessment of the situation is influenced by the limited capacity of the measurements. Showing measurement data on graphs or maps, supplementing them with the results of model calculations, occasionally helps the assessment of the situation and the work of the decision makers.

## Remaining work

In the following stages of this work, details of the system will be evaluated and the introduction of the developed system will be performed.

# SPACE DOSIMETRY FOR HUMAN SPACEFLIGHT AND BIOSATELLITE RESEARCH

*Attila Hirn, István Apáthy, Antal Csőke, Sándor Deme, András Gerecs, Eszter Pálfalvi, József K. Pálfalvi, Tamás Pázmándi, Andrea Strádi, Julianna Szabó, Balázs Zábori*

## Objective

Space dosimetry and space weather activities of the MTA EK research centre are concentrated in the Space Dosimetry Research Group. Several dosimeter systems developed by the group operate on board the International Space Station (ISS) with the aim of providing information on the dose distribution at different locations with different shielding conditions and also personal dosimetry. Maintenance, scientific and technical support during operation and upgrade of these systems are key tasks of the group. In parallel, different types of silicon detector telescope systems have been and are being developed for satellites in low Earth orbit. The activities reported in the present paper have been realized in cooperation with the Institute of Biomedical Problems (IBMP), Russian Academy of Sciences and S. P. Korolev Rocket and Space Corporation Energia.

## Methods

The Pille space-qualified thermoluminescent (TL) dosimeter system, developed in our institute, provides accurate and high resolution absorbed dose data. In 2018, a new Pille TL Reader (No. 20) was sent to the ISS to replace the unit No. 16 that already has been operated on board without any degradation or malfunction since 2003, but the warranty of which expired. Pille is operated as part of the service dosimetry system of the Russian Segment. It comprises a set of dosimeters and an on-board reader. For on-board stability analysis, from time to time, all dosimeters are placed on panel No. 327 for two weeks, and the quasi-homogeneous radiation field at that position is used as natural calibration radiation source. The correction factors for the individual dosimeters are then calculated from the results of the sensitivity measurements. In the frame of the commissioning of the new Pille Reader and the dosimeters delivered, first all new Pille dosimeters were read out with Pille Reader No. 16. This was followed by on-board cross-calibration campaigns, with each new dosimeter being paired with an old one and each pair being placed at different locations for 25 days and 36 days. Read-outs were performed by both Pille Readers.

Bion-M2 is a returnable biological satellite programme led by IBMP. The objective is to study zero-gravity and space radiation impacts on living organisms at about 800 km above the Earth's surface. TRITEL-B is one of the scientific payloads on the returnable capsule, to be developed in MTA EK, with the aim of supporting biological experiments with dosimetry data. Radiation transport calculations were performed with the Space Environment Information System (SPENVIS) online tool to support development of the detector concept based also on the three-dimensional silicon detector system, TRITEL.

## Results

In year 2018, approx. 6000 measurements were performed with the Pille system. The data obtained were evaluated. In the first read-out of the new Pille dosimeters, following an exposition of 122 days (85 days on ground, 37 days in space), the maximum deviation from the average was 4%, significantly smaller than the maximal deviation of  $\pm 10\%$  allowed by the international standards for TL detectors. In the cross-calibration campaigns, the deviation of the average for all Pille dosimeters were within  $\pm 10\%$ , except A0301 and A0311. These two dosimeters have been used for automatic read-out for years, their slight degradation was known. The accuracy of all of the new Pille dosimeters (No. A0151 – A0155) and the Pille Reader No. 20 met the specifications; their regular use on ISS is allowed.

By means of reconfiguration of the three silicon detector pairs in TRITEL to form a one-dimensional triple telescope with aluminium absorbers in-between the detector pairs, and integration of the passive detector package containing solid state nuclear track etch detectors and thermoluminescent detectors into the instrument, a measuring package capable of providing depth-dose and depth LET (Linear Energy Transfer) information for the biological experiments was proposed. The preliminary dose calculations have shown that the average dose rates expected at different depths differ only about 20% for the two possible inclinations of the Bion-M2 orbit. The highest absorbed dose rate is expected just behind the wall of the capsule ( $\sim 1$  mGy/h). The dose rates at the largest depth is  $\sim 0.5$  mGy/h.

## Remaining work

Evaluation and interpretation of the measurement data produced by the Pille and TRITEL dosimeter systems on board ISS, as well as maintenance of these instruments will be pursued. Definition and development of the preliminary design of the TRITEL-B experiment for the BION-M2 biosatellite will be continued.

## Related publications

- [1] A. Strádi: *Personal dosimetry in extreme environment*, Haditechnika (Miltech) **52(2)**, 23, in Hungarian (2018)
- [2] A. Hirn: *The TRITEL dosimetry system for astronauts and on board satellites*, Haditechnika (Miltech) **52(4)**, 46, in Hungarian (2018)
- [3] A. Hirn, V. Shurshakov, I. Apáthy, A. Csőke, S. Deme, A. Gerecs, O. Ivanova, A. Lishnevskii, T. Pázmándi, A. Strádi, J. Szabó, R. Tolochek and B. Zábori: *TRITEL-B: Concept for measuring depth-dose and depth-LET on the returnable biological satellite Bion-M2*, Proceedings of the 69<sup>th</sup> International Astronautical Congress, IAC-18-A1.5.11 (2018)

# TRITEL INSTRUMENT ON BOARD THE ESEO SATELLITE

*Balázs Zábori, Attila Hirn, András Gerecs, István Apáthy, Boglárka Erdős, Anna Baranyai*

## Objective

The development of the European Student Earth Orbiter (ESEO) was announced in the year 2008 by the European Space Agency (ESA) for students interested in space activities. ESEO is an educational hand on project of the ESA Education Office, carried out as part of the ESA Academy programmes. It is stated in the ESEO mission objectives: “measure the ionizing radiation environment in orbit”. The ESEO-TRITEL payload will fulfil this objective during the mission of the satellite. The MTA Centre for Energy Research (MTA EK) is responsible to support, coordinate and provide professional background for the ESEO-TRITEL student team which is responsible for the ESEO-TRITEL payload development activities. The activity of the University students’ teams was coordinated by SITAEL S.p.A. (Italy), System Prime and Integrator of the whole spacecraft platform.

## Methods

In order to study the cosmic radiation field in orbit for dosimetric purposes, the development of a three dimensional silicon detector telescope (TRITEL) with almost uniform sensitivity got underway in the former KFKI Atomic Energy Research Institute (AEKI, now part of MTA Centre for Energy Research) in the last decade. The instrument comprising three mutually orthogonal, fully depleted PIPS (Passivated Implanted Planar Silicon) detector pairs are designed to measure the energy deposition of charged particles. The main design goal in the frame of the ESEO mission is to design, develop, manufacture and verify through intensive test campaign a new, satellite version of the TRITEL instrument.

## Results

Following the authorisation ESA to manufacture the ESEO-TRITEL flight model an intensive acceptance test campaign was carried out covering specific manufacturing related inspections, functional tests, calibration activities, vibration tests, thermal-vacuum (T-VAC) tests, electromagnetic compatibility (EMC) tests. The ESEO-TRITEL team was responsible to carry out the extensive test programme in the light of the ECSS (European Cooperation for Space Standardization) standards. Most of the tests were carried out in the internal facilities of MTA EK, only some specific calibration activities, the vibration and EMC tests were performed in external locations. Finally, the flight model was accepted by ESA and it was delivered to Italy for higher level satellite integration and test activities. After the ESEO satellite integration it was shipped to the technology test centre of ESA for final satellite level acceptance testing, including vibration, T-VAC and EMC tests. It was verified that the satellite and the ESEO-TRITEL instrument are ready for launch (Fig. 1). The ESEO satellite was launched on 03.12.2018. from US (United States) Vandenberg Air Force Base on board a Falcon-9 rocket operated by SpaceX (the mission name was SpaceX’s SSO-A mission). The ESEO satellite activated itself just after separation from the launch carrier and started transmitting beacon signals, which were received by the ground control of the mission. The ESEO-TRITEL project is realized in the frame of PECS contract No. 4000112065 and the ESA PRODEX contract No. 4000124167.

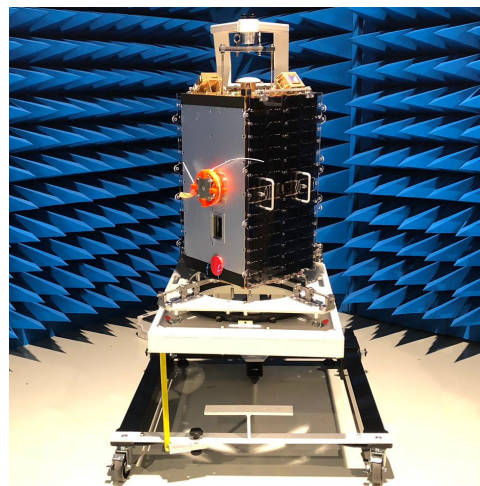


Figure 1: The integrated ESEO satellite ready for launch (source: ESA)

## Remaining work

After several in-orbit satellite functional and performance tests the ESEO satellite will start its nominal operation, which includes at least one-month full operation scenario for the ESEO-TRITEL instrument. The scientific data received will be analysed, interpreted and reported by the ESEO-TRITEL team in 2019.

## Related publication

- [1] B. Zábori et al.: *ESEO-TRITEL experiment to measure the cosmic radiation*, Proceedings of the 2<sup>nd</sup> Symposium on Space Educational Activities, SSEA-2018-117, 356 (2018)

# DOSE DISTRIBUTION INSIDE THE INTERNATIONAL SPACE STATION-3D / DOSIS 3D

*Julianna Szabó, Andrea Strádi, Attila Hirn, Balázs Zábóri, József K. Pálfalvi*

## Objective

The aim of the DOSIS 3D project is the measurement of the radiation environment inside the International Space Station (ISS). The project is organized by the European Space Agency (ESA) under the leadership of the German Aerospace Centre (DLR), with the participation of research groups from all around the world. MTA Centre for Energy Research (MTA EK) is responsible for the provision of passive radiation detectors for the measurement of the absorbed dose, Linear Energy Transfer (LET) spectra and dose equivalent. These activities are funded in the frame of the ESA PRODEX Experiment Arrangement No. 4000124183. DOSIS 3D had been started in the year 2012 and after several extensions it was prolonged till the remaining lifetime of the ISS. It consists of approximately half-year long exposure cycles (phases). The current report reflects the contribution of MTA EK until the end of 2018, with emphasis on the most recent phase No. 12.

## Methods

Thermoluminescent detectors (TLDs) and solid state nuclear track detectors (SSNTDs) are applied by the MTA EK Space Dosimetry Research Group to investigate the dose contribution of the low ( $< 10 \text{ keV}/\mu\text{m}$ ) and the high ( $> 10 \text{ keV}/\mu\text{m}$ ) LET cosmic radiation. The plastic detector boxes contain two SSNTD sheets and six or eight TLD pellets (half of them is made of  $^6\text{Li}$  enriched MTS-6 material, the other half is  $^7\text{Li}$  enriched MTS-7). In each phase there are 10 single boxes and a set of 3 boxes (arranged in the 3 directions of space) installed inside the European Columbus module. For a better understanding of the properties of the applied radiation detector systems, an extensive ground intercalibration program is applied as an indispensable part of the work with contributions from all participating investigators.

## Results

As in the previous phases, the doses measured in phase 12 by the MTS-6 pellets were somewhat higher than the MTS-7 signals, indicating the presence of secondary neutrons, see Fig. 1. Fig. 2. presents the dosimetric quantities measured by SSNTDs. The tendency observed in case of the different locations with different shielding conditions is similar for the high and for the low LET radiation: the highest doses were measured in Boxes 2, 6 and 7, as usually.

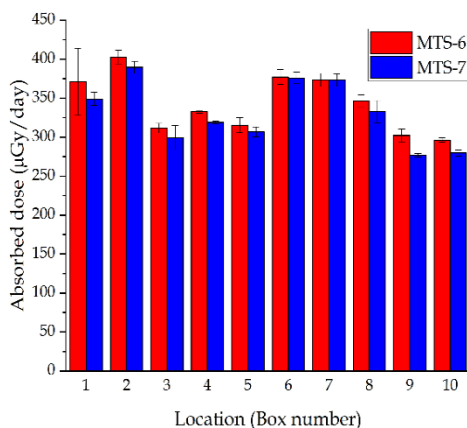


Figure 1: Absorbed dose rates obtained by TLDs, phase 12

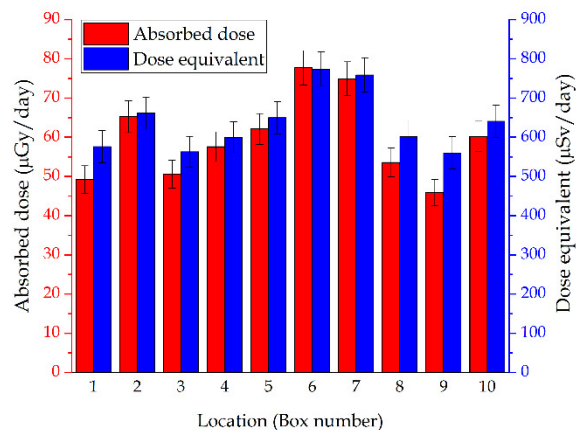


Figure 2: Absorbed dose and dose equivalent rates obtained by SSNTDs, phase 12

The doses measured by the MTS-7 pellets were appropriately combined with the SSNTD results to obtain the total absorbed dose and dose equivalent values. Their ratios gave quality factors between 2.4 and 2.9.

## Remaining work

According to the current plan the project continues till 2024. The interpretation of the vast amount of data is in progress. An interactive database is going to be built, serving the scientific community and holding essential information for the application of radiation protection standards for manned spaceflight and for any radiation susceptible experiment in space.

## Related publications

- [1] T. Berger, ... , J. Szabó, A. Strádi et al.: *The DOSIS 3D Project Onboard the International Space Station - Status and Science Overview of 6 years of measurements (2012-2018)*, 42<sup>nd</sup> Committee on Space Research Scientific Assembly, Pasadena, United States, Abstract Book p. 1941 (2018)
- [2] T. Berger, ... , J.K. Pálfalvi, J. Szabó, A. Strádi et al.: *DOSIS & DOSIS 3D Onboard the ISS - Status and Science Overview from 2009 – 2018*, 23<sup>rd</sup> Workshop on Radiation Monitoring for the International Space Station, Tsuruga, Japan (2018)

# RESEARCH & DEVELOPMENT ACTIVITIES IN SPACE WEATHER

*Balázs Zábori, Attila Hirn, András Gerecs, István Apáthy*

## Objective

The research on space weather and its effects will be more and more important in the near future, as a continuous increase in human presence is in progress in the Near-Earth region and the technology dependency of the human civilization has become higher than ever mainly in the fields of energy and telecommunication systems. To study space weather and to protect our technology, as a first step, it is necessary to develop and establish an advanced monitoring system to provide scientific data about the space radiation intensity and the status of the magnetosphere in order to achieve the possibility for a reliable forecast database. Thus development of new space weather related instrument technologies got underway at the Centre for Energy Research, Hungarian Academy of Sciences (MTA EK), based on silicon detector technology including magnetic field measurement capabilities. By having a compact design realized following CubeSat/SmallSat standards, the monitoring of space radiation and magnetic field environment will be possible with sufficient statistics in the Near-Earth region on board a fleet of CubeSats/SmallSats as a part of ESA's (European Space Agency) hosted payload mission concept. Additionally, the developed instrument technology can provide a low-cost alternative for supporting radiation damage estimations commercially for future satellite missions as well. All these activities are realised in international cooperation.

## Methods

In the frame of the Space Weather Service Network (SWE) segment of the ESA Space Situational Awareness (SSA) programme ESA requested an operational space weather prediction system with appropriate databases originating from near-real time service provider instruments/payloads in order to offer space weather related services. Since the space weather environment of the Earth is highly influenced by several physical parameters (magnetic field variability, cosmic ray intensity, solar activity, atmosphere, etc.) and mainly due to the complexity of the magnetosphere, a very good spatial and time resolution is required in space weather monitoring. To fulfil this goal ESA defined the Distributed Space Weather Sensor System (D3S) concept utilizing hosted primary and secondary payloads (instruments) for operational space weather monitoring on board as many platforms as possible.

In the framework of the ESA General Support Technology Programme (GSTP) MTA EK has initiated the RADCUBE In-Orbit Demonstration (IOD) mission including the development of a new instrument, called RadMag. The major goal of the RADCUBE mission is to demonstrate the space weather service capabilities of a CubeSat mission to the ESA SSA SWE programme segment. However, the development of the RadMag instrument is very much restricted by the technical constraints of a typical CubeSat mission, thus, in parallel, MTA EK initiated a similar development in collaboration with ESA experts, called D3S-RadMag instrument concept.

The major goal of this concept is to provide a market product combining the radiation and magnetic field measurement capabilities into one payload to be directly applicable within the D3S hosted payload concept of ESA. The conceptual approach shall take into account modularity as design driver in order to make possible to accommodate it on different platforms as a hosted payload. Modularity means that a general, core electrical system (data acquisition and control, power supply and communication) will be designed which can handle the sensor systems attached. The following can be added to the instrument core system in accordance with the given hosting mission/platform possibilities: different radiation measurement telescopes with signal processing, radiation hardness assurance (RHA) related monitoring capabilities (e.g. RHA boards, Total Ionizing Dose (TID) monitoring boards), magnetometer sensor(s) with signal processing (internal and external 3-axis magnetometer sensors). This concept provides a highly variable instrument, which can be fitted to the given hosted mission regarding the sensor system selection (sensor selection will be based on the expected space weather environment and mission constraints, like available volume, mass, power, etc.). As a significant optional component the instrument concept shall feature the capability of providing radiation hardness assurance and monitoring dosimetric quantities, like TID, which can be offer a commercial service for the platform system providers. This will make the instrument favourable for the possible platform providers and means higher chance to have it on board as a hosted payload as many times as needed. At the moment, there is no such complex instrument available on the market or under development as hosted payload candidate which can fulfil all of the above given needs, has the capability of variable sensor system for the given hosted mission and combines the space radiation and magnetic field monitoring capabilities.

## Results

The RadMag CubeSat instrument development reached its final design phase by closing the design of the Engineering Qualification Model (EQM). Prior to the design closure an Engineering Model (EM) was designed and manufactured for performance testing in order to verify the design concept. The instrument EM was tested in-house, at MTA EK, by using radiation sources. In addition, a test campaign was carried out at the Paul Scherrer Institute (PSI) in Switzerland with monoenergetic electron and proton beams. The test results verified that the instrument performance is in-line with the previously performed detailed radiation transport analysis.

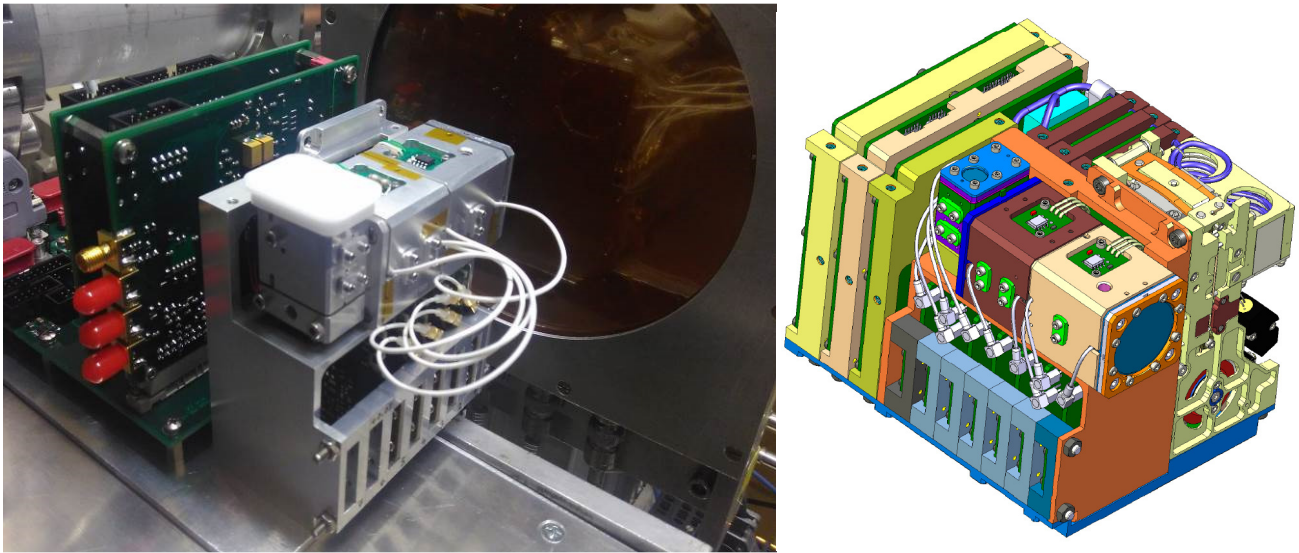


Figure 1: RadMag EM model proton beam tests at PSI (left); RadMag EQM model final design (right)

In the frame of the D3S-RadMag instrument development, the detailed instrument requirements list was elaborated following ESA’s standards and the general requirements of the D3S mission concept. The requirement list will be used during the detailed instrument design. In parallel the radiation telescope concept was iterated based on detailed radiation transport simulation activities (see Fig. 2) with the involvement of ESA experts in order to define the optimal measurement technique from performance, technological and cost point of view.

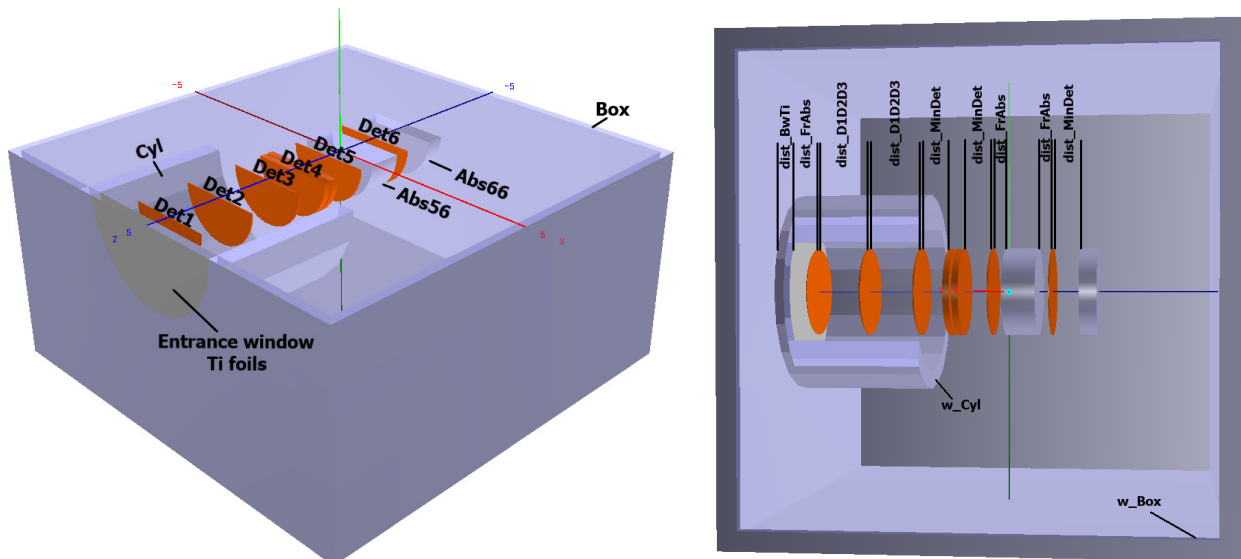


Figure 2: Concept of the D3S-RadMag radiation telescope geometry including entrance window, silicon detectors and absorber layers (cut-views)

**Remaining work**

In case of the RadMag instrument development the EQM model will be manufactured in 2019 followed by an intensive qualification test campaign in the frame of the RADCUBE mission. It will be pursued by the Flight Model (FM) manufacturing and acceptance testing. The launch of the satellite is expected in 2020 with a minimum of 6 months in-orbit operation for the RadMag instrument.

In case of the D3S-RadMag instrument development the design of the EM model shall be finalized by finishing the radiation transport simulations. The EM model shall be manufactured and tested in relevant facilities. In parallel, the first IOD flight opportunity for the D3S-RadMag instrument will be identified together with ESA and the related development roadmap shall be investigated.

**Related publication**

[1] B. Zábory, A. Hirn, J. Eastwood, P. Brown, C. Palla, T. Oddy, D. Nolbert, G. Santin, P. Nieminen, G. Marosy: *Space radiation and magnetic field environment specification for the RADCUBE space weather related CubeSat mission*, 69<sup>th</sup> International Astronautical Congress Paper, ISSN 0074-1795, IAC-18-A1.5.2 (2018)

# PREPARATION FOR EXPERIMENTAL STUDIES OF RADIATION RESPONSE AT THE CELLULAR LEVEL

*Balázs Madas, Emese Drozsdik*

## Objective

In the past years, mathematical models of radiation response have been elaborated with potential implications on the fundamental principles of radiation protection. Experimental validation of our model predictions is highly desirable. Therefore, the objective of the present study was to get acquainted with experimental techniques in basic radiation biology which can later be applied for validation of our theoretical results.

## Methods

We strengthened our existing national and international collaborations with experimental groups and established new ones. In these collaborations, we build on our skills in dosimetry and mathematical modelling, while we aim to be involved and to gain experience in experimental radiation biology. Specific research goals were to take the next steps in i) the estimation of the relative biological effectiveness (RBE) of cold neutrons for the induction of chromosome aberrations and micronuclei in blood lymphocytes, ii) the preparation of experiments on cell viability as the function of absorbed dose with biosensors, iii) the determination of the distribution of deoxyribonucleic acid (DNA) double strand breaks (DSBs) upon exposure to alpha-particles emitted by radium-223 and its progeny, and iv) the quantification of the radiation response of *in vitro* reconstructed bronchial epithelial tissue upon microbeam exposure with alpha-particles.

## Results

Exposure of lymphocytes to cold neutrons was planned for the mid-November cycle of the reactor. Ratio of absorbed dose from gamma-radiation and cold neutrons was measured in the previous cycle by thermoluminescent dosimeters. The total absorbed dose was surprisingly high with much higher dose contribution from  $\gamma$ -photons than expected, contradicting to theoretical calculations.

A first draft of experimental design has been prepared for cell viability measurements with biosensors involving the nanobiosensorics and space dosimetry group of our Research Centre. Survival curves will be determined by a methodology completely new in the field. The experimental setup can be applied to test our model predictions on low dose hyper-radiosensitivity and on induced radio-resistance relating the phenomena to mutation induction [1].

Hit and dose distributions in cancer cells exposed to alpha-particles emitted by radium-223 and its progeny have been determined by Monte-Carlo methods [2]. Results revealed that earlier measurements on cell size were inappropriate. New experiments were planned based on our computations. Simulations were used to estimate the contribution of alpha-particles to DNA damage in a mixed field exposure scenario [3].

Earlier, increased proliferation rate has been observed in *in vitro* reconstructed epithelium after high dose exposure with alpha-particles emitted by americium-241. The experiment was repeated this year with smaller doses precisely targeted with an alpha-particle microbeam. The motivation of these studies was to test our predictions on the induction of progenitor cell hyperplasia in the bronchial epithelium upon chronic exposure to radon progeny [4,5].

## Remaining work

Monte-Carlo simulations have to be performed for more precise estimation of absorbed dose in blood exposed to cold neutrons. In order to perform viability experiments with biosensors, funding should be secured. The manuscript on the cellular responses upon exposure to alpha-particles emitted by radium-223 and its progeny has to be prepared. Evaluation of tissue response upon microbeam exposure is on-going. A manuscript on the results is also expected to be submitted next year.

## Related publications

- [1] B.G. Madas, E.J. Drozsdik: *Computational modelling of low dose hyper-radiosensitivity and induced radioresistance applying the principle of minimum mutation load*, Radiat Prot Dosimetry. 2018; doi: 10.1093/rpd/ncy227
- [2] B.G. Madas: *Report on Monte-Carlo simulations of in vitro experiments with H460 cancer cell lines and Xofigo®*, Budapest, Hungary: MTA Centre for Energy Research; 2018 p. 21. Report No.: KFL-2018-319-01-01-F.
- [3] K. Bannik, S. Zitzmann-Kolbe, S. Jarke, M. Jarzombek, A. Sutter, G. Siemester et al.: *Radiobiological effects of a-particle radiation from Ra-223 in cancer cells*, 64th Annual Meeting of the Radiation Research Society; 2018; Chicago, IL.
- [4] E.J. Drozsdik, B.G. Madas BG: *Quantitative analysis of the potential role of basal cell hyperplasia in the relationship between clonal expansion and radon concentration*, Radiat Prot Dosimetry [revised manuscript submitted]. Available from: <https://arxiv.org/abs/1803.02630>
- [5] B.G. Madas, E.J. Drozsdik: *Effects of mucus thickness and goblet cell hyperplasia on microdosimetric quantities characterizing the bronchial epithelium upon radon exposure*, Int J Radiat Biol. 28; 94(11): 967-74 (2018)

# RESEARCH ON THE BIOPHYSICAL EFFECTS OF LOW DOSES OF IONISING RADIATION

Árpád Farkas, Balázs G. Madas, Péter Fűri, Emese Drozsdik, Ágnes Jókay, Tamás Pázmándi, Imre Balásházy

## Objective

The research objectives for the year 2018 were:

1. use of the Stochastic Lung Model for the quantification of cellular activity- and dose-distributions due to deposition and clearance of radon progenies in the airways at radiation exposure conditions characteristic of homes,
2. numerical modelling of low dose hypersensitivity using an analysis of the possibility to explain the phenomenon by the principle of the minimisation of mutations,
3. combination of the Lawrence Livermore National Laboratory (LLNL) voxel phantom and the Stochastic Lung Model (SLM) for the calibration of the whole body counter measurements.

## Methods

1. A numerical model for the quantification of deposition and clearance of the inhaled radon daughter products in airways has been developed and used. Applying the model absorbed doses in the nuclei of radiosensitive epithelial cells due to alpha-decay of the inhaled short-lived radon progenies were calculated.
2. A mathematical model has been developed in which the cells are supposed to die or survive depending on which of the two events results in a lower mutation number within the cell population.
3. The lung surfaces were reconstructed based on medical images provided by the Karlsruhe Institute of Technology. The Stochastic Lung Model was further developed to fill the airspace delimited by these surfaces with the branching airways of the human tracheobronchial tree.

## Results

1. Based on the simulation results, the radiation burden of the inhaled radon decay products is spatially inhomogeneous within the bronchial airways. This suggests that the characterization of radiation burden at the regional level (e.g. upper airways, bronchial airways, acinar airways) is not sufficient for the assessment of radiation risks. It was demonstrated that quantification of the exact radiation burden due to the inhaled  $^{214}\text{Po}$  is not possible without airway generation level modelling of mucociliary clearance.
2. The simulation results confirmed the theory that minimisation of mutations at any dose results in local minima of the survival curve. If a certain dose causes more mutations, then the minima are lower, which explains why hypersensitivity was observed predominantly in the case of cancerous cells.
3. The LLNL-SLM model described in the *Methods* section has been successfully constructed and tested. The spatial distribution of the inhaled radionuclides deposited in the model airways was simulated. The distribution of the activity due to the deposited isotopes was also computed.

## Remaining work

The results of the activity distribution in the voxel phantom will serve as inputs for the model, which estimates the amount of gamma radiation at the location of the detector of the whole body counter.

## Related publications

- [1] B. G. Madas and E. J. Drozsdik: *Effects of mucus thickness and goblet cell hyperplasia on microdosimetric quantities characterizing the bronchial epithelium upon radon exposure*, International Journal of Radiation Biology **94**, 967-974 (2018)
- [2] P. Fűri, Á. Farkas, B. G. Madas, W. Hofmann, R. Winkler Heil, G. Kudela, I. Balásházy: *The degree of inhomogeneity of the absorbed cell nucleus doses in the bronchial region of the human respiratory tract*, Radiation and Environmental Biophysics (under review)
- [3] E. Drozsdik and B. G. Madas: *Quantitative analysis of the potential role of basal cell hyperplasia in the relationship between promotion and radon concentration*, Radiation Protection Dosimetry doi:10.1093/rpd/ncy302 (2019)
- [4] B. G. Madas and E. J. Drozsdik: *Computational modelling of low dose hyper-radiosensitivity applying the principle of minimizing mutation rate*, Radiation Protection Dosimetry doi:10.1093/rpd/nc0000 (2019)

# RAPID SEPARATION OF ACTINIDES FROM HUMAN URINE, SOIL AND SEDIMENT MATRICES BY EXTRACTION CHROMATOGRAPHY

*Márton Zagyoai, Nóra Vajda (Radanal Ltd.), László Szentmihályi*

## Methods

Diglycolamide (DGA)<sup>®</sup> is a commercially available resin that contains N,N,N',N'-tetra-n-octyldiglycolamine on an inert support. Am, U, Pu and Th are separated by extraction chromatography using DGA resin. A previously applied method [1] was simplified by omitting the digestion and preconcentration steps before the step of separation on DGA resin. 100 mL of water and 100 mL urine samples acidified with 50 mL of HCl to 4M were loaded on to a 0.5 g DGA column. Alpha-sources of various actinides were prepared by co-precipitation with NdF<sub>3</sub> from solutions following separation. Activity measurements were performed with a Si  $\alpha$ -detector. We started developing this method for samples taken from a nuclear reactor coolant as well as for those from the environment, e.g. for soil and sediment samples. We used NaOH fusion on soil and sediment samples to get rid of silicate that badly affected the separation process.

## Results

This year we investigated further the effect of urea (Table 1.) [2] as a relevant constituent of human urine. We made model experiments with distilled water assuming that urea has an effect on the retention of americium and thorium, but the subsequent results did not verify this theory. We studied the effect of the skipping the step of urine destruction with NaOH on the retention of the four actinides. We found that the lack of destruction has a notable effect on the retention of thorium and uranium (Pi50 experiment.).

*Table 1: Recoveries of actinides in the presence of urea, in water and in a urine sample*

No. of experiment	Recovery (%)				Comment
	Th-230	U-233	Pu-239	Am-241	
Pi43	42	89	83	95	10 g urea in 150 ml solution
Pi44	46	105	92	105	10 g urea in 150 ml solution
Pi45	82	-	-	-	10 g urea in 150 ml solution
Pi46	33	81	59	65	150 ml solution without urea
Pi50/1	29	18	84	69	100 ml urine + 50 ml HCl without urine destruction
Pi50/2	20	2	6	6	deconstructed effluent of Pi50/1
Pi50/1+Pi50/2	49	20	90	75	

We compared the method we developed with a previous method [3] which included destruction and separation on TRU resin. We used urine samples from contaminated persons (Table 2).

*Table 2: Comparison of two methods*

with destruction, and separation on TRU resin					without destruction, separation on DGA resin			
Sample code	Recovery (%)	Am-241 activity concentration (mBq/L)	Uncertainty (%)	LD	Recovery (%)	Am-241 activity concentration (mBq/L)	Uncertainty (%)	LD
C	91	LD	-	1,8	64	LD	-	0,44
D	81	3,22	23	1,3	86	5,63	28	0,38
K	83	6,14	15	1,6	73	19,53	23	0,64

The lower recoveries of the DGA procedure are caused by the omission of the destruction step. We think other reasons are responsible for the other differences in the results. We will implement further experiments.

We have started applying the method to soil and sediment samples with NaOH fusion.

Table 3: Results of fused soil and sediment samples

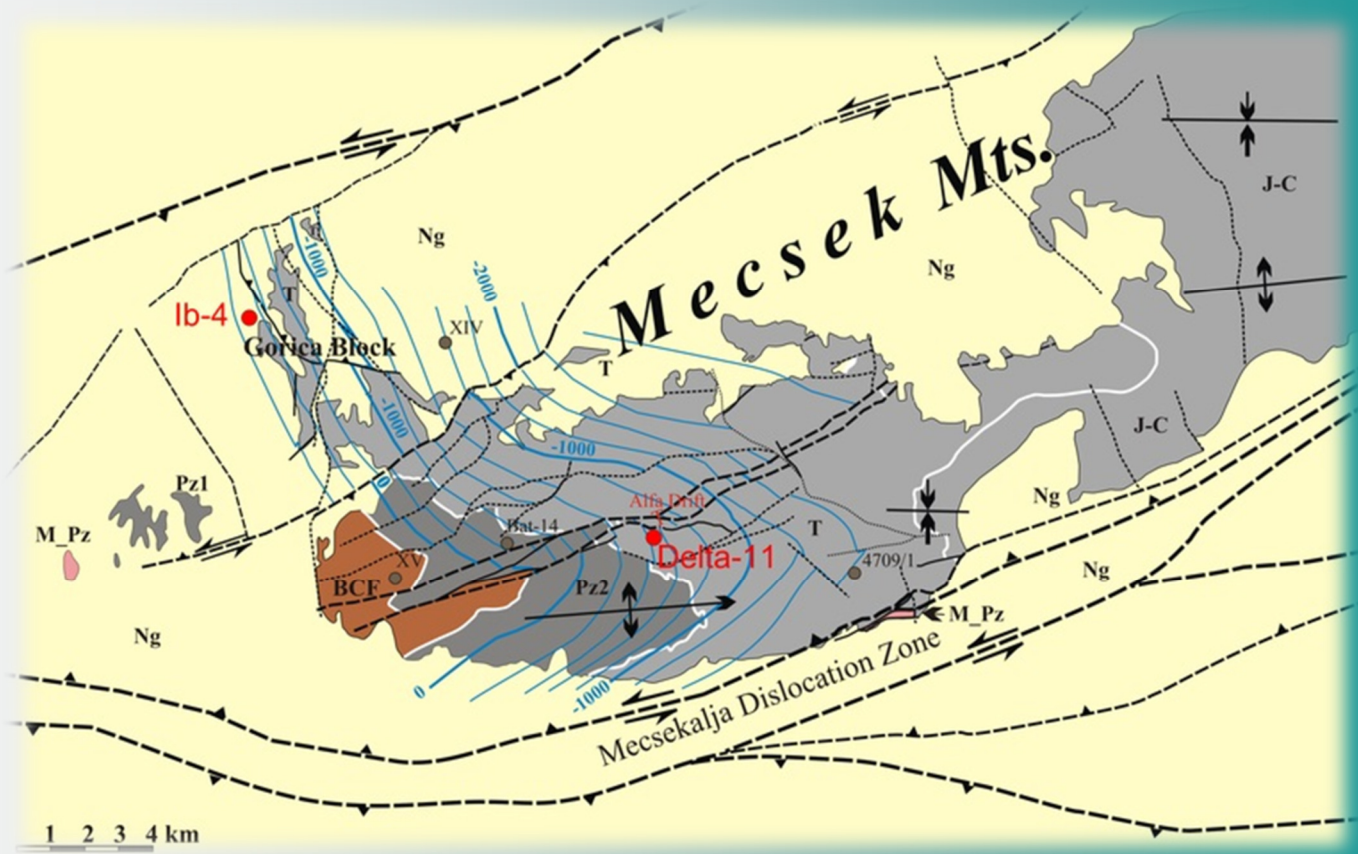
Sample code	326a			326b			375		
	Activity (Bq)	Bq/kg	Recovery (%)	Activity (Bq)	Bq/kg	Recovery (%)	Activity (Bq)	Bq/kg	Recovery (%)
Am-241	0,0080	1,59	84	0,0055	1,10	69	0,001	0,17	90
Pu-238	0,0033	0,65	66	0,0045	0,89	45	LD	-	35
Pu-239,240	0,0040	0,80	66	0,0042	0,84	45	0,004	0,7	35
U-234	0,0372	7,44	94	0,0672	13,44	66	0,100	20,02	45
U-238	0,0398	7,95	94	0,0632	12,65	66	0,104	20,86	45
Th 230	0,0241	4,81	100	0,0554	11,09	64	0,07	13,74	72
Th 232	0,0270	5,39	100	0,0558	11,17	64	0,07	13,74	72

### Remaining work

1. We will continue to develop rapid digestion methods (fusion, microwave digestion) for different matrices of soil and sediment samples.
2. Separation of actinides will be further examined for soil and sediment samples by extraction chromatography based on DGA resin. The high selectivity of DGA will probably make the preconcentration step unnecessary.
3. Feasibility of different  $\alpha$ -source preparation procedures (electroplating, micro co-precipitation) will be examined for processing suitable actinides into multiple or single-element sources.
4. Different spectrum processing software programs (Hypermet, Genie2000) will be used for the evaluation of the measured spectra.

### Related publications

- [1] J. Groska, N. Vajda, Zs. Molnár, E. Bokori, P. Szeredy, M. Zagyvai: *Determination of actinides in radioactive waste after separation on a single DGA resin column*, J. Radioanal Nucl Chem **309**, 1145–1158 (2016)
- [2] M. Zagyvai, N. Vajda, J. Groska, Zs. Molnár, E. Bokori, P. Szeredy: *Assay of actinides in human urine by rapid method*, J. Radioanal Nucl Chem **314**, 49–58 (2017)
- [3] N. Vajda, A. Törvényi, G. Kis-Benedek, C. K. Kim, B. Bene, Zs. Mácsik: *Rapid method for the determination of actinides in soil and sediment samples by alpha spectrometry*, Radiochim. Acta **97**, 1–7 (2019)



## IV. ENERGY AND ENVIRONMENTAL STUDIES



# TESTING OF $\text{MoS}_{2-x}\text{O}_x$ 2D SURFACES IN ELECTROCATALYTIC WATER SPLITTING

József S. Pap, Dávid Lukács, Tamás Ollár, Levente Tapasztó, Antal Koós, Dávid F. Srankó, Zsolt G. Kerner

## Objective

Our main scientific goal was to investigate the structure-reactivity correlations in electrocatalysts designed for the splitting of water.  $\text{MoS}_2$  is a promising electrode modifying material to improve the effectiveness of the hydrogen evolving reaction. The oxidation of 2D  $\text{MoS}_2$  crystals was shown to spontaneously occur upon ambient exposure at under-coordinated sites, such as edges and grain boundaries. By contrast, the oxidation of the defect-free basal plane has been predicted to be kinetically limited, conferring environmental stability to  $\text{MoS}_2$  crystal surfaces. However, the basal plane affinity towards ambient oxidation has so far remained experimentally unexplored. Beside the in-house financing, the full project had support from the VEKOP 2.3.2-16-2016-00011 "Strategic research group for the challenges of renewable energy based power systems" project from July 2017.

## Methods

We have prepared mechanically exfoliated  $\text{MoS}_2$  single layers on atomically flat Au (111) substrates by a recently developed exfoliation technique. The exfoliated  $\text{MoS}_2$  samples have been stored under ambient conditions (air, room temperature and ambient light) for periods of up to 1.5 years. Electrochemical measurements have been conducted on selected sample areas (0.4 – 0.8 mm diameter) of a single 2D  $\text{MoS}_2$  flake supported by a 100 nm thick Au(111) film on a glass substrate. Control measurements on the same Au (111) substrate as well as on a Pt plate and a non-oxidised  $\text{MoS}_2$  surface have been conducted in the same experimental configuration. To compare the performance of different samples in the Hydrogen evolving half-cell reaction (HER), linear sweep voltammetry was performed in a three-electrode configuration using 0.5 M sulphuric acid electrolyte at room temperature. Silver/silver chloride and Pt wire were used as counter and reference electrodes, respectively. Potential sweeps were acquired at a scan rate of 2 mV/s using a Bio-Logic SP-150 potentiostat (Fig. 1a, converted to Tafel plots in Fig. 1b).

## Results

We found that a simple annealing of the  $\text{MoS}_{2-x}\text{O}_x$  crystals under an  $\text{H}_2\text{S}$  atmosphere at 200°C for 30 minutes is able to fully restore the atomic structure of the pure 2D  $\text{MoS}_2$  phase. The electrochemical measurement demonstrated a highly increased catalytic HER activity of the 2D  $\text{MoS}_{2-x}\text{O}_x$  solid solution crystals, as compared to the reduced pure 2D  $\text{MoS}_2$  phase, which manifested in a lower onset potential (Fig. 1a, red curve) and a reduced Tafel slope (67 mVdec<sup>-1</sup>, Fig. 1b). This oxidation process enables the chemical modification of single atomic sites of 2D crystals, opening new routes towards their efficient defect engineering. An important example is that the O substitution sites present all over the basal plane substantially increase the catalytic activity of the 2D  $\text{MoS}_2$  crystals for electrochemical  $\text{H}_2$  evolution reaction. In line with the above results, in hydrodesulfurization catalysis we also showed that the exchange of mobile sulphur atoms plays a crucial role in creating the catalytically active sites (or at least one type of the active sites) on  $\text{MoS}_2$  surfaces.

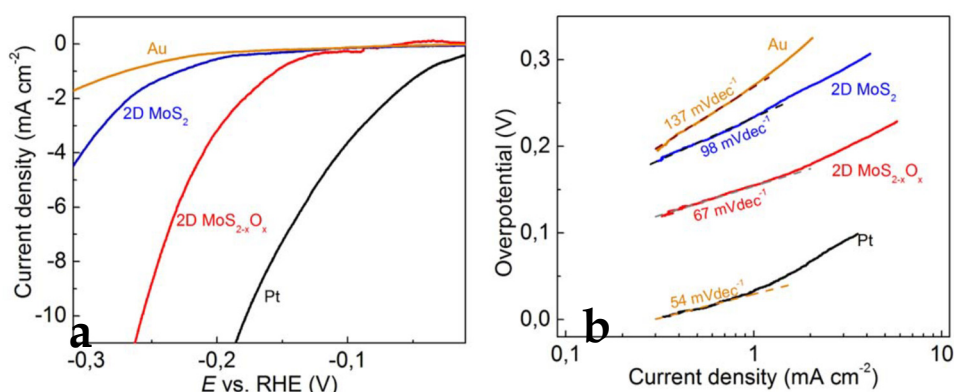


Figure 1: Catalytic activity of 2D  $\text{MoS}_{2-x}\text{O}_x$  for hydrogen evolution. Linear sweep voltammetry curves (a) and the corresponding Tafel plots (b) for: Au substrate,  $\text{MoS}_2$  single layer,  $\text{MoS}_{2-x}\text{O}_x$  single layer (1 year old), and Pt substrate, revealing a significantly higher catalytic activity of the 2D oxy-sulfide phase as compared to the pure  $\text{MoS}_2$  phase, attributed to the novel catalytically active O substitution sites emerging on the basal plane during the oxidation process (RHE = Reversible Hydrogen Electrode).

## Related publications

- [1] J. Pető, T. Ollár, P. Vancsó, Z. I. Popov, G. Z. Magda, G. Dobrik, C. Hwang, P. B. Sorokin, L. Tapasztó: Spontaneous doping of 2D  $\text{MoS}_2$  basal plane by oxygen substitution during ambient exposure, *Nature Chemistry* **10**, 1246–1251 (2018) <https://doi.org/10.1038/s41557-018-0136-2>.
- [2] Z. Varga, T. Szarvas, P. Tétényi, J. Hancsók, T. Ollár: The particular characteristics of the active sites of  $\text{MoS}_2$ ,  $\text{WS}_2$  catalysts in thiophene hydrodesulfurization, *React. Kinet. Mech. Cat.* **124**, 61–74 (2018)

# UNDERSTANDING OF THE DRY REFORMING REACTION FOR THE DEVELOPMENT OF NOVEL CATALYSTS

*Ferenc Somodi, Miklós Németh, Anita Horváth*

## Objective

The catalytic dry reforming reaction is of great importance because it yields hydrogen and carbon monoxide as reaction products in an equimolar ratio (dry reforming, (DRM):  $\text{CH}_4 + \text{CO}_2 \rightleftharpoons 2\text{CO} + 2\text{H}_2$ ) from sources such as, for example, a cleaned biogas. The catalytic properties of our novel samples designed for this reaction were explored further this year. There were two Ni-containing catalyst systems to study: i) the active metal was modified with indium (NiIn/SiO<sub>2</sub>) or platinum (NiPt/ZrO<sub>2</sub>) and ii) the ZrO<sub>2</sub> support was modified with Na<sub>2</sub>O.

## Methods

Beside the existing catalysts, which were prepared by an impregnation method, sol adsorption or deposition precipitation techniques, a bulk Na<sub>2</sub>ZrO<sub>3</sub> support was newly prepared from NaHCO<sub>3</sub> solution and ZrO<sub>2</sub> powder followed by high temperature treatments. Structural investigations were carried out by X-ray powder diffraction (XRD), X-ray Photoelectron Spectroscopy (XPS) and Transmission Electron Microscopy (TEM). Diffuse Reflectance Infrared Fourier Transform Spectroscopy (DRIFTS) was applied to detect the surface-adsorbed species in the presence of CO, CO<sub>2</sub> or a dry reforming mixture under different temperature conditions. Temperature-programmed dry reforming experiments were done in a plug flow reactor in excess methane. Subsequent temperature programmed oxidation (TPO) was carried out to quantify the deposited carbon. Decomposition of methane was investigated by mass spectrometry assisted pulse chemisorption experiments at 600 °C on freshly reduced and on carburized Ni/SiO<sub>2</sub> and Ni-In/SiO<sub>2</sub> dry reforming catalysts.

## Results

Concerning the Ni or NiPt/ZrO<sub>2</sub>(Na<sub>2</sub>O) systems, our detailed DRIFTS experiments in CO or CO<sub>2</sub> flow showed that CO adsorption on the H<sub>2</sub>-precovered catalysts (CO+H<sub>2</sub> surface reaction) resulted in the formation of formates around 300 °C. However, their bonding strength (wavenumber), decomposition route (to carbonates) and speed was markedly different on the samples. It can be suggested that when the surface-bonded formate's C-H vibration is as low as 2830-2800 cm<sup>-1</sup>, the sample has long term stable DRM activity or coke free operation due to the localized 0.6 wt% Na<sub>2</sub>O promotion.

Based on our earlier results, nanosize Na<sub>2</sub>ZrO<sub>3</sub> islands around Ni (or rather the dynamic Na<sub>2</sub>O-ZrO<sub>2</sub>-Ni/NiO<sub>x</sub>H<sub>y</sub> interface) have a decisive role in the effective coke removal from Ni. This is why 3%Ni/Na<sub>2</sub>ZrO<sub>3</sub> catalysts were prepared. The XRD, catalytic and DRIFTS results showed that the presence of 3-5 %Na<sub>2</sub>CO<sub>3</sub> residue (from the support preparation) completely deactivates the catalyst and blocks the Ni surface of big, 100 nm Ni particles. The removal of Na<sub>2</sub>CO<sub>3</sub> residue was successfully achieved by washing of the support. However, during the Ni introduction step, it could be re-formed again – although in a minute amount – on the surface, while the required bulk Na<sub>2</sub>ZrO<sub>3</sub> phase disappeared, and the catalyst had moderate dry reforming activity without coke formation. DRIFTS experiments on this washed sample firmly ascertained that the sodium content causes the 1800 cm<sup>-1</sup> band of bridged CO on Ni and the low wavelength formate C-H band (weak C-H bond) which can be decomposed easily.

Concerning our novel, coke tolerant, indium promoted system, DRIFTS experiments gave the following results. During CO chemisorption at room temperature, linear monocarbonyls, unstable tetracarbonyls and bridged carbonyls bound to nickel were detected on Ni/SiO<sub>2</sub> while only linear monocarbonyls were seen on NiIn/SiO<sub>2</sub>. The bimetallic character of the surface was reflected in the lower wavelength of the linearly adsorbed CO molecules (at around 2025 cm<sup>-1</sup>) which were present on the hydrogen-precovered surface at 300 °C with a surprisingly high concentration. Using a DRM mixture, the NiIn surface kept CO molecules up to 500 °C, while there was no metal-bonded CO on Ni/SiO<sub>2</sub> above 400 °C, probably due to the formation of nickel carbide. CO chemisorption after the reaction revealed clean but somewhat segregated NiIn sites on the bimetallic sample, in similar concentration as before the reaction, while on Ni/SiO<sub>2</sub> the available Ni surface significantly decreased. The presence of NiIn sites was ascertained on the NiIn/ZrO<sub>2</sub> sample as well. The catalytic activity of this sample was lower, but coke was not formed during the reaction.

Next, a methane activation step was investigated on our In-promoted catalysts. The mass spectrometry assisted, methane pulse experiments at 600 °C on freshly reduced and on carburized Ni/SiO<sub>2</sub> and Ni-In/SiO<sub>2</sub> dry reforming catalysts revealed that complete methane decomposition with stoichiometric hydrogen production on freshly reduced Ni/SiO<sub>2</sub> took place, while strong hydrogen chemisorption and partial methane decomposition was observed on Ni-In/SiO<sub>2</sub>. Hydrogen production decreased on both carburized catalysts and dissociative methane chemisorption without hydrogen formation was observed on the bimetallic catalyst. This difference in methane activation might be one of the reasons for the absence of coke on the bimetallic catalyst during dry reforming of methane.

## Remaining work

The related EK 161 project will be finished. The topic will be continued with an outlook to the related CO<sub>2</sub> utilization routes. Publications in preparation will be submitted soon.

**Related publications**

- [1] F. Somodi, G. Sáfrán, M. Németh and A. Horváth: *Hindered methane decomposition on a novel Ni-In/SiO<sub>2</sub> dry reforming catalyst*, 14<sup>th</sup> Pannonian International Symposium on Catalysis, oral presentation, Stary Smokovec, Slovak Republic, 3-7 September, (2018)
- [2] M. Németh, G. Sáfrán, A. Horváth, F. Somodi: *Hindered methane decomposition on a coke-resistant Ni-In/SiO<sub>2</sub> dry reforming catalyst*, *Catalysis Communications* **118**, 56-59 (2019) doi:10.1016/j.catcom.2018.10.003
- [3] J. Károlyi, M. Németh, C. Evangelisti, G. Sáfrán, Z. Schay, A. Horváth, F. Somodi: *Carbon dioxide reforming of methane over Ni-In/SiO<sub>2</sub> catalyst without coke formation*, doi:10.1016/j.jiec.2017.09.024, *Journal of Industrial and Engineering Chemistry*, **58**, 189-201 (2018)

# EFFECT OF PREPARATION AND SUPPORT OF AU-BASED CATALYSTS ON SELECTIVE OXIDATION OF ALCOHOLS

*Gergely Nagy, Dávid Srankó, György Sáfrán, Sándor Stichleutner, László Borkó, Antal Tungler, Zoltán Schay, Ferenc Somodi, Károly Lázár, Andrea Beck*

## Objective

As a continuation of the investigations and development of supported Au-containing catalysts for aerobic selective oxidation reactions, the effect of the preparation method and the support was studied in the case of monometallic Au and bimetallic Au-Cu and Au-Ag systems in aerobic benzyl alcohol or glycerol oxidation. The work was done in collaboration with the Italian Istituto di Scienze e Tecnologie Molecolari (CNR-ISTM) and Frascati National Laboratories (INFN), and the Chinese State Key Laboratory of Catalysis, Dalian Institute of Chemical Physics.

## Methods

Catalysts were prepared using various supports by the sol immobilisation method (SOL) and compared with ones produced by solvated metal atom deposition (SMAD). Catalytic tests were performed in benzyl alcohol (BnOH) oxidation in toluene, cyclohexane or xylene solutions without or with base ( $K_2CO_3$ ) addition, and glycerol (Gly) oxidation in aqueous solution with base addition (NaOH). For structural characterisation (HR)TEM, XPS, XAFS techniques and CO adsorption (followed by DRIFT spectroscopy and measured by QMS),  $CO_2$ -TPD and  $NH_3$ -TPD measurements were used.

## Results

In glycerol oxidation, increased activity and different selectivity (favoured transformation of glyceric acid to tartronic acid) of SOL prepared AuAg/ $Al_2O_3$  (Au/Ag=4/1 atomic ratio) and Au/ $Al_2O_3$  as compared to the ones made by SMAD was established. This was related to both the larger particle size and also to the higher surface enrichment of Ag on AuAg nanoparticles (NPs) on the SMAD samples, which further increased after calcination treatment. Additionally, Ag was more resistant to oxidation in the SOL sample, indicating its modified electronic state resulting from the more extensive interaction with Au. The Au and AuAg NPs were more stable against sintering in the SOL than in the SMAD derived catalysts. The stabilizing agent residues of the SOL catalysts slightly hampered the activity, and affected the selectivity. After its removal by calcination the tartronic acid selectivity further increased, accompanied by a reduction of glyceric acid and C-C cleavage products. The bimetallic SOL sample was more active than the monometallic Au/ $Al_2O_3$  (due to the promoting effect of Ag) with higher tartronic acid, but also C-C cleavage product selectivity. [1, 4, 7]

The large effects of the type and structure of the carbon support (Vulcan-XC72R, Norit GSX, X40S) were observed in glycerol oxidation for Au/carbon catalysts prepared by both SOL and SMAD methods, providing similar mean Au NP size (2.5-3.9 nm) (except Au/X40S\_SMAD of 7.1 nm mean diameter). In the case of the different supports which vary in surface area, pore size, functionalization and graphitization degree, the activity order of Au/Vulcan>Au/Norit>Au/X40S was found in both sets. All the SOL samples were more active, than the corresponding SMAD ones. [2]

Alumina and carbon (Vulcan) supported Au-Cu bimetallic systems produced by the SOL method with Au/Cu=1/4, 1/1, and 4/1 atomic ratio were compared in benzyl-alcohol oxidation, without any pre-treatment in a cyclohexane solution, at 120°C and with (Au+Cu)/BnOH=1/500 molar ratio without base addition. In contrast to earlier results on the similarly prepared AuCu/ $Al_2O_3$ , Au/Cu=1/1 with differing conditions: toluene solvent, 80°C, Au/BnOH=1/2000, there was no poisoning/deactivation detected, but the synergetic effect revealed earlier for Au/Cu=1/1 was confirmed, and found also for Au/Cu=4/1 both on alumina and Vulcan supports, and in the case of AuCu/ $Al_2O_3$  for Au/Cu=1/4 as well. (The corresponding monometallic Cu-catalysts had negligible or no activity.) Approaching the 100% conversion, the only detected product benzaldehyde started to transform further to benzoic acid. The same AuCu, Au and Cu NPs originated from the same sols, respectively, were all more active on alumina than on Vulcan support. [3, 5]

Au catalysts supported on non-reducible oxide ( $SiO_2$ ,  $Al_2O_3$ , MgO,  $MgAl_2O_4$ ) and non-oxide (hydroxyapatite, HAP) supports with different basicity and acidity were studied in benzyl alcohol oxidation (xylene solvent, 50°C, Au/BnOH =1/1300). According to the  $CO_2$ -TPD and  $NH_3$ -TPD measurements  $MgAl_2O_4$  and HAP contained both basic and acidic sites of different strength,  $Al_2O_3$  stronger acid and weaker basic, MgO only basic, while  $SiO_2$  had neither basic nor acid sites. The average size of the SOL derived Au particles were between 2.4 and 2.7 nm on the calcined samples (where no protecting agent was left around Au NPs), except for Au/ $Al_2O_3$  (1.7 nm) and Au/MgO (6.5 nm). In base free reactions (where the catalysts quickly deactivated) the order of the activity was Au/ $MgAl_2O_4$ >Au/ $Al_2O_3$ >Au/MgO>Au/HAP>Au/ $SiO_2$ =0. With base addition (where no deactivation was observed) the differences between the larger activities were smaller, but their order remained similar. The stronger basicity seemed to favour the reaction, while the acidity affected the selectivity by enhancing slightly the benzyl benzoate selectivity (16-22% vs 10-12% at about 70% conversion). [6]

## Remaining work

The publication of the unpublished results.

**Related publications**

- [1] A. Jouve, G. Nagy, F. Somodi, C. Tiozzo, A. Villa, A. Balerna, A. Beck, C. Evangelisti and L. Prati: *Gold-silver catalysts: Effect of catalyst structure on the selectivity of glycerol oxidation*, *J. Catal.* **368**, 324–335 (2018)
- [2] A. Jouve, M. Stucchi, I. Barlocco, C. Evangelisti, F. Somodi, A. Villa and L. Prati: *Carbon-Supported Au Nanoparticles: Catalytic Activity Ruled by Carbon Support*, *Topics in Catalysis* **61**, 1928–1938 (2018)
- [3] L. Prati, A. Villa, A. Jouve, A. Beck, C. Evangelisti and A. Savara: *Gold as a modifier of metal nanoparticles: effect on structure and catalysis*, *Faraday Discuss.* **208**, 395–407 (2018)
- [4] L. Prati, A. Jouve, M. Stucchi, S. Cattaneo, A. Villa, C. Evangelisti, A. Beck and R. Zanella: *Gold-silver catalysts: Effect of catalyst structure on the selectivity of glycerol oxidation* (oral presentation), Gold 2018 Conference, Paris, France, 15-18 July 15-18, 2018, Abstract Book
- [5] S. Stichleutner, A. Beck, G. Nagy, D. F. Srankó, Gy. Sáfrán, F. Schmidt, K. Lázár: *<sup>197</sup>Au Mössbauer study of nanosized Au-Cu/Al<sub>2</sub>O<sub>3</sub> bimetallic catalysts* (poster presentation), Conference on Mössbauer Spectroscopy in Materials Science, Prague, Czech Republic, 25 – 28 June, 2018, Abstract Book
- [6] G. Nagy, D. Srankó, K. Lázár, G. Sáfrán, A. Beck, S. Liu, T. Li, H. Tang, B. Qiao, R. Ge and J. Wang: *Support effect of Au catalysts in aerobic benzyl-alcohol oxidation: effect of acid-base properties* (poster presentation), 14<sup>th</sup> Pannonian International Symposium on Catalysis, Starý Smokovec, Slovakia, 3 – 7 September, 2018, Abstract Book
- [7] Teodóra Gál: *Study of bimetallic effect in alumina supported Au-Ag catalysts in aerobic selective oxidation of benzyl alcohol*, BSc. degree thesis, Budapest University of Technology and Economics, 2018, supervisor A. Beck

# BIOMASS CONTENT DETERMINATION OF BIOFUELS BY $^{14}\text{C}$ LIQUID SCINTILLATION COUNTER (LSC) METHOD

Tamás Korányi

## Objective

Biomass content determination of biocarbon - fossil carbon containing mixtures (biofuels, cellulose, lignocellulose and lignin derivatives) by radiocarbon ( $^{14}\text{C}$ ) liquid scintillation counting (LSC).

## Methods

Two kinds of LSC methods were/will be applied:

- **Direct counting:** The product mixture is dissolved directly in a scintillation cocktail and its biogenic carbon content was measured in LSC equipment. This method is only applicable using colourless or slightly coloured samples.
- **Sample combustion and carbon dioxide trapping:** Samples will be burned using air in a burning oven and the produced carbon dioxide will be trapped in a sodium hydroxide solution. The precipitate will be dissolved in the scintillation cocktail and measured by LSC. This method is under development, but it is not working yet.

## Results

Our Belgian partners (Prof. Bert Sels et al., Katholieke Universiteit Leuven) produced biogasoline by valorizing (hemi)cellulose pulp into light naphtha using a two-phase ( $\text{H}_2\text{O}$  : organic) catalytic slurry process. They directly integrated this process into existing light naphtha petrorefinery processes. They measured the biomass content of their biogasoline - fossil gasoline mixtures by gas chromatography (GC) (Table 1), but this methodology is unreliable because of neglecting some alkane products. We monitored the carbon origin of some of their samples by our direct LSC method and revealed the missing biocarbon content (Table 1). Due to the novel direct integration approach of bio-enriched gasoline production, we published these results in the prestigious journal Nature Energy [1].

Table 1: Biomass-derived content, based on GC analysis and LSC ( $^{14}\text{C}$  determination), of three selected samples [1]

Substrate	Fossil solvent	Biomass-derived content determined by GC (wt%)	Biomass-derived content determined by LSC (wt%)
Cellulose	Petroleum ether	10.7	12.1
Cellulose	Petrol	15.6	18.0
Carbohydrate pulp	Petrol	6.6	11.8

We started to determine the biocarbon content of catalytically converted biomass (cellulose, lignocellulose and lignin) samples of our Dutch colleagues (Prof. Katalin Barta et al., University of Groningen). Some promising preliminary results were obtained, but due to the low biocarbon content and the disturbing colour of most of their samples, using the sample combustion and carbon dioxide trapping method will give more reliable results for most of the Dutch samples.

Some other LSC related results will also be reported in another project (126\_2018).

## Remaining work

Building of the sample combustion and carbon dioxide trapping experimental setup has been started, but due to a delayed reconstruction work of our laboratory, we could not yet finish this work.

## Related publication

- [1] A. Deneyer, E. Peeters, T. Renders, S. Van den Bosch, N. Van Oeckel, T. Ennaert, T. Szarvas, T.I. Korányi, M. Dusselier and B.F. Sels: *Direct upstream integration of biogasoline production into current light straight run naphtha petrorefinery processes*, Nature Energy **3**, 969-977 (2018)

# SOD-LIKE ACTIVITY AND CYTOTOXICITY ASSESSMENT OF NEW ANTIOXIDANT SYSTEMS

Inna Székács, József S. Pap, Krisztina Kovács, Tünde Tóth, Róbert Horváth

## Objective

Superoxide dismutase (SOD) is an enzyme family that regulates reactive oxygen species (ROS) in living organisms. Malfunction of SODs leads to a harmful level of oxidative stress on the body. For therapeutic purposes, artificial complexes with catalytic antioxidant activity are envisioned as SOD-mimics to fix the regulation of ROS. Our objectives were to measure the SOD-like activity of Cu(II) complexes based on a phosphonate substituted SALAN-type ligand by direct and indirect methods, and rationalize their *in vitro* effect on cells, considering the coordination modes and the redox behaviour.

## Methods

The complexes were characterized by molecular (UV-visible, Circular Dichroism, Electron Paramagnetic Resonance, X-ray Absorption and Extended X-Ray Absorption Fine Structure (EXAFS)) spectroscopy, Electrospray Ionization Mass Spectrometry (ESI-MS), electrochemistry and geometry optimization using Density Functional Theory (DFT) calculations. SOD-like activity has been determined by the McCord-Fridovich method and directly by pulse radiolysis. Cytotoxicity has been studied on living cells with the optical biosensor Epic BT. Determination of the cell viability was done by using HoloMonitor M4.

## Results

All characterizations were done in aqueous solution at physiological pH (7-8). ESI-MS (Electrospray Ionisation Mass Spectrometry) showed an equimolar [Cu(L)] complex upon addition of Cu<sup>2+</sup> to L (L = (R,R)-1,2-cyclohexylenediamino-di-(R,R)-[(2-hydroxyphenyl)-methylphosphonic acid]) up to 1:1 molar ratio. Results from spectroscopy suggest a {2N,2O} coordination sphere, involving both oxygen donors from the phosphonate group. At Cu<sup>2+</sup>:L > 1, up to 1.9:1 ESI-MS shows [Cu<sub>2</sub>(L)]. The standard spectroscopic analysis indicates {1N,3O} binding mode including one phenolate oxygen donor for each Cu<sup>2+</sup> ion. The geometry optimized structure by DFT (Fig. 1) accords with this assignment. The Cu...Cu distance is 4.85 Å, the Cu-N bonds are ~2.00 Å, the Cu-O<sub>phenol</sub> bonds are 1.94 Å, while the Cu-O<sub>phosphonate</sub> bond lengths are 2.03 Å and 1.99 Å, respectively for the two centres. In addition, DFT predicts that the fourth positions are occupied by aqua ligands at 2.05 and 2.02 Å from the cupric centres. The average of the optimized distances (~1.99 Å) is in line with the Cu-N(O) = 1.98 by EXAFS (Extended X-ray Absorption Fine Structure).

The Cu<sup>2+/+</sup> formal potential ( $E^\circ$ ) under the reaction conditions is an important thermodynamic criterion of the SOD-like behaviour. The catalytic disproportionation process involves redox reactions between the reduced as well as the oxidized complex forms and O<sub>2</sub><sup>•-</sup>. The  $E^\circ$  for both complexes is in the appropriate range to expect SOD-like activity.

The  $k_{McCF}$  (M<sup>-1</sup>s<sup>-1</sup>) rate constants derived from the McCord-Fridovich test imply that [Cu<sub>2</sub>(L)] is an outstandingly active O<sub>2</sub><sup>•-</sup> scavenger, but [Cu(L)] also ranks among the better mimics. However, both lag behind the natural CuZn SOD enzyme. The rate constants were in agreement with those determined by pulse radiolysis, where the decay of O<sub>2</sub><sup>•-</sup> was directly monitored at 270 nm under real catalytic conditions.

The effects of the Cu-complexes and Cu<sup>2+</sup> on the functional state of surface-adhered living cells and on the cell adhesion process were explored in a serum-containing cell culture medium using an Epic BT optical biosensor. This device is usable for a label-free screening of the comprehensive effects of xenobiotics on the biological status of cells (e.g., cell viability, cell adhesion processes, cell integrity, signalling) [1]. The 2 h long measurements show no differences between the cells treated with [Cu(L)], [Cu<sub>2</sub>(L)] or Cu<sup>2+</sup> and the control. However, the exposure to [Cu<sub>2</sub>(L)] and Cu<sup>2+</sup> at 400 μM after 24 h of incubation leads to cell apoptosis. Time-based changes of cell proliferation and morphology parameters under the treatment with [Cu(L)], [Cu<sub>2</sub>(L)] and Cu<sup>2+</sup> at 400 μM were monitored for 72 h using a HoloMonitor M4 placed into an incubator. Control cells and cells treated with [Cu(L)] showed a normal morphology and proliferated exponentially. In contrast, [Cu<sub>2</sub>(L)] and Cu<sup>2+</sup> caused a ~4 h delay in cell proliferation. Surprisingly, Cu<sup>2+</sup> stimulates cell proliferation for 8 h, but then the proliferation is terminated. Changes in cell morphology begin after ~14 h of incubation with [Cu<sub>2</sub>(L)] and Cu<sup>2+</sup> and intensify over time, and disrupted cellular functionality leads to apoptosis. In summary, no notable cytotoxicity was registered for Cu-complexes at the reasonable concentration level (10-20 μM), but [Cu<sub>2</sub>(L)] at 400 μM causes cell apoptosis. Treatment with [Cu(L)] did not show visible cytotoxicity even at high concentrations which makes it a potential candidate for antioxidant therapies [2].

## Remaining work

The work was completed and a manuscript is in progress. Studies on other antioxidant complexes are among our plans.

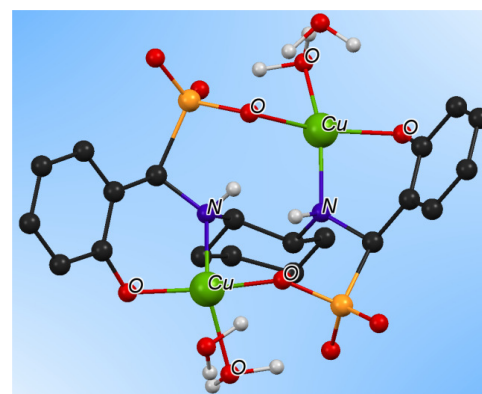


Figure 1: DFT optimized structure for [Cu<sub>2</sub>(L)]

**Related publications**

- [1] E. Farkas, A. Szekacs, B. Kovacs, M. Olah, R. Horvath, I. Szekacs: *Label-free optical biosensor for real-time monitoring the cytotoxicity of xenobiotics: A proof of principle study on glyphosate*, Journal of Hazardous Materials **351**, 80-89 (2018).
- [2] I. Székács, P. Tokarz, R. Horvath, K. Kovács, A. Kubas, M. Shimura, J. Brasun, V. Murzin, W. Caliebe, Z. Szewczuk, A. Paluch, L. Wojnárovits, T. Tóth, J. S. Pap, Ł. Szyrwił: *In vitro SOD-like activity of mono- and di-copper complexes with a phosphonate substituted SALAN-type ligand*, Chemico-Biological Interactions (2019)  
<https://doi.org/10.1016/j.cbi.2019.04.003>

# LONG-TERM PROSPECTS AND DEVELOPMENT OPPORTUNITIES OF THE DOMESTIC ELECTRICITY AND HEAT SUPPLY

*Endre Börcsök, Ágnes Gerse*

## **Objective**

In the context of this research related to the long-term development of the domestic electricity and heat supply, we addressed three main areas in 2018. As first area of interest, we focused on the heat sector by formulating the search for an optimal heat and domestic hot water supply portfolio of Budapest as a multiobjective optimization problem involving economic, environmental and human health aspects. Two additional fields of research were related to the electricity sector: the development of a regional electricity supply model and a country-level wind power production model.

## **Methods**

A multiobjective optimization methodology was applied in the context of the optimal heat supply portfolio of Budapest. The techno-economic assessment was complemented by monetizing the environmental impacts and the influence of the technology choices on human health. Among the technology options, the long-distance heating from Paks Nuclear Power Plant has also been considered and evaluated. The methodology was based on monthly heat demand profiles, distinguishing among three typological groups of buildings and optimizing the set and installed capacity of heating technologies for each of these groups. Two different approaches have been applied to the analysed multiobjective optimization problem involving three objectives. According to the first approach, the three objective functions were encompassed in an overall objective function by monetization and the problem was solved as a linear programming (LP) formulation of a simple transportation problem; while the second approach used a multiobjective optimization method.

For the electricity sector, the regional electricity supply model was implemented in Antares (A New Tool for Adequacy Reports and Economic Simulations), where we gratefully acknowledge the support of RTE, transmission system operator for electricity in France. Reflecting the complexity of the electric power system, a large set of input data was required to run the model, including power plant characteristics, cross-border transmission capacities, demand and generation patterns. By solving the unit commitment and the economic dispatch problem as a constrained least-cost optimization problem for the power system, resulting time series for cross-border exchanges and power plant generation are available at an hourly scale. Providing model-based-time series for simulations, the wind power production model for Hungary uses a reanalysis-based modelling approach. The hourly aggregate wind energy production is modelled by converting gridded hourly wind speed data into aggregate power output via the power curves of the wind turbines where hourly wind speed time series were retrieved from the ERA5 reanalysis archive, released by the European Centre for Medium-Range Weather Forecasts.

## **Results**

The results of heat supply optimization show that single family houses mostly rely in this simulation on ground and air source heat pumps while their winter peak demand is covered by heat from natural gas. The optimal heat supply of medium-scale and large-scale multi-flat buildings is based on district heating to a large extent where municipal solid waste and biomass are the base-load fuels and nuclear cogeneration appears in the intermediate range. For peak supply, heat production from natural gas was selected as an optimum with different configurations: individual heating systems are the most suitable for medium-scale multi-flat buildings while centralized supply via district heating is the best option for large-scale multi-flat buildings.

The regional electricity supply model was run and calibrated for eight countries. Although the main trends in the structure of generation and cross-border electricity exchanges are well reflected, modelling results may substantially differ when compared to actual market data given the limitations in the methodology. In the part of work related to wind energy, the availability of sufficiently long time series with virtually unchanged wind turbine fleet made Hungary an ideal test case for the applicability of ERA5 data for wind power modelling. The performance of the model has been evaluated against multiple criteria where hourly data were closely correlated to data from measurements.

## **Remaining work**

We would like to include further aspects of analysis in addition to the three criteria already included in the heat supply optimization model and assign weight factors to the set of criteria. The regional electricity supply model is planned to be extended to additional countries along with the improvement of data quality, while the further work on the wind power generation model could focus mainly on the model-based assessment of future national wind power development scenarios.

## **Related publications**

- [1] E. Börcsök, A. Gerse, J. Fülöp: *Applying Multiobjective Optimization for the Heat Supply in the Residential Sector in Budapest*, 12th IEEE International Symposium on Applied Computational Intelligence and Informatics, SACI 2018 May 17-19, Timisoara, Romania
- [2] A. Gerse, E. Börcsök: *Modelling the wind production of Hungary using ERA5 data*, 5th International Conference Contemporary Problems of Thermal Engineering CPOTE 2018 September 18-21, Gliwice, Poland

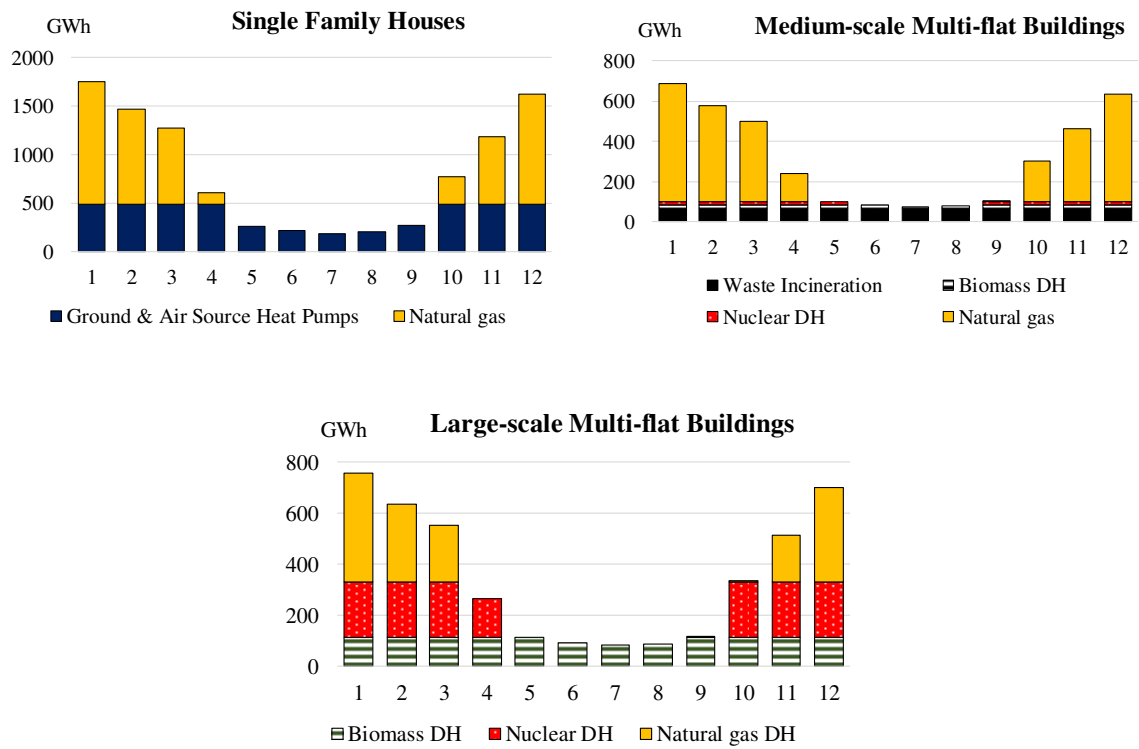


Figure. 1: Optimal heat supply portfolio for the Residential Sector in Budapest modelled by monetized value

# EFFECTS OF HETEROGENEITY IN POWER-GRID NETWORK MODELS

Géza Ódor, Bálint Hartmann

## Objective

Power-grids are becoming more and more heterogeneous as renewable small (solar, wind, geothermic) suppliers are connected. Therefore, the danger of desynchronization may increase. We have studied the effects of topological and intrinsic (node connection strength) disorder on the second order Kuramoto model with respect to simple homogeneous lattices. Our aim was to provide a description of the desynchronization transition, determine the fluctuations and the heavy tailed failure avalanche distributions, reported on several large blackout events. We have planned to explore possible Griffiths phases and to provide a measure of danger as the function of stochastic elements connected.

## Methods

We compared the phase synchronization transition of the second order Kuramoto model, a basic model describing AC electric networks, on 2D lattices and on large synthetic power-grid networks generated from real data. While admittance matrix of the transmission network is based on a real-life example (the Hungarian power system), matrix of the distribution network is the result of synthetic grid modelling. Equations of the second order Kuramoto model for the phases  $\theta_i$  and the global coupling control parameter  $K$  have been analysed numerically, using 4<sup>th</sup> order Runge-Kutta differential solvers. Here we introduced quenched heterogeneities, via the  $\omega_i$  intrinsic frequencies of the  $N$  nodes, connected via the  $A_{ij}$  admittance matrix. For the inertia parameter we used  $\alpha=1,3$  and we also considered the addition of Gaussian as well as exponentially distributed noise terms. We have measured the global phase synchronization order-parameter and determined the static/dynamic phase transition behaviour. We have also determined the distribution of the duration times from fully synchronous ( $R = 1$ ) to disordered ( $R = 1/N^{0.5}$ ) states, by random sample averaging.

## Results

As the continuation and extension of our 2017 project, we investigated the effects of distributed power supply elements. For the traditional electric system, we used binary  $\omega_{i,0}$  frequency distributions, with generators in the high voltage nodes:  $\omega_{i,0} = 10 + p_G$  while in the other consumer nodes:  $\omega_{i,0} = -1 + p_G$ , where  $p_G$  is a unit variance Gaussian random variable. To model a distributed/renewable system we applied for sources:  $\omega_{i,0} = 2,5 + p_G$  and for consumers:  $\omega_{i,0} = -1 + p_G$  randomly. Using adiabatic quench, we determined the steady state synchronization as the function of the global coupling (related to the maximum transmitted power between nodes). As the Figure shows, we obtained higher synchronization in case of the distributed/renewable model than in case of the traditional setup. We submitted this new result and a summary of the talk we presented at MTA in May to Fizikai Szemle, while we published the previous year results as: Géza Ódor, Bálint Hartmann, *Heterogeneity effects in power grid network models*, *Phys. Rev. E* 98 (2018) 022305. We presented the results by a talk on the AMCOS 2018 synchronization conference in Barcelona and the usage of GPU-s (Graphics Processing Units) for speeding up calculations at the GTC2018 conference in San Jose.

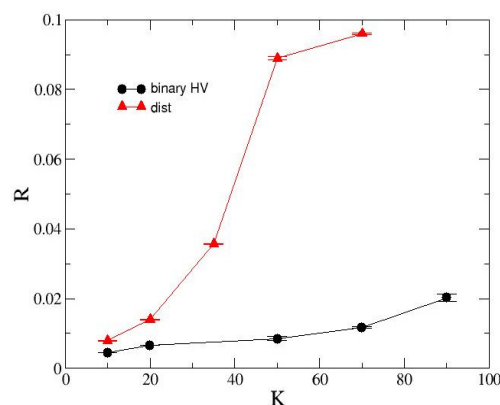


Figure 1: Comparison of the steady-state order parameter for binary classical and distributed energy source models

## Remaining work

We would like to better understand the stability of conditions of power-grids by using more detailed models and to compare our results with ENTSO (European Network of Transmission System Operators for Electricity) power failure data.

## Related publications

- [1] G. Ódor, B. Hartmann: *Heterogeneity effects in power grid network models*, *Phys. Rev. E* 98, 022305 (2018)
- [2] G. Ódor, B. Hartmann: *A heterogenitások hatásai villamos hálózati modelleken*, *Fizikai Szemle* 2019 Febr.

# CONDITIONING AND FINAL DISPOSAL OF HIGH-LEVEL RADIOACTIVE WASTE

*Margit Fábrián, Ottó Czömpöly, Felicián Gergely, János Osán*

## Objective

At the end of the nuclear fuel cycle high level radioactive waste (HLW) is generated that has to be disposed of in a safe way. Vitrification, where actinides from HLW materials are melted into a glassy form, is a feasible and widely accepted conditioning method. A promising borosilicate matrix glass composition was developed in the previous years. Lanthanides, chemically modelling the actinides present in the waste, were added to the matrix in the form of  $\text{CeO}_2$ ,  $\text{Nd}_2\text{O}_3$  and  $\text{Eu}_2\text{O}_3$ . The structural characterization of the loaded glass is important in order to determine the immobilization rates of the HLW. Previous neutron diffraction (ND) measurements, combined with Reverse Monte Carlo (RMC) simulation, revealed that lanthanide atoms can effectively incorporate into the matrix glass structure. In order to complement and support the structural studies, we aimed to investigate the oxidation state and the local environment of the incorporated lanthanide ions.

The final disposal of HLW is generally planned in deep geological repositories. The Boda Claystone Formation (BCF) is considered as the potential host rock of the future HLW repository in Hungary. We intended to study the retention capabilities of the argillaceous host rock as a natural barrier through a series of macroscopic experiments quantifying sorption of key radionuclides at a constant pH, and a solid-to-liquid (S/L) ratio at different equilibrium concentrations.

## Methods

For studies related to vitrification of HLW, two series of Ce-, Nd- or Eu-containing glassy samples were prepared and investigated. The composition of the borosilicate matrix (denoted as Matrix) is  $55\text{SiO}_2 \cdot 10\text{B}_2\text{O}_3 \cdot 25\text{Na}_2\text{O} \cdot 5\text{BaO} \cdot 5\text{ZrO}_2$ . The composition of the glassy specimens of the two series are  $90\text{wt}\%[\text{Matrix}] + 10\text{wt}\%X$ , and  $70\text{wt}\%[\text{Matrix}] + 30\text{wt}\%X$ , where X stands for  $\text{CeO}_2$ ,  $\text{Nd}_2\text{O}_3$  or  $\text{Eu}_2\text{O}_3$ . Glassy samples were prepared by the melt-quenching technique.

The lanthanide-containing amorphous samples as pressed pellets were investigated using X-ray absorption spectrometry (XAS). Measurements were performed at the  $L_2$  and  $L_3$ -edge of Ce and Nd, and at the  $L_3$  edge of Eu. Nuclear Magnetic Resonance (NMR) and Raman spectroscopy were also used to get complementary information on the boron environment.

Sorption on the host rock of the waste repository of radionuclides that may be released from the radioactive waste was modelled by laboratory experiments. A series of macroscopic experiments were performed for  $\text{Cs}^+$ ,  $\text{Ni}^{2+}$  and  $\text{Eu}^{3+}$  ions on five different core samples originating from a recent drilling in BCF. The argillaceous rock samples were ground to less than  $63 \mu\text{m}$  grain size. Sorption isotherms were measured at pH 8.0 via inductively coupled plasma mass spectrometry (ICP-MS) analysis of the liquid phase separated by centrifugation or ultrafiltration.

## Results

Structural characterization of the designed model glasses was completed with NMR, Raman spectrometry and XAS measurements verifying atomic level integration of lanthanides into the matrix-glass structure [1]. XAS experiments revealed that although cerium was added to the glass structure as  $\text{Ce}^{4+}$ , it integrates into the glass structure as  $\text{Ce}^{3+}$ , while europium remained in the originally added trivalent form. It was found that  $\text{Nd}^{3+}$  and  $\text{Eu}^{3+}$  ions do not form clusters within the glass structure, even at high concentrations, indicating that these lanthanides are homogeneously dispersed, hence providing a high stability of the compact glassy structure.

Partition coefficients ( $R_d$ ) between the solid and liquid phase for the selected ions correlate well to the illite and chlorite content of the recent BCF core samples, supporting the assumption that sorption mainly occurs on clay minerals [2]. The  $R_d$  values determined by ICP-MS for  $\text{Cs}^+$  are in line with earlier investigations carried out on core samples from past drillings using the radiotracer method.

## Remaining work

Leaching of radionuclides from the glasses which model vitrification of HLW will be studied. Macroscopic sorption experiments on the new core samples of BCF will be complemented with microscopic investigations.

## Related publications

- [1] M. Fabian, F. Gergely, J. Osán, S. Kesari, R. Rao: *Network structure of borosilicate glasses doped with lanthanides*, under submission (2019)
- [2] J. Osán, M. Fábrián, F. Gergely, I. Rigó, M. Veres, R. Dähn, D. Grolimund, S. Török: *Combined microanalytical study of U(VI) uptake capability of argillaceous rocks from Boda Claystone Formation, Hungary*. European Conference on X-ray Spectrometry, Ljubljana, Slovenia, 24-29 June 2018

# CHARACTERIZATION OF ATMOSPHERIC AEROSOL PARTICLES HAVING AN ENERGY GENERATION ORIGIN

János Osán, Csenge Dian, Endre Börösök, Levente Illés, Viktória Kovács-Kis, Szabina Török

## Objective

In recent decades European countries have made progress in reducing particulate air pollution due to concern about their health and climate effects. However, contrary to industrial sources, biomass combustion emissions are increasing in Eastern Europe. It has been shown that such particles contribute more than 40% of the fine particulate matter even in suburban and urban areas in Eastern and Central Europe. These results were obtained from a statistical analysis of large datasets of daily-taken samples characterized with an extensive set of analytical methods.

The aim of the present work was the identification of the sources based on investigation of samples collected for a few hours using a limited number of non-destructive analytical methods. In order to achieve this goal, a special cascade impactor sampling method was developed allowing simultaneous collection of samples which are reliable for use with different analytical methods. Total-reflection X-ray fluorescence (TXRF) is a very sensitive method for elemental analysis of the deposited particles. If Si wafers are used as collection substrates, the same samples can be investigated by scanning electron microscopy (SEM) without a carbon coating. Transmission electron microscopy (TEM) investigations become possible if the impactor is able to sample on TEM grids.

## Methods

For size-fractionated sampling of atmospheric particulate matter, a 9-stage May type cascade impactor was used covering a wide size range of 70 nm to 16  $\mu\text{m}$ , including part of the ultrafine particles. Impactor plates have been redesigned to hold 20 $\times$ 20 mm<sup>2</sup> Si wafers and TEM grids.

Samples were collected in suburban Budapest (Hungary) and in urban Cassino (Italy). Only the range of the fine fraction (70 nm to 2.5  $\mu\text{m}$ ) was considered for this study. Sample collection times varied from 20 min to 4 hours. Elemental analyses of the deposited particles were performed using TXRF in laboratory and using synchrotron radiation (SR) at Elettra (Trieste, Italy). Individual particles were visualized by SEM and TEM.

## Results

Measurements of test samples collected at two sites with different source profiles revealed that cluster-like soot and spherical organic particles can be sampled effectively in the 70–200 nm size fraction that is characteristic for both traffic and biomass combustion sources.

Urban and suburban sites are affected by both traffic and biomass combustion sources with different temporal characteristics [1]. In the 70–180 nm size range carbonaceous particles were found to be the most abundant as observed by SEM and TEM. TXRF was used to distinguish between traffic end-of-pipe (internal combustion engine) and biomass fuel burning sources based on the potassium (K) concentration [2]. In the 180–300 nm fraction the carbonaceous particles could be mostly related to biomass combustion. The K K $\alpha$  signal in this fraction was highest in Budapest during winter, while in Cassino (Italy) even in the summer period the K K $\alpha$  signal was above the average of Budapest. The reason for that is the intense use of wood in cooking stoves.

## Remaining work

Further investigation of the collected samples is planned in order to obtain information on molecular composition of fine and ultrafine particles using Raman spectroscopy and SR based X-ray absorption spectrometry.

## Related publications

- [1] M. G Perrone, S. Vratolis, E. Georgieva, S. Török, K. Šega, B. Veleva, J. Osán, I. Bešlić, Z. Kertész, D. Pernigotti, K. Eleftheriadis and C.A. Belis: *Sources and geographic origin of particulate matter in urban areas of the Danube macro-region: The cases of Zagreb (Croatia), Budapest (Hungary) and Sofia (Bulgaria)*, Science of the Total Environment **619-620**, 1515-1529 (2018)
- [2] J. Osán, Á. Farkas, E. Börösök and S. Török. *Non-destructive characterization of airborne particulate matter by combination of cascade impactor sampling and TXRF related methods*, European Conference on X-ray Spectrometry, Ljubljana, Slovenia, 24-29 June 2018

# STRATEGIC RESEARCH GROUP FOR THE CHALLENGES OF RENEWABLE ENERGY BASED SYSTEMS

*Bálint Hartmann, Attila Kazsoki, Lilla Visnovszky, Bálint Sinkovics, Viktória Sugár*

## Objective

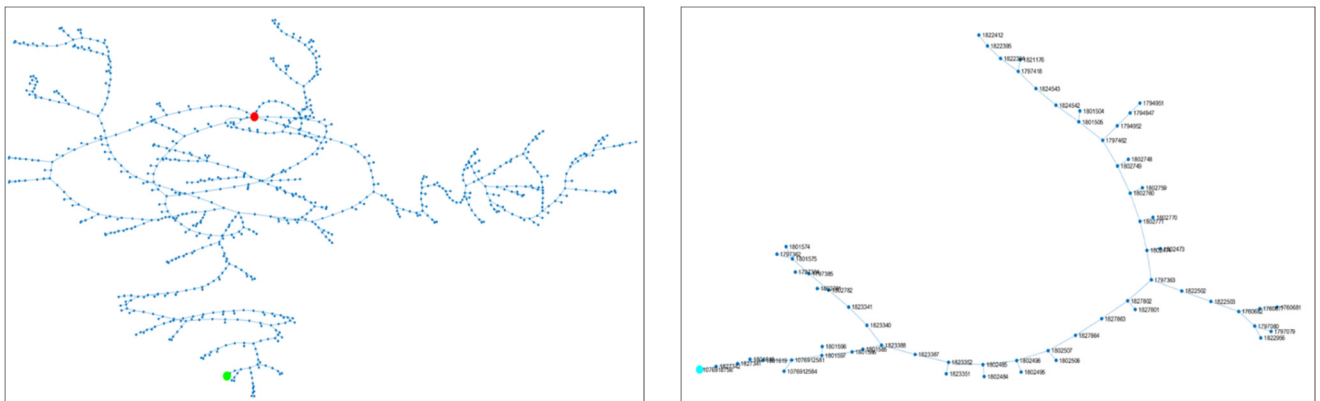
The primary aim of the second year of our research was to examine the possibilities of distribution network modelling, especially at medium voltage levels. The unification of data provided by different sources was to be carried out, and algorithms of complex network analysis were necessary to implement in MATLAB environment. Another aim of the year was to create a forecasting algorithm for solar photovoltaic electricity production. The model was based on the Bird clear-sky model, which has been corrected with various environmental and location parameters.

## Methods

Grouping of medium voltage distribution network topologies was done using principal component analysis and k-means clustering. Solar photovoltaic electricity production forecasting uses a combined physical model and a neural network that is relying on environmental parameters.

## Results

Topological data were received for six distribution system operator areas. In the case of two areas, only representative models were available, while for the remaining four areas, complete network data was provided by the distribution system operator. Unification of the datasets were carried out and a consistency check was performed. This revealed minor errors with two datasets, which necessitated further consultation with the data providers. For the distribution areas without errors, topology of 20 sample networks were available, representing 4 regions. For each feeder number of nodes, the average node degree, clustering coefficient and characteristic path length were calculated. The principal component analysis function of the Minitab 18.0 statistical software was used to identify the most valuable data of the underlying structure. Two principal components with the highest eigenvalue were selected as input for k-means clustering. The optimal number of clusters was determined, and representative networks of the resulting four clusters have been constructed.



# REDUCTION-OXIDATION EQUILIBRIA IN BODA CLAYSTONE MINERALS DETERMINED FROM $\text{Fe}^{3+}/\text{Fe}^{2+}$ RATIOS

Károly Lázár, Sándor Stichleutner, Zoltán Máthé\*

## Objective

Boda Claystone Formation (BCF) is considered as a potential repository site for high level nuclear waste in the near future. Migration of various radionuclides in BCF samples have extensively been studied in our laboratories previously. Possible influence of redox processes on migration of certain radionuclides was exposed recently. Thus, as a representative indicator of redox conditions,  $\text{Fe}^{3+}/\text{Fe}^{2+}$  ratios were determined in samples acquired from different regions of BCF.

## Methods

$^{57}\text{Fe}$  Mössbauer spectroscopy was primarily applied and complemented with X-ray diffraction and optical microscopy. Samples were obtained from boreholes drilled in three different regions in south-west of Mecsek Mountains, i/ in the Western Anticline (BAF-2, BAT-14), ii/ in the Alpha-1 exploratory tunnel at about 1000 m below the ground level (Delta), iii/ and from the Gorica block (Ib-4).

## Results

Beside direct redox properties,  $\text{Fe}^{3+}/\text{Fe}^{2+}$  ratios in minerals can also be correlated with processes of diagenesis. In correspondence with a consent of experts the primary stages of formation of BCF had taken place in the Perm geological age under arid and oxidative conditions by desiccation of salty lakes starting roughly 250 My ago. In correspondence, the primary iron bearing minerals in BCF samples are hematite ( $\text{Fe}_2\text{O}_3$ ), illite ( $\text{Al,Mg,Fe}_2(\text{Si,Al})_4\text{O}_{10}[(\text{OH})_2,\text{H}_2\text{O}]$ ) and similar chlorite. These minerals were identified in various proportions almost in each samples. In some exceptional samples originated from regions formed under reducing conditions pyrite ( $\text{FeS}_2$ ) and ankerite ( $\text{Ca,FeCO}_3$ ) were dominant. Each of these minerals were unambiguously identified from their Mössbauer spectra as well.

Changes in the  $\text{Fe}^{3+}/\text{Fe}^{2+}$  ratios were revealed in the illite component collected from different depths from BAF-2 borehole in the Western Anticline region. The greater is the depth the larger is the  $\text{Fe}^{2+}$  content in the illite/chlorite component. Simultaneously, proportion of hematite is decreasing with the depth (Fig. 1, left). Thus, formation of these two minerals was probably correlated during the genesis. In contrast, the  $\text{Fe}^{3+}$  contribution was dominant both in hematite and illite while  $\text{Fe}^{2+}$  was detected only in minor amounts ( $\sim 10\%$ ) in samples obtained from the other extended region, from Ib-4 drilling in Gorica block (Fig. 1, right). Thus, the differences of formation of BCF in the Western Anticline and in the Gorica block are clearly revealed in the Mössbauer spectra as well. Another process, weathering was also clearly reflected in  $\text{Fe}^{3+}/\text{Fe}^{2+}$  ratios of samples collected from BCF samples from 23 – 70 m depths (BAT-14 borehole, the upper 0 – 22 m covering layer is permeable marl). The hematite content was constant, whereas the relative  $\text{Fe}^{3+}$  content in illite decreased from 30 % to 20% and, in reverse, the  $\text{Fe}^{2+}$  content increased from 4 % to 14 % with the increase of depth. The comparison of these samples demonstrates that illite is more sensitive to weathering processes than hematite. In samples collected from greater depths (-1000 m, Alpha-1 tunnel) minerals containing exclusively  $\text{Fe}^{2+}$  (pyrite and ankerite) were also identified [1].

Effects of oxidizing (perchlorate, hypochlorite, hydrogen peroxide) and reducing (hydroxylamine, formaldehyde, hydrazine) chemicals were also tested in slurries. Neither reduction nor oxidation was found, the  $\text{Fe}^{3+}/\text{Fe}^{2+}$  ratios of minerals remained unaltered within a few weeks' storage [2]. However,  $\text{Fe}^{2+} \Rightarrow \text{Fe}^{3+}$  redox process may contribute to immobilization of certain species (e.g. via  $\text{Se(IV)} \Rightarrow \text{Se(0)}$ ) in long term interactions with minerals of claystone as was demonstrated in our earlier reports related to migration studies.

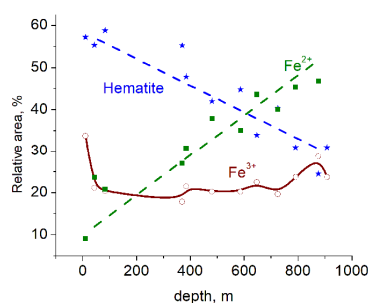
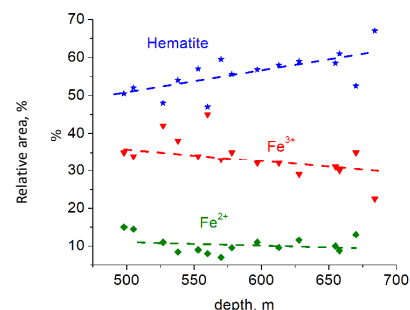


Figure 1: Relative proportions of hematite ( $\text{Fe}_2\text{O}_3$ ) and  $\text{Fe}^{2+}$  and  $\text{Fe}^{3+}$  components in illite Mössbauer spectra of samples collected from various depths in two different regions: BAF-2 borehole in the Western Anticline (← left) and Ib-4 borehole in the Gorica block (right →)



## Related publications

- [1] K. Lázár, Z. Máthé, S. Stichleutner: *Iron in minerals of Boda Claystone Formation*, MECAME2018, Mediterranean Conference on the Applications of the Mössbauer Effect, 27-31 May 2018, Zadar, Croatia
- [2] K. Lázár, Z. Máthé, S. Stichleutner: *Comparison of iron bearing minerals from regions of Boda Claystone Formation: Variations in genesis*, Mössbauer Spectroscopy in Materials Science, 25-28 June 2018, Prague, Czech Republic

\* Mecsekérc Environmental, Ltd.

# PREPARATION AND CHARACTERIZATION OF NANOPARTICLE SYSTEMS DEVELOPED FOR PLANT NUTRITION EXPERIMENTS

Zoltán Klencsár, Sándor Stichleutner, Viktória Kovácsné Kis

## Objective

Preparation and characterization of nanoparticle systems to be used in studies investigating the metal uptake and iron metabolism of plants.

## Methods

Samples were prepared either via a hydrothermal process (HP) or via electric wire explosion (EWE). Except for the samples prepared via EWE, the various nanoparticle samples studied were prepared by Gy. Tolnai, A. Ábrahám, A. Lengyel, Sz. Németh and R. Szalay. Powder X-ray diffractometry (PXRD),  $^{57}\text{Fe}$  Mössbauer spectroscopy ( $^{57}\text{Fe}$  MS), transmission electron microscopy (TEM), electron magnetic resonance (EMR) spectroscopy and inductively coupled plasma optical emission spectrometry (ICP-OES) were used to characterize the prepared nanoparticles. EWE and PXRD experiments were performed in cooperation with L.K. Varga at the Wigner Research Centre for Physics (Wigner RCP). ICP-OES measurements were performed by Z. May, whereas part of the TEM measurements were carried out in cooperation with L. Szabó, at the Research Centre for Natural Sciences, MTA. Magnetization measurements were performed by L. Kiss (Wigner RCP).

## Results

Iron-oxide-hydroxide nanoparticles were prepared in the form of a nanocolloid suspension by the use of a precursor enriched in  $^{57}\text{Fe}$ . TEM measurements confirmed that the product included nanoparticles of iron oxide or iron oxide-hydroxide, with characteristic sizes of 5 nm and 20-30 nm. At the same time,  $^{57}\text{Fe}$  MS measurements performed at  $\sim 80$  K on the frozen suspension sample suggested that a large fraction of the iron still resided in the precursor material  $\text{FeCl}_3$ .

Nanomagnetites were prepared under different conditions, among others under an inert gas ( $\text{N}_2$ ) atmosphere in order to achieve a high  $\text{Fe}^{2+}$  ratio of the samples [1]. TEM measurements and corresponding selected area electron diffraction (SAED) patterns confirmed the presence of magnetite nanoparticles with ca. 10 nm characteristic size in the samples, along with some larger (ca. 50 nm) nanoparticles, which latter were identified as maghemite. Beside the iron oxides, TEM also revealed the presence of ferrihydrite or ferric oxide-hydroxide nanoparticles in the samples.

A new nanoparticle colloid suspension sample was created via EWE in water from a 0.2 mm diameter pure iron wire. Filtering the immediate product yielded on the one hand a pure, water-like liquid, and on the other hand a dense deposit of particles on the filter paper. Similar to the results of our previous experiment [2], the latter was shown to consist mainly of  $\alpha\text{-Fe}$  and  $\text{Fe}_{1-x}\text{O}$  (non-stoichiometric wüstite) by  $^{57}\text{Fe}$  MS, whereas TEM/SAED measurements confirmed the presence of nanoparticles (ca. 10-100 nm) in both sample fractions, with attributes akin to those of magnetite. ICP-OES also confirmed the presence of 0.067 mg/l of iron in the filtered colloid suspension.

The effect of aging was assessed on magnetite/maghemite as well as on Zn-ferrite nanoparticle powders. For the magnetite/maghemite powder, using  $^{57}\text{Fe}$  MS we were able to show that aging leads to the oxidation of an  $\text{Fe}^{2.5+}$  iron species akin to that present in perfect magnetite, which confirmed that the original sample indeed contained magnetite [3]. In the case of crystalline and amorphous Zn-ferrite nanoparticle (ca. 5-6 nm) powders, TEM measurements and associated SAED patterns have confirmed the stability of both samples under ambient atmosphere over a year-long time period. For the latter samples the Zn:Fe atomic ratio was elucidated by ICP-OES measurements, and differences in the magnetic behaviour of the samples were reflected in magnetization measurements, the amorphous nanoparticles being characterized by an effective magnetic moment that is considerably lower than that of the crystalline sample.

## Remaining work

The sample prepared with iron enriched in  $^{57}\text{Fe}$  needs further treatment in order to achieve a more complete transformation of the precursor material into the nanoparticles. Preparation, characterization and application of further nanoparticle samples are needed in order to explore the significance of specific material properties in influencing plant-nanoparticle interactions.

## Related publications

- [1] A. Lengyel, Z. Homonnay, K. Kovács, Z. Klencsár, Sz. Németh, R. Szalay, V. Kis, F. Fodor, Á. Solti, M. Ristic, S. Music, E. Kuzmann: *Characterization of nanomagnetites co-precipitated in inert gas atmosphere for plant nutrition*, *Hyp. Int.* **239**, 38 (2018)
- [2] K. Lázár, L. K. Varga, V.K. Kis, T. Fekete, Z. Klencsár, S. Stichleutner, L. Szabó, I. Harsányi: *Electric explosion of steel wires for production of nanoparticles: Reactions with the liquid media*, *J. Alloys Compd.* **763**, 759 (2018)
- [3] Z. Klencsár, A. Ábrahám, L. Szabó, E. Gy. Szabó, S. Stichleutner, E. Kuzmann, Z. Homonnay, Gy. Tolnai: *The effect of preparation conditions on magnetite nanoparticles obtained via chemical co-precipitation*, *Mater. Chem. Phys.* **223**, 122 (2019)

# EXPLORING THE IMPACT OF NANOPARTICLES ON PRODUCTIVITY, METAL UPTAKE AND IRON METABOLISM OF PLANTS

Zoltán Klencsár, Sándor Stichleutner, Viktória Kovácsné Kis

## Objective

Characterization of nanoparticle systems, and their application in studies investigating the metal uptake and iron metabolism of plants.

## Methods

Nanoparticle samples were prepared via a hydrothermal process by Gy. Tolnai, A. Ábrahám, A. Lengyel, Sz. Németh and R. Szalay. Powder X-ray diffractometry (PXRD), <sup>57</sup>Fe Mössbauer spectroscopy (<sup>57</sup>Fe MS), transmission electron microscopy (TEM), electron magnetic resonance (EMR) spectroscopy and inductively coupled plasma optical emission spectrometry (ICP-OES) were used to characterize the prepared nanoparticles. PXRD experiments were performed in cooperation with L.K. Varga at the Wigner Research Centre for Physics (Wigner RCP). ICP-OES measurements were performed by Z. May, whereas part of the TEM measurements were carried out in cooperation with L. Szabó, at the Research Centre for Natural Sciences, MTA. Plant growth experiments were performed at the Department of Plant Physiology and Molecular Plant Biology of the Eötvös Loránd University.

## Results

Low-temperature <sup>57</sup>Fe Mössbauer spectroscopy measurements were performed on three different frozen suspensions of ferrihydrite/hematite nanoparticles, prepared by using different surfactant materials. The measurements revealed that more than 2/3 of all iron atoms is situated in ferrihydrite in the samples which also included hematite in different proportions along with a Fe<sup>2+</sup> species with parameters akin to those of FeCl<sub>2</sub>·2H<sub>2</sub>O.

Zn oxide-hydroxide nanoparticle powder was prepared, and was investigated by the means of TEM and PXRD. TEM confirmed the presence of nanoparticles with a characteristic size of 50-100 nm, whereas we found the powder to contain a mixture of ZnO and Zn(OH)<sub>2</sub> by PXRD. Further oxidation of the sample resulted in ZnO powder with a wide particle size distribution in the submicron range.

An Al(OH)<sub>3</sub> nanoparticle colloid suspension was prepared and investigated by ICP-OES and TEM. The Al concentration of the suspension was found to be 481 mg/L by ICP-OES. TEM has implied that the sample is composed of poorly ordered platelets with a thickness of a few nm, and lateral dimensions in the order of several tens of nanometers.

Several different nanohematite/nanoferrhydrite nanocolloid suspensions were tested in hydroponic cultures of iron deficient cucumber plants. The treated plants regenerated from iron deficiency in all cases at pH 5-6 but at pH 8.5 the nanomaterial suspensions deposited in the bottom of the pots as droplets. Cabbage plants were grown in iron deficient conditions (nutrient solution with CaCO<sub>3</sub>) for foliar spray experiments. Mn-Zn-ferrite nanoparticle suspensions were used at 0.02-2 mM concentration to the plants as a spray, in conjunction with an additional surfactant, which resulted in a slight greening of the leaves. In germination tests Mn-Zn-ferrite nanoparticle suspensions, used at 0.01, 0.1 and 1.0 mM concentrations, were found to stimulate germination of cucumber seeds. The results of germination tests performed with nano-Al(OH)<sub>3</sub> preparations applied in Petri dishes on white mustard seeds indicated that this nanomaterial does not have significant ecotoxicological effects on the germination of the seeds.

## Remaining work

Further nanoparticle samples and plant growth experiments are needed in order to explore the significance of specific material properties in influencing plant-nanoparticle interactions.

## Related publications

- [1] A. Lengyel, Gy. Tolnai, Z. Klencsár, V. Kumar Garg, A. Carlos de Oliveira, L. Herojit Singh, Z. Homonnay, R. Szalay, P. Németh, Sz. Bálint, M. Ristic, S. Music, E. Kuzmann: *The effect of carboxylic acids on the oxidation of coated iron oxide nanoparticles*, Journal of Nanoparticle Research **20**, 136 (2018)
- [2] A. Lengyel, Z. Homonnay, K. Kovács, Z. Klencsár, Sz. Németh, R. Szalay, V. Kis, F. Fodor, Á. Solti, M. Ristic, S. Music, E. Kuzmann: *Characterization of nanomagnetites co-precipitated in inert gas atmosphere for plant nutrition*, Hyperfine Interactions **239**, 38 (2018)
- [3] A. Lengyel, V.K. Garg, A.C. de Oliveira, S.W. da Silva, L.R. Guilherme, Z. Klencsár, Z. Homonnay, J.A.H. Coaquira, Gy. Tolnai, E. Kuzmann: *Mossbauer spectroscopy control of the preparation of citric- and mandelic acid functionalized nanomagnetites*, Hyperfine Interactions **17**, 239 (2018)
- [4] K. Lázár, L.K. Varga, V.K. Kis, T. Fekete, Z. Klencsár, S. Stichleutner, L. Szabó, I. Harsányi: *Electric explosion of steel wires for production of nanoparticles: Reactions with the liquid media*, Journal of Alloys and Compounds **763**, 759 (2018)
- [5] Z. Klencsár, A. Ábrahám, L. Szabó, E.Gy. Szabó, S. Stichleutner, E. Kuzmann, Z. Homonnay, Gy. Tolnai: *The effect of preparation conditions on magnetite nanoparticles obtained via chemical co-precipitation*, Mater. Chem. Phys. **223**, 122 (2019)

# THE EFFECT OF CHEMICAL COMPOSITION OF CONCRETE ON ITS LONG-TERM PERFORMANCE IN IRRADIATED ENVIRONMENT

*László Szentmiklósi, Katalin Gméling, Veronika Szinger-Szilágyi, Ildikó Harsányi, Boglárka Maróti, Tamás Fekete*

## Objective

During the construction of the new nuclear power plant units Paks II, the concrete structures will be made preferably from domestic raw materials. For this reason, we have to be prepared with suitable recipes of radiation-resistant, durable concretes with low activation susceptibility. The key to achieve that goal is the careful selection of the raw materials (gravel and sand) based upon the compositional data obtained by analytical and petrological methods. Analysis of the chemical composition of the concretes surrounding the reactor vessel is important, because they are exposed to high flux radiation, so their constituents might be substantially activated. Due to the neutron radiation, the high neutron-capture cross-section nuclides with short and long half-life become highly radioactive during the reactor operation time, while isotopes with long half-life remain radioactive for years following the reactor shutdown.

## Methods

To achieve the research objectives, we sampled systematically the Hungarian gravel and sand mines. From four different regions, sixteen mines were sampled. From every selected mine four assorted (particle size: 0-4, 4-8, 8-16, 16-32 mm) and washed samples were collected. In addition, some admixtures (basalt, andesite, limestone) from Hungarian mines (Colas Északkő Kft.) and binders (different types of cements) from Vác and Beremend were chosen for analysis, in total 100 samples. After adequate preparation, samples were subjected to chemical elemental analyses (NAA + PGAA = NEAAA (Neutron-based element analysis and activation assessment) and XRF) and partly to petrographic (macroscopic, microscopic and heavy mineral) investigations. Prompt gamma activation analysis (PGAA) and instrumental neutron activation analysis (NAA) were performed at MTA EK, while X-ray fluorescence (XRF) measurements were done at SZIKKTI Laboratory Ltd.

The following elements have significant activities even a year after the concretes were exposed for neutron radiation: Ce, Co, Cs, Eu, Fe, Hf, Sb, Sc, Ta, Tb, Cr, Pa, Sm, Sr, Zn, Th and U. All these trace elements are enriched in so-called heavy minerals (e.g. olivine, magnetite, amphibole, rutile, topaz, zircon) which are accessory constituents (<5%, but usually <0.1-0.01%) of the rocks and which have a density greater than 2.9 g/cm<sup>3</sup>. Heavy minerals mainly occur in sediments which contain low-quartz-content metamorphic rocks, igneous rocks or siliciclastic rocks. Until now macroscopic, microscopic and heavy mineral studies have been made on the gravels from three regions: the NW Hungarian Region, the NE Hungarian and the Mid-Danubian Region.

## Results

Based on the analytical and petrological results, we concluded that there are samples with remarkably lower, and also some with remarkably higher "impurity profile", originated in different mines. All sand and gravel samples have SiO<sub>2</sub> content above 90wt%. The major elements next to Si are Al, Fe, K and Na. Ca content is high in the Mid- and NW Hungarian gravels, while NE and SW samples have very low Ca content. Elemental analysis of the samples rated by particle size revealed that all element concentrations decrease with increasing particle size, except Cr, which has higher concentration in gravels than in sands. Grinding the samples with wolfram carbide mortar increases the W, La, Nd and also Co concentration of the samples. NE Hungarian gravel mines have the lowest trace element content, while samples from NW Hungary Babót, from Mid-Hungary Bugyi IX and Taksony, from SW Hungary Murakeresztúr II have lower trace element content.

Macro- and micro-scale gravel petrography of the samples proved diagnostic differences among the analysed three regions. It can be stated that the major rock types (and especially quartzite) are of metamorphic origin in all the observed regions. In the Mid-Danubian Region gravels have relative more igneous components compared to sedimentary ones, while in the NW Hungarian Region the gravels are more enriched in sedimentary component beside the metamorphic one. In the NE Hungarian Region gravels the cumulative ratio of igneous and sedimentary originated rocks are low (around 10 w%, and almost equal), expressing the maturity of those sediments. Based on heavy mineral studies, the gravels of the Mid-Danubian Region contain more heavy mineral carrier components.

The mine of Babót (NW Hungarian Region) has the most mature sediment formation, also indicated by high Si content at the expense of depleted other major and trace elements. Considering the radiation sensitivity, it can be stated that none of the long-lived radionuclides is enriched in the investigated sand and gravel samples compared to average Portland cement composition. However, Fe (0.5-1.5 wt%) and Cr, Sr (few hundred µg/g) show slightly higher concentrations, but all have half-lives less than a year. Cs, Co and Eu with years long half-lives are under 5 µg/g concentration in gravels. Concluding from our results, it is better to use crushed larger fractions of gravel, instead of sand to prepare low activation susceptibility shielding concrete.

## Remaining work

Samples from the SW Hungarian region need to be investigated by the petrological point of view. The gravel and concrete investigation project will be carried on in the framework of V4-Korea Joint Research program between 2018 and 2022.

# PREPARATION AND CHARACTERIZATION OF EFFICIENT SUPPORTED NANODISPERSED GOLD CATALYSTS

Gergely Nagy, György Sáfrán, Dávid Srankó, Tianbo Li\*, Shaofeng Liu\*, Junhu Wang\*,  
Andrea Vargáné Beck, Károly Lázár

## Objective

A joint bilateral project was established between the MTA EK and the Dalian Institute of Chemical Physics (DICP, China) for synthesizing and characterizing gold nanocatalysts and their use in aerobic oxidation of benzyl alcohol. The related tasks were divided between the two institutions. The preparation and characterization of  $\text{Al}_2\text{O}_3$ ,  $\text{SiO}_2$ ,  $\text{MgAl}_2\text{O}_4$ ,  $\text{MgO}$  and hydroxyapatite (HAP) supported catalysts and a part of their catalytic investigation (in xylene solvent at 60 °C, at 1 bar  $\text{O}_2$ ) was performed at MTA EK. The other part of the catalytic evaluation (in a solvent-free condition at 150 °C, 5 bar  $\text{O}_2$  in a sealed autoclave) was completed at DICP.

## Methods

The catalyst particles were characterized with transmission electron microscopy (TEM). Adsorption and temperature programmed desorption of  $\text{CO}_2$  and  $\text{NH}_3$  was used for characterizing of basicity and acidity.  $\text{CO}$  adsorption was measured with two methods: i/ diffuse reflectance infrared spectroscopy, and ii/ binary concentration pulse chromatography to probe the surface gold sites. Finally, catalytic measurements with analysis of products were performed.

## Results

The results of catalysis measurements on oxidation of benzyl alcohol at 60 °C, with 1 bar  $\text{O}_2$  in xylene solvent are reported in another account in this Progress Report. Here the results of certain characterization measurements (particle size, acidity and basicity, Figs. 1 and 2) and the results of catalytic tests at 150 °C, 5 bar  $\text{O}_2$  in solvent-free media are presented (Fig. 2).

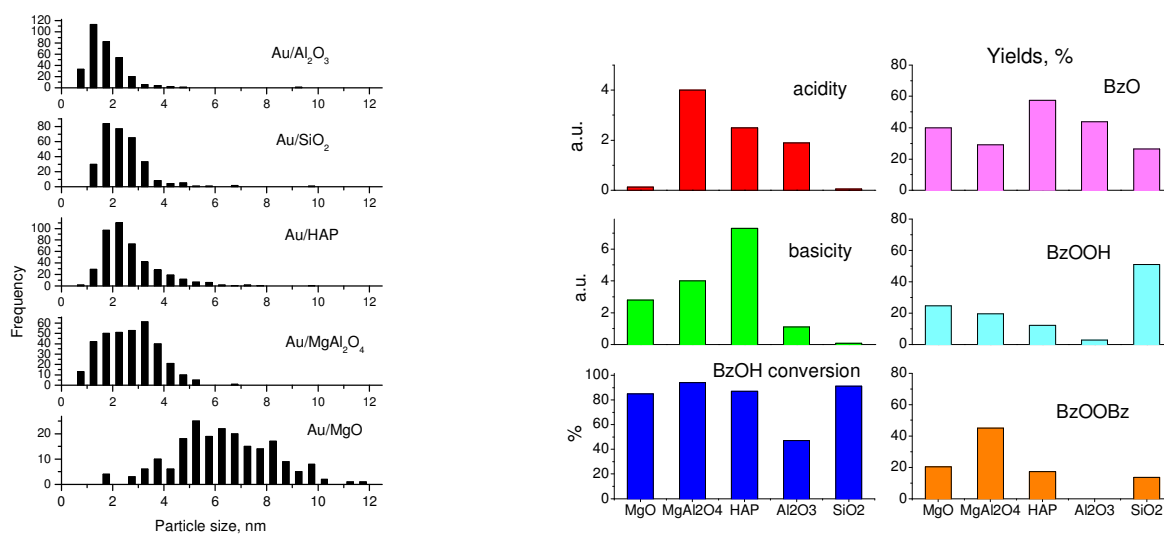


Figure 1: Distribution of gold particle sizes deduced from TEM images of the corresponding catalysts

Figure 2: Acidities and basicities of different supports, the conversion of benzyl alcohol at 150 °C in solvent-free media, and the yields of products after 5h reaction time

The initial reaction rates in benzyl alcohol (BzOH) oxidation were determined here at 60 °C (1 bar O<sub>2</sub> in xylene solvent). The corresponding turnover frequencies related to surface Au atoms (TOF<sub>surf</sub>) ranged between 1000-4000 h<sup>-1</sup> [1]. Reactions performed in China in solvent-free media at 150 °C for 5 h resulted in a high extent of conversions. Benzaldehyde (BzO), benzoic acid (BzOOH) and benzyl benzoate (BzOOBz) products were detected with good reaction yields, amounting to 500 – 3000 h<sup>-1</sup> TOF<sub>surf</sub> values. Thus, the excellent performance of the synthesized and characterized catalysts is confirmed [2].

### ***Related publications***

- [1] G. Nagy, D. Srankó, K. Lázár, G. Sáfrán, A. Beck, S. Liu, T. Li, H. Tang, B. Qiao, R. Ge and J. Wang: *Support effect of Au catalysts in aerobic benzyl-alcohol oxidation: effect of acid-base properties* (poster presentation), 14<sup>th</sup> Pannonian International Symposium on Catalysis, Starý Smokovec, Slovakia, 3 – 7 September, 2018, Abstract Book
- [2] G. Nagy, A. Beck, G. Sáfrán, Z. Schay, S. Liu, T. Li, B. Qiao, J. Wang, K. Lázár: *Nanodisperse gold catalysts in oxidation of benzyl alcohol: comparison of various supports under different conditions*, Submitted to Reaction Kinetics, Mechanisms and Catalysis

\* Dalian Institute of Chemical Physics, Chinese Academy of Sciences

# APPLICABILITY EVALUATION OF ADVANCED OXIDATION PROCESS FOR ELIMINATION OF NEUROPHYSIOLOGICAL ACTIVITY ANTIDEPRESSANT FLUOXETINE

Renáta Homlok, László Szabó, Gyuri Sági, Krisztina Kovács, Szabina Papné Góger, Tünde Tóth, Erzsébet Takács, László Wojnárovits

## Objective

This study aimed at seeking for an appropriate technology able to remove fluoxetine residue from a complex water matrix, where special attention needs to be paid to elimination of the neurophysiological activity [1].

## Methods

For the gamma radiolysis experiments with 1600 TBq activity  $^{60}\text{Co}$   $\gamma$ -source was used. For product analysis, liquid chromatography (LC) - tandem mass spectrometry (MS) techniques were employed. Products were separated using an Agilent 1200 LC. Density Functional Theory (DFT) was applied with the B3LYP functional using the Gaussian 09 software suite. Geometry optimizations were conducted at the B3LYP/6-311G++(d,p) level of theory, and the solvent effects of the aqueous media were considered with the Solvation Model Density (SMD) solvent model. Electronic energies were refined by single-point energy calculations using the 6-311++G(3df,3pd) basis set. Gibbs free energies were corrected for 1 M standard state of aqueous solution. For the docking studies, the virtual ligands - P4, P31, P35-37, fluoxetine and (S)-citalopram - were prepared using Schrödinger LigPrep (2016) tools applying the default settings. The physiologically relevant protonation states and tautomers were generated for both the (R)- and (S)-enantiomers using Epik. The docking calculations were carried out by Glide applying the standard precision (SP) protocol, and the rotatable groups were allowed to move.

## Results

The applicability of advanced oxidation processes (AOP) to eliminate the neurophysiological activity of fluoxetine was probed by generating a free radical system with  $\cdot\text{OH}$ -initiated peroxy radical mediated processes. A wide range of transformations was anticipated to occur on the fluoxetine skeleton based on product analysis experiments substantiated with computational calculations. By performing product analysis experiments along with quantum chemical calculations, the most probable reaction paths were analysed including aromatic hydroxylation, defluorination, O-dealkylation and C-dealkylation. The candidates for neurophysiological activity were further investigated by molecular docking. In the case of calculations our purpose was to differentiate between possibly active and inactive transformation products. The results of docking calculations were evaluated by analysing the interactions of the docked poses, and by comparing them with the X-ray structure of (S)-citalopram (a compound with neurophysiological activity). The (S)- and (R)-enantiomers do not show significant differences in terms of docking scores or overall layout. The docking poses were sensible for all compounds and matched to (S)-citalopram in terms of overall position. The majority of the degradation products gave scores similar to fluoxetine.

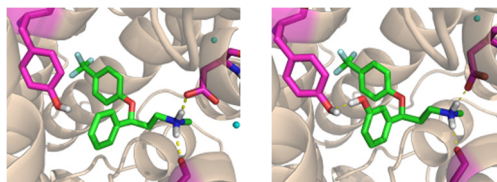


Figure 1: The proposed binding mode of fluoxetine (left) and a hydroxylated derivative (right). The ligands are shown in the middle, the hydrogen bonding side chains of the protein are on the edge of the figure, the protein itself is represented by a ribbon and the  $\text{Na}^+$  ions are visualized as small spheres. The colour structures show the medicine molecules investigated.

Molecular docking studies show (Fig. 1) that the hydroxylated derivatives are well accommodated in the binding pocket of the corresponding protein, suggesting that these compounds may retain the activity of the parent compound. Therefore, we suggest that performing the AOP treatment to reach an appropriate treatment stage without hydroxylated derivatives present might be a prudent approach to handle this problem. From a worst-case perspective, we suggest that prolonged treatment needs to be applied to further transform hydroxylated derivatives.

## Remaining work

The project was finished.

## Related publication

- [1] L. Szabó, V. Mile, D. J. Kiss, K. Kovács, T. Földes, T. Németh, T. Tóth, R. Homlok, Gy. T. Balogh, E. Takács, L. Wojnárovits: *Applicability evaluation of advanced processes for elimination of neurophysiological activity of antidepressant fluoxetine*, *Chemosphere* **193**, 489-497 (2018)

# ASSESSMENT OF ANTIBACTERIAL ACTIVITY, TOXICITY AND BIODEGRADABILITY OF PRODUCTS IN THE COURSE OF RADIOLYSIS INDUCED DECOMPOSITION OF SULPHONAMIDES

Krisztina Kovács, Szabina Góger Papné, Renáta Homlok, Tünde Tóth, Gyuri Sági, Anna Tegze, Erzsébet Takács, László Wojnárovits

## Objective

The present work is aimed at studying the removal of four sulphonamides (sulphanilamide (SAA), sulfaguanidine (SGD), sulfathiazole (STZ), sulfamethoxazole (SMX)) from their aqueous solutions by ionizing radiation with emphasis on the biological evaluation of the decomposition products. Biodegradability in river water and in activated sludge, the toxicity from three different trophic levels and the antibacterial activity were tested.

## Methods

The samples were irradiated using a  $^{60}\text{Co}$  panoramic type  $\gamma$  facility (dose rate =  $7.6 \text{ kGy h}^{-1}$ ) at room temperature, in aerated, 0.1 mM solutions.  $\text{H}_2\text{O}_2$ , which can form during irradiation, was eliminated by heterogeneous catalysis using  $5 \text{ g L}^{-1} \text{ MnO}_2$  (stirred overnight at  $20 \text{ }^\circ\text{C}$ ,  $\text{pH} = 10$ ). The removal efficiency was investigated by LC-MS/MS.  $\text{BOD}_5$  experiments were performed by using an OxiTop® Control BOD Respirometer System according to DIN EN 1899-1 (1998). Activated sludge and river water were used for inoculation. The acute toxicity to the *Vibrio fischeri* bioluminescent bacterium (a decomposer) was determined according to DIN EN ISO 11348-2 (1999) following 30 min incubation. The chronic growth inhibition on *Pseudokirchneriella subcapitata* (a producer) microalgae was implemented based on OECD test No. 201 (2011) after 72 h. *Daphnia magna* (a consumer) acute mortality tests were performed according to OECD Test No. 202 (2004). Activated sludge inhibition tests were carried out according to ISO 8192:1986 (1986) standard over a period of 180 min. In antibacterial susceptibility testing, *Pseudomonas aeruginosa* was chosen as the test organism. Broth microdilution assays were carried out by photometrical monitoring of bacterial growth, employing a Multiskan Ascent device.

## Results

Efficient removal of sulfonamides was achieved at 1.5 kGy absorbed dose. Readily biodegradable products can be attained at higher doses (1.5-2.5 kGy) both in river water and activated sludge. The  $\text{BOD}_5\text{COD}^{-1}$  ratios of the solutions in the activated sludge experiments displayed a shift to higher values as compared to results obtained in river water. There are significantly smaller amounts of bacterial species and lower microbial abundance in river water. Therefore, the low incidence of compatible enzyme producers prolonged the adaptation/acclimatization of the microbes. The ecotoxicity was dependent on both test organisms and the type of antibiotics used. Complete removal of toxic effects in the case of some sulfonamides required doses higher than 2.5 kGy at the concentration used. In respiration inhibition tests, the initial sulfonamides did not inhibit the metabolic activity of activated sludge and even co-metabolism was observed in the case of untreated SMX in the presence of a growth substrate (sodium acetate). Antibacterial activity was removed in parallel with the elimination of initial molecules. The strong correlation between concentration reduction of the parent molecule and the disappearance of antibacterial activity implies the formation of radiolytic products with no antibacterial potency in the case of SMX. [1]

Ionizing radiation treatment proved to be a suitable technique for eliminating the environmental risk of sulfonamide antibiotics. The results also showed that degradation of initial molecules is not always enough to eliminate harmful effects. For this reason, a complex biological assessment of treated solutions has to play an important role in the development and optimization of advanced treatment techniques.

## Related publication

- [1] Gy. Sági, A. Bezsenyi, K. Kovács, S. Klátyik, B. Darvas, A. Székács, C. Mohácsi-Farkas, E. Takács, L. Wojnárovits: Radiolysis of sulfonamide antibiotics in aqueous solution: Degradation efficiency and assessment of antibacterial activity, toxicity and biodegradability of products, *Science of the Total Environment* **622-623**, 1009-1015 (2018)

# SYNTHESIS OF CELLULOSE DERIVATIVE/CLAY COMPOSITE SUPERABSORBENTS BY GAMMA-IRRADIATION

Tamás Fekete, Erzsébet Takács, László Wojnárovits, Tünde Tóth, Szabina Papné Góger

## Objective

The aim of our work is the modification of the properties of cellulose derivative-based superabsorbents by the preparation of various copolymer and composite hydrogels. In the past we investigated the effect of the partial replacement of the cellulose derivative with natural or synthetic polymers. In the current work we examined the potential improvement of the gel properties by the addition of clay particles, which might allow the preparation of low-cost superabsorbents. As the composition has a large impact on the gelling behaviour, the effect of the clay component on the dependence of the gel properties on various synthesis parameters was investigated. The effect of the organic surface modification of the clay component on the gelation was also examined by using commercially available modified clays. The dependence of the gel properties on various synthesis parameters such as the absorbed dose and the solute concentration was also investigated for different clay contents.

## Methods

Aqueous mixtures of different types of clay and cellulose derivatives were prepared. Hydroxyethylcellulose (HEC) and carboxymethylcellulose were used as the polymer component, while native and organically modified montmorillonite clay was chosen as the inorganic additive. *N,N'*-methylenebisacrylamide crosslinking agent was also added in low concentrations to improve the gelling behaviour. The crosslinking of the aqueous mixtures was carried out by gamma irradiation. The swelling behaviour and the gel fraction were determined for the prepared gels, and their morphology and chemical composition were also characterized.

## Results

Cellulose derivative/clay mixtures required significantly higher solute concentrations for the gelation compared to the pure cellulose derivative solutions. While cellulose derivative/clay nanocomposites could be synthesized without the use of a crosslinking agent, not only higher dose and solute concentration was required, but relatively low swelling could be achieved for macroscopically stable gels. The gelation improved significantly in the presence of the cross linker; it allowed the use of mild synthesis conditions even in very low concentrations (0.5 w/w<sub>polymer</sub>% or less). The partial replacement of the cellulose derivative with natural montmorillonite clay powder led to the improvement of the swelling capacity (especially for hydroxyethylcellulose-based systems), while the increase in the gel fraction also became smaller. However, at higher clay content the gel fraction actually decreased, unless significantly higher solute concentrations were utilized. The organic modification of the clay also had an impact on the gel properties. The gelling behaviour was similar to that of the natural montmorillonite, leading to a similar gel fraction, but due to the organophilic clay surface the degree of swelling decreased. While the decrease in the swelling due to the high clay content or the surface modification of the clay may make them less suitable as superabsorbents, preliminary experiments showed that such systems may have high potential as adsorbents in the water treatment (Figure 1).

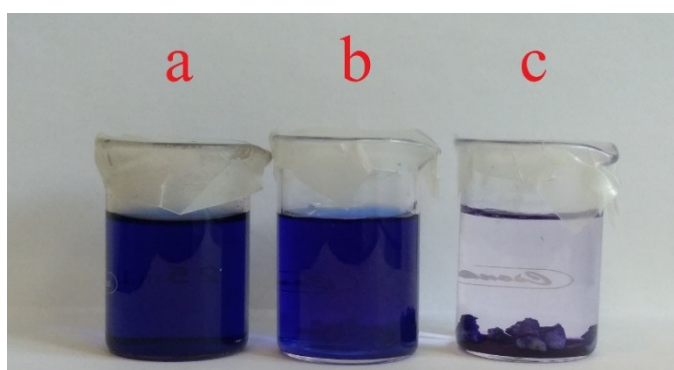


Figure 1: Comparison of the adsorption of toluidine blue dye from an aqueous solution by cellulose-based hydrogels: (a) no hydrogel, (b) pure HEC and (c) HEC/Montmorillonite composite hydrogel

## Remaining work

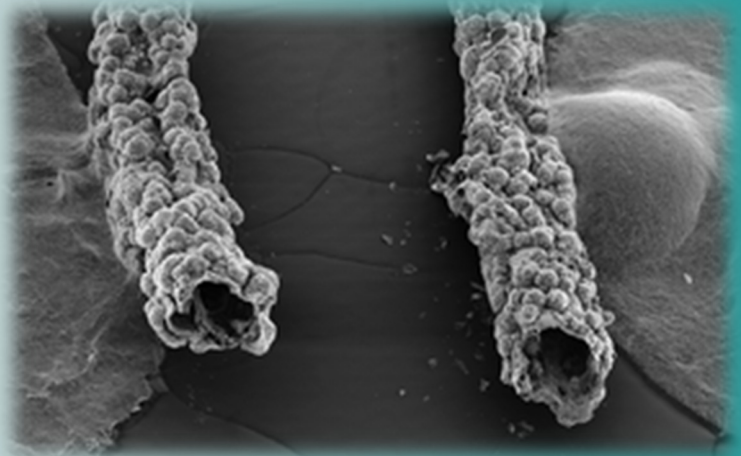
In the future the potential application of the prepared composite superabsorbents needs to be investigated in depth, especially regarding their use as adsorbents, such as the determination of the adsorption isotherms and the effect of the clay type on the adsorption efficiency for different types of pollutants.

## Related publication

- [1] T. Fekete and J. Borsa: *Polysaccharide-based polymer gels*, In: Thakur, V.K., Thakur, M.K. (eds.): *Polymer Gels: Science and Fundamentals*, 147-229, Springer Singapore (2018)



## V. NUCLEAR ANALYSIS AND CHEMISTRY



# COORDINATED RESEARCH PROJECT ON PHOTONUCLEAR DATA AND PHOTON STRENGTH FUNCTIONS

*Tamás Belgya and László Szentmiklósi*

## Objective

The main goals of this IAEA Coordinated Research Project (CRP) are to update the Photonuclear Data Library (1999) and to generate a Reference Database for Photon Strength Functions (PSF).

## Methods

Additional measurements to the  $^{242}\text{Pu}(n,\gamma)^{243}\text{Pu}$  reaction to subtract background from the target backing of Al and the Ti layer covering the Pu target. Analysis and unfolding of  $^{243}\text{Pu}$ ,  $^{73}\text{Ge}$  and  $^{74}\text{Ge}$  spectra. Modelling of  $\gamma$ -ray spectra with a Photon Strength Function (PSF) calculated using the Quasiparticle Random Phase Approximation and Nuclear Level Density (NLD) data.

## Results

Using an internal calibration, the spectra of partial gamma-ray production cross sections were obtained. Then, with the energy weighted sum rule,  $\sigma_0 = \sum_{E_i}^{B_n} E_i \sigma_{\gamma,i} / B_n$ , the thermal capture cross section  $\sigma_0$  was determined for the target nucleus. Here,  $B_n$  is the binding energy of the daughter nucleus,  $E_i$  is the gamma-ray energy and  $\sigma_{\gamma,i}$  is the partial  $\gamma$ -ray production cross section. The  $\gamma$ -multiplicity  $M$  was calculated by dividing the sum of the partial cross sections by  $\sigma_0$ . In Table 1., the experimental capture cross section and multiplicity values are given, which are important indicators of the model validity.

Table 1. Measured and literature data

Target	$\sigma_0$ (b) this work	$\sigma_0$ (b) literature	Daughter	Multiplicity this work
$^{72}\text{Ge}$	1.13(6)	0.9(1)	$^{73}\text{Ge}$	3.0(2)
$^{73}\text{Ge}$	18.7(5)	14.7(4)	$^{74}\text{Ge}$	5.1(1)
$^{77}\text{Se}$	36(4)	42(4)	$^{78}\text{Se}$	3.6(2)
$^{113}\text{Cd}$	21660(360)	20615(400)	$^{114}\text{Cd}$	4.1(1)
$^{242}\text{Pu}$	18.2(6)	18.5(5)	$^{243}\text{Pu}$	3.9(4)

For the validation of the recommended microscopic QRPA (quasiparticle random-phase approximation), a simulation was performed with the BITS (Bin Type Statistical simulation) program to describe the low-lying decay-scheme intensities and the decay gamma-ray spectra. The input level density data table were obtained from Stephan Goriley. The agreement between the simulation based on the QRPA model and the experimental spectra are rather good.

In cases where two possible capture spins can be excited, the contribution weights can be obtained from the evaluated capture cross section from the EXFOR database. Adding them up by weighting with these values gives the final result. For example, in the case of  $^{113}\text{Cd}$  neutron capture mainly influenced by the first strong  $1^+$  resonance makes an almost 100% contribution to the capture cross section. This we see from the almost complete agreement of the calculated and experimental running sum of decay probabilities for the  $1^+$  capture, while for  $0^+$  it is not agreeing [1].

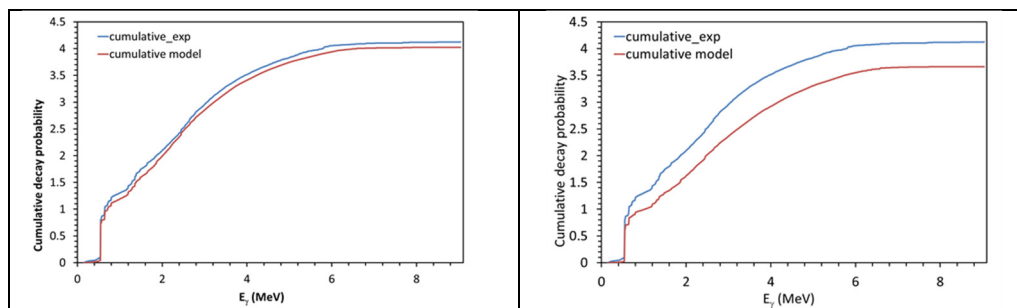


Figure 1: The calculated and measured cumulative sum of decay probability for pure  $1^+$  (left) and  $0^+$  (right) capture states in  $^{114}\text{Cd}$ . The calculated multiplicity is  $M = 4.02$  (left) and  $M = 3.66$  (right).

## Remaining work

Preparing publications on modelling of unfolded radiative neutron capture spectra.

## Related publication

[1] [https://www-nds.iaea.org/CRP-photonuclear/index\\_3RCM.html](https://www-nds.iaea.org/CRP-photonuclear/index_3RCM.html)

# STABILITY OF ALL-INORGANIC PEROVSKITE NANOCRYSTALS

Dániel P. Szekrényes, Szilárd Pothorszky, Dániel Zámbo, Dávid Srankó, Ferenc Somodi, Andrea Beck, György Sáfrán, András Deák

## Objective

Although all-inorganic perovskite ionic nanocrystals (e.g. CsPbBr<sub>3</sub>, as used in the present work) have promising optical properties, they suffer from instability issues related to the dynamic nature of stabilizing ligand shells. This is in contrast to classical quantum dot systems, where stable particle cores and covalently attached ligands provide sufficient long-term stability for advanced applications. The aim of the current research is to investigate the stability of the all-inorganic nanocrystals from the colloid chemical and optical points of view, using (i) modification of the ligand shell and (ii) incorporation into polymer matrices.

## Methods

CsPbBr<sub>3</sub> nanoparticles have been prepared based on literature protocols. During the co-precipitation of the Cs- and Pb-oleate precursors in toluene with tetraoctylammonium bromide (TOAB), vortex mixing was used to obtain nanoparticle sols typically on the ml scale. Two main approaches have been used to improve nanoparticle stability: stabilization of the particle's surface by introducing inorganic-organic ion pairs and incorporation of the nanoparticles in optically inert polymer films (polystyrene and Zeonor®). The former was achieved by phase transferring sulphur ions from an aqueous Na<sub>2</sub>S solution into toluene using TOAB. The latter was performed by spin-coating the mixture of nanoparticles and the respective polymer solution on glass substrates. The samples were characterized using dynamic light scattering (DLS - Malvern Zetasizer NanoZS), transmission electron microscopy (300kV JEOL JEM 3010) and a laboratory-built photoluminescence (PL) spectrometer ( $\lambda_{exc}=443\pm 6$  nm; filtered from a 150W Xe-lamp, detector: Thorlabs fibre coupled spectrometer).

## Results

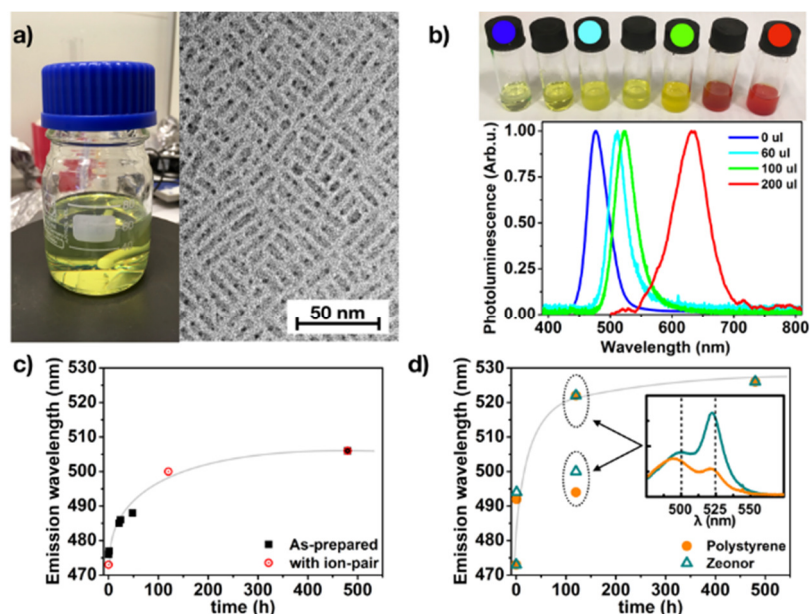


Figure 3: (a) Scaled-up particle synthesis results; (b) emission spectrum tuning with 50 mM tetrabutylammonium iodide; (c) aging (emission peak wavelength change) of the as-prepared particles in solution and (d) embedded in polymer films (inset shows the two PL emission peaks)

confinement as the particles are transformed from platelets to cubes at room temperature. The sulphur ions apparently have no significant impact on the kinetics of the process, as the points follow the same trend.

However, when the particles are embedded in a polymer matrix and the toluene solvent removed (oleic acid does not evaporate), two main differences can be observed (Fig. 1d). The emission wavelength is increasing faster compared to the solution values and its final value is also higher. Additionally, at an intermediate time (120 h) a splitting of the emission peak can be observed (see inset and the corresponding points marked by arrows). In solution, particle reshaping is competing with the partial formation of a non-fluorescent precipitate (presumably PbBr<sub>2</sub>) over long time scales, which reduces the actual particle size resulting in a bluer shifted emission. In the polymer film, however, the reduced mobility of the particles and ions presumably allows for a shape transformation with no, or much lower size reduction and particle loss, resulting in (i) more redshifted emission and (ii) the simultaneous presence of several particle populations.

## Remaining work

Work is currently in progress to compare the data to results obtained in the case of preparation under an inert atmosphere and to perform excitation-power dependent micro-PL measurements on the polymer embedded particles.

The nanoparticle synthesis has been scaled up to produce a few tens of millilitres which contains mainly nanoplatelets of 4-unit cell thickness (Fig.1a). The emission properties of the as-prepared nanoparticles could be tuned by introducing various amounts of iodide ions (Fig. 1b). Besides the successful emission tuning, the colloidal stability of the system was reduced strongly, and the particles precipitated with a gradual loss of PL intensity.

The introduction of sulphur ions has an ambiguous impact. It influences the particle size, which is slightly larger (11-12 nm) compared to the as-prepared particles (9 nm). However, it decreases the colloidal stability, leading to an increased amount of sediment upon centrifuging. Nevertheless, samples treated by S<sup>2-</sup> are optically more stable. They retain their PL emission upon acetone addition, whereas as-prepared samples lose most of their PL after 1 day.

The change of the emission wavelength of the particles that remained stable in solution (Fig.1c) indicates the changing quantum

# STRUCTURAL CHARACTERISATION AND BIOCOMPATIBILITY OF PHOSPHATE BASED GLASSES FOR BIOMEDICAL APPLICATION

Margit Fábíán, Viktória Kovács Kis, Csaba Araczkai, Zsolt Dallos

## Objective

Biomaterials are artificial or natural materials that are used to replace lost or diseased tissue and to restore form and function. Thus, the field of biomaterials has become an imperative area, as these materials are helpful in improvement of the quality and the longevity of human life. Our work focuses on the development of phosphate glasses and aims to find out the structural properties and biocompatibility of these glasses.

## Methods

Samples were prepared by melt-quench technique, from reagent grade powders ( $\text{SiO}_2$ ,  $\text{Na}_2\text{O}$ ,  $\text{CaO}$ ,  $\text{P}_2\text{O}_5$ ) melted in a Pt crucible. For the study of the short and intermediate range order neutron diffraction (ND) experiments were carried out using the neutron diffractometers at the 10 MW Budapest research reactor and at the 7C2 diffractometer in Saclay. Reverse Monte Carlo (RMC) simulation was applied to generate reliable 3-dimensional atomic configurations and to calculate the partial atomic pair correlation functions, coordination number and bond angle distributions. The glasses were analysed using Stokes Raman spectra, measured at 514.5 nm Argon ion laser on Renishaw in Via-Reflex Micro-Raman spectrometer. Nuclear Magnetic Resonance (NMR) experiments were recorded on the 600 MHz Varian NMR System installed in the Slovenian NMR Centre in Ljubljana. Bioactivity was studied *in vitro* using simulated body fluid (SBF). Bioactivity tests were performed at 37°C and 5%  $p(\text{CO}_2)$ .

## Results

Bioactive glasses have been prepared by melt-quench technique in the compositional range  $\text{SiO}_2(45)\text{CaO}(25)\text{Na}_2\text{O}(30-x)\text{P}_2\text{O}_5(x)$ ,  $x=0, 1, 3, 5$ ; signed with S45, S45P1, S45P3, S45P5, respectively.

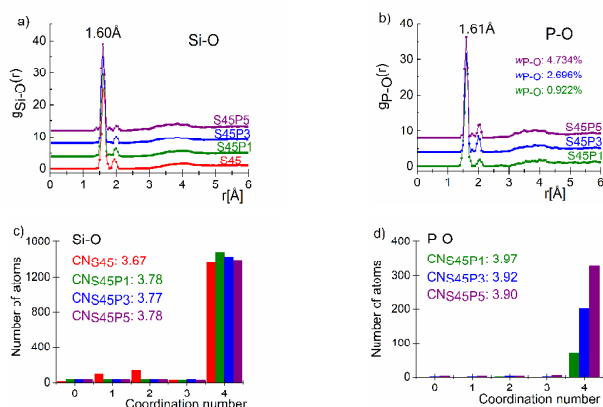


Fig 1: Si-O and P-O partial pair correlation functions and coordination number distributions calculated by RMC modelling

The RMC calculation based on ND data show well-defined first neighbour distances for Si-O at 1.60 Å (Fig 1a), P-O at 1.61 Å (Fig 1b), Ca-O at 2.35(55) Å and Na-O at 2.25(56) Å distributions. The average coordination number distribution shows that Si atoms are surrounded by 4 oxygen atoms (Fig 1c). RMC calculations have revealed that for all studied glassy compositions the P atoms are 4-fold coordinated by oxygen atoms (Fig 1d). These findings suggest that the network consists of  $\text{SiO}_4$  and  $\text{PO}_4$  units, which are supported by the bond angle distributions.

The  $^{29}\text{Si}$  NMR spectrum of glassy Si displays a single broad resonance centred at -77, -79, -81 ppm for S45P1, S45P3 and S45P5, respectively, that corresponds to the  $^{[4]}\text{Q}$  and  $^{[3]}\text{Q}$  Si environment, consistently with literature reports. The  $^{31}\text{P}$  NMR resonances came at 9.88, 9.15 and 8.12 ppm for S45P1, S45P3 and S45P5, respectively. These positions are specific for the P-Ca(Na) complexes, example  $\text{Ca}_2\text{P}_2\text{O}_7$ ,  $\text{Na}_4\text{P}_2\text{O}_7$ ,  $\text{Na}_3\text{PO}_4$ ,  $\text{Ca}_3(\text{PO}_4)_2$ . From NMR data the signs of the Si-O-P connections are missing. All Raman spectra contain two strong band centred near  $\sim 635\text{ cm}^{-1}$  and  $\sim 945 - 1080\text{ cm}^{-1}$  that can readily be assigned to the Si-O-Si; Si-O<sub>NBO</sub> and to the  $[\text{PO}_4]^{3-}$ ;  $[\text{P}_2\text{O}_7]^{2-}$ , respectively. From Raman analysis we detect the presence of non-bridging silicon-oxygen groups and changes in the inter-tetrahedral Si-O-Si bond environment. The concentration of non-bridging oxygens is increasing in  $\text{SiO}_4$  units with  $\text{P}_2\text{O}_5$  increase, it is surprising that even 1mol% can make difference. It has been found that the intensity and the frequency of the Raman lines depend on the concentration of the alkali and alkali-earth oxides in the bioactive glass.

To test the biocompatibility of the glasses, samples have been treated in SBF for different soaking times (3h, 3days, 7days, 21 days). After three hours all P containing samples exhibited a Ca and P rich layer on their surface. The hydroxyapatite layer was detected, which supports the biocompatibility of the glasses.

## Remaining work

Characterization of the bioactive layer as a function of composition and soaking time in comparison to the bone mineral component. The synchrotron X-ray diffraction measurements are under evaluation.

## Related publications

- [1] M. Fábíán, V.K. Kis: *Neutron diffraction and Raman spectroscopic study of bioactive silica based glasses*, American Neutron Scattering Conference, lecture, 24-28 June, 2018, Maryland, USA
- [2] M. Fábíán, V.K. Kis: *Bioactive glasses: structure characteristics and bone regeneration application*, 20<sup>th</sup> International School and Conference on Condensed Matter Physics, invited lecture, 3-7 September, 2018, Varna, Bulgaria
- [3] M. Fábíán et al. *The effect of phosphate on short-range order of sodium glasses*, under submission (2018)

# APPLICATIONS OF NUCLEAR ANALYTICAL TECHNIQUES

*Zsolt Kasztovszky, László Szentmiklósi, Boglárka Maróti, Ildikó Harsányi,  
Zoltán Kis, Veronika Szilágyi, Katalin Gméling*

## Objective

Elemental composition measurement using prompt-gamma activation analysis (PGAA) and instrumental neutron activation analysis (NAA). The compositional data measured here are easily applicable to catalysis, material science, geochemistry and heritage science. The access of non-Hungarian users to the instruments has been supported by transnational access programs, including CERIC-ERIC and H2020 IPERION CH.

## Methods

PGAA with cold neutrons has been applied in combination with NAA and portable X-ray fluorescence analysis (XRF) to measure major, minor and trace components of the samples, benefiting from the complementarities of these methods.

## Results

### *Heritage Science (Archaeometry)*

- The compositions of polished stone axes made from metamorphic rocks have been measured: a set of nephrite, serpentinite, metaandesite, blueschist, etc. archaeological and geological samples have been analysed. The objects were obtained from Hungarian museums, and from international collaborations, whereas the raw materials have been collected by fieldwork. The aim of the study is to identify the origin of the raw materials (i.e. the provenance of the objects). With the help of the PGAA method, certain rocks have been classified more precisely, and the possible places of origin of raw materials have been confined to a well-defined region. Three manuscripts have been published to summarize the results about stone tools made of high pressure metamorphic rocks [1, 2, 3]. An overview publication was also published about the applicability of the neutron techniques in the provenance research of archaeological stone objects [4].
- In collaboration with domestic user groups (Lendület, OTKA, “Bakota”), different historical bronze objects, such as axes, a spearhead, and decorative spirals were analysed by PGAA and pXRF to determine their chemical compositions [5]. Additional information was obtained using neutron radiography. Based on the results (e.g. the Sn, As and Ni content), conclusions regarding the production technique could be drawn.
- By far the most valuable cultural object that has been analysed by neutron methods at BNC is a bronze sculpture “The Budapest Horse and Rider” attributed to Leonardo da Vinci. The aim of the PGAA in this study was to confirm if the rider, the horse and its tail were cast with the same technique from the same raw material, and to determine the composition of the filling material identified earlier by non-invasive imaging. The various pieces of evidence point towards the conclusion that the sculpture was indeed made by da Vinci. The sculpture became the highlight of the re-opening ceremony at the recently renovated Museum of Fine Arts [6].
- A promotion video was made available on-line about the cultural-related activities of the Laboratory. A case study on a bronze spearhead of the Hungarian National Museum was presented and the synergetic use of multiple techniques was demonstrated [7].

### *Geology and Environmental research*

- Our laboratory, with PGAA and NAA measurements, took part in the IAEA organized inter-laboratory comparison studies of WEPAL (i.e. *Wageningen Evaluating Programs for Analytical Laboratories*), soil (ISE - *International Soil-Analytical Exchange*) and plant (IPE - *International Plant-Analytical Exchange*) samples with excellent results in the comparison to the reference data and to the results of other participating laboratories [8]. The NAA-PGAA e-learning tool is also being upgraded with the involvement of our staff members.
- A pilot study on 3 fossilized echinoids (sea urchins from the Middle Miocene) has been done at the NIPS-NORMA station. Neutron tomography, as well as bulk PGAA of a restricted volume within the investigated specimens is expected to provide compositional information both on the calcium carbonate shell and the inner part (stomach, divided into five parts) of the sea urchins. Such information could help ecologists and marine biologists to reconstruct the ancient palaeo-environment. 3D structure light scanning was also accomplished to accurately determine their dimensions and provide photorealistic appearance of the dataset obtained by neutron tomography.

### *Chemistry and Material science*

- Alkane oxyhalogenation attracts increasing attention as an alternative route for natural gas upgrading. Operando prompt gamma activation analysis, which correlated catalyst performance and surface halogen uptake, was applied along with of operando photoelectron photo ion coincidence spectroscopy and density functional theory. We have found that ethyl halide generation occurs on the catalyst surface in oxychlorination, while it primarily follows a gas-phase

radical-chain mechanism in oxybromination. Finally, dehydrohalogenation of the ethyl halide intermediate was favoured on a chlorinated surface, while in oxybromination, Br• radicals evolution led to polybromination, rationalizing the mechanistic difference that results in the observed selectivity trends [9].

### Remaining work

We will continue the applications of PGAA and NAA in thematic research projects and also in international TNA (Technology needs assessment) projects (IPERION CH, C-ERIC).

### Related publications

- [1] Zs. Bendó, Gy. Szakmány, Zs. Kasztovszky, K. T. Biró, I. Oláh, A. Osztás, I. Harsányi, V. Szilágyi: *High pressure metaophiolite polished stone implements found in Hungary*, *Archaeological and Anthropological Sciences* (2018) p 1-25 <https://doi.org/10.1007/s12520-018-0618-6>
- [2] E. Kereskényi, Gy. Szakmány, B. Fehér, Zs. Kasztovszky, F. Kristály, P. Rózsa: *New archaeometrical results related to Neolithic blueschist stone tools from Borsod-Abaúj-Zemplén County, Hungary*. *Journal of Archaeological Science: Reports*, **17**, 581-596 (2018)
- [3] F. Bernardini, E. Sibilía, Zs. Kasztovszky, F. Boscutti, A. De Min, D. Lenaz, G. Turco, R. Micheli, C. Tuniz, M. Montagnari Kokelj.: *Evidence of open-air late prehistoric occupation in the Trieste area (north-eastern Italy): dating, 3D clay plaster characterization and obsidian provenancing*, *Archaeological and Anthropological Sciences* (2018) 1-13, DOI 10.1007/s12520-017-0504-7
- [4] K. T. Biró; Zs. Kasztovszky: *Stone artefacts and neutrons - Case studies from Hungary*, *Journal of Archaeological Science: Reports* **19**, 669-673 (2018)
- [5] B. Maróti, I. Harsányi, Zs. Kasztovszky: *Non-destructive analysis of bronze objects from Füzesabony-Öregdomb*, *Communicationes Archaeologicae Hungariae* 81-84. (2018)
- [6] [https://www.szepmuveszeti.hu/kiallitasok/leonardo\\_budapesti\\_lovas/](https://www.szepmuveszeti.hu/kiallitasok/leonardo_budapesti_lovas/)
- [7] <https://youtu.be/rkipBjVzw8w>
- [8] Report of the Training Workshop on Intercomparison Feedback of Neutron Activation Analysis Proficiency Tests Performed in 2017. Ljubljana, Slovenia 6 – 10 November 2017. Ref. No: T3-TR-1700340 Implemented under the IAEA projects: NA-RB-1.4.2.1, TC-RAF1005 and TC-RER1016
- [9] G. Zichittella, M. Scharfe, B. Puértolas, V. Paunović, P. Hemberger, A. Bödi, L. Szentmiklósi, N. López, and J. Pérez-Ramírez: *Halogen-Dependent Surface Confinement Governs Selective Alkane Functionalization to Olefins*, submitted to *Angewandte Chemie*.

# DEVELOPMENT OF NUCLEAR ANALYTICAL TECHNIQUES, NUCLEAR DATA MEASUREMENTS & DISSEMINATION ACTIVITIES

László Szentmiklósi, Boglárka Maróti, Zoltán Kis, Tamás Belgya

## Objective

To develop our analytical capabilities and know-how in Prompt-Gamma Activation Analysis (PGAA) and Imaging (PGAI), to accurately determine related nuclear data, and to provide training and education for guest researchers and students

## Methods

The methods used were (n, $\gamma$ ) measurements, PGAA, PGAI-NT, evaluation of nuclear data and comparison to literature, computer programming, Monte Carlo modelling, teaching.

## Results

Within the framework of the OTKA Grant No. K124068 project we developed the Monte Carlo models of the PGAA and NIPS experimental setups using the recently released software package MCNP 6.2. The *geant4* implementation of the PGAA station is complete, while that for NIPS-NORMA is in progress. The ENDF/B-VIII.0 nuclear data library was used within both programs to avoid the bias due to differences in input parameters. The performances of the two software packages are being evaluated for prompt-gamma spectrometry as well as for neutron imaging.

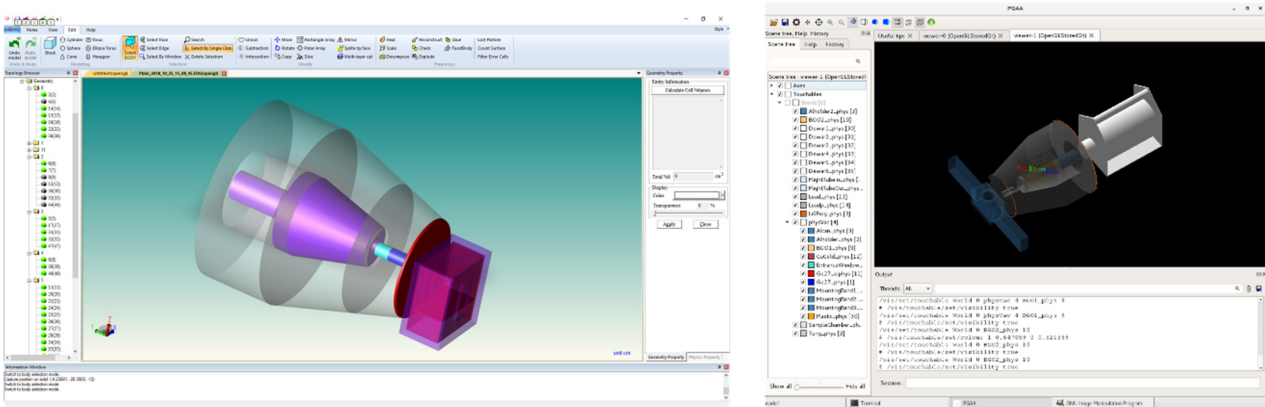


Figure 1: The MCNP 6.2/*geant4* models of the Budapest PGAA facility

We worked out two approaches, the voxel-wise 3D discretization, and the mesh-based geometry approach, to load sample geometries to the simulation environments. Voxel data can be directly taken from tomography after proper pixel binning, while the 3D meshes could be obtained either using a RangeVision SMART 3D structured-light scanner or from the advanced surface determination algorithm applied on segmented neutron/X-ray tomography data using the VG Studio MAX software.

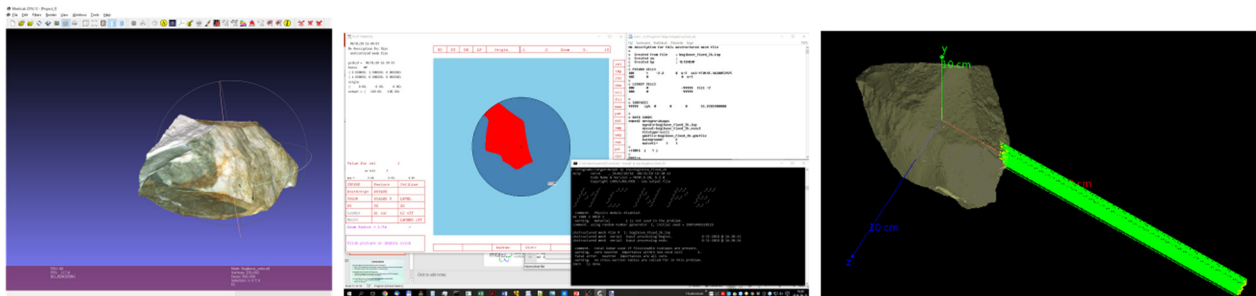


Figure 2: Photorealistic 3D-scanned model, and the MCNP 6.2/*geant4* representations of a gray flint stone sample

Simulations for self-attenuation and self-absorption beyond the present state-of-the-art are being developed to improve our analysis capabilities for irregularly shaped or structured objects. Experiments were carried out with the cold and thermal (polychromatic) neutron beams at PGAA to measure the neutron and gamma attenuation of layered structures. Combinations of metal foil pairs, as well as 3D assemblies of 7-mm unit cubes made of Cu, Sn, Fe, Pb, PTFE, and clay were used in the experiments to form the dataset to validate the Monte Carlo calculations. The X-ray emission spectrum of our X-ray generator was estimated with the SpekCalc software.

Using 3D additive manufacturing technology (a.k.a. 3-D printing), plastic replicas of complex-shaped objects as well as ad-hoc sample holders were fabricated [1,2], in collaboration with J. Janik, Reactor Department.

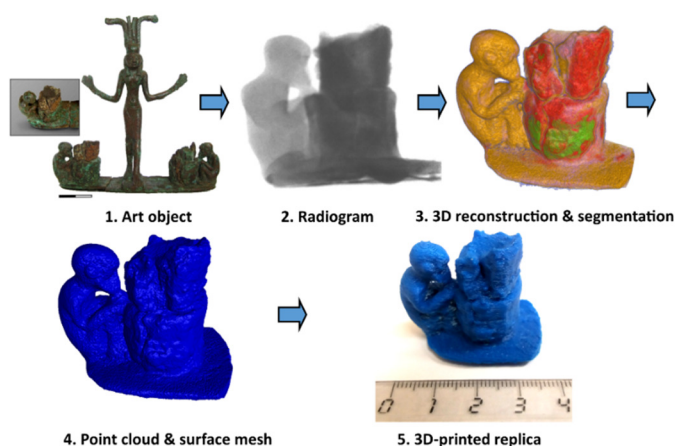


Figure 3: Steps to create a plastic replica of an analyzed object based on segmented neutron tomograms [1]

The analytical merits of PGAA, in-beam NAA, reactor-NAA and handheld XRF were compared on bronze alloys. A recommended analytical workflow was established to non-destructively characterize these alloys [3]. Neutron imaging was shown to be essential in the analysis of heterogeneous samples to complement the surface and bulk analytical results with 3D visual information. The conclusions were included in a PhD dissertation, which has been defended at the Hevesy György PhD School of Chemistry of the Eötvös Loránd University [4].

Data from two of last year's nuclear physics experiments were processed and papers were submitted for publication. To search for the bound deuteron singlet state, a radiative neutron capture experiment on hydrogen was made. The existence of the bound state singlet deuteron might have been evidenced by a two-step gamma-ray transition at about  $\sim 100$  keV below the primary gamma ray energy of 2223 keV. Even from a long measurement, we found no evidence for the two-photon transition in the region 2100-2210 keV, so an upper limit in the branching ratio  $R < 6 \times 10^{-6}$  or in cross section  $\sigma < 2 \mu\text{b}$  (two standard deviations uncertainty) was set, being an order of magnitude less than earlier measurements indicated.

Partial gamma-ray production cross sections from thermal neutron-capture were measured for the  $^{139}\text{La}(n,\gamma)$  reaction with a thick and a thin  $^{\text{nat}}\text{La}_2\text{O}_3$  target [6]. Here we successfully assessed the self-absorption difference of the two targets using the equivalent thickness approach. Absolute  $^{140}\text{La}$  cross sections were determined relative to the well-known comparator  $^{35}\text{Cl}(n,\gamma)$  cross sections from the irradiation of a stoichiometric  $^{\text{nat}}\text{LaCl}_3$  sample. The total cross section for radiative thermal neutron-capture on  $^{139}\text{La}$  was determined to be 8.58 (50) barns from the sum of experimentally measured cross sections observed to directly feed the  $^{140}\text{La}$  ground state.

### Education and dissemination activities

- The neutron-energy-distribution of the RAD facility was determined, based on the activation-foil approach, with the involvement of a summer-student, Guilhem Paradol, from Univ. of Grenoble, France (mentored by T. Belgya).
- A PhD course at Eötvös University, 'Nuclear Analytical Methods and their Application in Earth Sciences and Archaeometry I-II.' was taught.
- Lectures and hands-on training at the Central European Training School on Neutron Techniques 2018
- PGAA laboratory training for BME and ELTE students

### Related publications

- [1] L. Szentmiklósi, B. Maróti, Z. Kis, Z. Kasztovszky: *Integration of neutron-based elemental analysis and imaging methods and applications to cultural heritage research*, J. Archaeol. Sci. Reports. **20**, 476–482 (2018)
- [2] L. Szentmiklósi, B. Maróti, Z. Kis, J. Janik, L. Z. Horváth: *Use of 3D mesh geometries and additive manufacturing in neutron beam experiments*, J. Radioanal. Nucl. Chem. (2019) DOI: 10.1007/s10967-019-06482-0
- [3] B. Maróti, Z. Révay, L. Szentmiklósi, K. Kleszcz, D. Párkányi, T. Belgya: *Benchmarking PGAA, in-beam NAA, reactor-NAA and handheld XRF spectrometry for the element analysis of archeological bronzes*, J. Radioanal. Nucl. Chem. **317**(2), 1151-1163 (2018)
- [4] B. Maróti: *Non-destructive analysis of metals and alloys using prompt gamma activation analysis and complementary methods*, PhD dissertation, Eötvös Loránd University, Hevesy György PhD School of Chemistry, DOI: 10.15476/ELTE.2018.146
- [5] T. Belgya, S. B. Borzakov, M. Jentschel, B. Maróti, Y. N. Pokotilovski, L. Szentmiklósi: *Experimental search for the bound state singlet deuteron in the radiative  $n - p$  capture*, ArXiv. 1809.00680 (2018) 1–10.
- [6] A. M. Hurst, A. Ureche, B. L. Goldblum, R. B. Firestone, M. S. Basunia, L. A. Bernstein, Zs. Révay, L. Szentmiklósi, T. Belgya, J. E. Escher, I. Harsányi, M. Krticka, B.W. Sleaford, and J. Vujic: *Radiative-capture cross sections for the  $^{139}\text{La}(n,\gamma)$  reaction using thermal neutrons and structural properties of  $^{140}\text{La}$* , Phys. Rev. C, Phys. Rev. C **99**, 024310 (2019)

# VALENCY STATES OF IRON AS PROBED BY MÖSSBAUER SPECTROSCOPY

Károly Lázár, Sándor Stichleutner, Zoltán Klencsár

## Objective

Iron is an important constituent in various systems and identification of its valency ( $\text{Fe}^{3+}$ ,  $\text{Fe}^{2+}$  or  $\text{Fe}^0$ ) is essential for interpreting the observed properties. Recently, iron-based magnetic silica/polymer nanocomposites used for targeted drug delivery and conversions of different iron compounds in a process applied for separate recovery of Zn and Fe from  $\text{ZnFe}_2\text{O}_4$  galvanization sludge as well as formation and stabilization of various iron alloys and compounds during electric explosion of wires in various liquid media were studied.

## Methods

$^{57}\text{Fe}$  transmission Mössbauer spectroscopy was applied principally, amended with other appropriate techniques.

## Results

Magnetic dual drug delivery system was developed for targeted combined administration of anticancer mitoxantrone and anti-inflammatory prednisolone. 100 nm mesoporous silica globules were grown around 10 nm maghemite nucleation cores, and were functionalized with appropriate compounds. Mössbauer spectroscopy revealed the dominance of  $\text{Fe}^{3+}$  state and maghemite structure in the cores of nanoparticles [1].

$(\text{NH}_4)_2\text{Fe}(\text{SO}_4)_2 \cdot 6\text{H}_2\text{O}$  (Mohr's salt) and  $\text{NH}_4\text{Fe}(\text{SO}_4)_2 \cdot 12\text{H}_2\text{O}$  were applied to accomplish separate recovery of iron and zinc from the  $\text{ZnFe}_2\text{O}_4$  component of galvanization sludge. It was demonstrated that the sulphation reaction with ammonium iron sulphates could be performed at lower temperatures than with other iron sulphates used conventionally. Various reaction intermediates were identified by Mössbauer spectroscopy providing means to interpret the conversion processes [2].

Method of electric explosion of wires (EEW) was applied to produce nanoparticles from iron and ASI-304 steel as well as from Kovar alloy wires in various liquid media (water, paraffin oil, ethylene glycol, siloxane). Metallic globules were obtained principally in various size distributions, as expected. However, wide variety of products was also identified which were condensed from reactions of vaporized components formed from both the metal wire and the decomposed liquid medium in a short life-time plasma of the discharge process [3]. Mössbauer spectra provided an appropriate tool to analyse the various the various products (Figure 1).

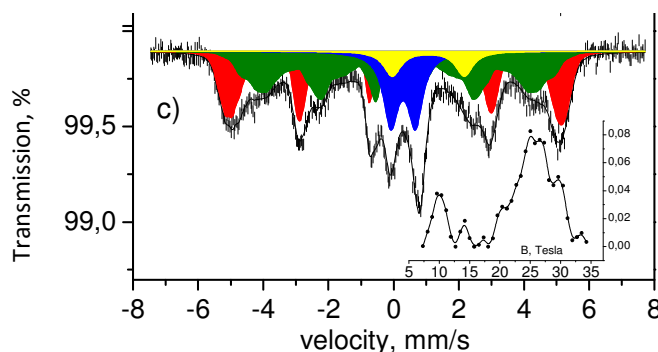


Figure 1:  $^{57}\text{Fe}$  Mössbauer spectrum of products formed in EEW of  $\text{Fe}_{45}\text{Ni}_{26}\text{Co}_{19}$  Kovar alloy in ethylene glycol. Decomposition of spectrum: fcc FeNiCo alloy (red), and carbide component (olive) with distribution of hyperfine fields shown in the inset at the bottom right. Yellow and blue: minor doublets.

## Related publications

- [1] M. Popova, I. Trendafilova, Á. Szegedi, D. Momekova, J. Mihály, G. Momekov, L. F. Kiss, K. Lázár, N. Koseva: *Novel  $\text{SO}_3\text{H}$  functionalized magnetic nanoporous silica/polymer nanocomposite as a carrier in a dual-drug delivery system for anticancer therapy*, *Microporous and Mesoporous Materials* **263**, 96-105 (2018)
- [2] F. Fekete, L. P. Bakos, K. Lázár, A. M. Keszler, A. Jánosity, L. Zhibin, I. Miklós Szilágyi and L. Kótai: *Recycling the industrial waste  $\text{ZnFe}_2\text{O}_4$  from hot-dip galvanization sludge*, *Journal of Thermal Analysis and Calorimetry* **134**, 1863-1872 (2018)
- [3] K. Lázár, L. K. Varga, V. Kovács Kis, T. Fekete, Z. Klencsár, S. Stichleutner, L. Szabó, I. Harsányi: *Electric explosion of steel wires for production of nanoparticles: Reactions with the liquid media*, *Journal of Alloys and Compounds* **763**, 759-770 (2018)

# RADIOGRAPHY AND TOMOGRAPHY AT BRR

Zoltán Kis, László Horváth, László Szentmiklósi

## Objective

To develop and apply imaging instrumentation and methodology at the Budapest Research Reactor (BRR).

## Methods

The development and application of *fast neutron sensitive screens* have been being continued in collaboration with the PSI (Paul Scherrer Inst.), Switzerland and Pennsylvania State University, US. A systematic *investigation of casting defects* for objects and the *systematic study of porous materials* (geology, paleontology, ceramics) were carried out by evaluating tomographic datasets.

## Results

Simple and inexpensive ZnS-based *fast neutron imaging screens* have been developed, and their performance has been compared to a commercially available one at RAD station. The in-house screen produces about 60% of light intensity of the commercial polypropylene/ZnS screen (Fig.1a), which is mainly due to the lower hydrogen density of the optical epoxy compared to polypropylene by the same amount. A spatial resolution of around 1.6 mm has been achieved (Fig.1b). Fast neutron tomography was applied to image an energy storage and *power generation system for planetary exploration missions* with lithium metal as fuel. We measured a 1/3 volume ratio for each burnt, partly burnt and unburnt region. The results have great value for improving and optimizing the future oxidizers. The *casting defects* of a heatsink made of aluminum alloy were detected as shown in Fig.1d. The overall porosity is 0.21%, however, the largest voids are concentrated in a relatively small volume pointing a likely fatigue during the lifetime of the piece. In a pilot study, in cooperation with Wismar University, 3D imaging of the *moisture-dependent spread of injection agents* (synthetic resins) in bricks was evaluated. Such knowledge should be used to mitigate damages of mostly historical buildings because there are no legal standards how to realize functional sealing. In Fig.1e one can see the planar cuts of the bricks after injection showing the spatial distribution of the agent. A clear dependence on the moisture level (90%, 70% and 50%, from right to left) could be detected, and the distribution was compared against the untreated sample (most left). It could be seen that the injection process had a problem in the case of the 70% moisture level. Again, a pilot study was accomplished for the *detection of the salt transport by non-destructive neutron methods* in building materials. Soluble salt is considered as one of the most common causes for decay of building materials. Desalination using poultices relies on the principle that salts dissolved in water are transported from the salt-contaminated, porous, mineral building materials into the poultice. The process of salt transport between a salt-loaded (NaCl) substrate and the poultice was followed by neutron radiography driven PGAI (Prompt-gamma Activation Imaging) measurements. In Fig.1f one can see the temporal behavior of the Cl concentration (upper three curves: poultice, lower five curves: stone) in a four days period.

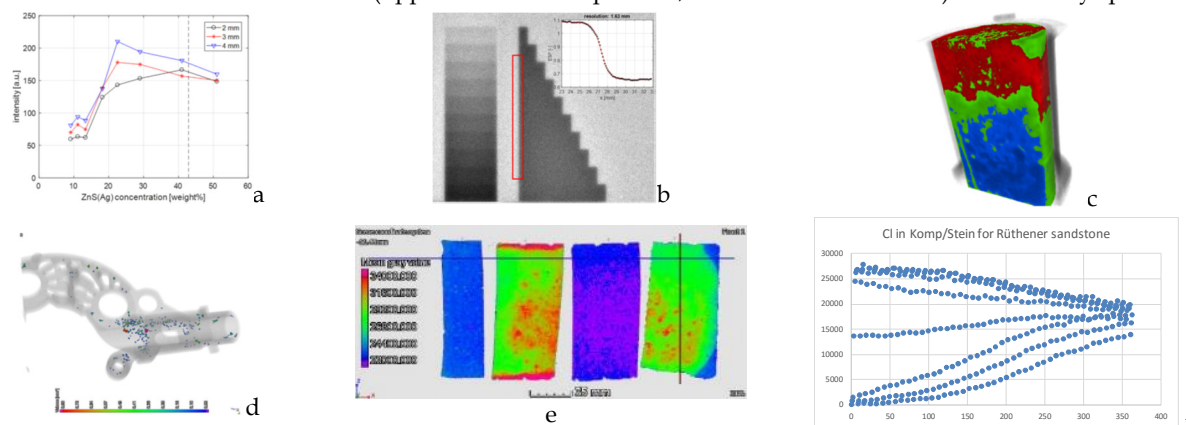


Figure 1: Neutron imaging results: see text for further information

## Related publications

- [1] J. G. Tarbay, B. Maróti, Z. Kis: *Introducing the spear project: The tale of the Late Bronze Age spearhead with wooden shaft from the Marshland of Kikinda, Serbia*. J. Archaeol. Sci. Reports. **21**, 268–274 (2018)
- [2] R. Zboray, R. Adams, Z. Kis: *Scintillator screen development for fast neutron radiography and tomography and its application at the beamline of the 10 MW BNC research reactor*, Appl. Radiat. Isot. **140**, 215–223 (2018)
- [3] L. Szentmiklósi, B. Maróti, Z. Kis, Z. Kasztovszky: *Integration of neutron-based elemental analysis and imaging methods and applications to cultural heritage research*, J. Archaeol. Sci. Reports. **20**, 476–482 (2018)
- [4] Z. Kis, E. Bakonyi: *Neutron Tomography of the Budapest Horse and Rider*, In: Kárpáti, Z. (ed.) *Leonardo da Vinci & the Budapest Horse and Rider*. pp. 191–201. Museum of Fine Arts, Budapest (2018)
- [5] D. Di Martino, M. Bellanova, E. P. Cippo, R. Felicetti, A. Scherillo, J. Kelleher, Z. Kis, G. Gorini: *A neutron diffraction and imaging study of ancient iron tie rods*, J. Instrum. **13**, C05009 (2018)
- [6] V. Crupi, B. Fazio, A. Gessini, Z. Kis, M. F. La Russa, D. Majolino, C. Masciovecchio, M. Ricca, B. Rossi, S. A. Ruffolo, V. Venuti: *TiO<sub>2</sub>-SiO<sub>2</sub>-PDMS nanocomposite coating with self-cleaning effect for stone material: Finding the optimal amount of TiO<sub>2</sub>*, Constr. Build. Mater. **166**, 464–471 (2018)

# PREPARATION AND STUDIES OF POLYSACCHARIDE DERIVATIVE-BASED NANOSTRUCTURES

*Tünde Tóth, Sándor Kurunczi, Tamás Fekete, Róbert Horváth*

## Objective

The aim of our work is to develop superabsorbent nanofibers made from natural resources, namely polysaccharides and their derivatives. Most of the practically applied superabsorbents (acrylate-based gels being the most widely used) are non-biodegradable. Therefore, producing gels with high water uptake made from renewable and biodegradable materials is of great practical importance. Such a renewable source is cellulose, the most abundant renewable material on earth, which can also be easily functionalized for absorption due to its hydroxyl groups. The basic steps we wish to develop are the electrospinning of cellulose derivatives from an aqueous solution using different spinning parameters, the irradiation of the nanofibers for initiating crosslinking by different doses, and the analysis of the products. Another field of our activity is the development of carboxymethyl-dextran (CMD) layers for biosensors and cell adhesion experiments. We focused here on the surface structure of the CMD thin layers and their mechanical characterization by an Atomic force microscope (AFM).

## Methods

The materials used are cellulose based polymers, hydroxyethyl-cellulose (HEC) and carboxymethyl-cellulose (CMC). Both types are strong gel forming materials which could be utilized as superabsorbents after crosslinking. Two types of HEC with different molecular weight (720k and 1300k Da) and one type of CMC (700k Da) were used. Analytical quality, multiple-distilled water was used as the solvent, occasionally in combination with isopropyl alcohol. The electrospinning setup consisted of three primary components, a high voltage power supply, a pump and syringe with a metallic needle, and a grounded collector. The resulting nanofibers were investigated with a scanning electron microscope (SEM). The nanostructure of the CMD layers has been studied by a Nanosurf Flex AFM system.

## Results

The solution concentration of CMC 700 was not high enough for generating the entanglements of macromolecules which is necessary for fibre formation. Since the viscosity of more concentrated solutions was too high for electrospinning, the experiments with CMC 700 were suspended. In the case of HEC 720 and HEC 1300, different spinning parameters were tried (concentration of solution, voltage, needle-collector distance, see Table 1).

Table 1: Conditions used for electrospinning with solutions of HEC 720 and HEC 1300

Sample	Concentration (w/w %)	Voltage (kV)	Spinneret-collector distance (cm)	Sample	Concentration (w/w %)	Voltage (kV)	Spinneret-collector distance (cm)
HEC 720	1,6	20	12	HEC 1300	0,5	35	25
HEC 720	1,6	30	12	HEC 1300	1	35	25
HEC 720	1,6	20	22	HEC 1300	1,5	37,5	25
HEC 720	1,6	30	22	HEC 1300	2	35	25

Solutions of HEC 1300 with a water-isopropyl alcohol solvent mixture (water/isopropyl alcohol ratios were 1:3 and 3:7) were prepared and tested in the electrospinning process. Although during electrospinning it looked like the experiments were successful. SEM investigation showed that electrospinning occurred instead of fibre formation. No fibres, but only small droplets and particles reached the collector, forming spheres with diameters of 1-2  $\mu\text{m}$ .

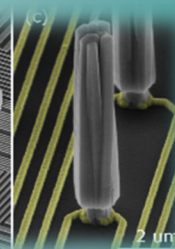
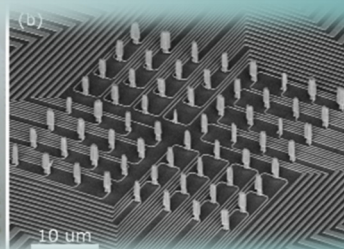
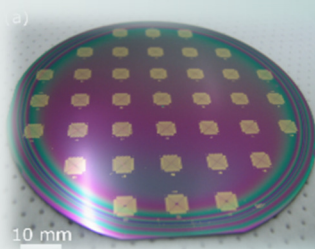
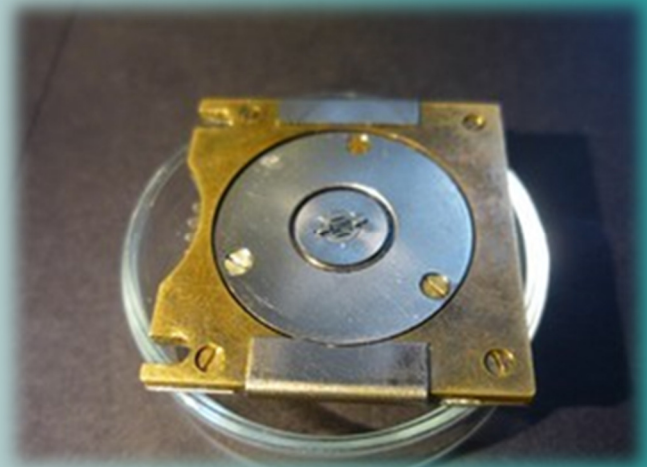
In the biosensor and cell adhesion work, the AFM revealed a homogeneous, smooth surface of CMD layers as prepared by our spin-coating method. The mechanical characterization of these layers (force spectroscopy) showed stiff layers in the dried state, while these dextran layers become fully hydrated in aqueous solution and soft. These soft CMD layers will be used in cell adhesion studies.

## Remaining work

We wish extend the studies with other polysaccharides, characterizing the nanofibers, and finding new materials for the production of crosslinkages in polymers.



## VI. RESEARCH AND DEVELOPMENT IN INSTITUTE OF TECHNICAL PHYSICS AND MATERIAL SCIENCES



# A NEW GENERATION ELECTRON MICROSCOPE FOR THE OPEN LABORATORY OF THE HUNGARIAN MATERIALS SCIENCE

(VEKOP-2.3.3-15-2016-00002)

*Béla Pécz, János Lábár*

A new laboratory with the first spherical aberration corrected TEM/STEM in Hungary was opened on 11th of June 2018 in our Institute. The work started years earlier, when members of the Thin Film Physics Department took study trips to different laboratories in order to learn the technique. The first proposal was submitted to NKFIH in 2016, then with their specific support a second step proposal to our Ministry of Economy. It was a continuous work for two years to get the support, select the appropriate model and carry out a very rigid public procurement procedure. Finally, a Thermo Fisher Scientific FEI THEMIS 200 model was selected with an image corrector. The preparation of the appropriate room started with moving an old microscope to another room, as the group wanted to keep and run the existing 200 kV analytical and the 300 kV high resolution (equipped with an EELS (Electron Energy Loss Spectroscopy)) microscopes beside the new one. A far more sophisticated installation environment with a very stable, precise temperature controlled air condition and stray magnetic field cancel system was constructed.

The onsite tests after installation exceeded our expectations and the factory guaranteed parameters. Factory stated TEM resolution at 200 kV is 0.09 nm, i.e. 90 pm. The tests show that a resolution of 70 pm is attainable.

The microscope can be operated at 80 kV still having a very good resolution thanks to the spherical aberration corrector. Sensitive materials including 2D layers can be investigated at that low voltage operation.

The analytical measurements in the new microscope are provided by the SuperX system comprised of 4 EDS detectors built into the column. There is no need to tilt the sample in order to get a good signal to noise ratio.

In the following we will show some examples proving the superior capability of the microscope.



Figure 1: The new microscope in the laboratory

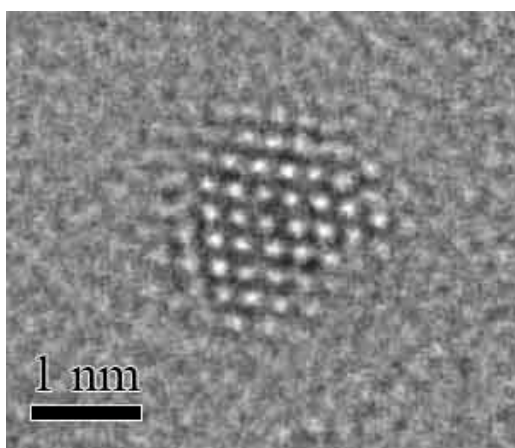


Figure 2: The image shows a small gold particle at atomic resolution. As the spherical aberration ( $C_s$ ) is intentionally set to a very small negative value, the atoms appear with bright contrast on the image.

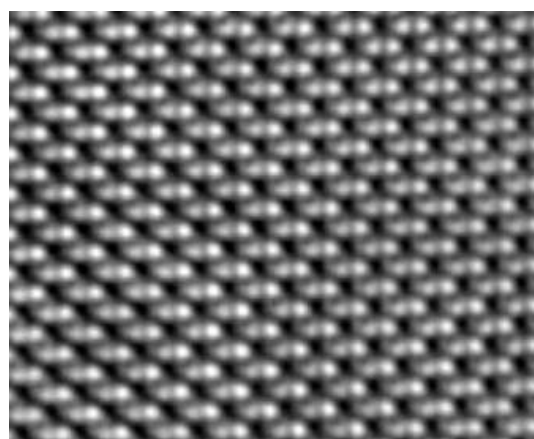


Figure 3: Diamond lattice imaged in TEM mode revealing the diamond dumbbells with the distance of 89 pm, (400) lattice spacing in diamond. This is a very important demonstration of the resolution power. In the case we do not have the resolution below 90 pm these two close dots (i.e. two rows of carbon atoms) are imaged as one intensity spot in the high resolution image.

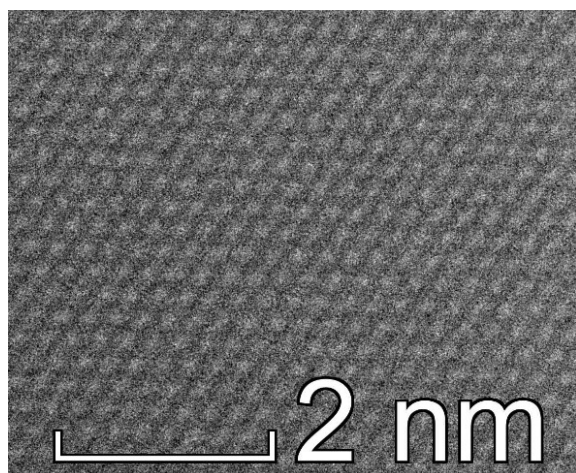


Figure 4: Graphene foil in high resolution imaged at 80 kV

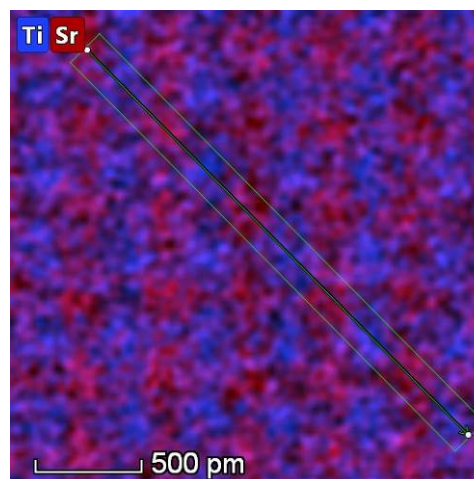


Figure 5: Although this is not a probe corrected microscope the power of the EDS mapping can be demonstrated on a  $\text{SrTiO}_3$  thin specimen in which the Ti and Sr atoms can be distinguished.

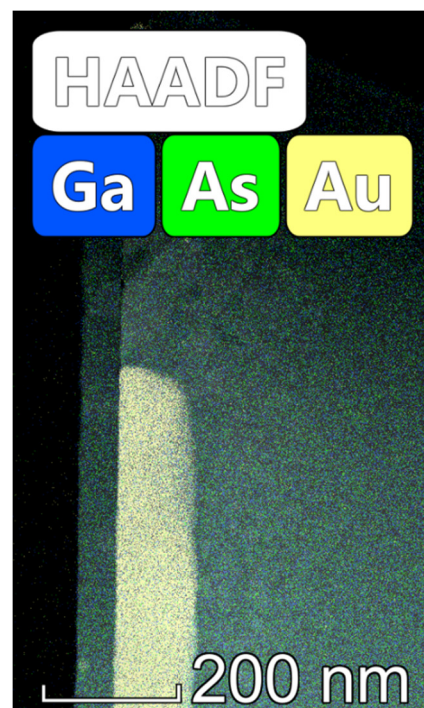
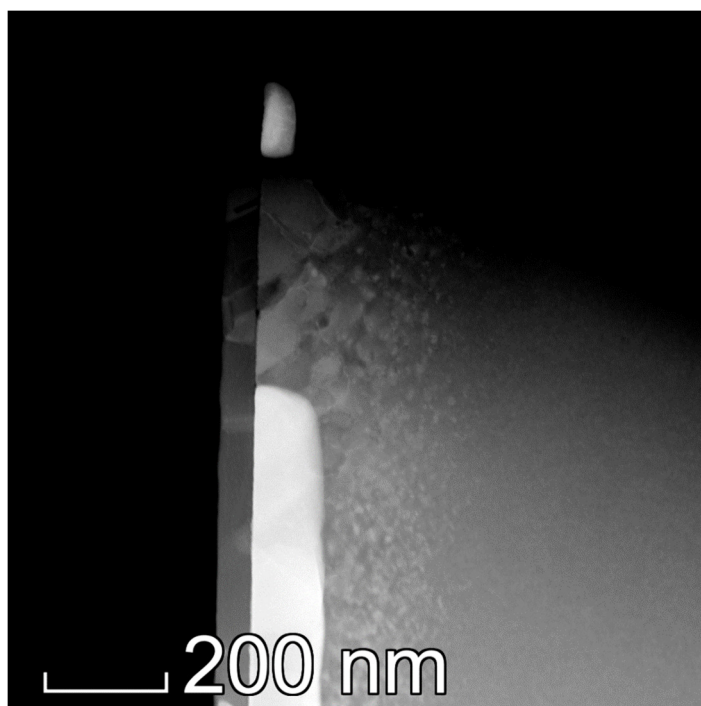


Figure 6: The above images are taken in STEM mode. The left one is an HAADF (High-angle annular dark-field) image showing gold grains with high intensity, as the brightness is monotonically increasing with the atomic number ( $Z^2$ ). This itself makes possible to map the details of any specimen in which we can observe variations of  $Z$ . However, the right side image is a spectrum image taken on the same area of the sample (Au/GaAs sample ion beam mixed and annealed) We can observe not only gold crystallites (in the reality they contain already some gallium therefore the colour in the EDS map is darker than the yellow colour of gold) is embedded into GaAs, but a thin GaAs on the top of the sample as well. The results were presented at the Workshop dedicated to the 85<sup>th</sup> birthday of Prof. J. Gyulai.

The new contrast mechanism of the corrected TEM, namely imaging with negative  $C_s$ , facilitated the identification of the crystallographic phase of a precipitate by comparing the experimental image to the simulated images of the possible phases. An Al-alloy with low (0.14wt%) Zr-content contained spherical precipitates embedded in the Al-matrix. EDS analysis showed that the precipitate contains Zr and Al, but the elemental ratio could not be determined due to the undefined contribution of the surrounding, encapsulating Al-matrix. Two phases appeared in the literature to describe such spherical Al-Zr precipitates, both with identical cubic crystal structure. The difference between the two is that in the first, Al atoms sit at the corners of the cube and Zr atoms at the centres of all faces and in the second their positions (and so the proportion of the elements) are reversed. We recorded an experimental image with negative  $C_s$  from a region that contained such a precipitate of 12 nm diameter, together with the surrounding matrix. Simulated images were also calculated for both phases and for the Al-matrix.

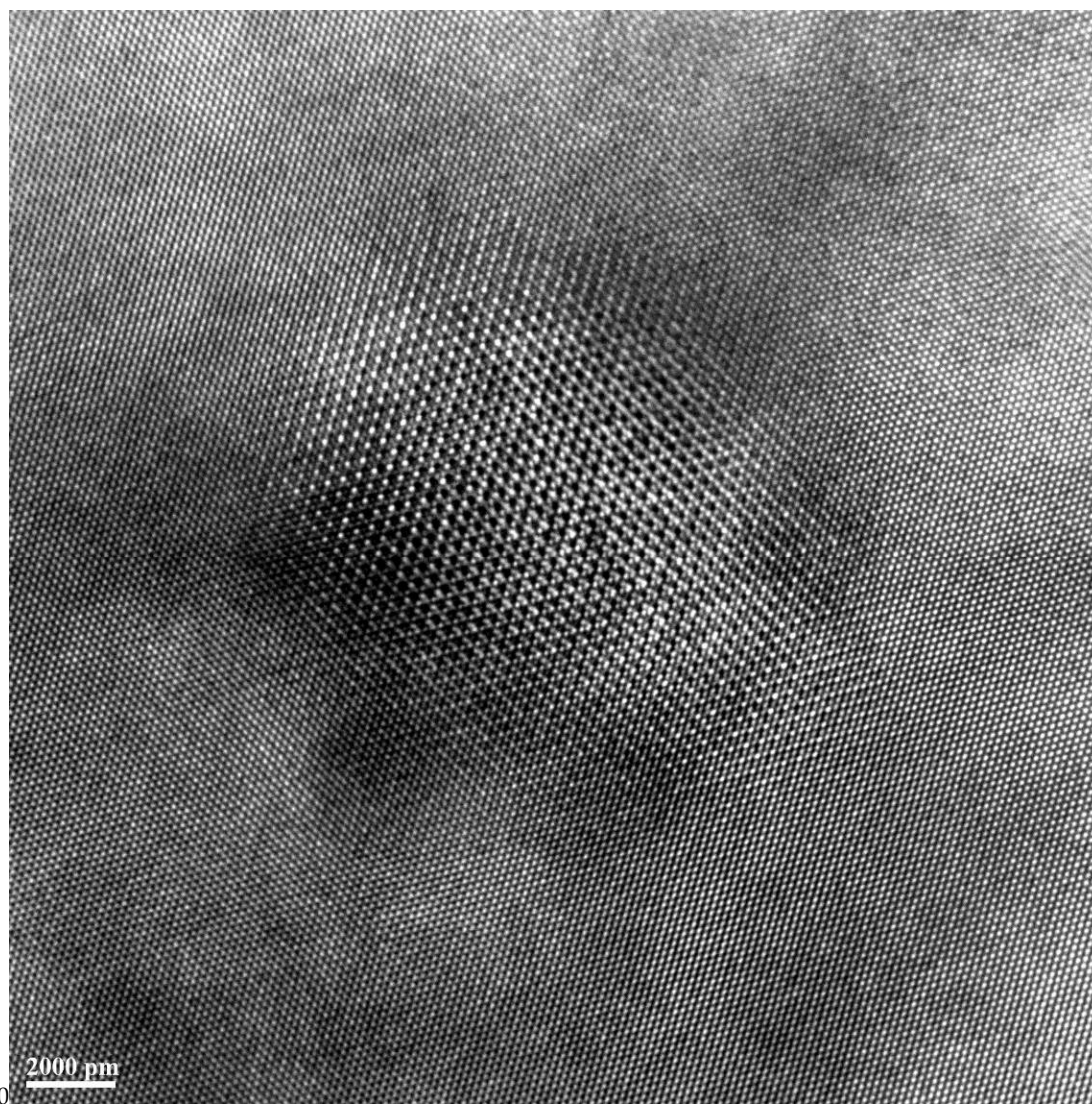


Figure 7: A magnified, selected region of the above image shows (below) the transition from the Al-matrix to the precipitate. There is serious overlap between the matrix and the precipitate in the transitional region. Atomic columns are bright with negative  $C_s$ . Structural features with the same size are marked with blue in the matrix, in the transitional region and in the precipitate.

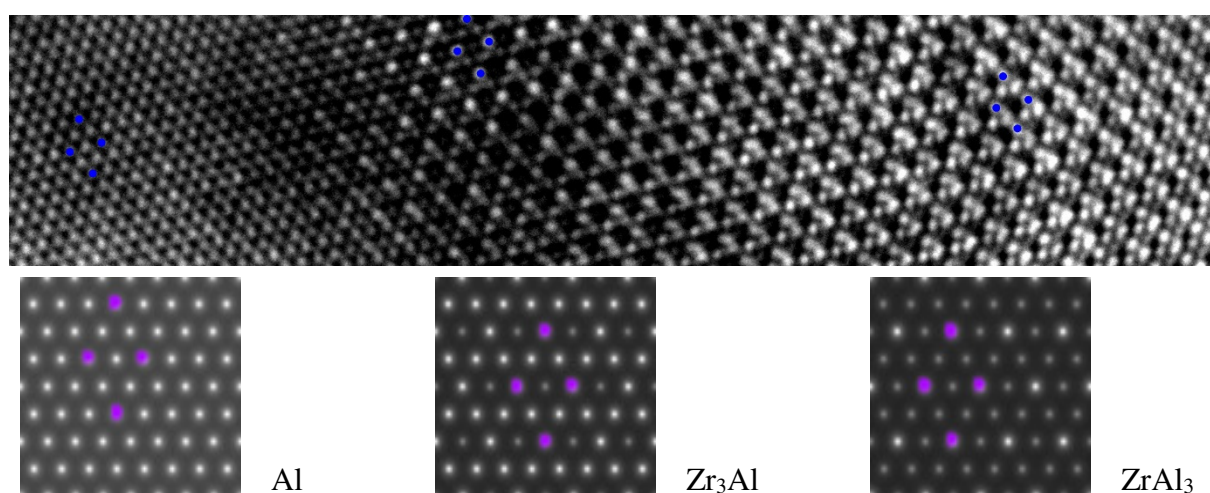


Figure 8: The projected potentials were calculated with the JEMS program for the [111] direction of all three structures. The same structural features are also marked in the simulated images.

It can be seen that on the one hand there is perfect match between measured and simulated images for the matrix. On the other hand, simulated image for phase  $Zr_3Al$  perfectly matches the measured one (four times bright triangles with a darker spot in the middle), while the simulated image of the other phase is completely different, making phase identification unambiguous. The precipitate is cubic  $Zr_3Al$ .

# SINGLE-ATOM CATALYSTS BASED ON DOPED $\text{MoS}_2$ SINGLE LAYERS FOR EFFICIENT HYDROGEN EVOLUTION

(ERC StG, Lendület, Korea-Hungary Joint Laboratory, Graphene Flagship)

J. Pető, P. Vancsó, G. Dobrik, T. Ollár (EK-FKL), Z. Popov (MISis-Moscow), C. Hwang (KRISS-Korea), P.B. Sorokin (MISis-Moscow) and L. Tapasztó

Single atom catalysts have recently shifted into the spotlight of heterogeneous catalysis research. Among their major appeals are the ultimate efficiency of material utilization and the simple and well-defined nature of the active centres, holding the promise of rational catalyst design. The major challenges are the preparation of a high density of firmly bound individual single-atomic centres, as well as establishing reliable structure-activity relationships. Both platinum group and transition metal atoms were found to be catalytically active in single-atomic form. Embedded in the proper matrix, also non-metal atoms can become catalytically active centres. We demonstrate that 2D crystals can provide an efficient template for realizing single-hetero-atom catalysts with a high density of non-metal single-atomic active sites. Such single-atom catalysts obtained through substitutional doping of 2D  $\text{MoS}_2$  crystals with oxygen can provide the advantages of an easy and versatile synthesis, a supreme site density, and a well-controlled and characterized active site structure.

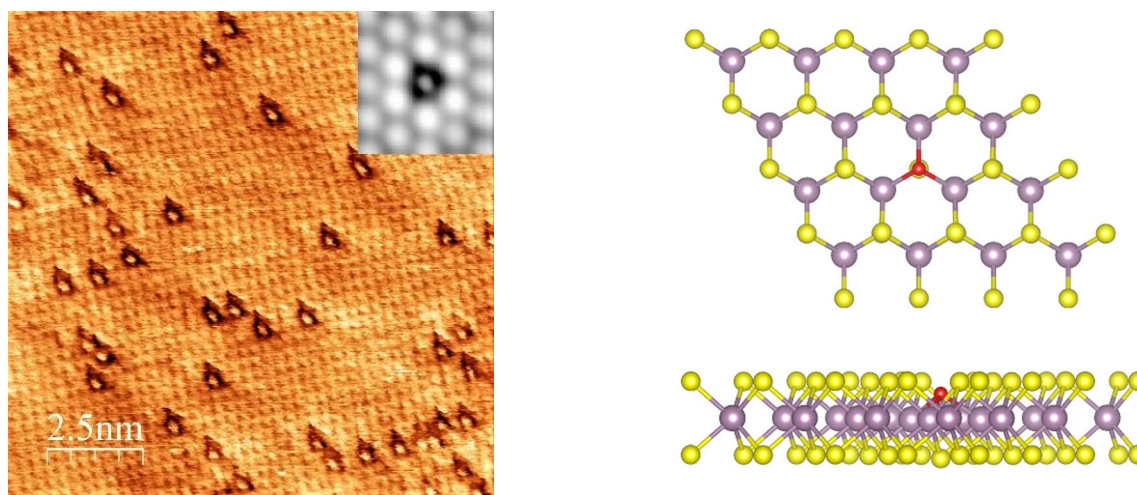


Figure 1: Atomic resolution STM image of  $\text{MoS}_2$  monolayers showing single oxygen atoms replacing individual S atoms in the crystal lattice; Calculated atomic structure of the oxygen substitution sites (red) in 2D  $\text{MoS}_2$  host crystals (Mo-grey, S-yellow)

By means of atomic resolution STM investigations we were able to image a novel oxidation reaction of the  $\text{MoS}_2$  single-layers at single-atom level, providing unexpected insights. In contrast to the generally accepted view, our results clearly evidence that the basal plane of 2D  $\text{MoS}_2$  crystals spontaneously oxidized upon long-term ambient exposure. Instead of O chemisorption or full conversion to  $\text{MoO}_3$ , a novel oxygen substitution mechanism has been revealed, where individual S atoms of the basal plane are one by one replaced by oxygen atoms giving rise to a new 2D  $\text{MoS}_{2-x}\text{O}_x$  solid solution crystal. As  $\text{MoS}_2$  single layers are the most widely investigated 2D materials besides graphene, the ability to chemically modify their single atomic sites provides a novel strategy for highly efficient defect engineering as well as synthesizing novel 2D crystals with tuneable chemical compositions.

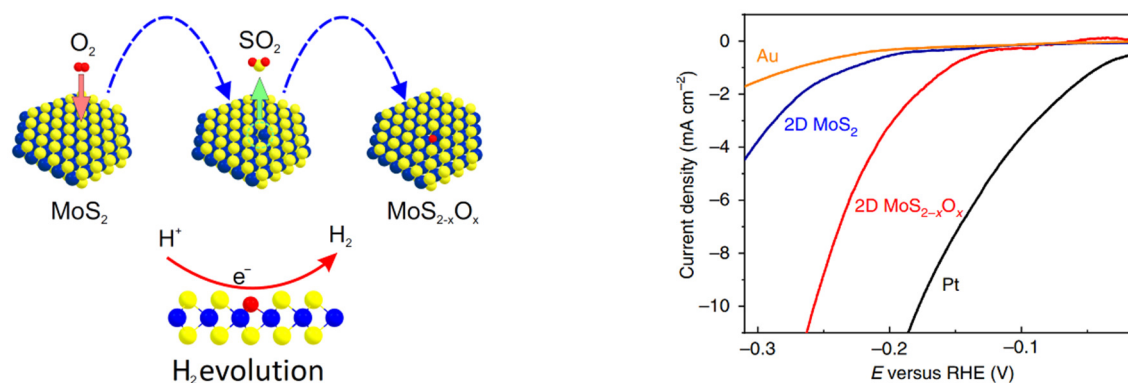


Figure 2: Oxygen atoms spontaneously incorporate into the structure of  $\text{MoS}_2$  single layers under ambient conditions giving rise to solid solution type 2D molybdenum oxy-sulfide crystals. The single atomic oxygen substitution sites catalytically activate the basal plane of  $\text{MoS}_2$  for hydrogen evolution as evidenced by the voltammogram curves.

Most importantly, we have observed a significantly enhanced catalytic activity for hydrogen evolution of 2D  $\text{MoS}_{2-x}\text{O}_x$  as compared to its pure 2D  $\text{MoS}_2$  form. We have shown that the individual O atom dopants are responsible for significantly increasing the catalytic activity. The Tafel slope for  $\text{MoS}_{2-x}\text{O}_x$  crystals was decreased to  $67 \text{ mV dec}^{-1}$  as compared to pristine  $\text{MoS}_2$  ( $98 \text{ mV dec}^{-1}$ ) and approached that of the Pt ( $54 \text{ mV dec}^{-1}$ ). Introducing the electronegative O atoms generates sites with higher electron affinity ( $-0.88 e^-$ ), which gives rise to localized negative charges attracting  $\text{H}^+$  to participate in reductive coupling to form  $\text{H}_2$ . Consequently, 2D  $\text{MoS}_{2-x}\text{O}_x$  crystals emerge as highly efficient, non-precious, earth-abundant catalysts for  $\text{H}_2$  evolution with a high density of single-atomic active sites on their basal plane. Upon optimization, such catalysts hold the potential to closely approach the catalytic activity of platinum at much lower costs.

Synthesizing single atom catalysts with well dispersed identical active centres is highly challenging. Even today, the relatively low site density is a major limiting factor for the activity of single atom catalysts, as the stable anchoring (strong bonding) of individual heteroatoms to substrates is required for preventing their aggregation. Our results evidence that 2D transition metal chalcogenides can provide ideal substrates for the stable anchoring of various heteroatoms, through substituting single atoms from the host crystal lattice with various heteroatoms. These findings open the way towards developing non-metal single atom catalysts by using transition metal chalcogenide single-layers as an active substrate, opening new perspectives in single atom catalysis.

# DIRECT-INDIRECT BANDGAP AND SEMICONDUCTOR-METAL TRANSITIONS IN MoS<sub>2</sub> SINGLE-LAYERS AT MODERATE STRAIN

(ERC StG, Korea-Hungary Joint Laboratory, Lendület)

J. Pető, P. Vancsó, G. Dobrik, P. Nemes-Incze, G. Kukucska (ELTE), J. Koltai (ELTE), L. Tapasztó

Strain-engineering the properties of 2D MoS<sub>2</sub> crystals has been intensely investigated for the last couple of years. Tuning the band structure by applying mechanical strain can provide an efficient way to fit the properties of the material to the specific requirements of various electronic and opto-electronic applications. Theoretical studies predict a steady decrease of the bandgap upon increasing of uni- and biaxial strain. Furthermore, it is expected that increasing the strain leads to a direct-indirect bandgap transition that was predicted to occur between 0,47 – 2,7 % strain depending on the theoretical model, while increasing the strain up to about 10% is predicted to give rise to a semiconductor-metal transition. Photoluminescence (PL) measurements confirmed that tensile strain can reduce the optical bandgap of 2D MoS<sub>2</sub> crystals. However, the experimental demonstration of the direct-indirect gap and semiconductor-metal transitions remained challenging.

Here we study MoS<sub>2</sub> nanobubbles emerging at the interface of MoS<sub>2</sub> single layers with Au(111) substrate. Such bubbles are shown to induce a few percent of biaxial tensile strain in the MoS<sub>2</sub> lattice. We employed Raman spectroscopy to determine the amount of strain in MoS<sub>2</sub> nanobubbles, and scanning tunneling microscopy (STM) and spectroscopy investigations to directly measure the fundamental bandgap of the strained MoS<sub>2</sub> monolayers.



Figure 1: Nanobubble formation at the MoS<sub>2</sub>/Au(111) interface. a) STM image revealing the presence of several nanoscale MoS<sub>2</sub> bubbles. b) 3D STM image of an individual MoS<sub>2</sub> nanobubble.

In order to experimentally determine the amount of mechanical strain induced in the MoS<sub>2</sub> lattice in the bubble areas, we performed confocal Raman spectroscopy measurements and calculations. The best agreement was found when considering 2% of bi-axial tensile strain.

By tunneling spectroscopy on MoS<sub>2</sub> nanobubbles, we were able to measure the fundamental bandgap of MoS<sub>2</sub> single layers subjected to 2% of biaxial tensile strain. We found that this strain decreases the bandgap of  $1.4 \pm 0.15$  eV below the 1.7 eV optical gap, evidencing that the direct to indirect bandgap transition has already occurred at 2% tensile strain, in good agreement with DFT calculations. Furthermore, the combination of a few percent of tensile strain with the intrinsic *n* doping of the MoS<sub>2</sub> layers can provide a metallic character to MoS<sub>2</sub> single-layers already starting from modest strain values (2-3%).

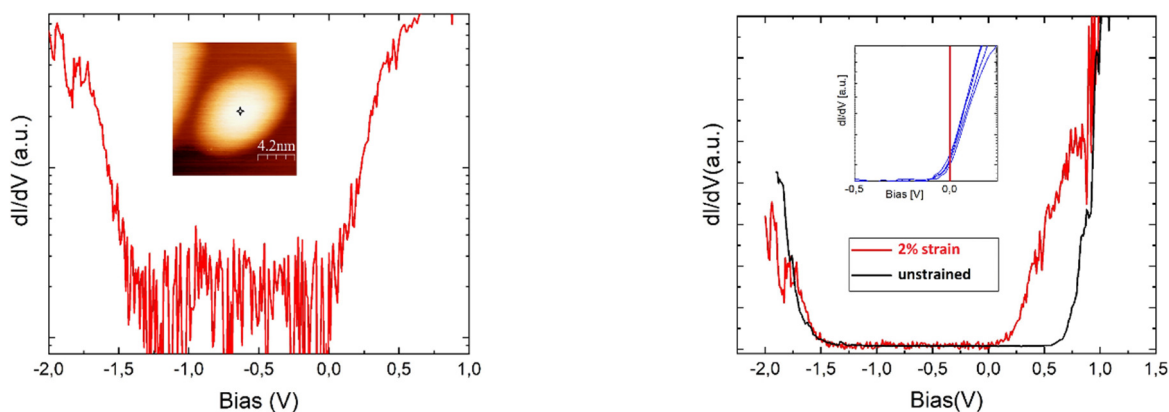


Figure 2: a) Tunneling spectrum on a  $\text{MoS}_2$  nanobubble revealing a bandgap of about 1.4 eV. b) Comparison of the tunneling spectra of strained and unstrained  $\text{MoS}_2$  monolayer. The inset shows that the Fermi level of strained bubbles can shift inside the conduction band, conferring a metallic character to the strained  $\text{MoS}_2$  crystal.

To understand the mechanism of the strain-induced changes in the band structure, we have performed DFT calculations. These calculations show that at 2% of tensile strain the bandgap is reduced by about 0.46 eV, and becomes an indirect gap between the K and  $\Gamma$  points of the Brillouin-zone, in good agreement with our experiments. Furthermore, the calculations evidence that the bandgap reduction is almost entirely due to the downshift of the conduction band, again in excellent agreement with our experimental observation (Fig 2b).

These findings experimentally demonstrate a particularly efficient strain-engineering of the fundamental gap, which can be exploited in electronic applications, for example, by strain patterning type I heterojunctions. Furthermore, our results also clearly reveal the limitations of the strain-engineering approach. The direct-indirect transition restricts the opto-electronic applications, while the semiconductor-metal transition puts a strong limit on electronic applications above 2% of strain, where the 2D  $\text{MoS}_2$  crystals acquire a metallic character.

# MEASURING THE EDGE STATES OF $\text{Pt}_2\text{HgSe}_3$ , A ROOM TEMPERATURE TWO-DIMENSIONAL TOPOLOGICAL INSULATOR CANDIDATE

(Lendület LP2017-9, ERC StG NanoFab2D, H2020 Graphene Flagship)

K. Kandrai, P. Vancsó, G. Kukucska (ELTE), J. Koltai (ELTE), Á. Hoffmann, A. Vymazalová (Czech Geological Survey), L. Tapasztó, P. Nemes-Incze

The realization that the geometrical concept of topology has a profound influence on the band structure of solids is no doubt one of most surprising and wide-reaching discoveries in the last decades of condensed matter research. Materials that are characterized by the  $\mathbb{Z}_2$  topological invariant, are insulating in the bulk and have conductive edge channels on their surfaces or edges. These edge states carry dissipationless current and could be a platform to realize topological quantum computation. A prototype of this is actually graphene, but the fact that the material is a topological insulator remains a theoretical curiosity, due to the negligible spin orbit coupling (SOC) strength of carbon. Therefore, the hunt is on for materials that have a large topologically non-trivial band gap, preferably in the room temperature regime ( $>77$  meV).

Jacutingaite ( $\text{Pt}_2\text{HgSe}_3$ ), a naturally occurring layered mineral has been recently predicted to be a topological insulator, with a band gap above room temperature. One can consider it a “heavy metal” version of graphene, with large SOC. By performing scanning tunnelling microscopy (STM) measurements on the material, we reveal the honeycomb-like configuration of the basal plane states (see Fig 1a, b). Our density functional theory (DFT) calculations predict a topologically non-trivial gap of 110 meV. This value is reproduced by tunnelling conductance measurements on the bulk basal plane. Its topological character is confirmed by calculating the  $\mathbb{Z}_2$  invariant. In Fig. 1e we can observe how the density of states within the gap increases, if we move the tip of the STM closer to a monolayer step edge on the surface. This observation is expected if the topological edge state resides within the band gap. By mapping the tunnelling conductance within the gap, as a function of position, it becomes clear that the increased density of states follows the step edge, with a decay of  $\sim 5$  Å into the bulk, as expected from DFT calculations (see Fig. 2).

The identification of the topological edge states makes  $\text{Pt}_2\text{HgSe}_3$ , a prime candidate for applications of 2D topological insulators, with the promise of achieving room temperature dissipationless transport, or the realization of a topological superconductor.

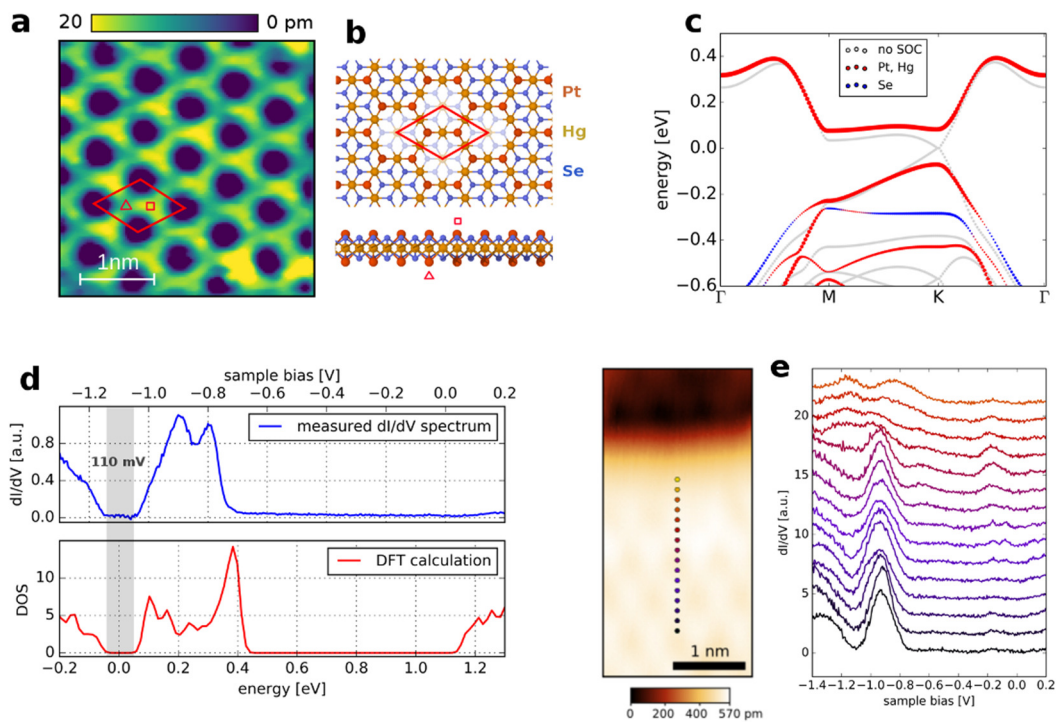


Figure 1: STM measurements on  $\text{Pt}_2\text{HgSe}_3$ . (a) Atomic resolution STM image of the basal plane, showing the honeycomb structure of  $\text{Pt}_2\text{HgSe}_3$ . (b) Atomic lattice of a single layer of  $\text{Pt}_2\text{HgSe}_3$ . (c) DFT calculation of its bands. Grey plot shows the bands of a single layer without spin orbit coupling. Red and blue bands are calculated with spin orbit coupling taken into account. The colour represents the contribution of Pt and Hg atoms. (d) Density of states measured on the basal plane (blue) and calculated via DFT (red). (e) Tunnelling conductance measurements nearing a monolayer edge, showing the appearance of states inside the predicted topological band gap.

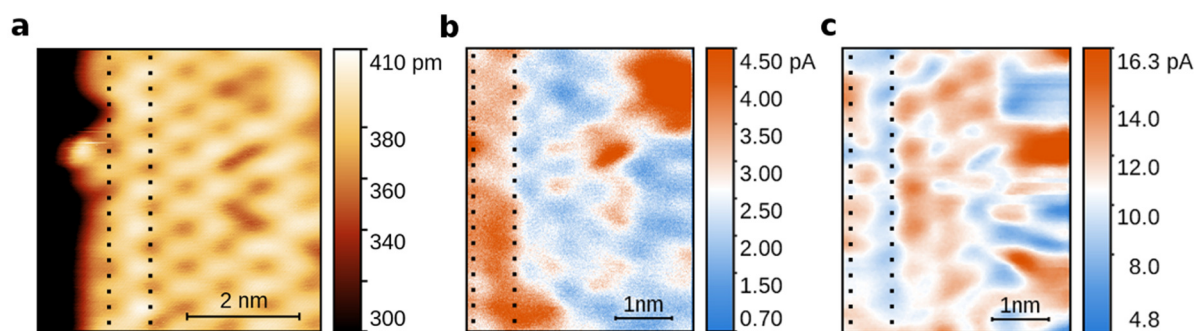


Figure 2: Images of the topological edge state. (a) STM topographic image of a monolayer step edge. Tunnelling conductance images measured at the edge, at a sample voltage inside the band gap: (b) and out of the band gap in the conduction band: (c).

# HIGHLY ORDERED GRAIN BOUNDARIES IN CVD $\text{MoSe}_2$ SINGLE LAYERS

(ERC StG NanoFab2D, Graphene Flagship)

A. A. Koós, P. Vancsó, G. Dobrik, L. P. Biró and L. Tapasztó

The chemical vapour deposition (CVD) growth method is one of the most widely investigated techniques to achieve a scalable growth of macroscopic area 2D crystals. However, CVD grown layers also suffer from a few drawbacks as compared to high quality, but microscopic exfoliated 2D transition metal dichalcogenide (TMDC) flakes. In general, CVD grown layers are expected to contain a much higher concentration of grain boundaries that are known to substantially affect their electronic and optical properties. Grain boundaries in TMDC materials are often characterized by structural disorder and a substantial local modification of the band gap that both act as source of charge carrier scattering, degrading the electronic quality of CVD grown sheets. Nevertheless, growing large area single crystalline domains is highly challenging. Even if one can drastically reduce the nucleation site density, it requires an extremely slow growth process. Consequently, growing macroscopic areas of TMDC single layers of high structural and electronic quality is a particularly important, yet unsolved challenge.

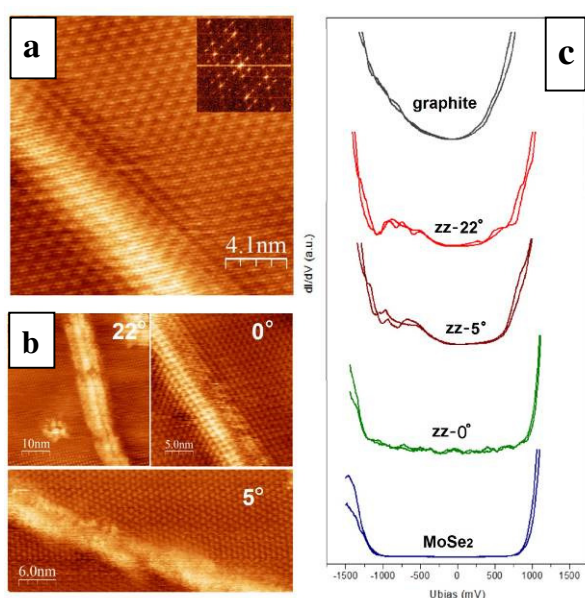


Figure 1: a, b) Atomic resolution STM images of mirror twin grain boundaries in CVD  $\text{MoSe}_2$  running along various crystallographic orientations measured relative to the zigzag direction. c) Representative tunnelling spectra of various grain boundaries.

In general, grain boundaries provide a strong intrinsic limitation to the structural and electronic quality of the CVD grown single layers. Consequently, revealing their atomic and electronic structure is of particular importance. We were able to achieve atomic resolution STM images on or around several  $\text{MoSe}_2$  grain boundaries, as shown in Figure 1. All atomic resolution STM images evidence that the atomic lattices on the two sides of a  $\text{MoSe}_2$  grain boundary have closely matching orientations. The prevalence of this special class of grain boundaries is due to the rotationally aligned CVD growth of  $\text{MoSe}_2$  on graphite. We found that the most often observed mirror twin boundaries (MTBs) running along the zigzag directions are highly ordered, while those enclosing an angle with the zigzag direction (but still preserving the rotational alignment of the two sides) are characterized by a more disordered atomic structure. To get insight into the electronic structure of the  $\text{MoSe}_2$  grain boundaries, we have also performed tunnelling spectroscopy measurements on various GBs (Fig. 1c). Tunnelling spectra on disordered MTBs enclosing a nonzero angle with the zigzag crystallographic direction display a substantially reduced band gap due to emerging midgap electronic defect states. By contrast, tunnelling spectra of zigzag grain boundaries are very similar to those recorded on the defect free  $\text{MoSe}_2$  regions, evidencing that zzMTBs do not perturb strongly the electronic properties of the crystal. To understand the electronic properties of the experimentally observed zzMTBs in more details, we have performed DFT calculations on several possible zzMTB geometries.

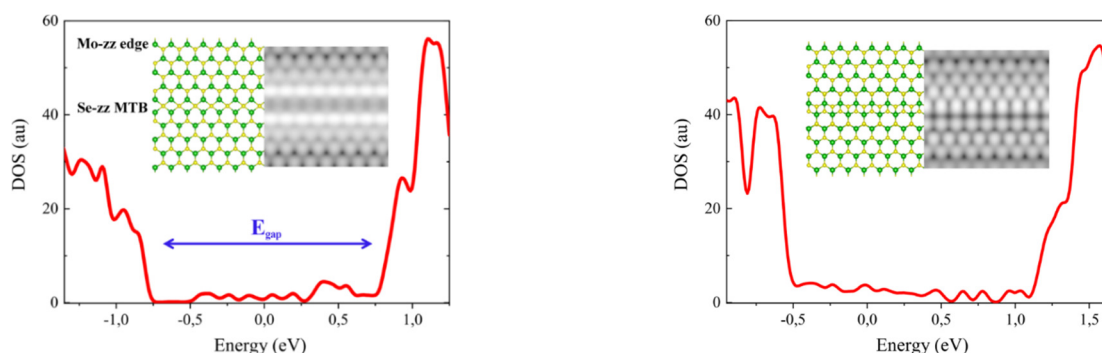


Figure 2: Calculated atomic and electronic structure of various  $\text{MoSe}_2$  MTBs with (Se) zigzag orientation. The inset shows the simulated STM images of the corresponding atomic structures.

We have shown that in contrast to other types of grain boundaries, mirror twin boundaries running parallel to the zigzag crystallographic direction of the  $\text{MoSe}_2$  lattice are characterized by a highly ordered atomic structure and leave the electronic structure almost unaffected; while grain boundaries with other orientations display a more disordered structure and substantially modify the band gap locally. Zigzag mirror twin boundaries do not degrade the electronic quality of CVD grown  $\text{MoSe}_2$  single layers.

# MECHANICAL STRAIN PUTS A TWIST ON DIRAC FERMIONS IN GRAPHENE

(Lendület LP2017-9, ERC StG NanoFab2D, H2020 Graphene Flagship)

P. Kun, G. Kukucska (ELTE), G. Dobrik, J. Koltai, J. Kürti (ELTE), L. P. Biró, L. Tapasztó, P. Nemes-Incze

One of the hallmark properties of graphene is that backscattering of charge carriers is prohibited for smooth potentials. This is a major characteristic of the massless Dirac quasiparticles in graphene and was recognized early on, in the very first charge transport measurements of single graphite layers. Forbidden backscattering in perfect graphene is intimately linked to the pseudospin property of Dirac fermions and lies at the heart of the exceptional electrical properties of graphene.

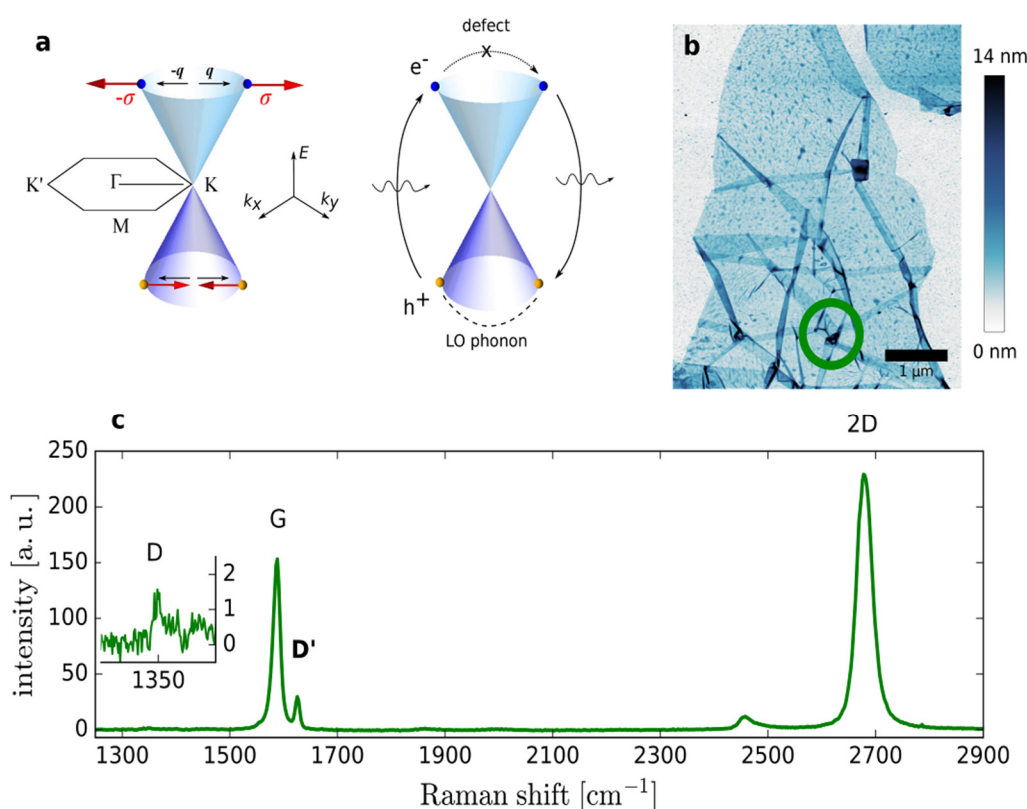


Figure 1: Anomalous D' peak intensity in Raman spectroscopy measurements on crumpled graphene. (a) Pseudospin conservation and intra-valley scattering in graphene, emphasizing the process leading to the D' peak. (b) AFM image of a crumpled graphene sample, with the Raman measurement position shown by green circle. (c) Raman spectrum measured on the crumpled graphene, showing a D' peak with an intensity 300 times the D peak intensity.

The “spin-like” property is a result of the crystal symmetry of graphene and determines the phase that the Dirac wavefunction acquires while scattering. In non-perfect graphene, if mechanical strain is present, the resulting deformation of the crystal lattice can be described as a pseudo-magnetic field. Charge carriers propagating in such strained areas acquire an additional phase, similarly to the Aharonov-Bohm effect. The “twist” in the wavefunction due to this extra phase can lift the ban on complete backscattering, as we show in an optical experiment.

For the first time, we have presented experimental evidence that pseudospin effects have a dramatic influence on the double resonant Raman spectra, more precisely on the intensity of the D' peak (see Fig. 1). Until now, this defect induced peak has only been observed for lattice defects (vacancy, grain boundary, etc.) and not for smooth potentials (pseudomagnetic field patterns). Each type of defect has a specific D' peak to D peak intensity ratio, characteristic of the defect in question. We measure this fingerprint on crumpled single layer graphene and find an anomalously high D' peak intensity. Since the D' peak involves complete backscattering (see Fig. 1a), increased intensity is a hallmark of increased backscattering due to the pseudo-magnetic field. Numerical calculations reproduce the measured “Raman fingerprint”, taking into account the pseudo-magnetic field pattern produced by the crumpling (see Fig. 2).

Our results lead to a better understanding of charge carrier scattering in strained graphene. This is especially important, since strain fluctuations are thought to be the bottleneck limiting the mobility of high-quality graphene devices.

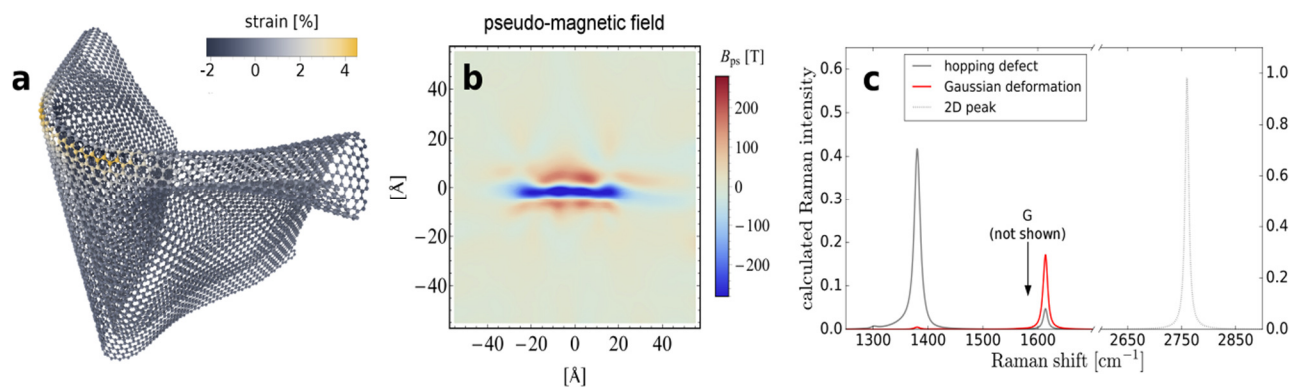


Figure 2: Calculated Raman spectra on crumpled graphene. (a) Molecular dynamics simulation of a twice folded rectangular graphene layer. (b) Calculated pseudo-magnetic field ( $B_{ps}$ ) within the rectangular graphene layer. (c) Calculated peak intensities of the doubly resonant processes (D, D', 2D). For scattering on strain patterns (red peak), the calculation reproduces the measured D' and D peak intensities.

### Related publication

- [1] P. Kun, G. Kukucska, J. Koltai, J. Kürti, L. P. Biró, L. Tapasztó and P. Nemes-Incze: *Strong intravalley scattering on graphene corrugations revealed by Raman spectroscopy*. arXiv (2018). at <http://arxiv.org/abs/1801.08861>

# DYNAMIC STRAIN IN GOLD NANOPARTICLE SUPPORTED GRAPHENE INDUCED BY FOCUSED LASER IRRADIATION

(OTKA-K119532)

A. Pálinkás, P. Kun, A. A. Koós, and Z. Osváth

Graphene on noble-metal nanostructures constitutes an attractive nanocomposite with possible applications in sensors or energy conversion. In this work we study the properties of hybrid graphene/gold nanoparticle structures by Raman spectroscopy and Scanning Probe Methods. While we found that successive high intensity laser irradiation increased gradually the doping and the defect concentration in SiO<sub>2</sub> supported graphene, the same irradiation procedure did not induce such irreversible effects in the graphene supported by gold nanoparticles (NPs). Moreover, the laser irradiation induced dynamic hydrostatic strain in the graphene on Au NPs, which turned out to be completely reversible. A thin gold film of 5 nm was deposited onto a SiO<sub>2</sub>(285 nm)/Si substrate by an electron-beam evaporation system (AJA). Gold nanoparticles were formed on areas of 5×5 μm<sup>2</sup> by local laser heating of the gold layer using a confocal Raman microscope (WITec) and a focused, 6 mW laser-power @633 nm. CVD graphene was transferred onto the substrate (gold layer and gold NPs) using thermal release tape (TRT) method. Multiple Raman-spectroscopy measurements were performed on each selected region with low (0.6 mW) and high (6 mW) laser power. The samples' morphology was investigated by Atomic Force Microscopy both before and after the laser annealing.

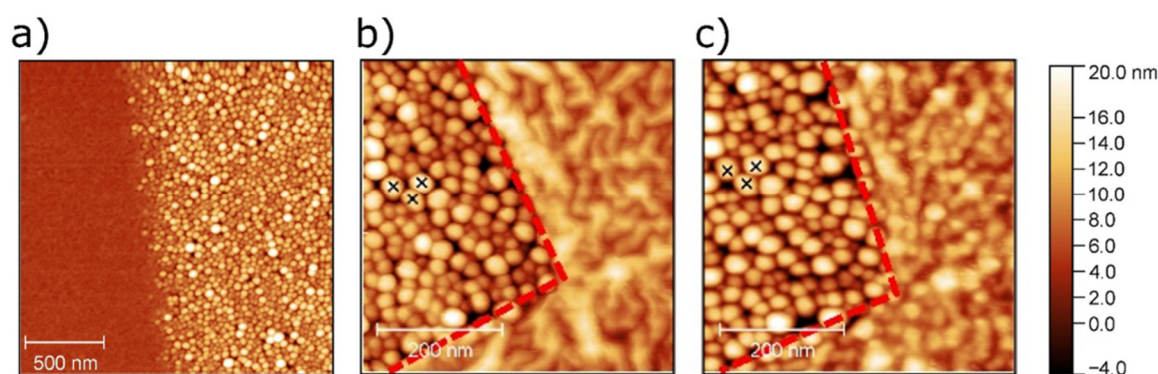


Figure 1: (a) AFM image showing the border of as-evaporated (left) and annealed (right) gold region. (b-c) AFM images showing both graphene covered and bare gold NPs, (b) before, and (c) after subsequent laser annealing. The corner-like graphene edge is marked with red dashed line, while three individual bare gold NPs are marked with black symbols.

The AFM image in Fig. 1a shows both the as-evaporated gold layer (left side) and an irradiated part (right side) with the borderline in the middle. Dome-like gold NPs formed on the irradiated part with diameter of 32 nm and height of 11 nm in average. Fig. 1b and 1c show AFM images of the same corner-like graphene edge, right after the transfer process and after multiple high power laser annealing, respectively. The initially formed nanoparticles remained unchanged after subsequent laser annealing (see for example the NPs marked with black crosses in Fig. 1. b-c, and the configuration of the NPs surrounding them). We can observe in Fig. 1b that the covering graphene is rippled in various longish shapes. In turn, in Fig. 1c the individual NPs are well outlined beneath the graphene, meaning that graphene follows better the shape of NPs after laser annealing. We performed successive Raman maps with 488 nm and 633 nm laser excitation on graphene/Au NPs in a 5×5 μm<sup>2</sup> area with 20×20 pixels. Low (0.6 mW) and high (6 mW) power measurements were performed alternately. The higher laser power was used explicitly to anneal locally the samples, while with low powers we characterized the effect of the applied heating.

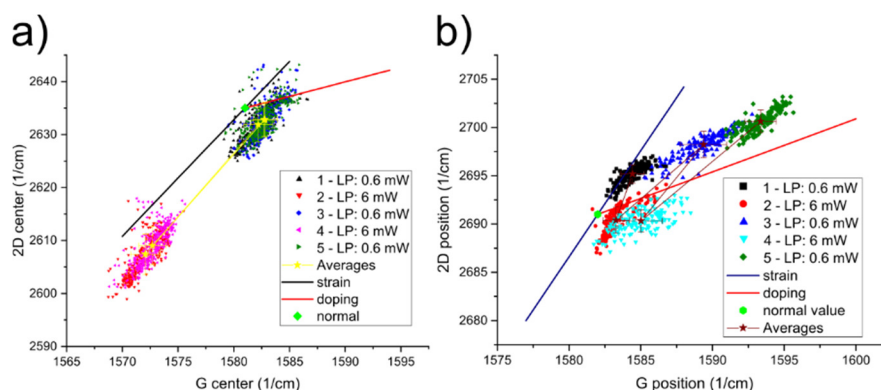


Figure 2: Correlation plot of the 2D-G Raman peak positions of (a) Au NPs supported and (b) Si/SiO<sub>2</sub> supported graphene. Subsequent Raman data measured with laser power of 0.6 mW (1, 3, 5) and 6 mW (2, 4).

In Fig. 2 we plotted the correlation plots of the 2D-G Raman peak positions of graphene. The average of the first low power measurement was at  $(\omega_G; \omega_{2D}) = (1582.2; 2631.9 \text{ cm}^{-1})$ , which corresponds to a small tensile strain  $\epsilon_{\text{hidr1}} = 0.08\%$  and p-doping of  $E_F = -89 \text{ meV}$ . The following high power measurements (data sets no. 2 and 4) show a significant shift of both G and 2D peaks, which is nearly parallel with respect to the pure hydrostatic strain slope. We fitted the average values and found a slope of  $2.37 \pm 0.02$ , which is close to 2.2 (the “strain” slope). Note that the effect is reproducible, the peak shifts are very similar in the two cases. The induced dynamic hydrostatic strain is  $\epsilon_{\text{hidr2}} = 0.48\%$ . Furthermore, the low power measurements are also very reproducible, the data sets no. 3 and 5 have averages close to the first one. On average, neither the strain nor the doping was changed significantly, as shown in Fig. 2a. For comparison, we prepared a sample where graphene was transferred directly to a standard,  $\text{SiO}_2(285 \text{ nm})/\text{Si}$  substrate. In Fig. 2b we plotted the corresponding 2D-G peak positions. After high intensity laser irradiation, significant increase in the p-type doping occurred, as is clearly seen from subsequent low intensity correlation plot data (sets no. 3 and 5, respectively). The shift of the averages follows the pure p-doping slope of 0.55 very well.

These results point out the role of the substrate in the laser irradiation induced effects on graphene, and can have implications in the development of graphene/plasmonic nanoparticle based high temperature sensors.

### ***Related publication***

- [1] Pálinkás, P. Kun, A. A. Koós, and Z. Osváth: *Dynamic strain in gold nanoparticle supported graphene induced by focused laser irradiation*, *Nanoscale* **10(28)**, 13417-13425 (2018) doi: 10.1039/c8nr02848f.

# OPTICAL VAPOUR SENSING ON SINGLE WING SCALES AND ON WHOLE WINGS OF THE *ALBULINA METALLICA* BUTTERFLY

(OTKA K 111741, OTKA K 115724)

K. Kertész, G. Piszter, Zs. Bálint, and L. P. Biró

Nowadays, monitoring the air quality of homes, work places, and industrial facilities is becoming more and more important. For the efficient characterization of the ambient atmosphere, gas and vapour sensors are required which combine high sensitivity and chemically selective detection of volatile organic compounds with low power consumption and fast response time and operate in ambient air. Sensors based on photonic-crystal-type nanoarchitectures may offer an optimal solution to this problem due to the fast development of the response signal (colour change) and relatively easy optical readout combined with small size.

The *Albulina metallica* butterfly species is specific in that males have structural colours on both of their wing surfaces (Fig. 1). In our earlier work, we showed that the vivid wing colorations are generated by quasi-ordered, “pepper-pot”-type photonic nanoarchitectures. We showed, that despite the almost-identical scanning electron microscope images of the photonic nanoarchitectures (Fig. 1), there are minor but characteristic differences between the two sides in respect to the size and distribution of the air holes filling the chitin matrix. Direct space analysis of the electron microscope images showed that the typical first-neighbour distance of the embedded air holes is characteristically different for the blue and gold-green wing scales causing the different structural colors.

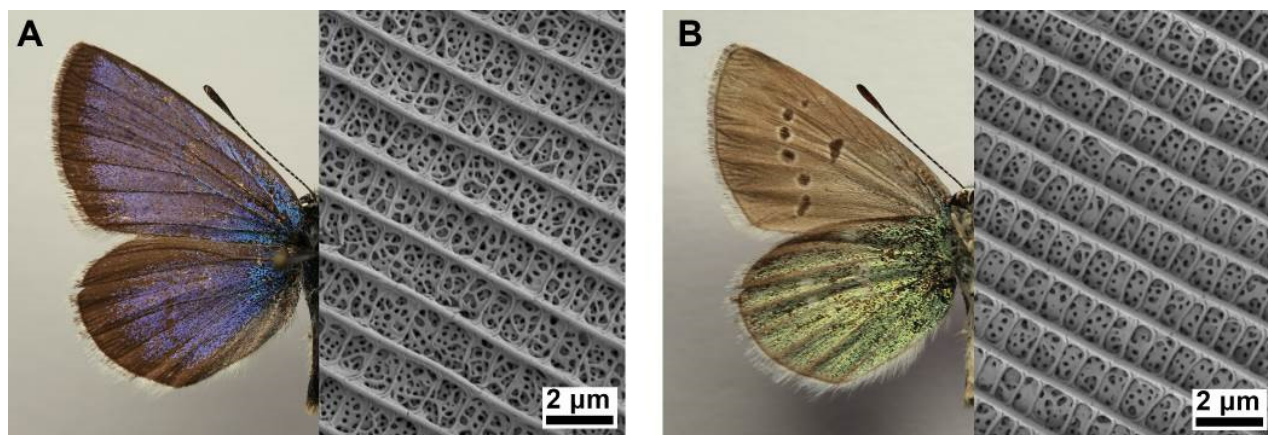


Figure 1: Photos of an imago and scanning electron micrographs of wing scales of *Albulina metallica* male specimen. The (A) blue and (B) gold-green wing surfaces are shown.

Selective chemical sensing of two qualitatively similar, but quantitatively different, “pepper-pot”-type photonic nanoarchitectures, which occur in the dorsal (blue) and ventral (gold-green) cover scales in the wings of the male *Albulina metallica* butterflies, were investigated using ten different vapours. The capillary condensation of vapours yielded characteristic response curves in relative reflectance both for the chemical substances and for the two different structures in the concentration range of 5% to 50% vapour in artificial air. This shows that, by combining different nanoarchitectures in an array of sensors, selectivity can be enhanced by using the “fingerprinting” of various vapours and storing the characteristic responses on the different elements of the array.

As the complete wings are optically complex objects, we also investigated the behaviour of single scales, both by using a microscope and collecting the signals not from the entire wing, but from one single scale only, and by removing single scales from the wing and placing them on microscope slides for individual characterization. Complete immersion of separated single scales in ethanol showed significant changes from blue to green, and from gold-green to red (Fig. 2A). We also performed vapour sensing measurements on ten blue and ten gold-green single wing scales while applying a 50% concentration of chloroform and water vapours. The average of the ten measurements on each side and for each vapour is plotted in Fig. 2B. It was shown, that single scales exhibit similar, chemically selective sensing both in reflected light and transmitted light as was found on the whole wings.

The effect of stacked wing scales on the vapour-sensing properties was also investigated. We measured transmittance of light across one, two, and three stacked scales during 50% ethanol vapour exposition. It was found that the optical response increases with the number of stacked scales showing that by increasing the volume of interaction between the vapours and the nanoarchitectures the sensitivity can be significantly enhanced.

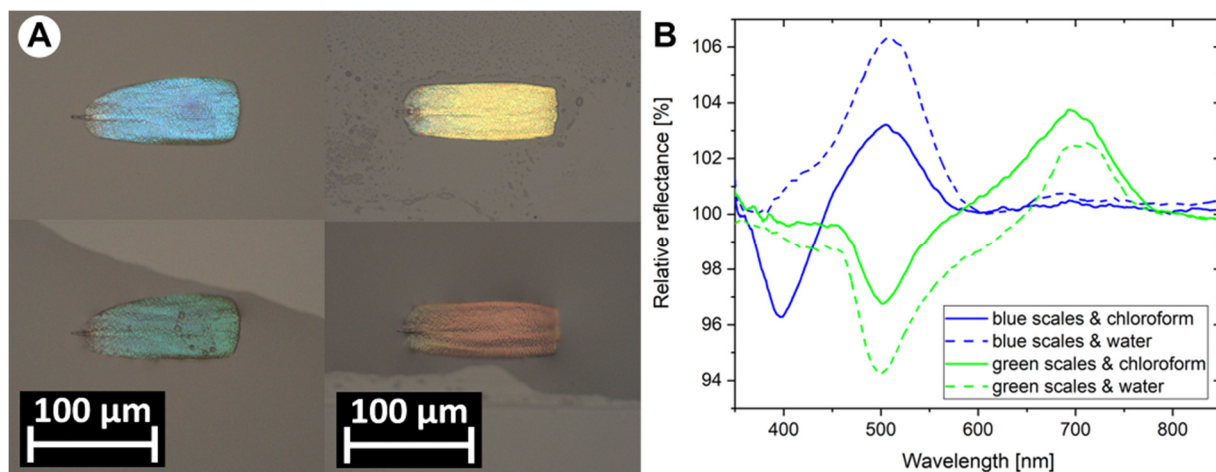


Figure 2: (A) Reflected light optical micrographs of *Albulina metallica* single scales in air (upper) and submerged in ethanol (lower): the color changes from blue to green and from gold-green to red, respectively. (B) Average of vapour sensing signals (in reflected light) on single blue and gold-green *Albulina metallica* wing scales using 50% chloroform and water vapours, as noted. Measurements were performed on single scales still attached to the wing membrane.

These findings show that naturally tuned photonic nanoarchitectures can be used to construct miniature sensor arrays consisting of one or a few scale stacks with different chemical selectivity, enabling the production of small (approximately 100 μm size) and material specific vapour sensors with optical readout.

# OPTICAL SPECTROSCOPY OF INDIVIDUAL NANOSCALE OBJECTS

(Hungarian Scientific Research Fund: FK-128327, KH-129578, K-112114 and K-119532)

D.P. Szekrényes, S. Pothorszky, D. Zámbo, N. Nagy, Z. Osváth, Z. Zolnai and A. Deák

The preparation and investigation of well-defined nanostructured materials contributes to a better understanding of their structure-property relationship. This is an essential background for the development of advanced functional systems in the field of photonics and optoelectronics.

In our research, we use a broad range of experimental approaches and techniques to prepare well-defined nanostructured materials and to study their interaction with light. In the highlighted projects we employ noble metal derived nanostructures, which show a very intense absorption and scattering due to the appearance of localized surface plasmon resonances. By combining optical microscopy, imaging spectroscopy and high sensitivity detection, we are able to carry out absorption or scattering measurements even down to the single nanoparticle level. This in turn allows access to a more rigorous interpretation of the relationship between the optical properties and the structure or surface properties of the investigated nanostructures.

One possible method for the preparation of nanostructured plasmonic surfaces is nanosphere templating of thermoplastic polymer layers. The gold-coated polymer replica of a Langmuir-Blodgett film consisting of sub-micron silica spheres can be used to create localized and propagating surface plasmons at the nanostructured substrate. This structure was used to investigate the signal enhancement related to indentations in the gold surface layer during micro-Raman scattering experiments.<sup>1</sup> The indentations were prepared based on the above mentioned colloidal templating and the voids filled with 4-mercaptobenzoic acid (MBA) loaded gold nanospheres. The periodic void structure has been designed to allow selective excitation of a single void in a way that at the laser wavelength of the micro-Raman setup, the cavity-type plasmon modes localized at the metallic void interface can be effectively excited. The surface modification of the gold particles by MBA was studied in detail and the number of MBA molecules present on a single gold nanoparticle inferred from optical and electrophoretic-mobility measurements to be ca. 210. Correlative scanning electron microscopy and micro-Raman measurements allowed the investigations at the single void level. Raman signal from a single MBA loaded gold nanoparticle in the cavity was already detectable. The number of particles present at a single void-site provided a straightforward way to control the number of molecules excited during the experiments. By measuring the signal strength as a function of particle number, trapped inside a single nanovoid and comparing it with a reference sample (clusters of given number of particles on a flat gold surface), a 25-fold experimental signal enhancement attributed to the nanostructured nature of the interface could be inferred.

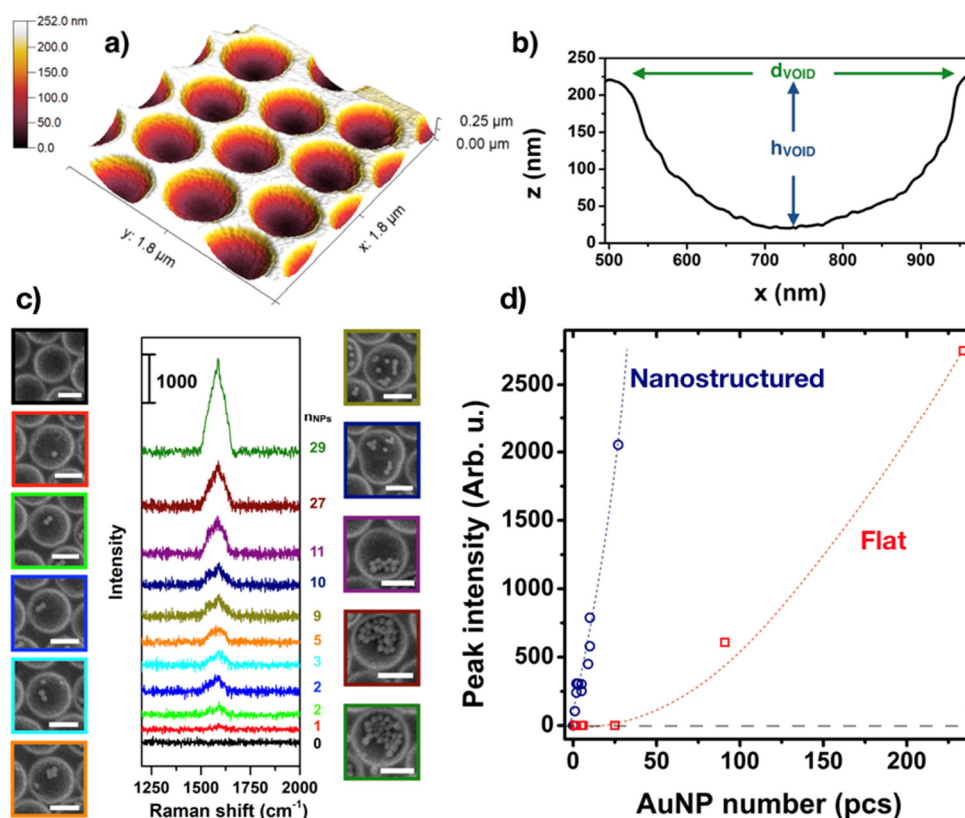


Figure 1: AFM image of the metallic void array (a) and a typical height profile across an individual void (b). Raman spectra obtained from exciting individual voids containing different number of MBA coated gold nanoparticles (c). Intensity of the  $1578 \text{ cm}^{-1}$  peak of MBA as a function of excited particle number measured on the nanostructured and the reference flat gold surface (d).

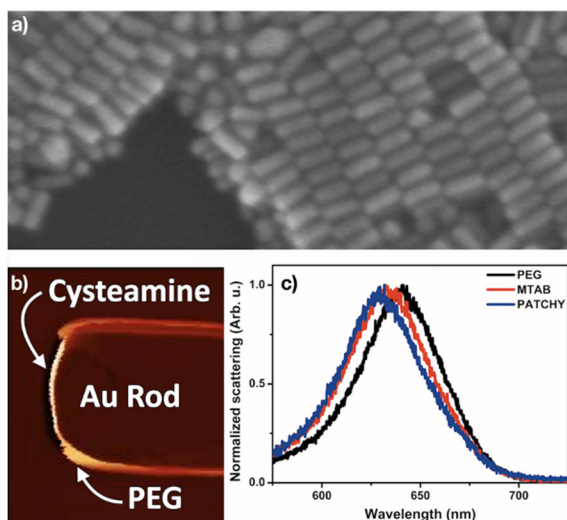


Figure 2: SEM image of the as synthesized  $115 \times 55$  nm gold nanorods (a). Single particle AFM image showing the well-defined surface chemical patch developed at the tip of the nanorod (b). Scattering spectra of individual nanorods having different surface coatings (c).

(Indium tin oxide) substrates were modified by the combination of nanosphere lithography and ion-bombardment to create a nanopattern with sharp boundaries between the irradiated and masked regions. Then, single particle scattering spectra of gold nanorods distributed over the nanopattern are investigated in detail. For nanorods located purely on either the masked or implanted areas, the spectra can be adequately interpreted in terms of a classical damped harmonic oscillator model, taking the chemical interface damping into account. When the particles overlap the masked and irradiated areas, however, markedly different behavior is found depending on the actual arrangement. For the rods experiencing a symmetric inhomogeneity (that is by bridging between two masked regions), damping varies smoothly with the extent of substrate inhomogeneity. For the asymmetric case (rods overlapping the boundary between the implanted and masked zones) a sudden increase of the damping is found, which is rather independent on the specific extent of substrate inhomogeneity. Comparing the damping variations with the related intensity changes indicates that substrate inhomogeneity at such length scales results in a different behaviour than predicted by the classical damped harmonic oscillator model applied for nanoparticles encapsulated or homogeneously surrounded by molecular coatings.

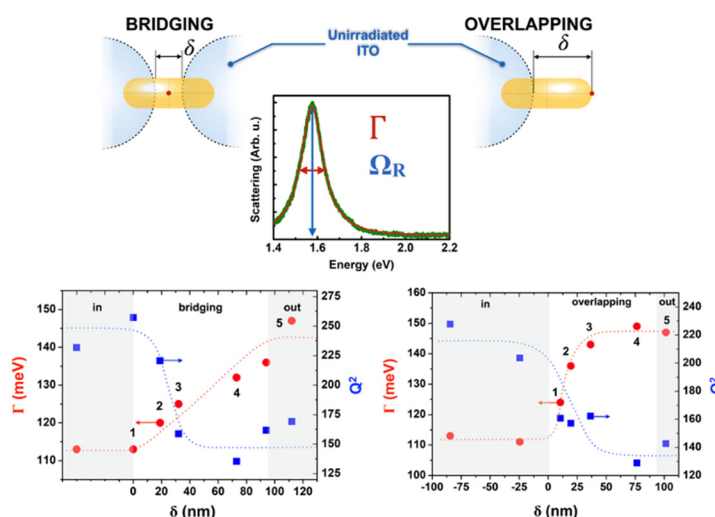


Figure 3: Schematics depicting the two main spatial arrangements of a nanorod over a  $\text{Xe}^+$  irradiated nanopattern derived using a nanosphere monolayer mask (top). The width of the resonance ( $\Gamma$ ) and the corresponding quality factor ( $Q^2$ ) plotted as a function of the relative position of the rod over the nanopattern (bottom).

## Related publications

- [1] D. Zámbo, D. P. Szekrényes, S. Pothorszky, N. Nagy, A. Deák: *SERS Activity of Reporter-Particle-Loaded Single Plasmonic Nanovoids*, J. Phys. Chem. C, 122:(41) 23683–23690 (2018) <https://doi.org/10.1021/acs.jpcc.8b06716>
- [2] D. P. Szekrenyes, S. Pothorszky, D. Zambo, Z. Osváth, A. Deák: *Investigation of Patchiness on Tip-Selectively Surface Modified Gold Nanorods*, J. Phys. Chem. C, 122:(3) 1706–1710 (2018) <https://doi.org/10.1021/acs.jpcc.7b11211>
- [3] Z. Zolnai, D. Zámbo, Z. Osváth, N. Nagy, M. Fried, A. Németh, S. Pothorszky, D. P. Szekrényes, A. Deák: *Gold Nanorod Plasmon Resonance Damping Effects on a Nanopatterned Substrate*, J. Phys. Chem. C, 122:(43) 24941–24948 (2018) <https://doi.org/10.1021/acs.jpcc.8b07521>

# NON-DESTRUCTIVE EVALUATION SYSTEM FOR THE INSPECTION OF OPERATION-INDUCED MATERIAL DEGRADATION IN NUCLEAR POWER PLANTS

(EU H2020 - Grant agreement № 755330.)

*A. Gasparics and G. Vértesy*

The long-term operation (LTO) of existing nuclear power plants (NPPs) has already been accepted in many countries as a strategic objective to ensure adequate supply of electricity over the coming decades. In order to estimate the remaining useful lifetime of NPP components, LTO requires reliable tools. The objective of EU H2020 project: "Non-destructive Evaluation System for the Inspection of Operation-Induced Material Degradation in Nuclear Power Plants" (NOMAD - <https://nomad-horizon2020.eu/>) is the development, demonstration and validation of a non-destructive evaluation tool for the local and volumetric characterization of the embrittlement in operational reactor pressure vessels (RPVs). In order to address these objectives, the following steps will be taken:

- Development and demonstration of a non-destructive evaluation (NDE) tool for the characterization of RPV embrittlement, especially accounting for material heterogeneities and exceeding the existing information from surveillance programs.
- Extension of the existing database of RPV material degradation by adding correlations of mechanical, microstructural and NDE parameters as well as including quantification of reliability and uncertainty.
- Application of the developed tool to cladded material resembling the actual RPV inspection scenario.

NOMAD takes into account the priorities of reactor operation, responding to stringent safety requirements from regulators, and seeks to foster convergence of nuclear safety approaches. The approach to be developed within NOMAD will deliver information complementary to and exceeding the information obtained by destructive tests of surveillance samples, which are currently assumed to represent the whole component and do not take into account possible local material variations. NOMAD aims to fulfil requirements for nuclear safety in the framework of assessment of lifetime operation. Thereby, it covers the specific challenge and scope of the call: Continually improving safety and reliability of Generation II and III reactors.

The NOMAD consortium gathers nine important institutions in the field of European nuclear energy and development of the non-destructive techniques, all stakeholders in the assessment of the lifetime operation of NPPs. The consortium has been formed by Fraunhofer Institute for Non-destructive Testing IZFP (Germany, coordinator), SCK•CEN Belgian Nuclear Research Centre (Belgium), VTT Technical Research Centre of Finland Ltd. (Finland), SVTI Swiss Association for Technical Inspections (Switzerland), Coventry University (Great Britain), Hungarian Academy of Science - Centre for Energy Research (Hungary), Paul Scherrer Institut (Switzerland), Tecnatom S.A. (Spain), HEPENIX Technical Service Ltd. (Hungary).

Our institute contributes to the NOMAD project with own micromagnetic testing method: so called Magnetic Adaptive Testing (MAT). MAT is a recently developed method for non-destructive characterization of ferromagnetic materials which is based on systematic measurement and evaluation of minor magnetic hysteresis loops. This method will be tested and evaluated regarding its applicability for the determination of the material changes and the variation of the material properties during exposure to neutron irradiation.

As shown in our several previous research activities, MAT provides more sensitivity for material degradation than the major hysteresis loop and has an improved feature of measurement error suppression. An additional significant advantage of this method is that there is no need for magnetic saturation of the measured samples, which eases the practical application.

A specially designed Permeameter with a magnetizing/sensing yoke is applied for measurement of families of minor loops of the magnetic circuit differential permeability. The magnetizing coil is fed with a triangular waveform current with step-wise increasing amplitudes and with a fixed slope magnitude in all the triangles. The voltage signal in the pick-up coil is proportional to the differential permeability of the magnetic circuit. The MAT evaluation delivers large set of so-called magnetic descriptors from the measured data. The optimal descriptor as an output is selected by careful correlation analysis.

Even in the early phase of the project realization, we could obtain promising experimental results on Charpy and on block type specimens that were aged by thermal treatments or neutron irradiations. An example obtained on Charpy specimens are made of 22NiMoCr37 material can be seen in Figure 1; where the optimally selected MAT descriptor is seen as the function of the neutron fluence. Here we got monotonous correlation with the degree of irradiation, the scattering was ~5%, while the difference between samples irradiated by  $5.1 \times 10^{19}$  n/cm<sup>2</sup> and  $1 \times 10^{20}$  n/cm<sup>2</sup> achieved the 13% and 30%, respectively.

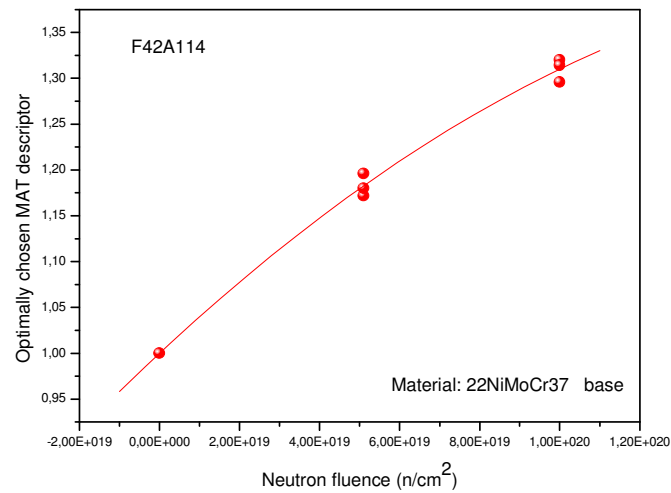


Figure 1: The output of the MAT method (the value of the descriptor) as the function of the independent parameter (neutron fluence) to be determined, in case of 22NiMoCr37 Charpy specimens

### Related publications

- [1] G. Vértesy, A. Gasparics, I. Szenthe, F. Gillemot, I. Uytendhouwen: "Inspection of reactor steel degradation by magnetic adaptive testing" in Special Issue "Non-destructive Inspection" of Materials – Open Access Journal (2019) [https://www.mdpi.com/journal/materials/special\\_issues/NDI\\_18](https://www.mdpi.com/journal/materials/special_issues/NDI_18)
- [2] G. Vértesy, A. Gasparics, I. Szenthe, F. Gillemot: "Magnetic nondestructive inspection of reactor steel clad blocks" in Global Journal of Advanced Engineering Technologies and Sciences GJAETS (2019) <https://www.gjaets.com>

# CONTACT ANGLE MEASUREMENTS WITH $R-\theta$ TYPE CAPILLARY BRIDGES

(OTKA FK 128901)

N. Nagy

Measurement of low contact angles is challenging. The investigated surface is immersed in the test liquid in case of the captive bubble method, therefore the characterization of swelling or porous layers is problematic. In case of the Wilhelmy balance method, the samples must have regular geometry and identical surfaces along the contact line, therefore coatings and thin films cannot be characterized. The developed indirect method combines the accuracy of the Wilhelmy method and the general usability of the sessile drop method.

The method is based on the use of a liquid bridge as a probe: the capillary bridge of the test liquid is stretched between the rim of the base of a cylinder and the investigated surface under equilibrium conditions. The advancing contact angle on the sample can be measured during the stepwise decrease of the bridge length. The receding contact angle is determined during the retraction of the cylinder. The contact angle is calculated from Delaunay’s analytical solution, while the necessary parameters are determined from the measured capillary force and from the automated analysis of the captured image of the bridge length. The contact angle on the cylinder’s rim changes continuously during the decrease and increase of the liquid length. The bridge is formed from a pendant drop. This unique feature ensures that the advancing contact line finds dry (not prewetted) surface.

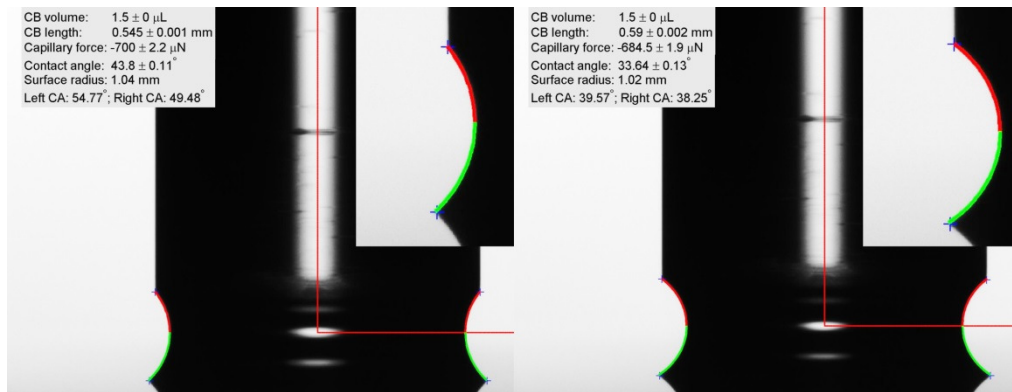


Figure 1: Typical results of the evaluation (left: approaching, right: reversal phase). The measurement was carried out on a thermal SiO<sub>2</sub> surface. The insets show the left magnified contours. Blue crosses: margins of the liquid bridge identified by the program; red lines: coordinate system; red and green curves: analytical solution for the top and bottom half of the capillary bridge, respectively. The main determined parameters are listed in the upper left corner.

Precalculated look-up tables were built up for *nodoid* type axisymmetric liquid bridges in the relevant parameter space. Parameter sensitivity investigations can be carried out based on these tables avoiding the difficulty of solution of the inverse problems. Another advantage of these tables can be found during the evaluation: the significant difference between measured and precalculated values indicates that the bridge is not axisymmetric or it is not in equilibrium. This verification ensures that the determined contact angle is reliable without the use of a second camera.

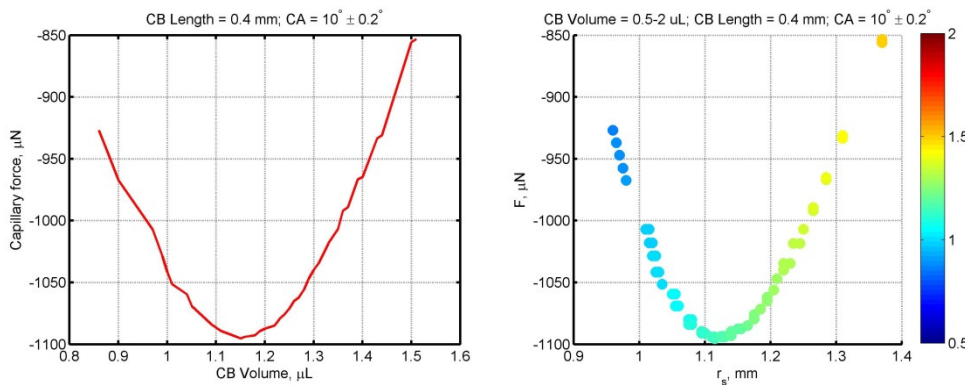


Figure 2: Sensitivity of the capillary force ( $F$ ) and the contact radius ( $r_s$ ) on the volume change of the capillary bridge. The colour bar shows the bridge volume. The capillary force of an evaporating liquid bridge can increase or decrease depending on the actual bridge geometry. The direction of change is determined by the change of the curvature of the nodoid surface.

The method was proved to be valid and highly sensitive, while its repeatability is so good as the repeatability of the sessile drop method with two times longer contact lines. The capability of the measurement of ultra-low contact angles was demonstrated on acid-treated superhydrophilic glass surfaces. The capillary force, as well as, the contact angle does not exhibit hysteresis on these surfaces. For more details, please refer:

N. Nagy: Contact angle determination on hydrophilic and superhydrophilic surfaces by using  $r$ - $\theta$  type capillary bridges, *Langmuir*, under review.

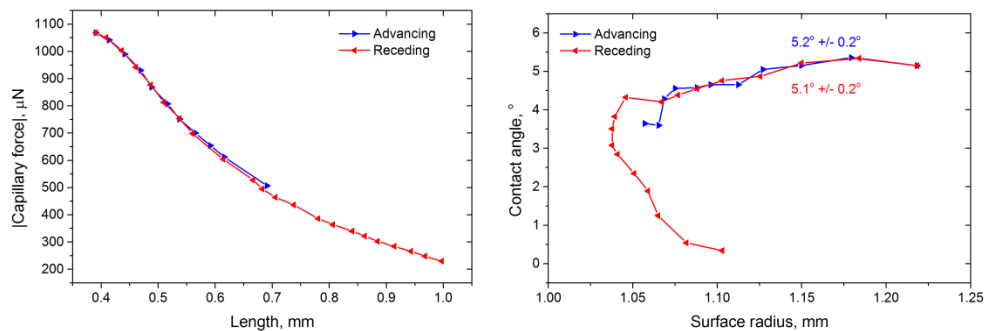


Figure 3: Capillary force and contact angle measured on an acid-treated glass slide. The capillary force does not exhibit hysteresis. The advancing and receding contact angles are equal within their standard deviation.

# IN SITU MONITORING OF ZrO<sub>2</sub> SURFACES DURING OXIDATION

(CAK, OTKA K115852)

P. Petrik, A. Romanenko, B. Kalas, L. Peter, T. Novotny, E. Perez-Fero, E. Agocs, T. Lohner, Z. Hozer, N. Nagy

One of the major applications of Zr is its use as cladding tubes in nuclear power plants. The corrosion and oxidation of different Zr alloys is an intensively investigated major safety issue. We used ellipsometry to characterize surfaces of zirconium tubes and plates for nuclear applications. We have shown earlier that ellipsometry can be used even on the surface of tubes with a diameter of 9.1 mm, when applying proper focusing. We also determined reference refractive indices for both zirconium and zirconium oxide, and demonstrated the capability of ellipsometry for the determination of the thickness and refractive index of the surface oxide applying different oxidation parameters. In this study, we characterized processed zirconium surfaces using the technique developed in our previous work. We used both ultra violet-visible-near infrared and mid-infrared ellipsometry to study the thicknesses of the surface layers as well as the dielectric functions of both the layers and the substrate. We also developed a heat cell that allows multiple angle of incidence ellipsometry measurement at elevated temperatures. We used this setup to monitor the temporal behaviour of hydrogenated and oxidized zirconium surfaces.

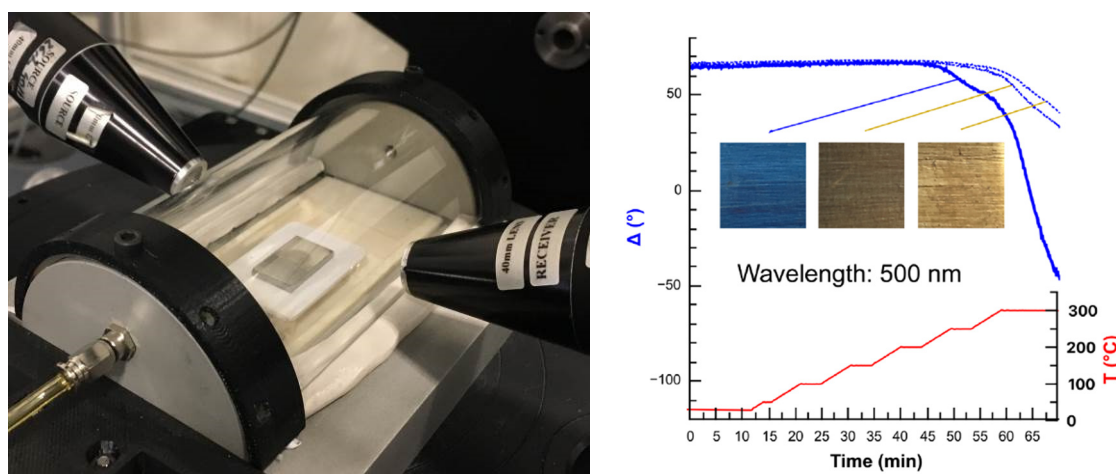


Figure 1: Left-hand side: Hydrogen-filled E125 zirconium wafer mounted on the heating stage in the cell for environmental ellipsometry. The ring-shaped spot in the middle of the wafer is the part that has been processed using electrochemical hydrogenation. Right-hand side: In situ ellipsometry measurements on three identical zirconium substrates of an E125 alloy processed under different conditions. The red curve shows the temperature profile. Blue curves are the  $\Delta$  (phase shift – the ellipsometric angle that is more sensitive to the change of thickness of the surface layer) values measured by ellipsometry at the wavelength of 500 nm (dotted lines show measurement under Ar flow). The solid line is a measurement in air at a temperature of 28 °C and humidity of 41%. In the inset, showing the samples after the heat treatment, the different colours reveal different thicknesses of surface layers caused by oxidation.

## Related publication

- [1] P. Petrik, A. Romanenko, B. Kalas, L. Péter, T. Novotny, E. Perez-Feró, B. Fodor, E. Agocs, T. Lohner, S. Kurunczi, M. Stoica, M. Gartner, Z. Hózer: *Optical Properties of Oxidized, Hydrogenated, and Native Zirconium Surfaces for Wavelengths from 0.3 to 25  $\mu\text{m}$  - A Study by Ex Situ and In Situ Spectroscopic Ellipsometry*, Phys. Status Solidi. 1800676. (2019) doi:10.1002/pssa.201800676

# MULTILAYERS FOR TUNEABLE RESONANCE IN ELLIPSOMETRIC BIOSENSORS

(OTKA K115852 and M-ERA.NET WaterSafe)

B. Kalas, A. Romanenko, K. Ferencz, P. Petrik

For biosensing applications Bloch surface waves (BSW) can be utilized that are excited at the surface of one-dimensional photonic crystals (1DPC). In the ultraviolet (UV) wavelength range numerous proteins have characteristic absorption peak so measuring in this range selective measurements can be carried out. The main advantage of BSW-based sensors compared to the structures used in surface plasmon resonance (SPR) is the tuneability of the resonance wavelength at which the biosensor operates. The resonance wavelength can be easily tailored by changing the layer thicknesses or by modulating the optical properties of the applied materials. Other advantage of BSW is that by using 1DPC structures narrower dip and bigger propagation length (and thus enhanced biosensor performance) can be achieved in the wavelength spectra due to the small absorption (no metal layers are applied in the structures).

In this work we realised a structure by alternating  $\text{SiO}_2$  and  $\text{ZrO}_2$  nanolayers and thus we constructed a 1DPC suitable for biosensing application in the UV range. The optical measurements were carried out in a self-made Kretschmann-Raether flow cell combined with a spectroscopic ellipsometer (Woollam M-2000DI).

$\text{SiO}_2$	8 nm
$\text{ZrO}_2$	8 nm
$\text{SiO}_2$	160 nm
$\text{ZrO}_2$	45 nm
$\text{SiO}_2$	160 nm
$\text{ZrO}_2$	45 nm
$\text{SiO}_2$	160 nm
Fused Silica substrate	

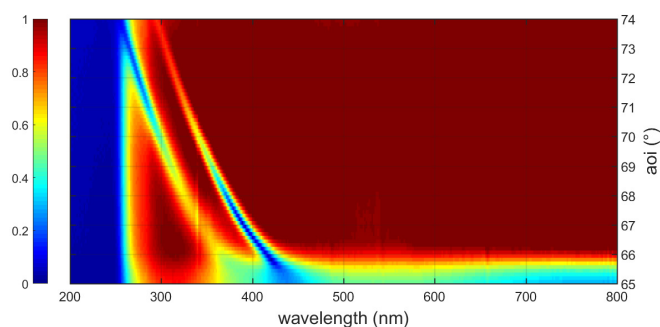
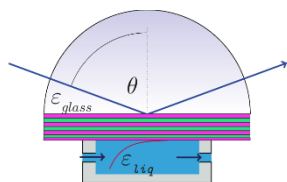


Figure 1: The schematic figures of the 1DPC structures and the used flow cell

Figure 2: The measured reflection map (normalized intensity of  $p$ -polarized reflection) of the 1DPC structure in the flow cell. The vertical axis shows the angle of incidence in degrees.

## Related publication

- [1] B. Kalas, E. Agocs, A. Romanenko, P. Petrik: *In Situ Characterization of Biomaterials at Solid-Liquid Interfaces Using Ellipsometry in the UV-Visible-NIR Wavelength Range*, Phys. Status Solidi. 1800762. (2019) doi:10.1002/pssa.201800762.

# SUSTAINABLE AUTONOMOUS SYSTEM FOR NITRITES/NITRATES AND HEAVY METALS MONITORING OF NATURAL WATER SOURCES

(„WaterSafe”, M-ERA.NET-2014, NKFI-OTKA: NN 117847)

M. Fried A. Saftics, S. Kurunczi, P. Petrik, Z. Labadi

The international (with Romanian and University of Pannonia partners) project („WaterSafe”) aimed to develop a new autonomous system based on micro electrochemical sensors and ultra-thin solar cells for concentration measurement of different ionic species in natural water sources.

It focused on three directions: 1) new materials with high efficiency in solar energy harvesting and fabrication of small ultra-thin solar cells together with the power stabilizing device, able to supply the needed voltage to the sensors and electronics module; 2) new microsensors and materials for detection of nitrites/ nitrates and heavy metals in water; 3) low cost autonomous energy system integration and fabrication.

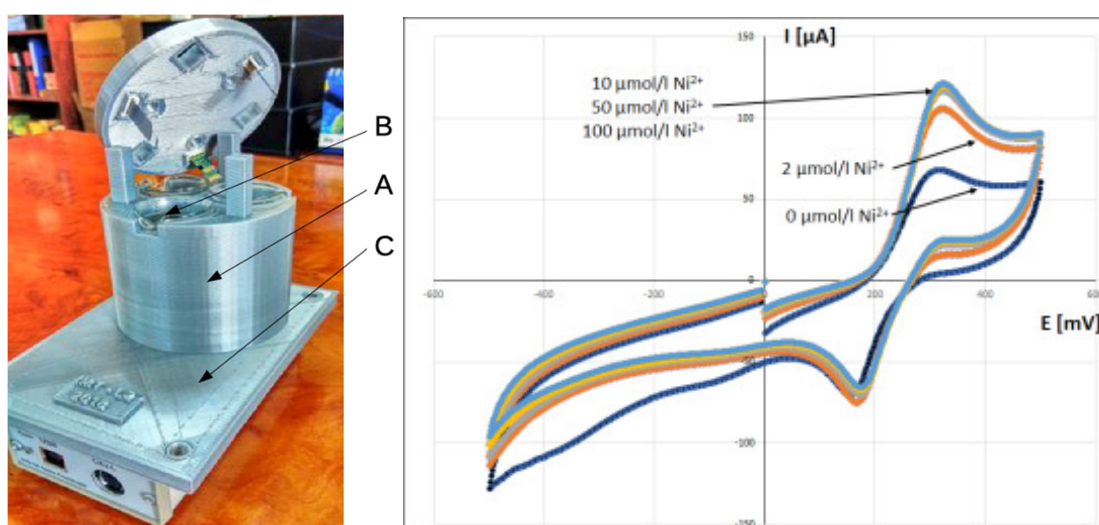


Figure 1: (Left-hand side) Measurement set-up: A -cylindrical camera B - 3 electrochemical cells C - data acquisition and display. (Right-hand side) CV curves of Ni sensing filament layers with different Ni concentrations.

We (MFA) investigated the developed (by University of Pannonia) metal-ion-bonding (Ni, As) special proteins (flagellar filaments) by optical (Spectroscopic Ellipsometry) and electrochemical (Cyclic Voltametry) methods. We performed promising electrochemical measurements with these new types of sensor-chips. The latest results were checked by comparative control measurements performed by partners from NANOM (Brasov, Romania), proving that the sensor-chip (protein) stability is good enough and even the sensor chips can be re-used after 1 month and chemical cleaning. This later investigation series prove that the prepared chips can be used after several months and more than once.

More information about the results of the project can be read on the webpage of the project:

[http://www.icf.ro/pr\\_2016/WaterSafe/Obtained\\_results.html](http://www.icf.ro/pr_2016/WaterSafe/Obtained_results.html)

# DIFFUSION AND REACTION KINETICS GOVERNING SURFACE BLISTERING IN RF SPUTTERED $a\text{-Si}_x\text{Ge}_{1-x}\text{:H}$ THIN FILMS

M. Serényi, A. Hámori and B. Kalas

The structural and surface quality of the material is one of the most critical issues regarding of their large scale application in electronic devices based on hydrogenated amorphous silicon (a-Si:H) [1], germanium (a-Ge:H) [2] and a-SiGe:H. Atomic hydrogen migration occurs in the amorphous network. The high temperatures applied during growth of those materials, e. g. during chemical vapour deposition, or device operations enhance the diffusion of H atoms, in particular of those liberated from their bonds to the host atoms. Such enhanced diffusion favours the migration of H atoms towards nanovoids where they very likely form molecular  $\text{H}_2$  since the reaction  $2\text{MeH} \rightarrow \text{H}_2 + \text{Me-Me}$  is an exothermic one (Me indicates the host atom: Si or Ge). The accumulation on the wall of voids causes the evolution of hydrogen bubbles and then the formation of blisters. Some efforts have been made to understand the microscopic mechanisms determining the rupture of the MeH bonds and formation of  $\text{H}_2$  rich voids at the origin of the blisters in order to prevent them. The objective of this work was to find a way to determine the threshold temperature below which surface blistering does not occur in hydrogenated  $a\text{-Si}_x\text{Ge}_{1-x}$ ,  $0 \leq x \leq 1$ . This is achieved by a theoretical model that takes into account both the kinetics of the rupture of the MeH bonds and, in particular, the diffusion of the atomic H. The experimental results suggesting our theoretical approach have been obtained by Secondary Neutral Mass Spectrometry (SNMS) and by surface light reflectivity measurements, as regards of the time of the onset of blistering and its activation energy by Arrhenius plots. The data supplied by the latter plots allow the validation of the theoretical model. The calculated critical temperature for blistering is of the same order of magnitude as the experimentally observed one. The experimentally determined Vegard's law-like dependence of the blistering activation energy [3,4] on the Si concentration in the  $a\text{-Si}_x\text{Ge}_{1-x}$  alloys is interpreted by a simple formula and related 3D-like diagram.

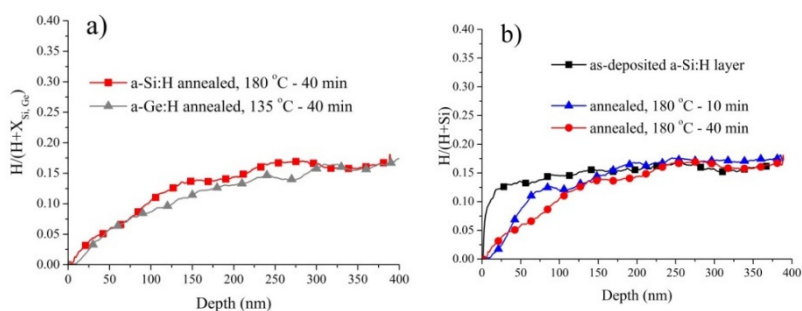


Figure 1: SNMS depth profile of hydrogen in annealed a-Si and a-Ge layer after 40 minutes of annealing (a), and after 10 and 40 minutes in a-Si layer (b)

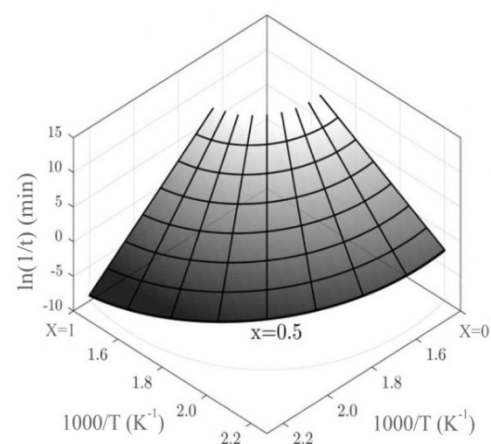


Figure 2: Graphical representation of blistering onset vs. temperature in a polar coordinate system. The left-hand vertical plane belongs to the Si and the right one to the Ge Arrhenius plot.

## Related publications

- [1] C. Frigeri, M. Serényi, Zs. Szekrényes, K. Kamarás, A. Csik, N. Q. Khánh: *Effect of heat treatments on the properties of hydrogenated amorphous silicon for PV and PVT applications*, Sol. Energy **119**: 225-232 (2015) <https://doi.org/10.1016/j.solener.2015.07.004>
- [2] M. Serényi, C. Frigeri, A. Csik, N. Q. Khánh, A. Németh, Z. Zolnai: *On the mechanisms of hydrogen induced blistering in RF sputtered amorphous Ge*, CrystEngComm, **19**: 1486-1494. (2017) <https://doi.org/10.1039/C7CE00076F>
- [3] M. Serényi, C. Frigeri, R. Schiller: *Vegard's-law-like dependence of the activation energy of blistering on the x composition in hydrogenated a-Si<sub>x</sub>Ge<sub>1-x</sub>*, J. Alloys Compd. **763**: 471-477 (2018) <https://doi.org/10.1016/j.jallcom.2018.05.269>
- [4] M. Serényi, A. Csík, A. Hámori, B. Kalas, I. Lukács, Zs. Zolnai and C. Frigeri: *Diffusion and reaction kinetics governing surface blistering in radio frequency sputtered hydrogenated a-Si<sub>x</sub>Ge<sub>1-x</sub> (0 ≤ x ≤ 1) thin films*, Thin Solid Films, in press.

# MAKYOH TOPOGRAPHY

*Ferenc Riesz*

Makyoh topography is an optical tool for the qualitative flatness testing of specular surfaces, based on the defocused detection of a collimated light beam reflected from the tested surface. By inserting a square grid into the path of the illuminating beam, the height map can be calculated by integrating the gradients obtained from the distortion of the grid's reflected image (quantitative extension).

In the past year, activities were concentrated both on methodology and applications.

Applying the grid creates not only the structured illumination necessary to calculate the large-scale surface shape, but aids in qualitative visual evaluation as well. If the grid's image is sharp, the simultaneous qualitative observation of the sample morphology in high resolution is possible within the same image, in addition to the low-resolution height map. We have studied the conditions for this sharpness [rie18]. A sharpness criterion was given based on a wave optics model, while the necessary instrumental settings were calculated using geometrical optics. In addition, it was shown that only lens-based set-ups allow positioning of the grid to be sharp on the Makyoh image; for mirror-based set-ups this is not possible because of geometrical instrumental constraints (Fig. 1).

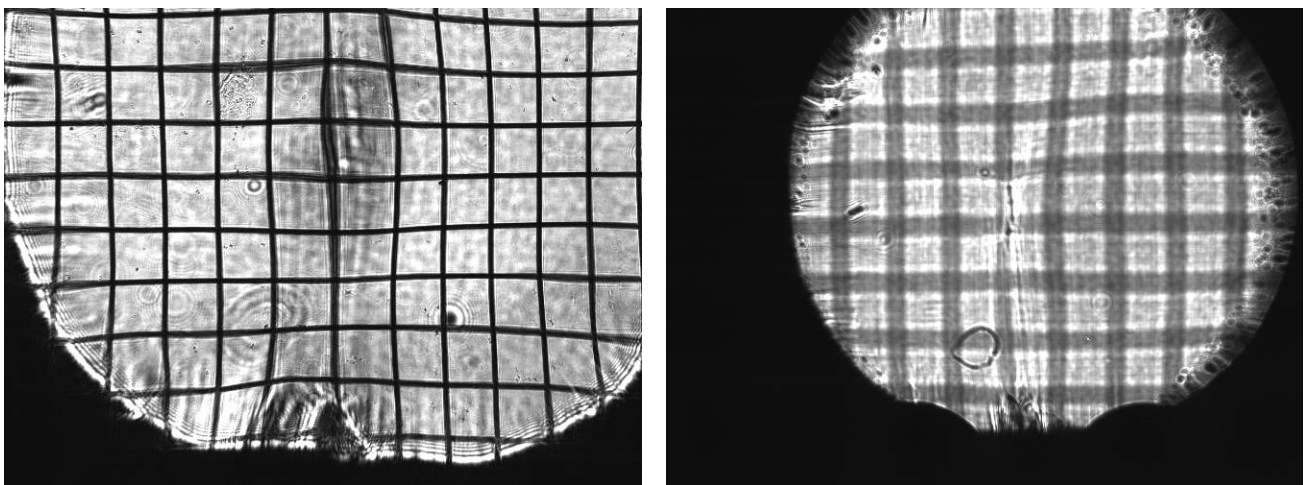


Figure 1: Makyoh-topography image of a silicon wafer using structured illumination. Left panel: lens-based set-up, showing a sharp grid image; right panel: mirror-based set-up, showing diffraction effects masking the Makyoh image.

For in-house research, deformation measurements of Si-based thin-film ( $\text{SiO}_x$ ,  $\text{SiN}_x$ ) structures were performed for stress evaluation.

## **Related publication**

- [1] F. Riesz: *Structured-illumination Makyoh-topography: optimum grid position and its constraints*, Surf. Topogr. Metrol. Prop. 6 45009. (2018) doi:10.1088/2051-672x/aaeb86.

# REFRACTIVE INDEX VARIATION OF MAGNETRON-SPUTTERED A-Si<sub>1-x</sub>Ge<sub>x</sub> BY “ONE-SAMPLE CONCEPT” COMBINATORY

(OTKA K115852 and M-ERA.NET WaterSafe)

T. Lohner, B. Kalas, P. Petrik, Z. Zolnai, M. Serényi and G. Sáfrán

Gradient a-Si<sub>1-x</sub>Ge<sub>x</sub> layers have been deposited by “one-sample concept” combinatorial DC magnetron sputtering onto one-inch-long silicon slabs (Fig. 1). Characterizations by electron microscopy, ion beam analysis and ellipsometry show that the layers are amorphous with a uniform thickness, small roughness and compositions from x = 0 to x = 1 changing linearly with the lateral position.

By focused-beam mapping ellipsometry we show that the optical constants also vary linearly with the lateral position, implying that the optical constants are linear functions of the composition (Fig. 2). Both the refractive index and the extinction coefficient can be varied in a broad range for a large spectral region. The precise control and the knowledge of layer properties as a function of composition is of primary importance in many applications from solar cells to sensors.

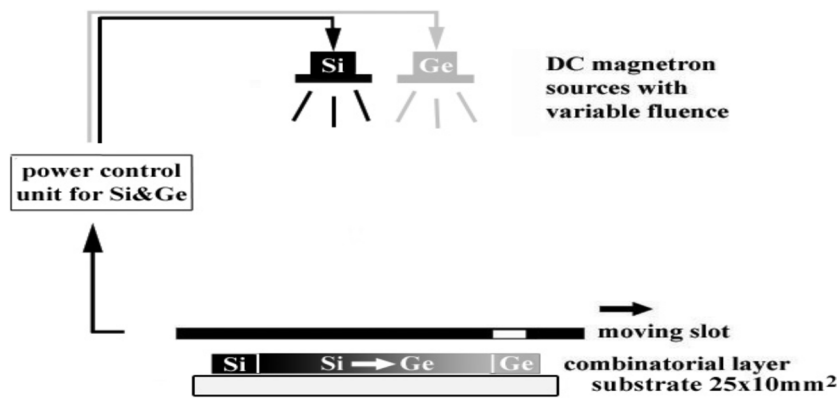


Figure 1: Set-up used for the combinatorial deposition of the a-Si<sub>1-x</sub>Ge<sub>x</sub> layer

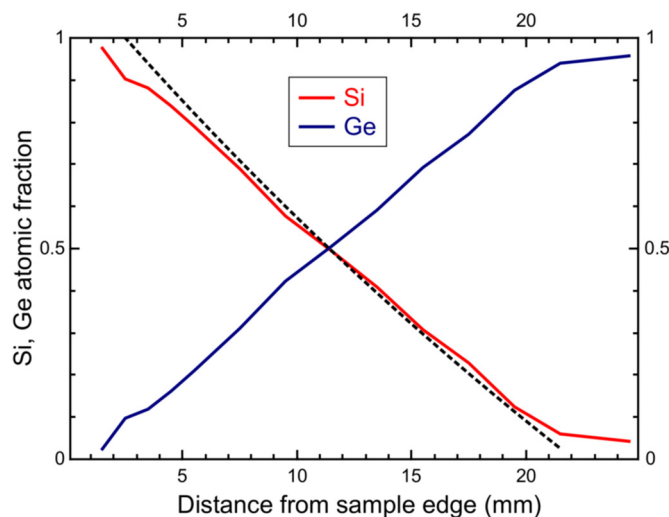


Figure 2: Atomic fraction as a function of position along the center line of the combinatorial sample measured by Rutherford backscattering spectrometry. The black dotted line shows the distribution of the atomic fractions of Si and Ge based on the calibration using energy dispersive spectrometry (EDS) in a scanning electron microscopy.

# KOFAH - ADVANCED FUNCTIONAL MATERIALS FOR AUTONOMOUS SENSOR NETWORKS

*G. Battistig, Zs. Baji, I.E. Lukács, Gy. Molnár, N.Q. Khánh, A.E. Papp, L. Pósa, J. Radó, S. Soleimani, M. Szappanos, E. Tunyogi, J. Volk, Zs. Zolnai*

In 2018, we continued the work on i) piezoelectric thin films, ii) piezo-MEMS sensors and vibrational energy harvesters as well as on iii) the integration of sensor node demonstrators, such as vibration analyser, tyre sensor, and intelligent bondage.

The project parallelly comprises all three levels: material (i), device (ii) and system (iii).

## **Material: piezoelectric thin films**

In order to conduct research on advanced CMOS compatible piezoelectric thin films a new sputtering system was purchased and installed. Apart from general use of the tool the project-specific goal is to deposit piezoelectric AlN, and alloyed XAlN (X=Sc, Cr, etc.) layers. High quality piezoelectric layers are essential components of the micro-vibration energy harvesters and actuators targeted by the project.

The setup containing three-magnetrons with the appropriate SW enable both automatic and manual operation. Two of the magnetrons can be operated in DC or pulse DC mode, whereas the third one is working in RF mode. The system can handle various size substrates ranging from small pieces up to 6" wafers. The ultimate vacuum of the load-lock equipped deposition chamber is  $< 1 \times 10^{-7}$  mbar. Deposition or reactive deposition of single layers and multilayer structures as well as co-deposition is also possible.



*Figure 1: The VAKSIS sputtering system in operation in the clean-room of the Lab (building 29.b)*

The related tender was successfully completed in 2017 and the contract with VAKSIS Co, Turkey signed in September 2017. In order to provide the required footprint and services our staff removed an outdated system and reorganized the lab. The company delivered and installed the system in due time (May 2018), so the introduced technology became an organic part of the processing line (Fig. 1). Though special emphasis was put on the formation of piezoelectric layers, other projects will also benefit from the facility.

The optimization of AlN deposition conditions through more than 50 tests led to a reasonable trade-off between deposition rate (400-500 nm/h) and thickness uniformity ( $\pm 2-3\%$ ), whereas the optimum sample temperature was found to be around 300 °C. According to cross-sectional SEM analysis and X-ray diffraction the optimized AlN layers show columnar crystal structure with high degree of c-axis orientation. The obtained longitudinal piezoelectric charge constant was around 3 pC/N for 0.7-1.4  $\mu\text{m}$  thick AlN, which agrees well with literature data. These preliminary tests provide a solid starting point for the upcoming research on high-piezoelectric-constant XAlN alloys.

## **Device:**

### *a) Piezo-MEMS sensors*

In 2018 we continued the work on spiral shaped piezo-MEMS accelerometers and started research also on metal substrate based vibrational energy harvesters. In the former part we demonstrated a low-volume, stress-free, piezoelectric micro-electromechanical system (MEMS) cantilever array for fully implantable hearing aids [1]. The 9-element spiral-matrix is sensitive to middle part of audible frequency range (1200-2300Hz) through the proper resonant frequency of the individual spirals tuned by dimensions of the cantilevers based on the results of Comsol simulations.

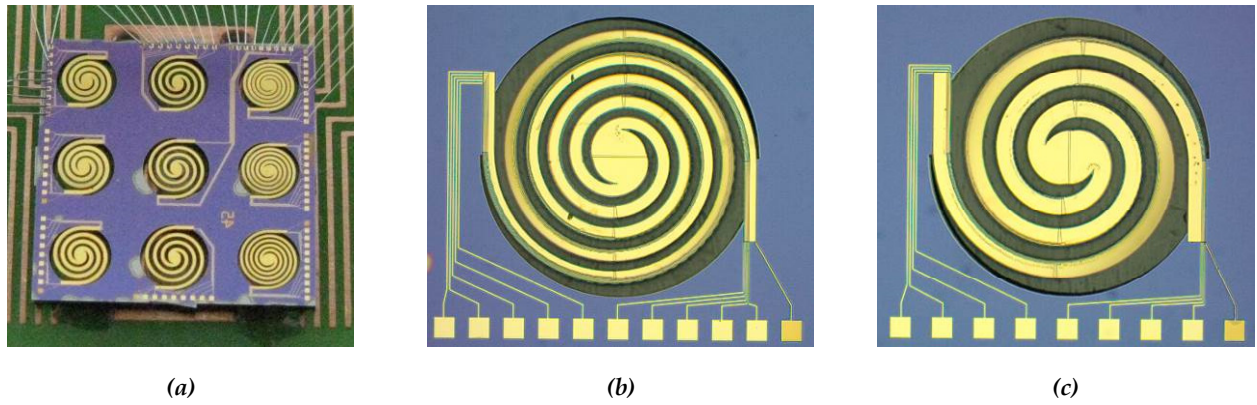


Figure 2: 9-element wire bonded Fermat-spiral array (a) and two typical cantilevers (four- and three-turn types, b and c, respectively)

Moreover, each spiral was designed with a multielectrode structure fitted to various mode shapes (Fig 3) to collect more than one ambient frequencies with a single cantilever.

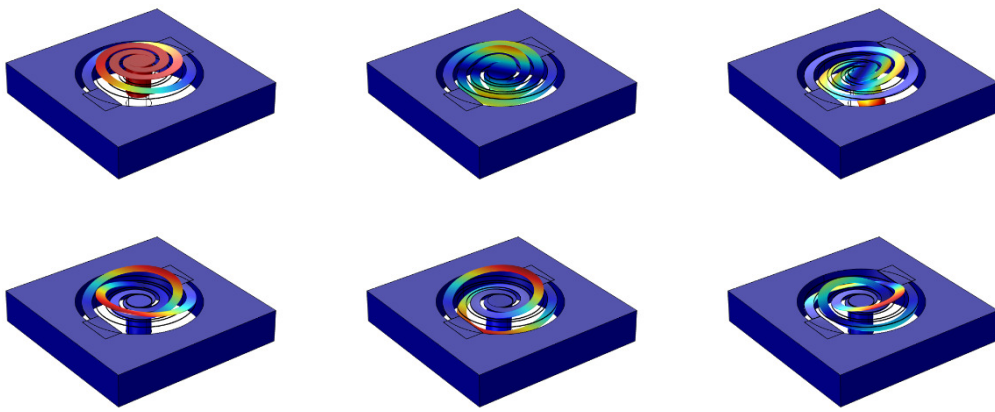


Figure 3: Simulation of various mode designs for multi-frequency accelerometers to optimize the electrode positions

The test device was fabricated by a 30-step micromachining process. Fermat spiral geometry ensures the reduced device footprint, which was formed by deep-reactive ion etching (DRIE). The uniformity of cantilever thickness is controlled by the Si-on-Insulator (SOI) wafer. The biocompatible piezoelectric material aluminum nitride (AlN) was deposited by reactive radio frequency (RF) sputtering from an AlN target.

The fundamental resonances and upper harmonics were collected for each cantilever by the laser Doppler vibrometer at the Technical University of Vienna. During the measurement the cantilevers were mounted on a minishaker which was excited by white-noise signal. The results show a good agreement between the theoretical and measured frequencies. In 2019, we will measure the generated electrical signal vs. the excitation frequency and acceleration, and test the mode selectivity of the optimized electrodes.

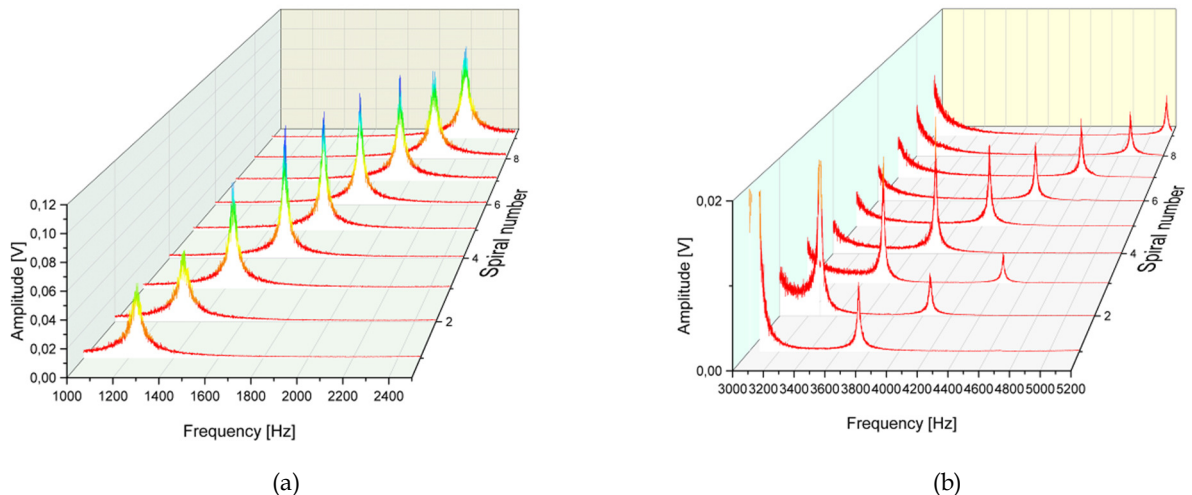


Figure 4: Laser Doppler vibrometer input voltage during white-noise excitation. The resonant frequencies fall in the range of 1200-2300 Hz (a) and harmonics in 3000-5200 Hz (b) depending on the geometry.

**b) Piezo-on-metal harvester**

As a second objective of the Device work-package, we started to optimize piezo-cantilevers for energy harvesting as well. In order to supply sufficient electrical power for autonomous sensor nodes using RF communication we need energy harvesters larger than the standard MEMS structures. For the 1-10 cm<sup>2</sup> area-range standard Si based technology is often found to be too expensive. Moreover, in harsh vibrational environment and for demanding applications, such as medical implants, the mechanical robustness of single crystalline Si is insufficient.

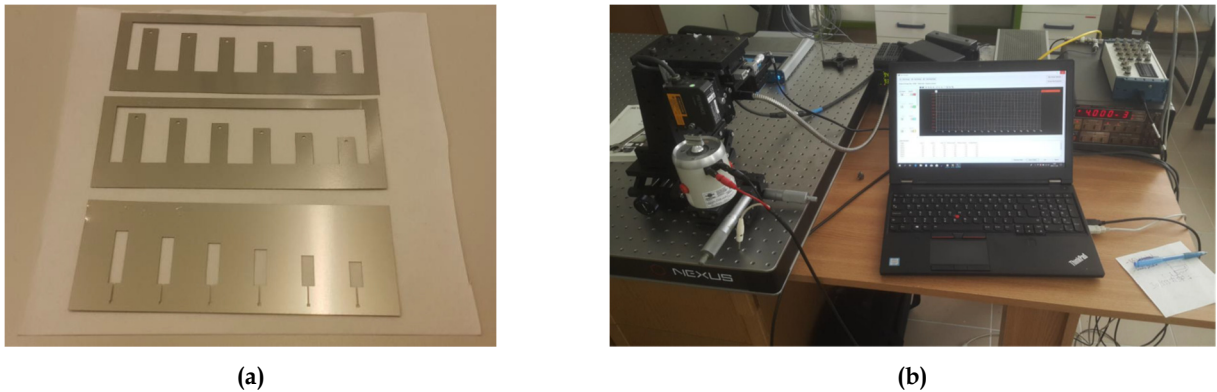


Figure 5: Ni and stainless-steel cantilever arrays after laser cutting (left upper and centre image) and the geometrically fitting stencil mask for top contact deposition (bottom left image) (a). Measurement setup for testing the output voltage and power of the piezo/metal harvester at controlled frequency and acceleration (b).

Hence, our aim was to combine MEMS technology with metal substrates. Stainless steel has a 50 times higher fracture toughness than single crystal Si. Moreover, the cantilever geometry was shaped at room temperature by high precision stencil laser cutting tool by our industrial partner (Alpha Assembly), which provides an economic technology compared to Si 3D micromachining. As harvester substrates we compared Ni (100  $\mu$ m) and stainless-steel (SUS 304, 80 and 120  $\mu$ m) sheets. Figure 5a shows the Ni and stainless-steel cantilever arrays. The length of the cantilevers was varied between 12-22 mm, expecting resonance frequencies in the 150-650 Hz range.

The simplified fabrication technology was implemented in the cleanroom. Pulsed DC sputtered AlN piezo layer of 1.2  $\mu$ m was deposited first in our new vacuum system (Vaksis) followed by the electron beam deposition of the top electrode through a stencil mask (Fig. 5a). Individual cantilever beams were simply cut by scissors and wire bonded before mounting them on the shaker based measurement setup (Fig. 5b). The obtained open circuit voltage was 430 mV at an acceleration of 9.81 m/s<sup>2</sup> (1G) for the 18 mm cantilever at resonance (201 Hz). At an optimal load resistance of 220 k $\Omega$  and output power of 540  $\mu$ W was obtained [2], which requires significant improvement in 2019. Nevertheless, we could demonstrate a simple, room temperature hybrid fabrication process for metal-MEMS harvesters.

**System:**

**a) Tyre deformation monitor**

3D MEMS force sensors mounted at the internal sidewalls of vehicle tyres continuously provide information about the actual mechanical deformation of the tyre in operation (Fig. 6). The monitoring of the elastic deformation and its sudden changes offers feedback about the load and friction via characterizing the shape of the tyre sidewalls.

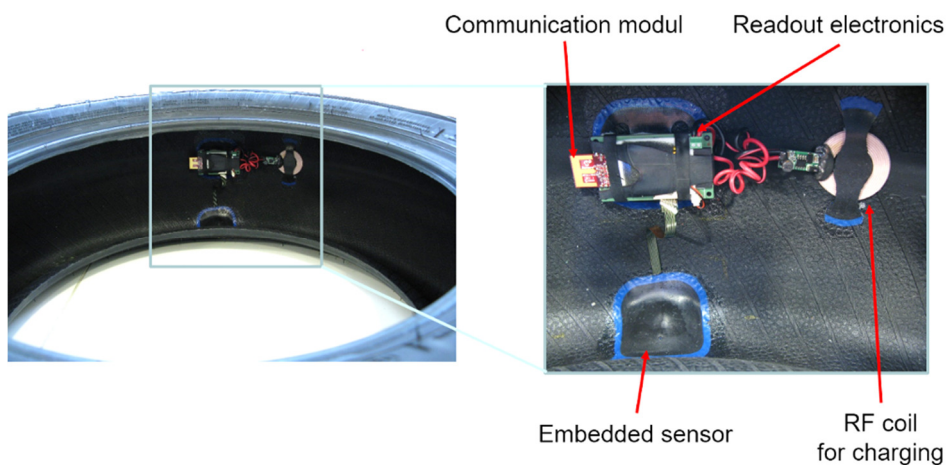


Figure 6: The integrated tyre monitoring test tool

The tyre deformation on a vehicle is proportional to the acting forces on the wheel – longitudinal, lateral, and vertical - carrying information on the contact between the tyre and road surface (figure 7). The accomplished application uses RF communication between the rotating wheels and vehicle control. The signal per rotation depends on the number of sensors mounted in the

wheel. The sampling frequency of 100 Hz fits well with the sampling frequency of the CAN bus communication of a car. We also integrated an RF coil for external charging of the battery of the readout electronics.

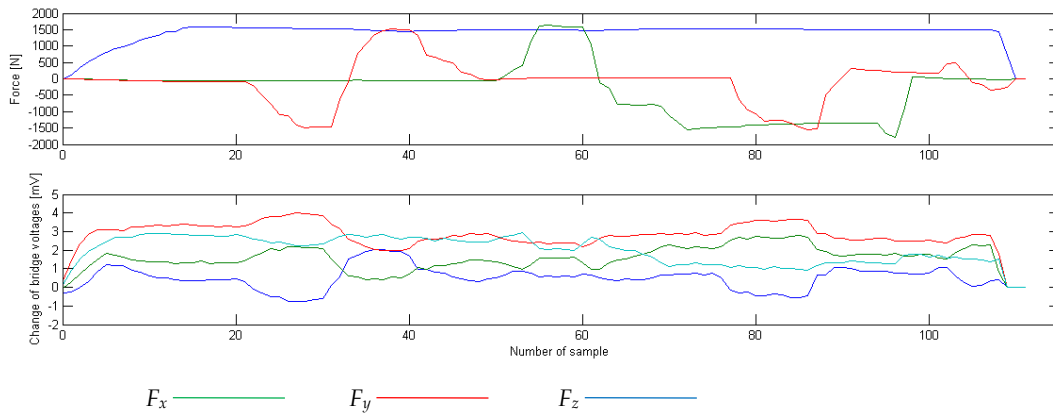


Figure 7: The correlation between the out-of-balance voltages of the 3D force sensor and the acting forces on the tyre.

A tyre equipped with an integrated sensor is being used on an autonomous Nissan Leaf for the preliminary test in co-operation with MTA SZTAKI (Fig. 8). Among the other positive results, we demonstrated the long operating lifetime of the system by operating the sensor for >100 km running mileage.



Figure 8: The test tyre mounted on the Nissan Leaf with the readout electronics placed in the trunk during the charging process.

**b) Vibration analyser**

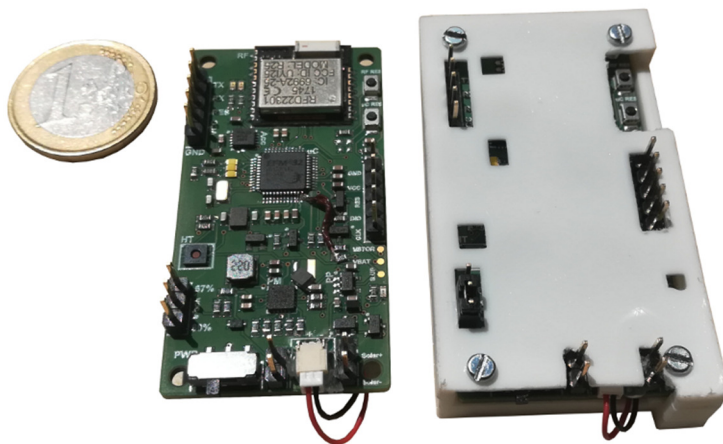


Figure 9: The second version of VibrAn with and without case (Euro for scale)

based on the weighed combination of user settings and ambient energy (Fig. 10). We tested and calibrated the system in laboratory environment with reference sensors, as well as on a vibrating duct in order to simulate real life applications.

Our vibration analyser – or VibrAn for short – is a complex, wireless, ambient energy powered and easy-to-use solution for vibration analysis. It was designed to incorporate the latest commercial technologies and achievements in the field of energy harvesting and wireless sensor networks with an emphasis on energy efficient spectrum estimation algorithms for embedded systems. This solution is implemented on a small printed circuit board and contains all the necessary commercial circuit components for hybrid energy harvesting; acceleration sensing; data acquisition, data storage and analysis; as well as wireless communication (Fig. 9) [3].

The on-board microcontroller was programmed to select the most energy-efficient data handling algorithm (direct transfer or embedded analysis)

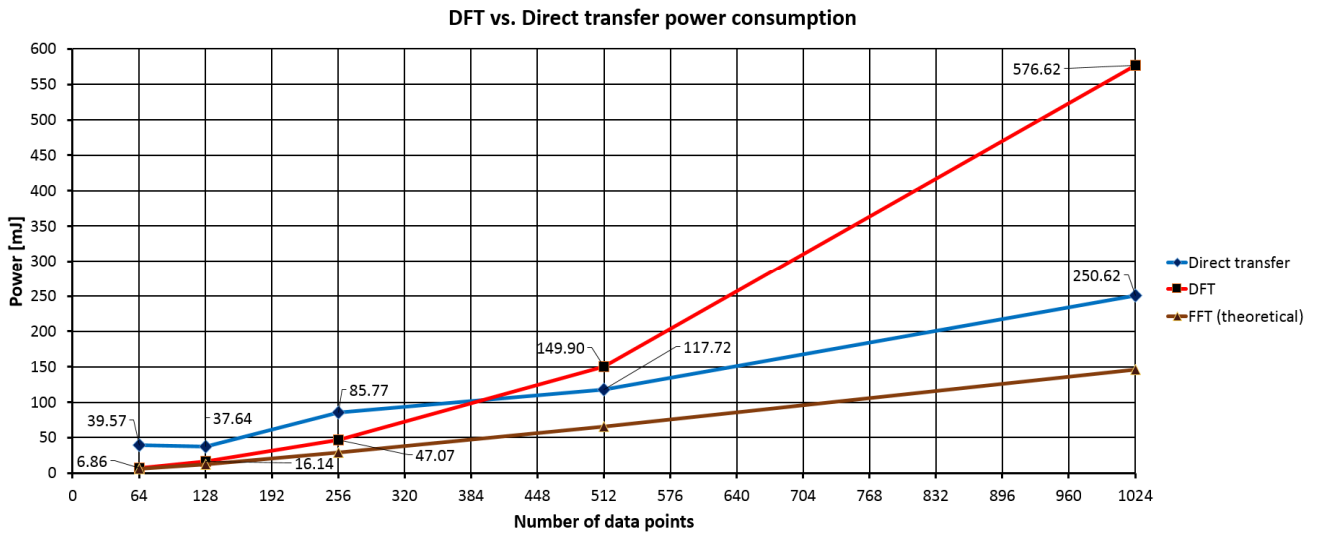


Figure 10: Power consumption comparison of three different data handling methods

The accelerometer is able to measure vibrations up to 100 Hz without aliasing, however, around 200 Hz it is guaranteed to appear. The maximum extracted power from the piezoelectric beam was 781  $\mu$ W with resistive load, and 244  $\mu$ W with complex load (energy management IC). The highest measured efficiency of the energy management chip (BQ25570) was 81%. In order to perform a 2000 data acceleration measurement (with RF data transmission) with the system 30 mW average power was needed. If this measurement was to be solely powered by energy harvesting, it around 2-3 hours would be required to harvest the necessary amount of energy. In the real life application (Fig. 11) we managed to harvest a total of 2.25 mJ energy in 4 hours and 20 minutes.

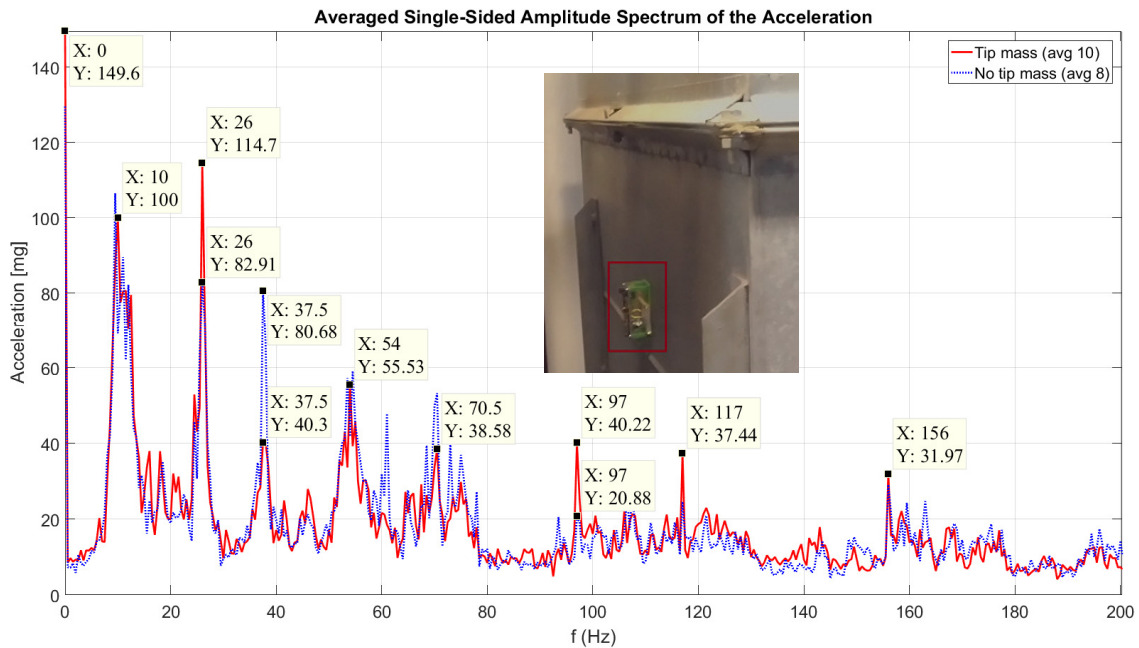


Figure 11: The vibration spectrum recorded by the sensor on the side-wall of the an air-duct in the engine room for air-conditioning of the clean room facility. The sensor offers early failure detection of air conditioner's fan.

The presented small device consists of commercially available components, provides an interface to study and test vibrational energy harvesters. In order to maximize the harvested energy, the main vibrational frequency of the piezoelectric cantilever can be tuned by a moving mass. The proposed system can support the R&D on energy harvesters by providing an interface to test new designs. Future work will focus on improving energy harvesting by incorporating our own energy harvester and decreasing RF communication power consumption by designing our own low power RF protocol. The final target is to achieve an autonomous system transforming the ambient energy into electrical energy.

**Related publications**

- [1] J. Radó, P. Udvardi, S. S. Lucky, K. Peter, I. Bársony, P. Révész, J. Volk: *Low-Frequency Piezoelectric Accelerometer Array for Fully Implantable Cochlear Implants*, PROCEEDINGS 2 : 13 Paper: 1059 (2018)
- [2] M. K. Tóth: *Vibrációs energiahasznosító eszközök készítése és minősítése*, BSc szakdolgozat, BM-VIKE, supervisor: J. Volk
- [3] M. Szappanos, J. Radó, G. Battistig, P. Földesy, J. Volk: *Energy*

# INVESTIGATION OF MEMRISTIVE STRUCTURES<sup>1</sup>

G. Battistig, Zs. Baji, I.E. Lukács, Gy. Molnár, N.Q. Khánh, A.E. Papp, L. Pósa, J. Radó, S. Soleimani, M. Szappanos, E. Tunyogi, J. Volk, Zs. Zolnai

Resistive switches or memristors are two terminal passive electric components, whose resistance can be reversibly varied between two or several states by the voltage is applied. They are built as a capacitor like metal-insulator-metal structure, in which the two electrodes are connected by a conductive filament of nanometer dimension. Despite their simple structure they show complex operation, which offers many promising applications. Using them as simple memory cell (RRAM) is close to commercialization. Memristors have approached or even exceeded the specifications of contemporary flash memories. However, their more promising complex applications, such as their integration as memory and processing unit in neuromorphic computing are still subjects of intensive research.

The NEMS group joined the cooperation with the group of András Halbritter at the Department of Physics of BME in studying resistive switches in 2017. That group has large experience in characterization of memristive systems ( $\text{Ag}_2\text{S}$ ,  $\text{AgI}$ ,  $\text{SiO}_x$  or  $\text{Nb}_2\text{O}_5$ ) using an STM arrangement. Relying on our nanofabrication expertise and facilities, the target of this collaboration is the development, characterization and optimization of on-chip resistive switches. The devices were initially fabricated by electron beam lithography, then further scaled down to  $<10$  nm by controlled electrical breakdown process. Recently nanofabricated  $\text{Ag}_2\text{S}$  and  $\text{SiO}_x$  resistive switches were successfully prepared and this research was continued in 2018. The devices are fabricated at MFA while the electrical characterizations are performed at BME. In 2018 OTKA grant (K 128534) was obtained for the collaborative research on nanometer scale resistive switching memory devices lead by András Halbritter.

In case of Ag based resistive switching devices the  $1/f$  type noise was studied at BME using the STM setup vs. the surrounding solid electrolyte ( $\text{Ag}_2\text{S}$ ,  $\text{AgI}$ ). As control experiments noise measurements were performed on pure Ag nanowires lacking any resistive switching media (see Figure 1, black dots). These Ag nanobridges were lithographically designed at MFA and thinned by feedback-controlled electromigration technique (see insets of Figure 1). The measurements revealed that the magnitude of the noise not, only the total resistance does depend on the surrounding material. This result implies that the noise arises from the internal fluctuation of the Ag nanowire rather than from environmental effects. The resistance dependence of the noise is quantitatively captured by a theoretical model (fitted lines in Figure 1). The article is under review at Nanoscale.

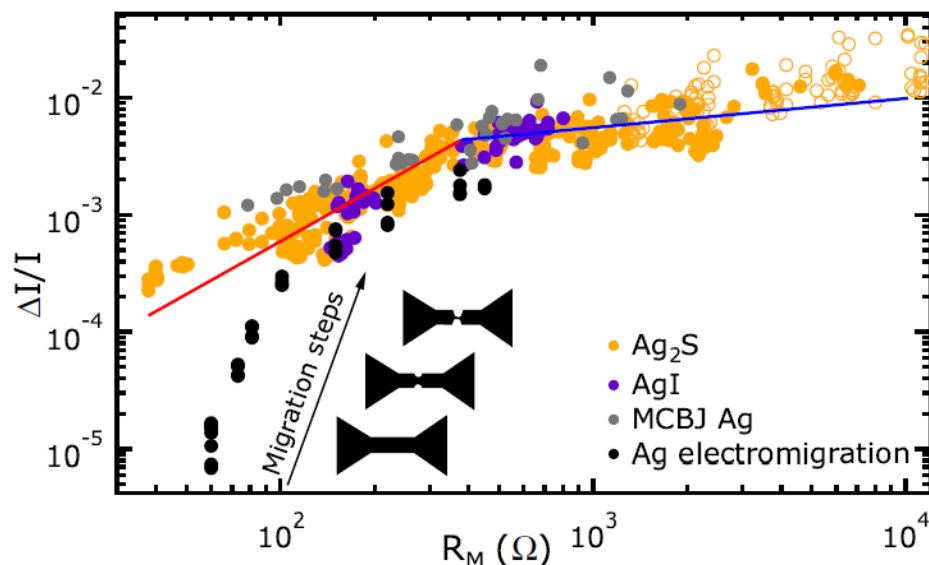


Figure 1: The current noise ratio values as a function of the mean resistance. Ag nano filaments were formed in STM based  $\text{Ag}_2\text{S}$  (yellow) and  $\text{AgI}$  (purple) memristive nanojunctions, as well as in pure Ag MCBJs (grey) and electromigrated Ag nanobridges (black). The blue and red lines represent the best fit to the  $\text{Ag}_2\text{S}$  data.

In  $\text{SiO}_x$  memristors the switching is based on the amorphization and crystallization of a Si rich region. In this memristive system a dead time effect can be observed: once the device is switched OFF, it is blocked in the OFF state for the period of the dead time. Tuning its length would have essential role in the application of  $\text{SiO}_2$  RRAM. Based on our paper, published in 2017, we further investigated the nature of the dead time. The measurements revealed that the dead time shows clear dependence on the pressure, but the Ar plasma treatment of the  $\text{SiO}_2$  surface has no effect, whatsoever. Furthermore, an aging effect was observed, as we “wrote and erased the device” several times, the length of the dead time increased.

Similar to the Ag based memristors, noise measurements were performed on graphene- $\text{SiO}_x$  resistive switching devices. The active region of the  $\text{SiO}_x$  switch is formed between graphene electrodes in a gap of few nm (see red region in Figure 2.c). This nanogap is created by electrical breakdown of initially contiguous graphene nanostripe, cut by electron-beam lithography

<sup>1</sup> In cooperation with Budapest University of Technology and Economics, Faculty of Natural Sciences, Institute of Physics

(Figure 2.a). By optimizing the geometry of the patterned graphene and the electrical breakdown protocol, we could break the graphene constrictions in a controlled way. The constrictions could be narrowed step by step and finally few nm (<5 nm) dimension gaps were generated. The low-frequency  $1/f$  type noise was measured at several stages of the breakdown process and finally obtained in the tunnelling regime. Afterwards, the  $\text{SiO}_x$  switching site was formed in the nanogap, and the noise was measured at the different memristor states. This systematic measurement allows the separation of the noise by the graphene electrodes from the noise of the resistive switch. In the near future noise measurement during the dead time is planned.

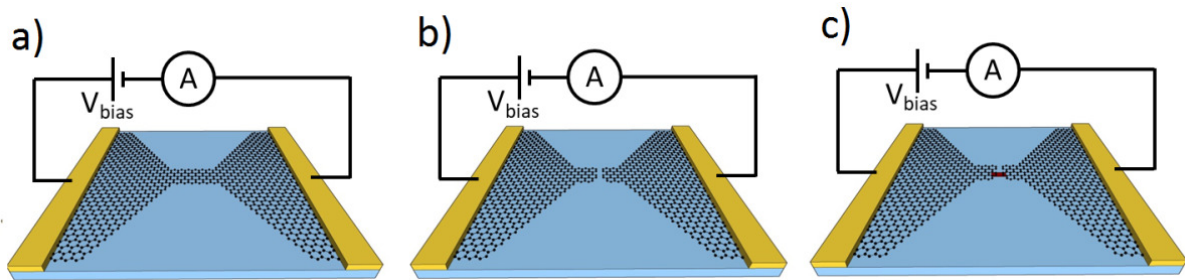


Figure 2: Illustration of the processing steps for forming of a nanometer-dimension  $\text{SiO}_x$  switch

Beside both memristive systems above, transition metal-oxides such as niobium oxide, tantalum oxide, vanadium oxide are also well-established resistive switching compounds. We plan to study those memristive systems at ultrasmall dimensions. The size limits for well controlled RRAM operation have to be established. Since BME had a significant experience in  $\text{Nb}_2\text{O}_5$  layer contacted in STM arrangement, it was the first material, which was realized in on-chip implementation. In the Nanotechnology laboratory several devices were fabricated to study the effects of the structure (vertical or lateral arrangement) and electrode materials (graphene, gold, niobium). The structures were patterned by electron beam lithography, while the niobium oxide was deposited by reactive sputtering. The test measurements showed promising results, we could reproduce the same switching effects as observed in the STM arrangement. In the near future further optimizations are needed to result in more stable devices. Fabrication and process optimisation of  $\text{VO}_2$  based samples is also in progress.

# LARGE-ANGLE DUAL SCATTERING CONTRIBUTION IN THE MEDIUM ENERGY ION SCATTERING SPECTRA OF THIN GOLD LAYERS AND GOLD NANOPARTICLES

(OTKA K112114)

G. Battistig, Zs. Baji, I.E. Lukács, Gy. Molnár, N.Q. Khánh, A.E. Papp, L. Pósa, J. Radó, S. Soleimani, M. Szappanos, E. Tunyogi, J. Volk, Zs. Zolnai

In this work we show the role of large-angle dual scattering (DS) events appearing as a wide background in the medium energy ion scattering (MEIS) spectra of gold nanostructures. The facility at the International Institute of Accelerator Applications at Huddersfield, UK, has been used for the analysis of thin Au layers deposited on glass substrate and plasmonic Au-silica core-shell nanoparticles (NPs) deposited on Si substrate. The typical Au layer thickness was 10-20 nm and the core/shell nanoparticle size was 25/40 nm. MEIS analysis has been performed with 100 keV He<sup>+</sup> ions for scattering angles of 90° and 125°. Note, these conditions are standard in MEIS experiments. In the size range of 10-100 nm, both for thin layers and spherical particles, besides small-angle multiple scattering, large-angle dual (and plural) scattering also gives strongly increasing contribution to the single scattering (SS) spectra of gold. The estimation of the DS yield is essential for quantitative spectrum evaluation and preliminary optimization of the measurement conditions.

The single scattering MEIS spectra of planar Au layers and spherical Au nanoparticles were simulated with the RBS-MAST [1] and SIMNRA [2] codes, considering the detailed 3D sample geometry. The surface roughness of the Au layers and the spherical shape and first neighbour configuration of the nanoparticles was considered. Atomic force microscopy (AFM) and field emission scanning electron microscopy (FESEM) have been applied as complementary characterization methods.

In our case dual scattering offers significant yield in a wide energy range, which consists of (i) an additional peak overlapping the single scattering spectra of gold and (ii) a smooth low energy background overlapping the glass or Si substrate signal. For 90° and 125° scattering angles the DS peak to SS peak ratios in the (i) energy range seem to be quite similar. The low energy (ii) DS yields, however, strongly differ resulting in 10-15%, and only 2-3% signal levels compared to the corresponding SS peak heights for the two different scattering angles.

We estimate the DS yield contribution in two different manners: with individual particle trajectory simulations provided by the SIMNRA code [2], and with calculations based on a simplified geometrical model for DS events using parametrized functions for He<sup>+</sup> stopping, cross-sections, and charge neutralization processes [3]. For planar Au layers SIMNRA simulations and the results of the simplified geometrical model show good agreement for the dual scattering yields. Similar DS yield calculations had been performed for thin ZnO and Cu<sub>2</sub>O layers [4]. The results show that the procedure can be applied for a wide range of different materials in the calculation of MEIS spectra.

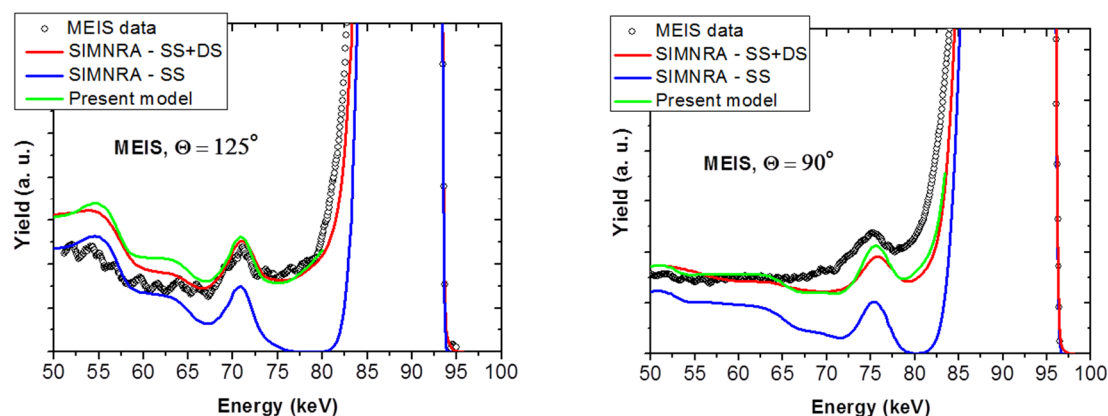


Figure 1: MEIS spectra of a 10 nm Au/2 nm Cr<sub>2</sub>O<sub>3</sub>/glass layer system and SIMNRA simulations with only single scattering (SS) and single+dual scattering (SS+DS) calculations. The green line shows the low energy part of the spectrum according to our simple geometrical model for dual scattering [3]. Neutralization for the incoming He<sup>+</sup> projectiles is considered in the calculations.

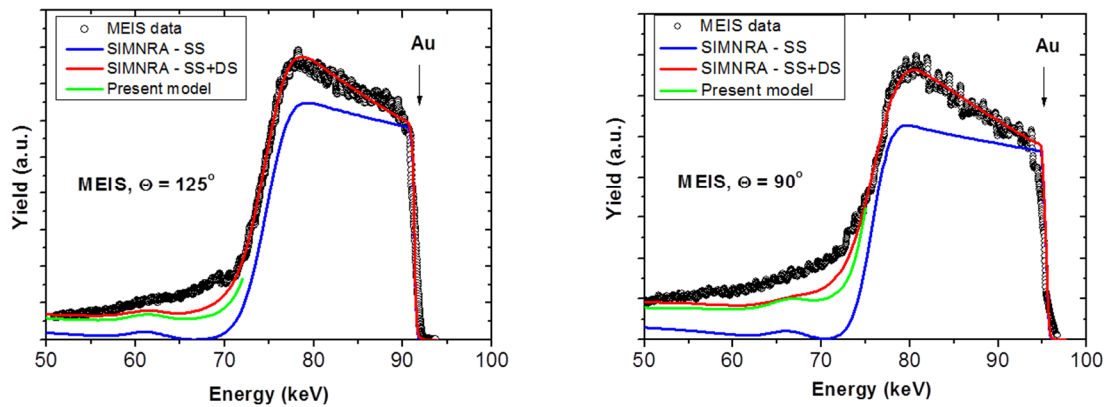


Figure 2: Same as it is in Fig. 1 but for a 20 nm Au/2 nm  $\text{Cr}_2\text{O}_3$ /glass substrate system.

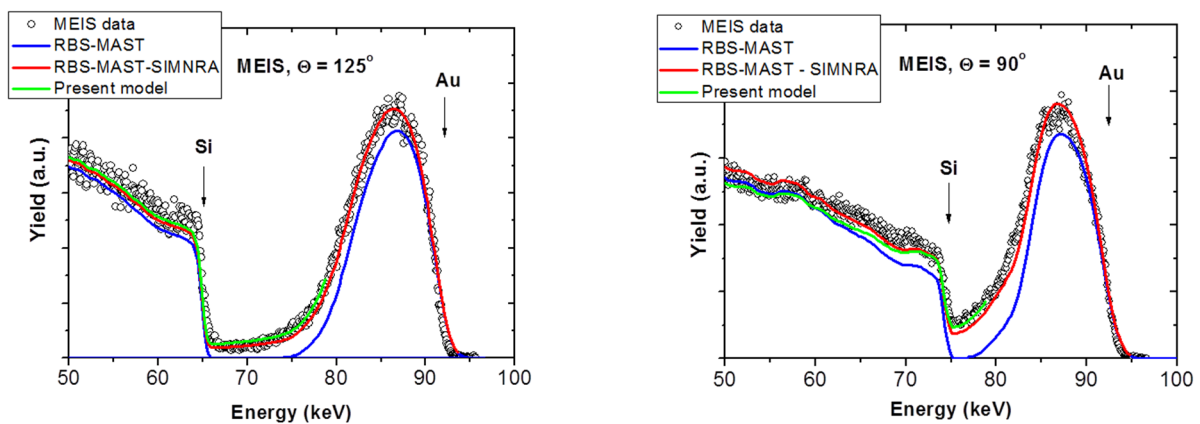


Figure 3: MEIS spectra of a monolayer of 25 nm diameter Au core/9 nm thick silica shell spherical nanoparticles deposited on Si substrate and 3D spectrum simulations with only single scattering (SS) and single+dual scattering (SS+DS) calculations. SS yields are calculated with RBS-MAST while DS yields are with SIMNRA, respectively. The green lines show the low energy part of the spectra according to our simple geometrical model for dual scattering [3].

## Related publications

- [1] Z. Hajnal, E. Szilágyi, F. Pászti, G. Battistig: *Channeling-like effects due to the macroscopic structure of porous silicon*, Nucl. Instrum. Methods **B 118**, (1996)
- [2] M. Mayer: *Improved Physics in SIMNRA 7 - Max-Planck-Gesellschaft*, Nucl. Instrum. Methods **B 332**, 176 (2014)
- [3] Z. Zolnai, A. K. Rossall, J. A. van den Berg, A. Deák, S. Pothorszky, D. Zámbo, L. Illés, and G. Battistig: *Large-Angle Dual Scattering Yield in the MEIS Spectra of Gold Nanostructures*, Proc. HRDP 9 conference, 25-29 June 2018, Uppsala, Sweden
- [4] K. Rossall: *Examining the effect of the depth profile on the electrical properties of transition metal oxide thin films*, Proc. HRDP 9 conference, 25-29 June 2018, Uppsala, Sweden

## ECSEL JU “POSITION-II PROJECT, “TOWARDS NEXT GENERATION OF SMART CATHETERS AND IMPLANTS”

*(A pilot line for the next generation of smart catheters and implants – POSITION-II, H2020-ECSEL-2017-1-RIA-two-stage-783132)*

*P. Fürjes, O. Bálint-Hakkel, I. Bársony, F. Bíró, P. Földesy, Z. Hajnal, P. Hermann, V. Rakovics, I. Réti, Z. Szabó*

The POSITION-II project is to realize a breakthrough in Europe in the development of smart catheters with embedded functions. By the introduction of open Flex to Rigid (F2R) technology platforms for miniaturization, in -tip AD conversion, wireless communication, MEMS transducer technology and encapsulation novel systems for minimal invasive surgery and medical examination will be developed. The availability of these open platforms will allow manufacturers to improve the performance of smart catheters at a lower cost and will enable the development of completely new minimally invasive smart instruments. The 46 member European consortium is led by Philips.

Our group was invited upon the previous successful cooperation in the ECSEL “INCITE” project where together with the Polish Foundation of Cardiac Surgery Development (FRK) and the Polymer Engineering group of BME we jointly developed a laparoscope demo system with tweezers integrated force sensor chips and electronics.

In the present project our group has two tasks:

- Design and development of a 3D Flex-to-Rigid compatible force sensor for tip head integration of the catheter, where, alternative solutions will be evaluated and realized in response to the need of capacitive transduction. Similarly to the piezoresistive force sensor we developed in the frame the INCITE project. A force-transfer and -amplifier rod will be formed from the handle layer of the SOI wafer, whereas the deforming membrane will be the 40µm thick device layer with isolated read-out capacitors on top. In this early phase of the project model calculations and preliminary experiments are being led to finalize the design, elaborate specific processing steps as well as the F2R compatible process flow.
- Material selection and process development for encapsulation and evaluation for biocompatible protective coatings of complex electronic devices to be implanted in the human body. Our contribution is the design and production of test chips and involvement in performing in-vivo tests.

Our general goal is to elaborate a capacitive type force sensor on flexible substrates. This will open the way towards various future applications in medical and robotic fields forming the basis of joint developments with domestic industrial partners in medium term.

# LOW POWER COMBUSTIBLE-TYPE NANOSENSORS FOR GAS DETECTION IN HARSH ENVIRONMENT

(Hungarian-Russian Collaborative Research Program is 2017-2.3.4-TÉT-RU-2017-00006)

P. Fürjes, O. Bálint-Hakkel, I. Bársony, F. Bíró, P. Földesy, Z. Hajnal, P. Hermann, V. Rakovics, I. Réti, Z. Szabó

On the basis of our previous results summarized in the excellent PhD work of Ferenc Bíró about processing of micro-hotplates and micro calorimetric gas sensors, a bilateral collaboration with the group of National Research Nuclear University MEPhI (Moscow Engineering Physics Institute) was initiated. Our joint R&D proposal was positively evaluated in both countries and the three year project started officially on April 1<sup>st</sup>, 2018 with the final goal to develop the *prototype* of solid state micro gas sensors for detection of hydrocarbons, CO and NH<sub>3</sub> concentrations up to their lower explosion limits.

In the first year the micro-hotplate structure was further improved to minimize its power consumption and temperature non-uniformities by means of novel filament geometries and applying new materials. The detrimental effect of temperature gradients arising along the filament and across the hotplate was proven. The operation temperature reduction to 500°C or below plays crucial role in mass transport related degradation effects. Catalysts operating efficiently at reduced temperature is also essential part of the work. This task is shared with the Russian partner and subject of the 2<sup>nd</sup> year of the project. In the reporting period

1. The geometry of the Pt filament for uniform temperature was modified and temperature gradients  $\ll 0.5^\circ\text{C}/\mu\text{m}$  towards the perimeter were reduced. Thereby the mass transport was minimized and the lifetime of the sensor is expected to exceed the minimum one year. The heat sink contact wire was introduced in the centre the conventional double-spiral geometry modified such as to provide extra power along the perimeter of the heated area. Both versions have small variations in filament diameter and widths to find the best structure. Some of the characteristic designs are shown in Fig 1. A new patterning technology of the Pt filament was also introduced replacing the lift-off technique by a dry etching process of Pt in our DRIE system using Ar-SF<sub>6</sub> gas mixture. The perfect patterns and sidewalls facilitate further processing, eliminate sidewall flakes, increase yield and uniformity of filament. Identical filament pairs are badly needed in the Wheatstone-bridge configuration of the final device.



Figure 1: Mask images of selected filament geometries for formation of uniform temperature hotplates

2. Uniform and reproducible crystalline Si filaments were formed from SOI (silicon on insulator) wafers using the buried oxide for achieving uniform thickness and identical geometry. Cantilevers are suspended on stress compensated SiO<sub>2</sub>-Si<sub>3</sub>N<sub>4</sub> membrane to eliminate possible ruptures of the cantilevers. Compared to metals higher resistivity of device silicon ensures higher filament resistance at the same temperature i.e. the cross section of the current routes should be increased to achieve the sufficient resistance. With the c-Si based design the electromigration can be reduced by > two orders of magnitude.

The heated area of these filaments can be completely covered on both sides with catalyst or passive pastes by drop deposition

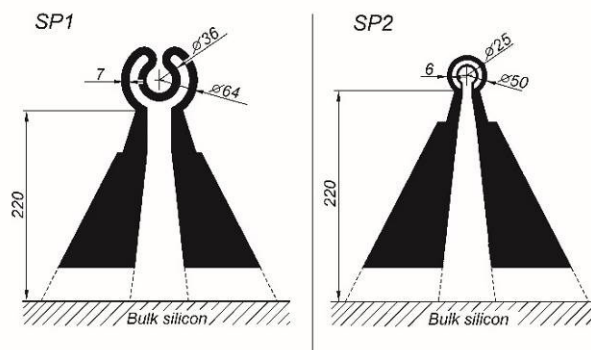
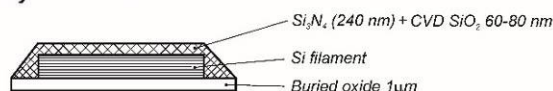
**Filament geometries****Layer structure**

Figure 2: Suspended silicon filaments layouts and the layer stack below.

Observing the resistance variations and also the “all-around” catalyst deposition, two filament geometries were designed (Fig. 2 top). The layer structure is identical for both filament geometries. The top side of the filaments are covered with  $\text{Si}_3\text{N}_4$ - $\text{SiO}_2$  layers, while the bottom side is covered with the buried oxide (Fig. 2 bottom). The silicon-nitride is the diffusion barrier against oxidation of silicon at the top, consequently in this design we expect the oxidation of the silicon filament to occur only at the bottom side reducing the resistance drift. The processing of the first test wafer will be expected end of January 2019.

**Related publications**

- [1] Bíró F.: Metánérzékelés mikropellisztorral, PhD. védés, Pannon Egyetem, 2018.02.26.
- [2] F. Bíró, Z. Hajnal, C. Dücső, I. Bársony: *The Role of Phase Changes in  $\text{TiO}_2$  /Pt/ $\text{TiO}_2$  Filaments*, *Journal of Electronic Materials*, **47(4)**, 2322-2329 (2018)
- [3] I. Bársony, F. Bíró, Z. Hajnal, C. Dücső: *Means of temperature assistance in gas sensing*, In: *Emerging Sensing Technologies Summit*, pp. 31-33. (2018)
- [4] F. Bíró, I. Bársony, Z. Hajnal: *Microhotplate constraints*, *Advances in Microelectronics: Review*, Chapter in Vol. 2, Book Series. Accepted, will be published in Q1 2019.

# BIOMECHANICAL TISSUE CHARACTERIZATION BY FORCE SENSITIVE SMART LAPAROSCOPE OF ROBIN HEART SURGICAL ROBOT

*(Intelligent Catheters in Advanced Systems for Interventions - INCITE, ENIAC CALL 2013-1 (partners: Philips Research - The Netherlands, FRK - Poland, BME))*

*P. Fürjes, O. Bálint-Hakkel, I. Bársony, F. Bíró, P. Földesy, Z. Hajnal, P. Hermann, V. Rakovics, I. Réti, Z. Szabó*

To obtain real-time multi-parametric information about physical and anatomic conditions of affected tissues during Minimal Invasive Surgery (MIS) operation is crucial for precision and safety. [1] The integrated 3D force and tactile sensors should provide these information about the different organs and tissues touched.

### Integrated 3D force sensors for Minimal Invasive Surgery applications

Piezoresistive vectorial force sensors were designed according to the proposed force ranges and manufactured by 3D bulk micromachining process [2]. Two different MEMS sensors were electro-mechanically integrated into a metal laparoscope tweezers with the pre-processing electronics for analogue-digital data conversion and communication with the robot control system (Fig. 1-1). The sensors were embedded in biocompatible elastic polymer.

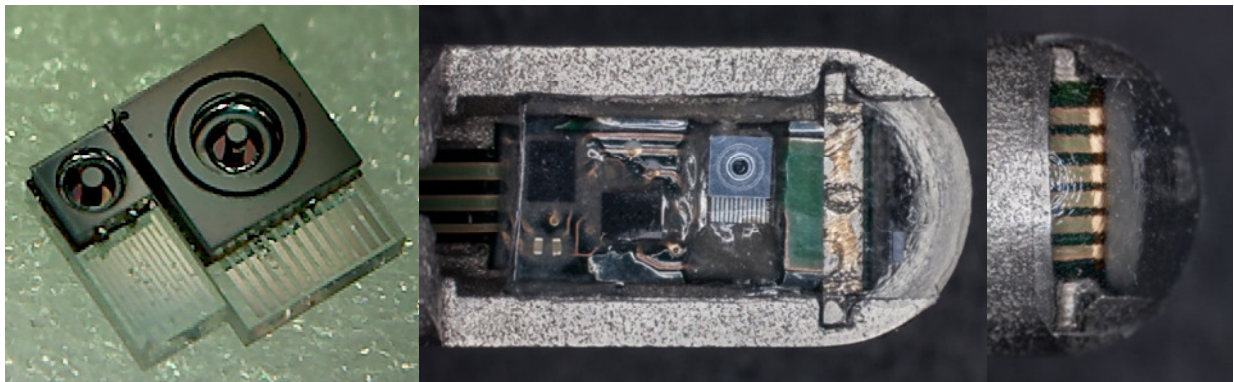


Figure 1: Individual force sensor chips before mounting and wire bonding: 1x2.5mm<sup>2</sup> chips for head mounted tactile sensing (left) and 2x3mm<sup>2</sup> for gripping force (right). The medical grade stainless steel laparoscopic tweezers with the integrated electronics - covered by the (transparent) flexible biocompatible elastomer.

### Biomechanical measurements by robot integrated laparoscope

Tissue hardness measurements were performed using real animal tissue perpendicularly touched with the gripper. The signals of the tip tactile sensor were collected and analysed with reference to a constant uniform protrusion of the laparoscope (Fig. 1-2).

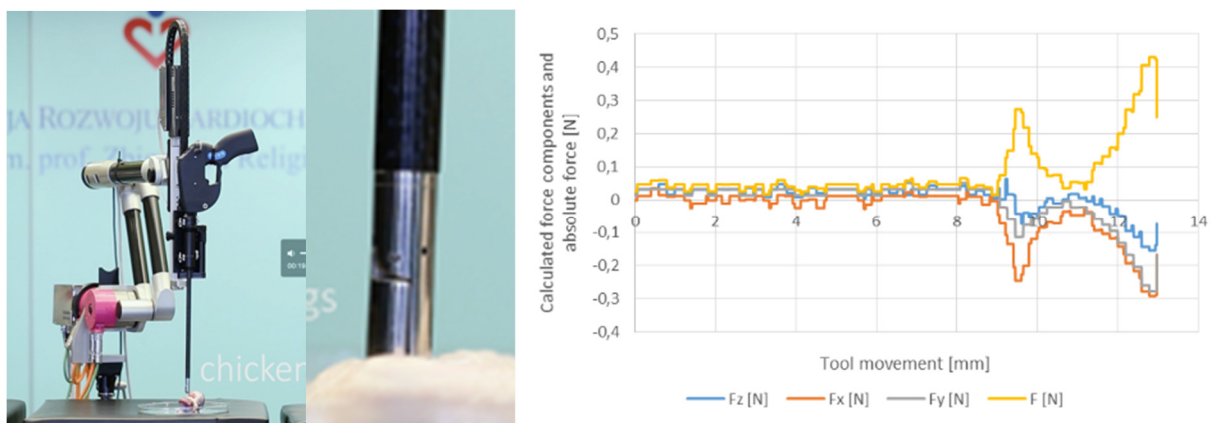


Figure 2: Testing tissue hardness: the laparoscope protruded perpendicularly at constant speed into a chicken wing. Measured forces (N) versus distance (mm) as the laparoscope approaches and touches chicken bone and muscular tissue. Touching depth is at 9mm.

The measured force values clearly indicate the contact depth and the mechanical characteristics of the tissue. When pressing the soft muscle a continuous increase of force was detected starting with a slight slope. When the hard bone was pressed, a higher slope is recorded directly from the starting point on. The tissue- characteristic force signals offer the possibility of their automatic distinction.

A simple setup was constructed to mimic blood vessel and check whether the sensor built in the grasper is able to identify an artery by measuring the pulses. A liquid filled silicone tube was grasped and the signals of the force sensor were recorded along with pressure sensor readings while the microfluidic pump was operating in pulsed mode. Fig. 1-3 demonstrates that the sensitivity of the measurement depends on the preset clamping force, as expected from the blood pressure measurement protocol.

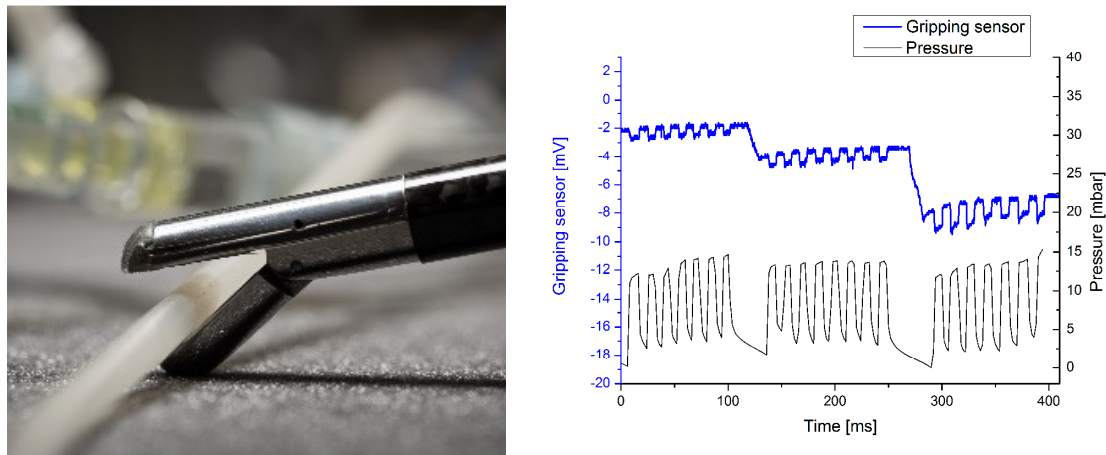


Figure 3: The signals of the grasping force sensors and the pressure sensor built in the fluidic system when applying pulse mode pressure. The three series are taken using different preset grasping forces.

### Summary

Studies of the prototype “smart” sensory laparoscopes have verified their usefulness in real-time force feedback robotic systems by identifying the state of tissue and determining the clamping force of the grasper in a surgical system. Implementing this “smart” tool into the surgery robot system, the human-machine synergy was also demonstrated by the Polish partner by applying two-directional haptic control.

### References

- [1] Z. Nawrat, “State of the art in medical robotics in Poland: Development of the Robin Heart and other robots”, *Expert Rev. Med. Devices* 9(4), 353–359 (2012)
- [2] J. Radó, Cs. Dücső, P. Földesy, G. Szebényi, Z. Nawrat, K. Rohr, P. Fürjes, „3D force sensors for laparoscopic surgery tool”, *Microsystem Technologies*, 2017, doi:10.1007/s00542-017-3443-4

### Related publications

- [1] Ł. Mucha, Cs. Dücső, G. Szebényi, P. Fürjes: *Prototypic force feedback instrument for minimally invasive robotic surgery*, Medical Robots 2018 Conference, Zabrze, Poland, 2018
- [2] J. Radó, Cs. Dücső, P. Földesy, I. Bársony, K. Rohr, L. Mucha, K. Lis, W. Sadowski, D. Krawczyk, P. Kroczyk, Z. Małota, G. Szebényi, H. Sántha, Z. Nawrat, P. Fürjes: *Biomechanical Tissue Characterisation by Force Sensitive Smart Laparoscope of Robin Heart Surgical Robot*, Proceedings of Eurosensors 2018 Conference, Graz, Austria, 2018 (Proceedings 2018, 2(13), 1035; <https://doi.org/10.3390/proceedings2131035>)
- [3] J. Radó, Cs. Dücső, P. Földesy, G. Szebényi, H. Sántha, K. Rohr, L. Mucha, K. Lis, W. Sadowski, D. Krawczyk, P. Kroczyk, Z. Małota, Z. Nawrat, P. Fürjes: *Force sensitive smart laparoscope of Robin Heart Surgical Robot*, Proceedings of Design, Test, Integration and Packaging of MEMS/MOEMS – DTIP 2018 Conference, Rome, Italy, 2018 (IEEE Xplore 8394204, DOI: 10.1109/DTIP.2018.8394204)

# POLYMER MICROFLUIDIC SYSTEMS FOR MEDICAL DIAGNOSTICS

(KTIA VKSZ\_14-1-2015-0004)

*P. Fürjes, O. Bálint-Hakkel, I. Bársony, F. Bíró, P. Földesy, Z. Hajnal, P. Hermann, V. Rakovics, I. Réti, Z. Szabó*

Precise and fast PoC monitoring of disease related blood marker molecule or bacteria levels could be crucial in effective therapies. In a dedicated Lab-on-a-Chip (LoC) solution the microfluidic system has to transport the sample and the washing buffer to the active area of the chip, while mixing and incubating the sample with the reagents. As incubation and read-out require specified timing, precise sample handling and flow control are essential. The use of biological sample also requires bio-inert surface properties with minimized non-specific adsorption and coagulation in the channels. We target to develop a polymer based microfluidic cartridge for autonomously controlled sample transport in an integrated bioanalytical device. [1]

## **Autonomous microfluidic systems for blood protein detection**

A microfluidic system was designed and manufactured for transporting whole blood or plasma at a precisely controlled sample rate to be integrated into Point-of-Care Lab-on-a-Chip based diagnostic devices. The detection of cardiovascular diseases was in focus in cooperation with 77 Elektronika Ltd. In the "Multiparaméteres Point of Care in vitro diagnosztikai rendszerek fejlesztése" project a specific microfluidic system was designed, actually the geometry was modified to fulfill requirements of optical detection with real blood sample. Accordingly, a new microfluidic system compatible with the bioanalytical specifications (sample volume, targeted detection limits, surface blocking, etc.) had to be designed. With the 77 Elektronika Kft. we are developing Lab-on-a-Chip based diagnostic device for a specific project of the Science University of Pécs to support human in-vitro fertilisation also.

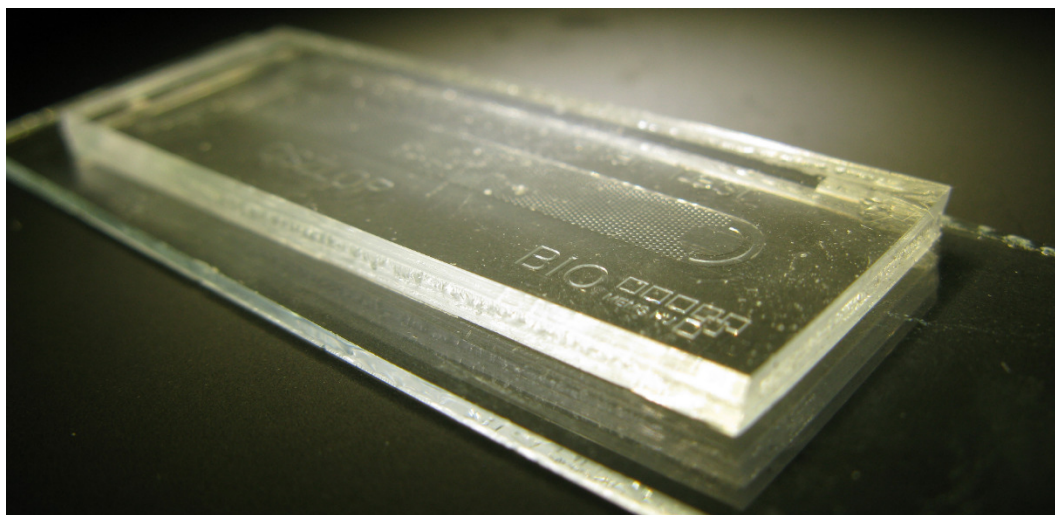


*Figure 1: Microfluidic cartridge for testing of autonomous sample transport and preparation*

The material composition of the laboratory stage / pre-industrial cartridge was optimised for the required sample flow rate, the optical and mechanical properties. The embedding protocol of PDMS-PEO molecules was modified considering the molecular weight, concentration and physical parameters of the PDMS polymerisation process (temperature, time, surface treatments of the molding master).

## **Surface modification of polymers compatible with industrial fabrication technologies**

Our laboratory has been involved in the development of precision injection molding technology and surface modification processes of micro structured polymer cartridges. Hydrophilic and non-fouling features are crucial requirements of the autonomous fluid sample transport in the microfluidic cassette, therefore surface modification of the polymer substrate is necessary. We conducted wet and dry chemistry experiments to create adequate surfaces. The surfaces were characterised using several surface analytical methods. The long term stability of the surfaces was examined by contact angle measurements. Surface-chemistry functional groups were identified by Attenuated Total Reflectance Fourier Transformed Infrared (ATR FT-IR) spectroscopy. The morphology was inferred from Atomic Force Microscopy (AFM) images, whereas the thickness and homogeneity monitored by ellipsometry. The modified surfaces retained their hydrophilic character for two months period. (Figure 2).

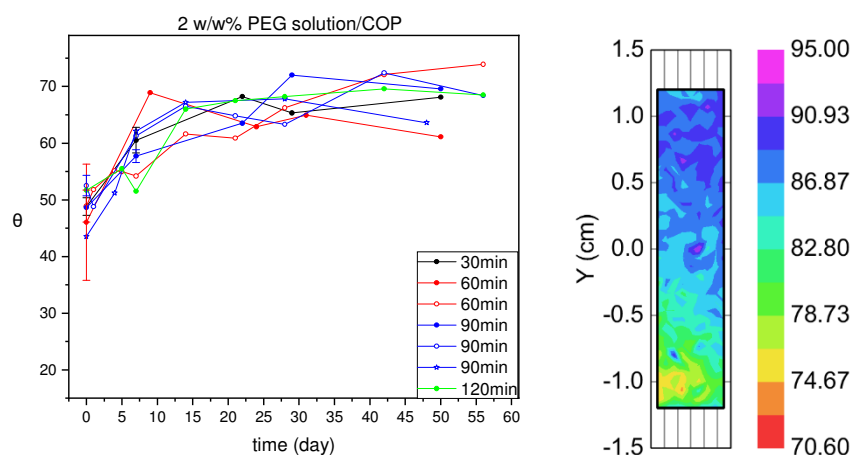


Figure 2: Long term stability of water contact angle (left) on hydrophilic PEG layer deposited by wet chemistry and ellipsometry thickness map (right).

The ATR FT-IR spectra showed that a homogenous hydrophilic layer could be formed on the polymer surface by wet chemical methods. Evaluation of the ellipsometry and AFM measurements revealed that the thickness of the layer is typically  $\sim 100$ - $200$  nm (depending on the parameters of the preparation).

### High resolution silicon mold insert for injection molding microfluidic systems

Our research laboratory is participating in development precise micro-injection molding of plastics for high throughput fabrication of microfluidic systems in in cooperation with the 77 Elektronika Kft. and Z-Microsystems GmbH. The applicability of the technology is not trivial for fabrication microstructures, as the definition of the molding parameters and the development of molding master is quite critical. The MEMS Lab developed a reliable technology for fabrication molding master using bulk silicon micromachining technology by 3D Deep Reactive Ion Etching (DRIE) of crystalline silicon wafer. The final structure was developed by DRIE with adequate surface roughness and wall angle for the injection molding technique. The geometry transfer achieved by the developed molding master is demonstrated in Figure 3.

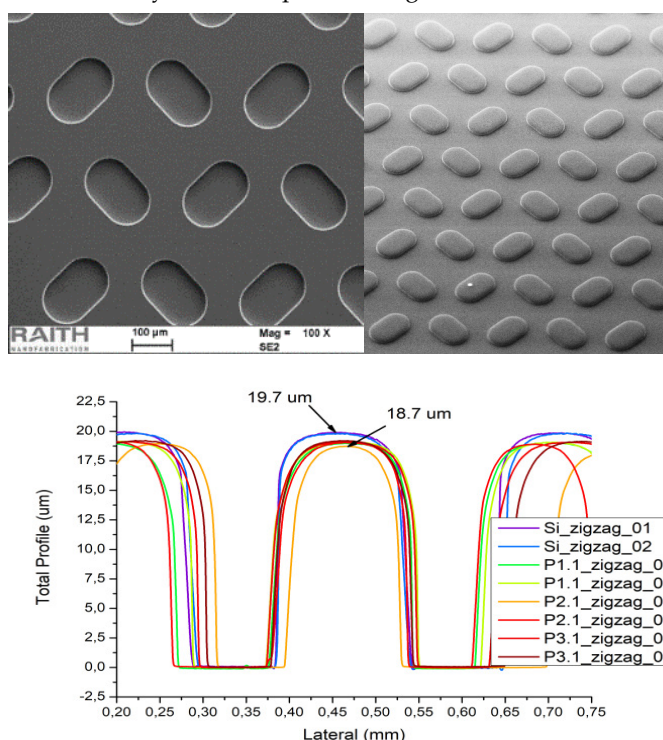


Figure 3: The microstructure of the fabricated silicon molding master (top left), the injection molded polymer sample (top right) and the profiles compared (below).

### Related publications

- [1] L. Gervais, E. Delamarche: *Toward one-step point-of-care immunodiagnostics using capillary-driven microfluidics and PDMS substrates*, Lab Chip **9**, 3330-3337 (2009)
- [2] E. Holczer, P. Fürjes: *Effects of embedded surfactants on the surface properties of PDMS; applicability for autonomous microfluidic systems*, Microfluidics and Nanofluidics **21**: 81 (2017) doi:10.1007/s10404-017-1916-5

# FINITE ELEMENT MODELLING AND SIMULATION IN THE DEVELOPMENT OF MEMS AND MICROFLUIDICS DEVICES

*P. Fürjes, O. Bálint-Hakkel, I. Bársony, F. Bíró, P. Földesy, Z. Hajnal, P. Hermann, V. Rakovics, I. Réti, Z. Szabó*

Initial design as well as specific optimization tasks mostly involve not only the careful structural and process engineering, but also various simulations of device operation in microtechnology. Numerical simulations enable assessment of stability of the device components under various external conditions, as well as trial modifications of the studied devices, adaptation to varying requirements, etc.

Modelling and simulation also has the advantage of lower resource needs and faster trial evaluation cycles. In the following we present a couple of examples of applied models and simulations, carried out in the COMSOL finite element modelling (FEM) framework. FEM provides approximations of arbitrary accuracy for device and environmental components. Systems of coupled partial differential equations can be numerically solved in practically any configuration of device components and environmental conditions, with simplifying assumptions about the local behaviour of the various state-functions and physical variables. As multiple physical quantities are being simultaneously solved for in the iterations of the simulations, hence their colloquial name, *multiphysics*.

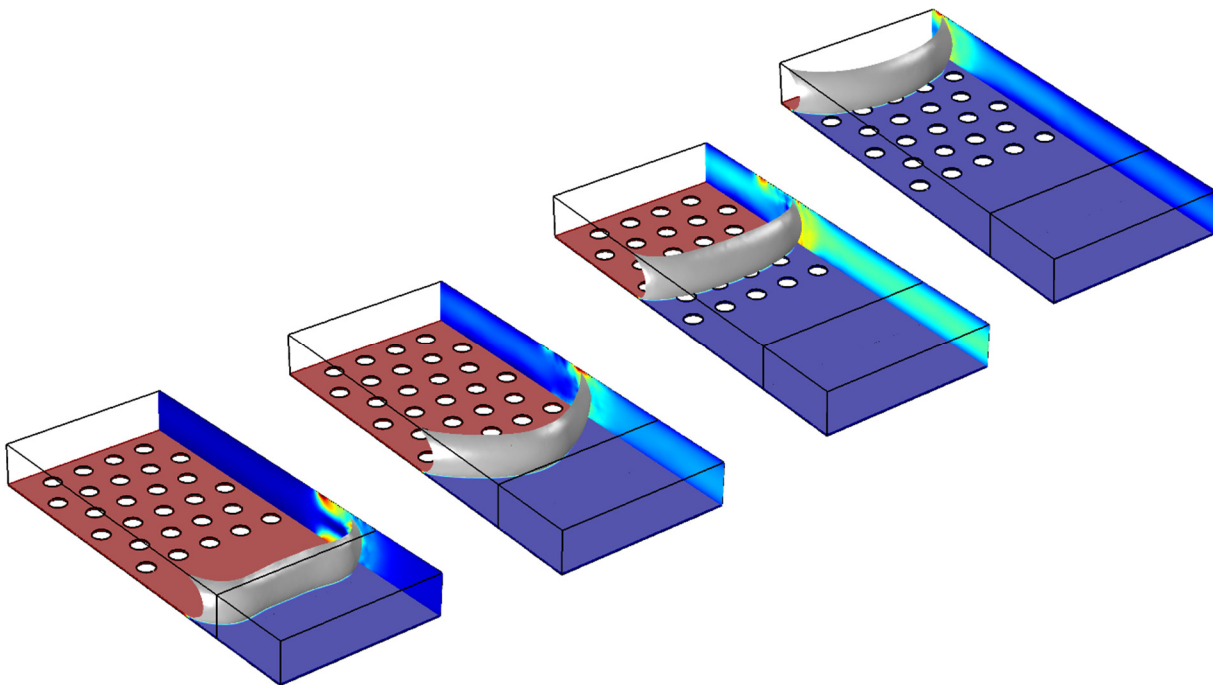


*Figure 1: Time steps (from left to right: 0.02, 0.08, 0.14, 0.20 ms) of water entering a surface modified capillary channel. The channel width is 200  $\mu\text{m}$ , height is 50  $\mu\text{m}$ . The bottom of the farther part of the channel is modified by cylindrical steps of 2  $\mu\text{m}$  height. In the beginning only the closer half of the channel is filled by the liquid, during the time steps the changes in form and gradual progress of the air/water interface are well observable. Comparison of various surface morphologies is ongoing.*

## ***Effect of the surface morphology on capillary flow in microfluidic channels***

Control of fluid flow in microchannels has been a field of intense development in the past decade. A promising direction is the changing of wetting properties by modification of surface morphology in the channel to accelerate (or decelerate) the progress of the fluid surface at desired regions. Numerical adjustment of the interface geometry to the fluid properties and desired control parameters requires several time-dependent simulations of the behaviour of the fluid (most of the times air-water) system.

# POLIMER BASED OPTICAL WAVEGUIDES FOR BIOMEDICAL APPLICATIONS

(VEKOP-2.2.1-16-2017-00001)

*P. Fürjes, O. Bálint-Hakkal, I. Bársony, F. Bíró, P. Földesy, Z. Hajnal, P. Hermann, V. Rakovics, I. Réti, Z. Szabó*

Optical Mach-Zender Interferometer (MZI) form the basic unit of the detecting layer of a glass supported Lab-on a Chip cassette. Based on prior optical simulations we formed waveguide structures with  $2 \times 2 \mu\text{m}^2$  cross-section on a glass support (Figure 1). We used epoxy based resists (SU-8, DWL and EpoCore) which were selected by the consortium members. Devices suitable for optical characterization were formed by using available photolithography technology.

Besides optimizing the parameters of the individual steps of the lithography process (time and dose of the exposure, mask distance, baking temperature), we also conducted experiments with different cladding layers (SU-8, EpoClad). We verified the morphology and the adhesion of the wave guide layers by Scanning Electron Microscopy (SEM). Following the successful implementation of this part of the project the MZI containing cassettes were given to the consortium partners for functional tests.

In the next stage of the development we will investigate the possibility of embedding the microstructures in material systems which are compatible with industrial technologies.

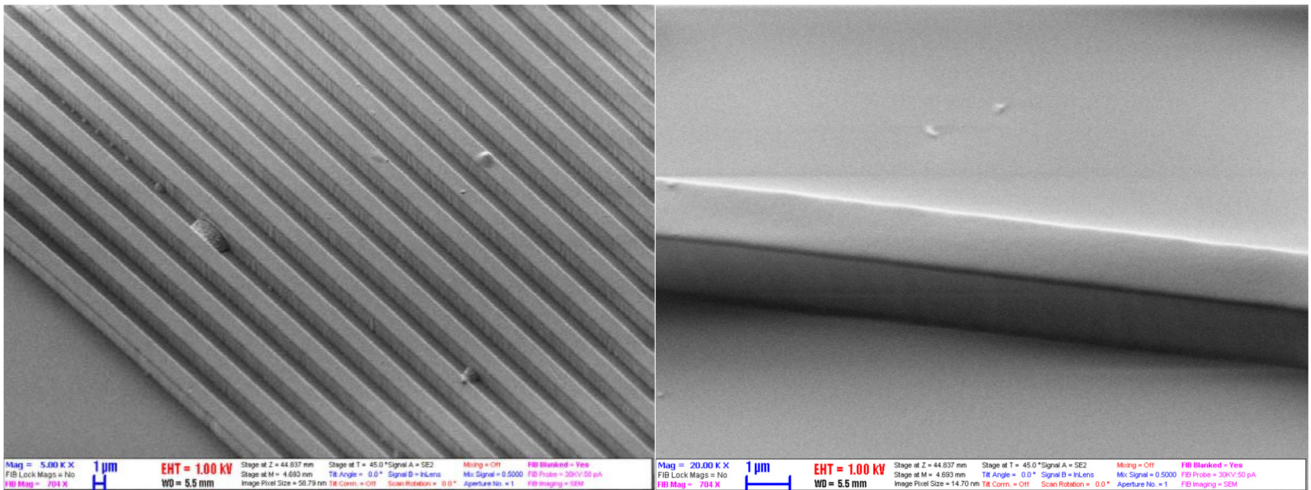


Figure 1: Waveguide structures of Lab-on a Chip system

# CELL AND PARTICLE MANIPULATION AND SCREENING IN MICROFLUIDIC SYSTEMS

(OTKA CK 83821, VEKOP-2.2.1-16-2017-00001)

*P. Fürjes, O. Bálint-Hakkel, I. Bársony, F. Bíró, P. Földesy, Z. Hajnal, P. Hermann, V. Rakovics, I. Réti, Z. Szabó*

The demand for microfluidics enabling fast and effective preparation and analysis of liquid samples in microscale diagnostic (Lab-on-a-Chip) systems underlined the importance of studying these phenomena. Due to the governing physical phenomena on microscale, classical sample preparation methods, such as efficient mixing of fluids as well as size-dependent separation and sorting or filtering of corpuscles in the liquid samples becomes a challenge. Novel microfluidic structures have to be developed based on the physical laws of this size domain.

## *Development microfluidic system for efficient separation circulating tumour cells (CTC)*

In cooperation with the research groups of István Rajta and András Guttmann we participated in the design and fabrication of special microfluidic systems dedicated to sorting and separation circulating tumour cells. The channel system containing 3D tilted pillar structures of high specific surface was designed according to the results of preliminary Finite Element Modelling. The behaviour of the fabricated microfluidic system was defined by analysis of the movement of human tumour cells, to validate the FEM simulation. The computational fluid dynamics (CFD) assisted chip design and the entire microfabrication process was demonstrated with some preliminary test results on flow characteristics [1].

As a continuation of our previously published work, we presented a detailed evaluation of a microfabricated cell capture device utilizing a doubly tilted micropillar array. The device was fabricated using a novel hybrid technology based on the combination of proton beam writing and conventional lithography techniques. The resulting unique hybrid device had a small central region with the doubly tilted micropillar array for improved cell capture, fabricated by PBW (proton beam writing), while the surrounding area of the chip was generated using UV lithography. This novel combination extended the potential of conventional microstructuring techniques, generating high interest both from engineering and biological application points of views. Tilted pillars offer unique flow characteristics and support enhanced fluidic interaction for improved immunoaffinity based cell capture. The performance of the microdevice was evaluated by an image sequence analysis based in-house developed single-cell tracking system. Individual cell tracking allowed in-depth analysis of the cell-chip surface interaction mechanism from hydrodynamic point of view. Simulation results were validated by using the hybrid device and the optimized surface functionalization procedure. Finally, the cell capture capability of this new generation microdevice was demonstrated by efficiently arresting cells from a HT29 cell-line suspension.

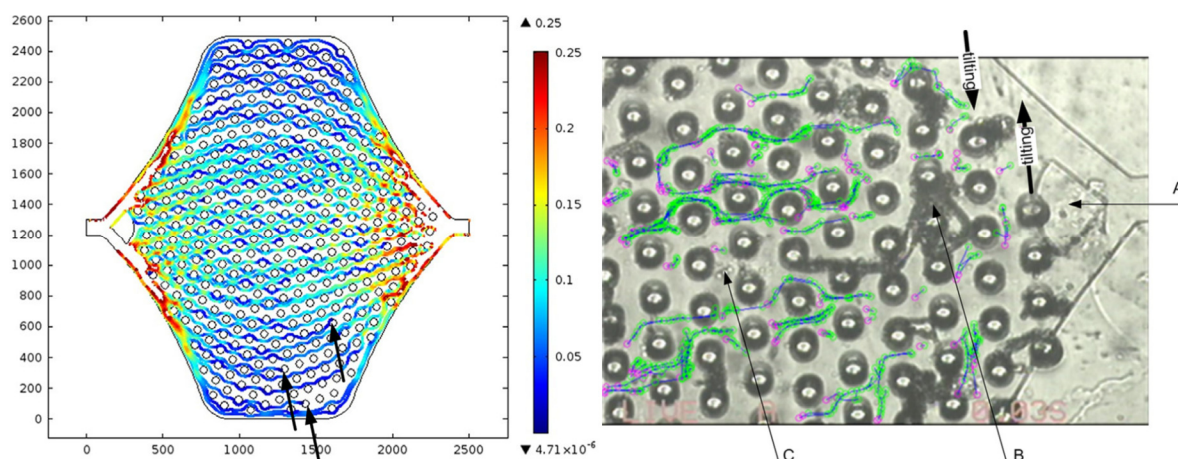


Figure 1: Calculated steady-state streamlines based on the developed model, expressed in term of fluid velocity (mm/s) (left). X and Y axes represent the geometrical scaling with micrometre unit. A representative screenshot from the acquired and processed image sequence video, showing the flow distributor (A), a clogged (B) and a free flowing cell clusters (C). Blue lines represent the observed cell trajectories.

## *Modelling and characterisation of droplet generation, trapping and detection in impedance based cell analytical microfluidic system*

Droplet based microfluidics have developing relevance in the field of Lab-on-a-Chip technology. In these multi-phase flow devices, the continuous sheath emulsion enables to generate, manipulate, mix, focus and separate encapsulated chemical reagents or biosamples as assay of living cells. Therefore, cell-analytical and diagnostic procedures can be automatized on microscale, although the precise control and monitoring of droplet parameters and behaviour are essential for their reliable

application. Accordingly, this work focuses on design and characterisation of a hybrid polymer microfluidic system having integrated electrode system (Fig. 2). The developed system is capable of creating, manipulating, trapping and monitoring droplets having precisely determined size fitted to general cell diameter. [2, 3]

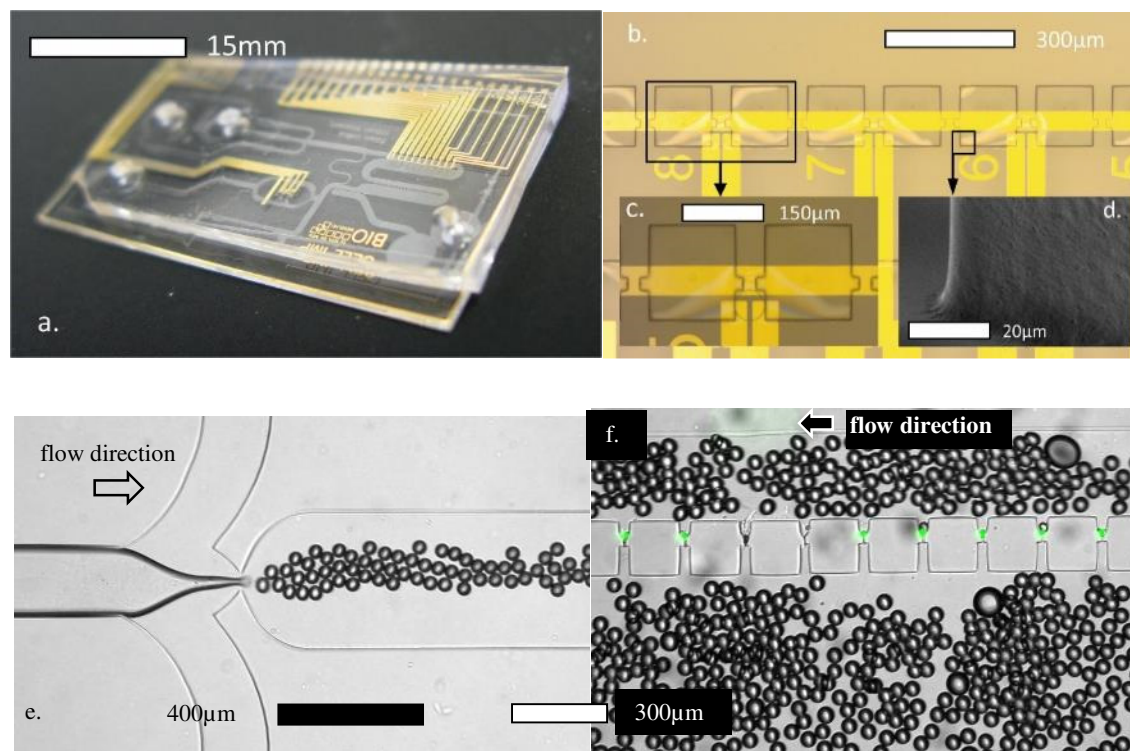


Figure 2: Metal (Au) electrodes integrated in SU-8 based hybrid microfluidic system (a). For proper alignment, electric insulation and transparency the channels are formed in multi-layered SU-8 (b, c). SEM view presents the interface between the thin insulation and the thick channel forming SU-8 layers (d). Droplets generated in the two-phase microfluidic system (e) and encapsulated fluorescent beads trapped in the perforated cavities of the model microfluidic system (f).

The influence of flow characteristics of two-phase microfluidic systems was analysed regarding the droplet generation, particle encapsulation and trapping processes. Droplets were dispersed in oil continuous phase with the requirement of precise size distribution to enable effective cell entrapment controlled by the applied flow parameters. Hydrodynamic behaviour of the microfluidic system was modelled by Finite Element Method (FEM) using COMSOL Multiphysics and compared to experimental results. The applicability of droplet based cell encapsulation and hydrodynamic trapping and the capability of impedance spectroscopy based droplet and cell detection were also characterised.

### References

- [1] I. Rajta, R. Huszánk, A.T.T. Szabó, G. U. L. Nagy, S. Szilasi, P. Fürjes, E. Holczer, Z. Fekete, G. Járvas, M. Szigeti, L. Hajba, J. Bodnár, A. Guttman: *Tilted pillar array fabrication by the combination of proton beam writing and soft lithography for microfluidic cell capture: Part 1 Design and feasibility*, *Electrophoresis*, **37:3** 498–503 (2016)
- [2] E. Holczer, O. Hakkal, P. Fürjes: *Fabrication of hybrid microfluidic system on transparent substrates for electrochemical applications*, *Proceedings of Eurosensors 2017 Conference, Paris, France, 2017* (Proceedings, **1(4)**, 326 (2017) doi:10.3390/proceedings1040326)
- [3] A. B. Tóth, E. Holczer, O. Hakkal, E. L. Tóth, K. Iván, P. Fürjes: *Modelling and characterisation of droplet generation and trapping in cell analytical two-phase microfluidic system*, *Proceedings of Eurosensors 2017 Conference, Paris, France, 2017* (Proceedings **1(4)**, 526 (2017); doi:10.3390/proceedings1040526)

### Related publications

- [1] G. Járvas, T. Varga, M. Szigeti, L. Hajba, P. Fürjes, I. Rajta, A. Guttman: *Tilted pillar array fabrication by the combination of proton beam writing and soft lithography for microfluidic cell capture Part 2: Image sequence analysis based evaluation and biological application*, *Electrophoresis*, **39**, 534–539 (2018)
- [2] A. B. Tóth, E. Holczer, A. Füredi, O. Hakkal, E. L. Tóth, K. Iván, P. Fürjes: *Modelling and characterisation of droplet generation, trapping and detection in impedance based cell analytical microfluidic system*, *Lab-on-a-Chip Europe 2018 Conference, Rotterdam, The Netherlands, 2018*

# SOLID STATE NANOPORE AND NANOCAPILLAR BASED BIOANALYTICAL SYSTEMS

(KTIA VKSZ\_14-1-2015-0004)

*P. Fürjes, O. Bálint-Hakkel, I. Bársony, F. Bíró, P. Földesy, Z. Hajnal, P. Hermann, V. Rakovics, I. Réti, Z. Szabó*

Nanoporous membranes are fundamental components of the transport modulation based label free electrochemical biosensors envisioned for high sensitive molecule detection. [1] The sensitivity and the specificity of these sensors are significantly affected by the pore geometry what has to be fitted to the size and conformation of the target molecules. Precise tailoring of nanopore geometries and alignment to target molecule conformation and size improves the signal-to-noise level of the identification method - in our case the electrochemical impedance spectroscopy (EIS). The pore geometry engineering is essential for reliable and reproducible manufacturing of integrable solid state nanopore-arrays in molecule diagnostic devices. Other important issue is the adequate selection of the applied material composition. Commercialization of the nanopore based biosensors or Lab-on-a-Chip devices seems to depend on the development of precise and high throughput nanofabrication techniques enabling reliable and reproducible shaping of nanopore geometries in extremely thin, but mechanically stable solid state membranes having electrical resistance as high as possible:

- Different (5-10nm thick  $\text{TiO}_2$ ,  $\text{AlO}_x$  and  $\text{HfO}_2$ ) dielectric layers were deposited by ALD (atomic layer deposition) and tested electronically to select the adequate insulation layer to be able to integrate multi-electrode array for EIS measurements.

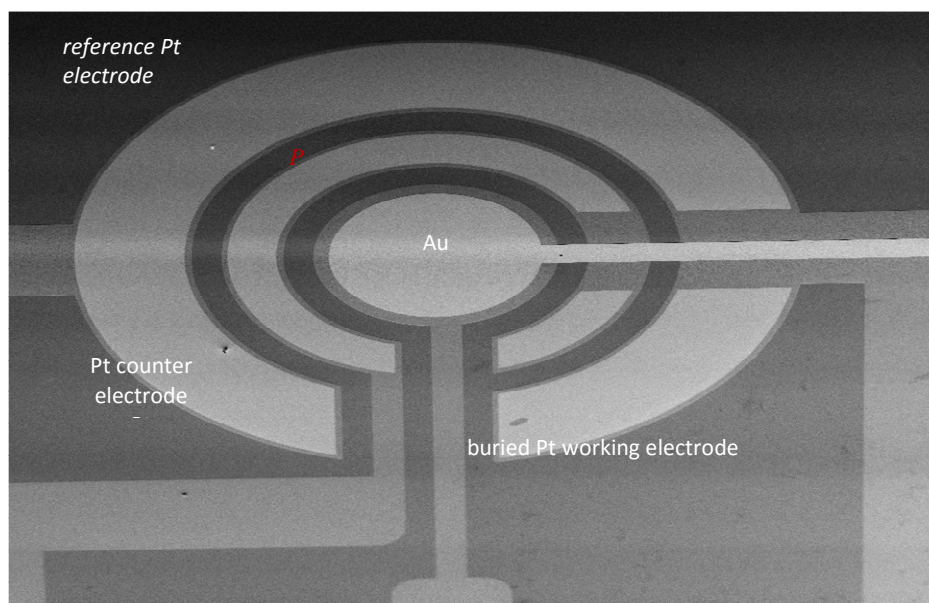


Figure 1: Integrated electrodes for on-chip EIS measurement

## Related publication

- [1] I. Makra, A. Brajnovits, Gy. Jágerszki, P. Fürjes, R. E. Gyurcsányi: *Potentiometric sensing of nucleic acids using chemically modified nanopores*, *Nanoscale* **9**, 739-747 (2017), doi: 10.1039/C6NR05886H

# SURFACE-ENHANCED RAMAN SCATTERING ACTIVE PERIODIC 3D STRUCTURE FOR TRAPPING AND HIGH SENSITIVE MOLECULAR ANALYSIS OF PARTICLES OR CELLS

*P. Fürjes, O. Bálint-Hakkel, I. Bársony, F. Bíró, P. Földesy, Z. Hajnal, P. Hermann, V. Rakovics, I. Réti, Z. Szabó*

Raman spectroscopy is finding many applications in biology, life sciences and other areas. Raman scattering is inherently weak, but its sensitivity can be improved by implementing surface-enhanced Raman scattering (SERS). SERS evolves in the vicinity of nanostructured metallic surfaces or nanostructures achieving several orders of magnitude enhancement in the Raman signal and extremely improved sensitivity reaching the attomolar ( $10^{-18}$  M) concentration ranges [1]. This highly sensitive detection performance of SERS was utilized for analysing molecules located in the few nanometer distance or immobilised on the surface of micro and nanoparticles trapped in a specially designed microstructure.

In a previous work the highly sensitive molecule recognition performance of a specially designed SERS substrate was demonstrated. The general inverse pyramid structures were fabricated as cavities in perforated membrane applicable for particle and cell filtering, sorting and trapping. In the voids of the gold covered substrate size compatible particles functionalised by different molecules were trapped, their SERS signal was detected and the different molecules were recognised.

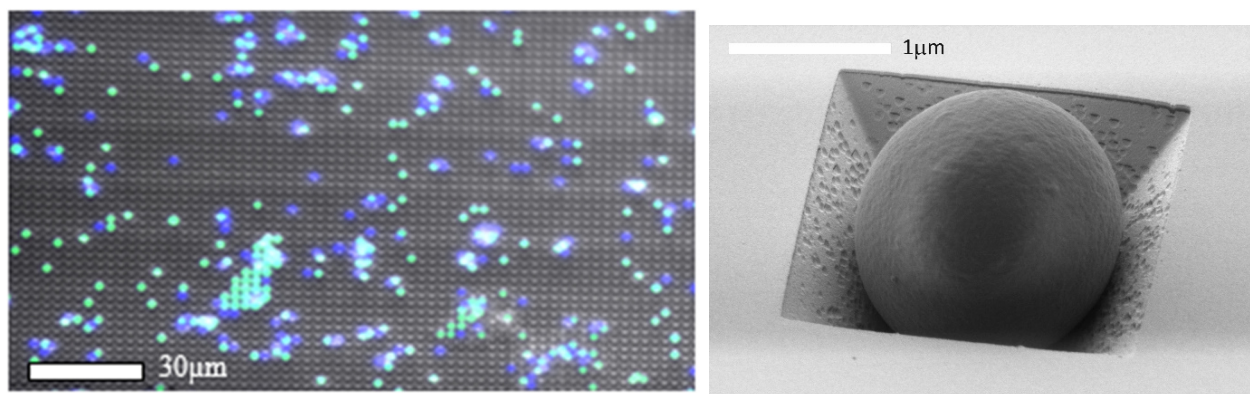


Figure 1: Fluorescent beads with appropriate 2µm diameter (Sigma Aldrich - green and Spherotech - blue) entrapped in the periodic array of perforated pyramidal structures: multichannel fluorescent (left) and SEM image (right)

The fluorescent molecules were analysed by SERS utilizing the plasmonic enhancement by the structured surface of the traps. The definite and sensitive differentiation of the molecules immobilized on the polystyrene bead surfaces are presented in Figure 2, where a huge increase in the Raman signal can be observed on the SERS surface.

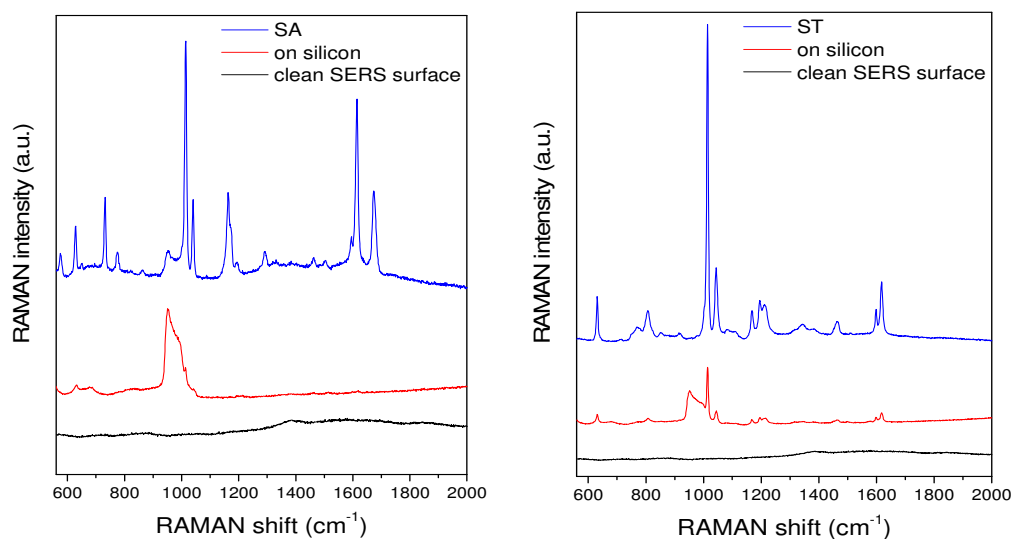


Figure 2: Comparison of the SERS spectra recorded on the clean SERS substrate (black) and different fluorescent beads on silicon (red) and trapped in the periodic array (blue). SA - Sigma Aldrich and ST - Spherotech fluorescent beads, respectively

In our approach special size fitted SERS active substrate was prepared by micromachining techniques in silicon wafer to be applicable for particle entrapment. Subsequently, gold nanospheres were trapped in the pyramidal cavities. SERS performance of the hierarchically combined structures was analysed and compared by using a highly diluted benzophenone solution and octadecanethiol surface functionalization. The recorder spectra are demonstrated in Fig. 3.

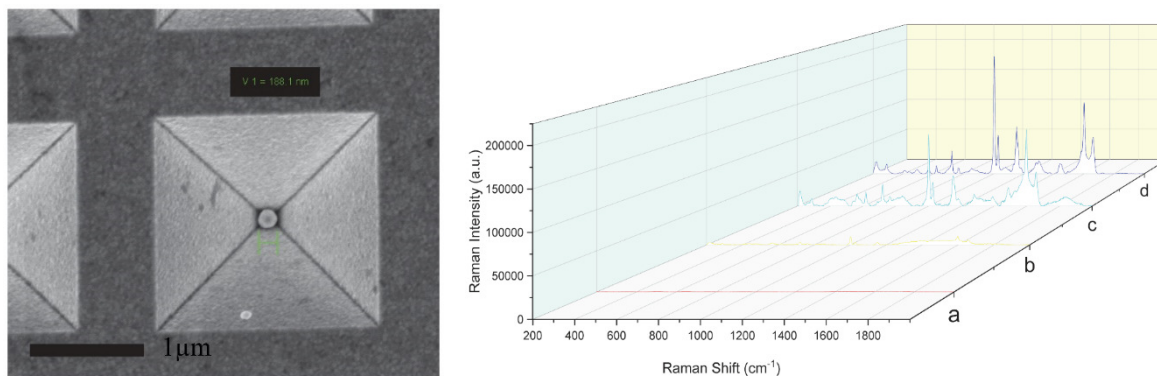


Figure 3: Scanning electron microscopic images of the periodic array of gold coated inverse pyramids with the entrapped gold nanoparticle (left). Reference normal Raman (right, curve a) and surface enhanced Raman spectra of benzophenone recorded on array of gold coated inverse pyramids (right, curve b), array of gold coated inverse pyramids with entrapped nanoparticles (right curve c) and the latter with octadecanethiol surface functionalization (right, curve d).

The applicability of special periodic 3D structure was demonstrated for simultaneous particle (or cell) or nanoparticles trapping and extremely sensitive Surface-Enhanced Raman Spectroscopy based detection of molecules immobilized on the surfaces of the confined beads.

#### References

- [1] I. Rigó, M. Veres, P. Fürjes, SERS active periodic 3D structure for trapping and high sensitive molecular analysis of particles or cells, Proceedings of Eurosensors 2017 Conference, Paris, France, 2017 (Proceedings 2017, 1(4), 560; doi:10.3390/proceedings1040560)

#### Related publications

- [1] I. Rigó, M. Veres, O. Hakkel, P. Fürjes: Hierarchically Combined Periodic SERS Active 3D Micro- and Nanostructures for High Sensitive Molecular Analysis, Proceedings of Eurosensors 2018 Conference, Graz, Austria, 2018 (Proceedings 2018, 2(13), 1069; <https://doi.org/10.3390/proceedings2131069>)
- [2] I. Rigó, M. Veres, P. Fürjes: SERS active periodic 3D structure for trapping and high sensitive Raman-spectroscopy of molecular surface analysis of particles or cells, Lab-on-a-Chip Europe 2018 Conference, Rotterdam, The Netherlands, 2018

# INTELLIGENT WOUND PATCH FOR ONLINE MONITORING WOUND HEALING PROCESSES – WOUNDER

(National Research, Development and Innovation Fund (NKFIA) via NVKP\_16-1-2016-0018)

P. Fürjes, O. Bálint-Hakkel, I. Bársony, F. Bíró, P. Földesy, Z. Hajnal, P. Hermann, V. Rakovics, I. Réti, Z. Szabó

In the clinical practice, the proper care of wounds obtained in accidents, postoperative and ulcerative ulcers is of primary importance. It is a basic expectation of the treating physician to obtain continuous or regular information on the healing of the wound. In case of a home-based hospitalization, the control of wound is time consuming and difficult for the physician, but remote monitoring of the appropriate parameters can help in effective curing. The task of the “intelligent bond” we developed is to facilitate the work of the physician and the cure of the patient by monitoring the process of healing. In case of a problem the user and the physician should be warned about the need for a check or a replacement.

An intelligent tool was developed to provide continuous information about various parameters of the wound healing, such as temperature, humidity, and the tightness of the bandage. [1] Targeting a final wireless, point-of-care application we focused on the minimisation of the energy consumption of the electronics. Appropriate sensors were chosen and integrated into a flexible PCB. Low power consumption electronics were also developed to solve the preliminary signal processing and communication tasks using Bluetooth protocol. Data processing and visualisation software was also developed. For testing the proper functionality of the sensor system, as well as their influence on the operation behaviour of the sensors various tests and calibrations were elaborated by using different wound dressings applied in medical practice.

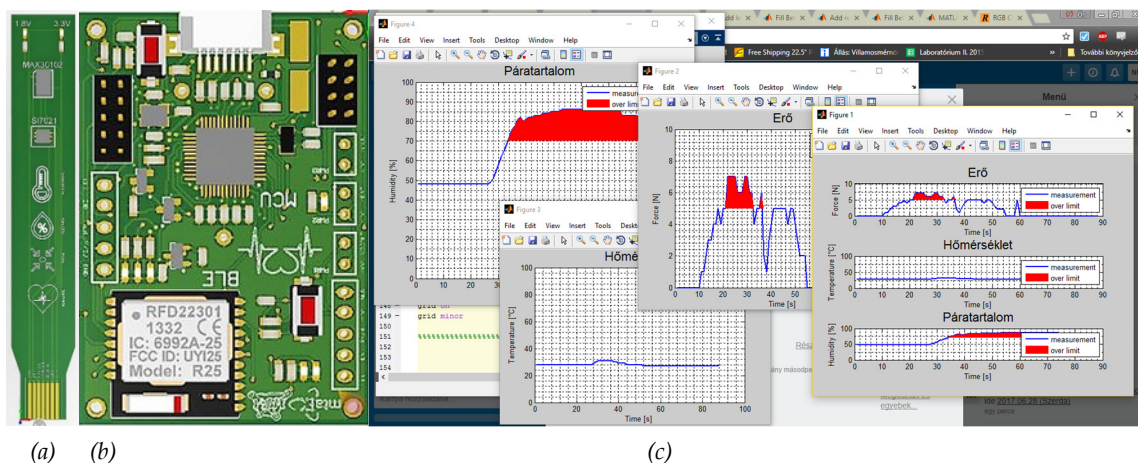


Figure 1: Flexible PCB for sensors (a) and signal processing electronics (b) for wound healing monitoring system. The sensor data can be visualized in the application specific software (c) – WoundER / PC.

## Related publication

- [1] T. R. Dargaville, B. L. Farrugia, J. A. Broadbent, S. Pace, Z. Upton, N. H. Voelcker: *Sensors and imaging for wound healing: A review*, *Biosensors and Bioelectronics* **41**, 30–42 (2013)

# INVESTIGATION OF METAL (Ni) INDUCED LATERAL CRYSTALLIZATION OF AMORPHOUS Si THIN FILMS AT LOW TEMPERATURE

(TÉT-10-1-2011-0570)

G. Z. Radnóczy, B. Pécz, I. Stoimenos, N. Frangis, N. Vouroutzis (AU, Thessaloniki)

The well-known Metal Induced Lateral Crystallization (MILC) process was studied at low temperature to characterize the various ways of crystallization taking part in the process. At low temperature crystallization is dominated by the movement of the  $\text{NiSi}_2$  particles forming the characteristic whiskers (Figure 1a). Further growth of the whisker sidewalls is suppressed in contrast to experiments carried out at higher temperatures. Consequently, the morphology of the resulting crystalline structure will be dominated by whiskers growing in various directions. Whiskers growing in 111-type directions often change growth direction to other equivalent 111-type direction forming a  $70.5^\circ$  kink.

Tetrahedral  $\text{NiSi}_2$  inclusions forming during crystallization and previously observed in Si whiskers grown by the MILC process were also observed in these experiments confirming that the whisker growth is very similar to other experiments (Figure 1b).

Analytical measurements were also carried out using the newly installed Themis microscope's SuperX detector system to confirm the presence of Ni at whisker tips. Unfortunately, the preparation process (etching the glass substrate under the 50 nm thick a-Si/Si film) mostly removed the  $\text{NiSi}_2$  clusters leading the whisker growth, however in some exceptional cases enough silicide was preserved. Such a whisker tip is imaged in STEM-HAADF mode and shown in the figure below together with the elemental map for Ni and Si (Figure 1c).

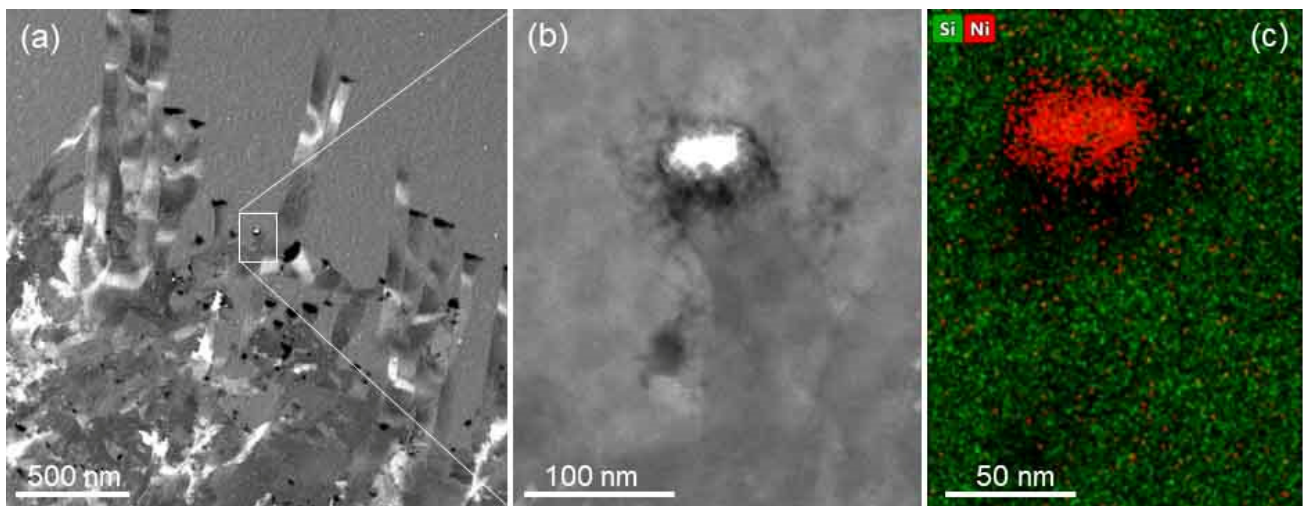


Figure 1: a.) HAADF overview image of a group of mostly parallel whiskers. Black regions at the whisker tips are holes where the  $\text{NiSi}_2$  clusters were etched during preparation. b.) an exceptional whisker with a preserved  $\text{NiSi}_2$  cluster showing as a bright region due to Z-contrast and c.) EDX elemental map of Ni and Si of the region imaged in b.)

## Related publication

- [1] N. Vouroutzis, J. Stoemenos, N. Frangis, G. Z. Radnóczy, D. Knez, F. Hofer, and B. Pécz: *Structural characterization of poly-Si Films crystallized by Ni Metal Induced Lateral Crystallization*, Scientific Reports, **9**, Article number: 2844 (2019)

# DESIGN OF CORROSION RESISTIVE SiC NANO-LAYERS

A. S. Rácz, M. Menyhárd

We have demonstrated earlier that applying ion beam induced mixing (IBM) at room temperature on C/Si/C/Si/C multilayer structures nano-sized SiC production occurred. It has also been shown that the appearance of nano-sized SiC rich layer improves considerably the corrosion resistance of the irradiated sample. A correlation between the corrosion resistance of the sample and the amount and distribution of SiC determined by AES depth profiling has been found [A.S. Racz et al., ACS Appl. Mater. Interfaces, 2017, 51, 44892–44899]. This observation provides the possibility of tailoring corrosion resistance of a given sample; one must determine and produce the SiC amount and distribution necessary to reach the desired corrosion resistance. If one wishes to design a protective coating allowing for various constrains concerning the layer structure, determining the optimal irradiation conditions using an experimental approach is rather time consuming and expensive, however. Therefore, we looked for applying simulation techniques.

Here we report on corrosion resistance measurements on samples produced by IBM at room temperature applying various irradiation conditions and samples containing C and Si layers of various thicknesses and numbers being on Si substrate. For ion bombardment we have used the easily available Ar<sup>+</sup> and Xe<sup>+</sup> ions. The amount and distribution of the SiC has been determined by TRIDYN simulation (not by AES depth profiling). The effective areal density of SiC (introduced in our previous work) was calculated from the SiC distribution and an excellent correlation between these quantities and the measured corrosion resistances has been found (Figure 1). Therefore, having any request for a given corrosion resistance by the help of the TRIDYN simulation we can determine the irradiation conditions considering the other constrains by the layer thicknesses and numbers as well. This enables a high freedom for the design of the protective coating layer.

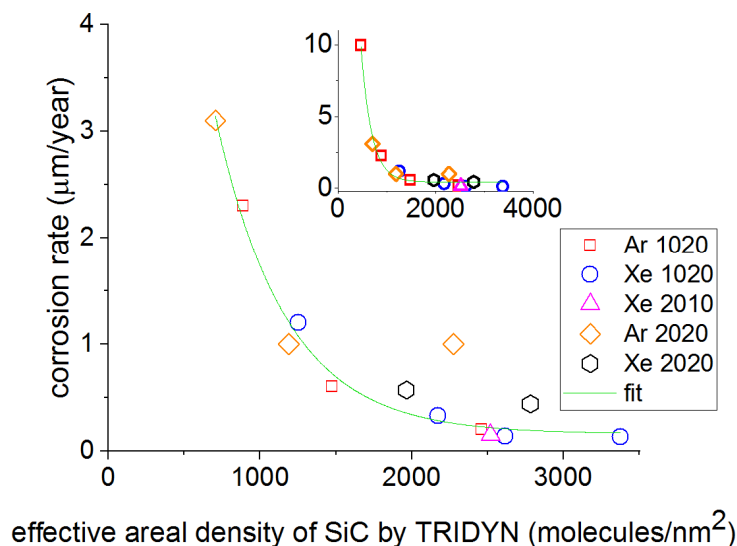


Figure 1: The experimentally measured corrosion rate vs. effective areal density of SiC determined by TRIDYN simulation; inset enlarged y axis.

## Related publication

- [1] A. S. Racz, M. Menyhard: *Design of corrosion resistive SiC nano-layers*, ACS Appl. Mater. Interfaces, **10**:(26), 22851–22856 (2018)

# HIGHLY SAFE GAN METAL-OXIDE-SEMICONDUCTOR TRANSISTOR SWITCH

(SAFEMOST)

L. Tóth, Zs. Fogarassy, I. Cora, D. Gregušová (IEE), J. Kuzmík (IEE) and B. Pécz

In the frame of the international SAFEMOST project we continued the complex structural study of the InGaN/AlGaN/GaN heterostructures prepared by our colleagues at IEE SAS, Bratislava. The main goal was to influence the electrical polarization of the layers through incorporation of a suitable mechanical stress and thus reaching normally-off operation of the switching device.

In 2018, installation of a new aberration corrected TEM (of the type FEI Themis) in our lab opened new possibilities in our characterization spectrum. The use of the aberration corrected objective lens improved the point-to-point resolution by a factor of two (down to 0.09 nm). Also, use of several new methodologies (like scanning transmission techniques with various detectors, EDS mapping, etc.) became possible in the lab.

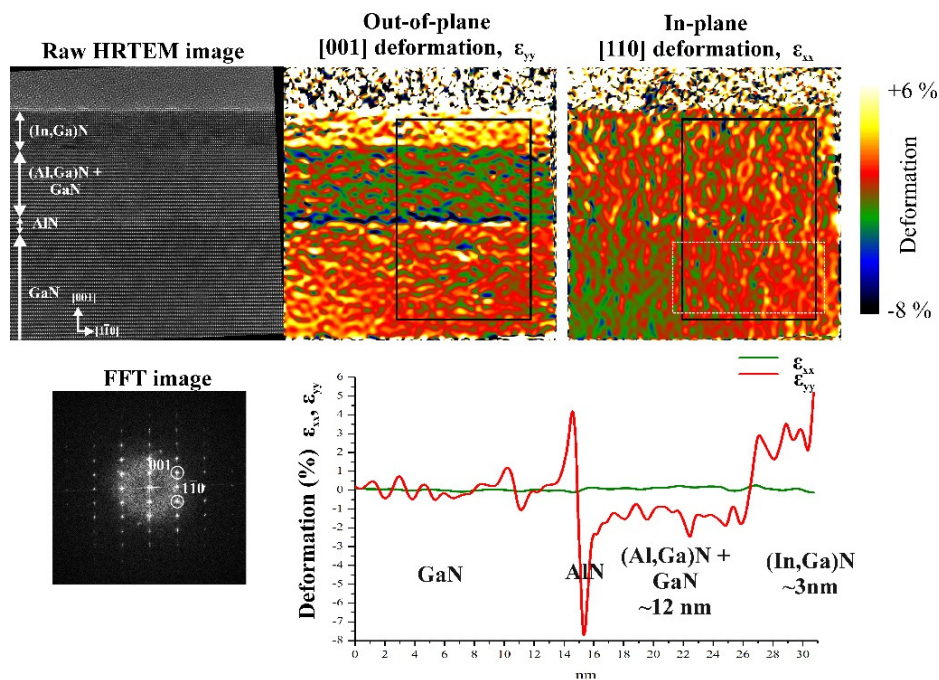


Figure 1: Determination of local variation of the deformation tensor in a InGaN/AlGaN/GaN sample by means of the GPA technique in the aberration corrected new Themis electron microscope.

By applying the new Themis electron microscope, local variation of the of the strain tensor components were determined using geometrical phase analysis (GPA) technique (Figure 1). Starting from high resolution images of the cross-sectional specimens and their Fourier transform, the in-plane and out-of-plane deformation components of the crystal lattice were calculated with a special software (relative to a non-deformed reference area in the same TEM lamella). It turned out that the in-plane strain component is practically zero, while the out-of-plane component followed the chemical composition of the layer structure. This means large negative strain in the AlN layer, small (1-2%) negative change in the AlGaN, and somewhat larger (3-4%) positive strain in the InGaN film (Figure 2). The elemental maps taken with the EDS system confirmed our observation. This result supports the model of the Slovakian colleagues on the polarization effects observed by electrical measurements. These samples were found be suitable for the realization of normally-off MOS HEMT (High-electron-mobility transistors) after some additional processing steps.

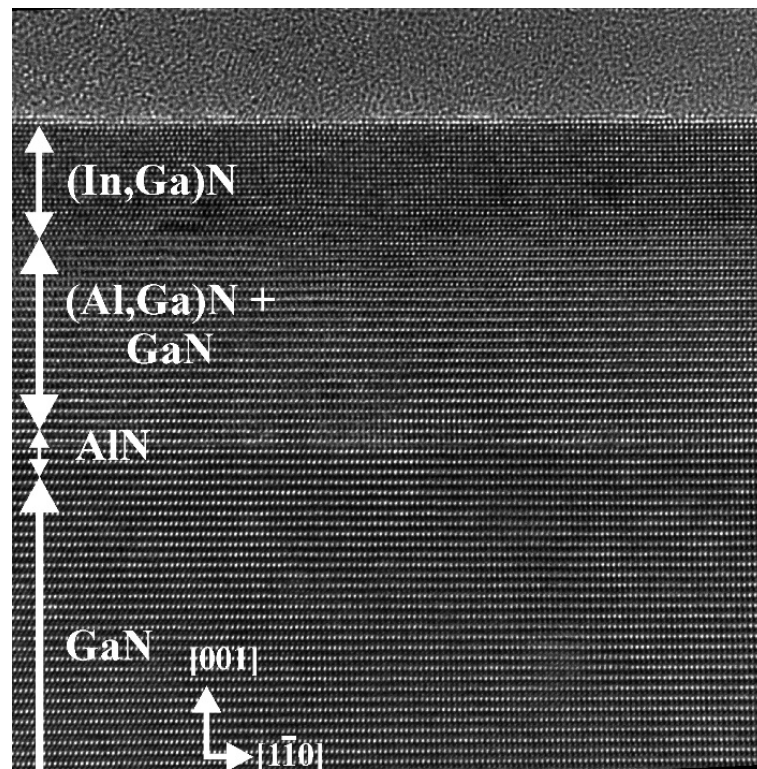


Figure 2: High resolution micrograph of the InGaN/AlGaN/GaN cross sectional sample taken with the new 200 kV Themis electron microscope used for the above GPA analysis.

# IN SITU TEM AND EX SITU HEATING EXPERIMENTS ON $\kappa$ - $\text{Ga}_2\text{O}_3$

(MTA Postdoctoral Fellowship and bilateral CNR- MTA)

I. Cora<sup>a</sup>, Zs. Fogarassy<sup>a</sup>, B. Pécz<sup>a</sup>, F. Mezzadri<sup>b</sup>, F. Boschi<sup>b</sup>, M. Bosi<sup>b</sup>, R. Fornari<sup>b</sup>, A. Recnik<sup>c</sup>

<sup>a</sup>MTA EK MFA, <sup>b</sup>IMEM-CNR, Parma, <sup>c</sup>Jožef Stefan Institute, Ljubljana

$\text{Ga}_2\text{O}_3$  is a wide bandgap semiconducting oxide ( $\sim 4.7$  eV), promising for UV optoelectronics and power electronics.  $\text{Ga}_2\text{O}_3$  layers were grown onto (001) surface of  $\alpha$ - $\text{Al}_2\text{O}_3$  by vapour phase epitaxy [1]. *Ex situ* heated samples up to 1000 °C and studied by XRD, DSC, TEM and simulations using JEMS software package. The *in situ* heating of cross sectional and plan view TEM lamella was also done in TEM up to 980°C in order to follow and study the  $\kappa \rightarrow \beta$  (orthorhombic to monoclinic) structural transformation.

The structure of  $\kappa$ - $\text{Ga}_2\text{O}_3$  is ordered in 5-10 nm large (110)-twinned domains, and each domain has an orthorhombic structure with  $Pna2_1$  space group symmetry [2]. This phase is a new polymorph among the Ga-oxides.

During the *in situ* heating experiment the structural changes and the transformation was acquired on movie and the samples were studied in detail (BF, HRTEM, SAED, simulations). Fornari *et al.* [3] earlier studied the DSC curve of the transformation and they reported a weak endothermic bent up to 650°C. We connect this bent to the moving of grain/twin boundaries, antiphase boundaries, and the enlargement of domain size in the material. Between the very spectacular  $\kappa \rightarrow \beta$  phase transformation we identified no amorphous phase.

The kinetically driven phase transformation from  $\kappa$  to  $\beta$  is topotaxial, since the direction of the oxygen stacking is the same. We determined the structural relationship between the two phase and we modelled the interface. Beside the  $\beta$  and  $\kappa$ , the metastable  $\gamma$  phase also appears at lateral interface between  $\beta/\kappa$  and next to  $\kappa$  as well.

With the *ex situ* heating (up to 820°C with 2°C/min speed) of  $\kappa$ - $\text{Ga}_2\text{O}_3$  we had another transformation. We found the  $\kappa \rightarrow \gamma$  phase transformation (Figure 1). The  $\gamma$ - $\text{Ga}_2\text{O}_3$  is cubic metastable phase. We studied its crystal structure by HRTEM and SAED and concluded a most probable crystal structure of it. The interface between them was also studied.

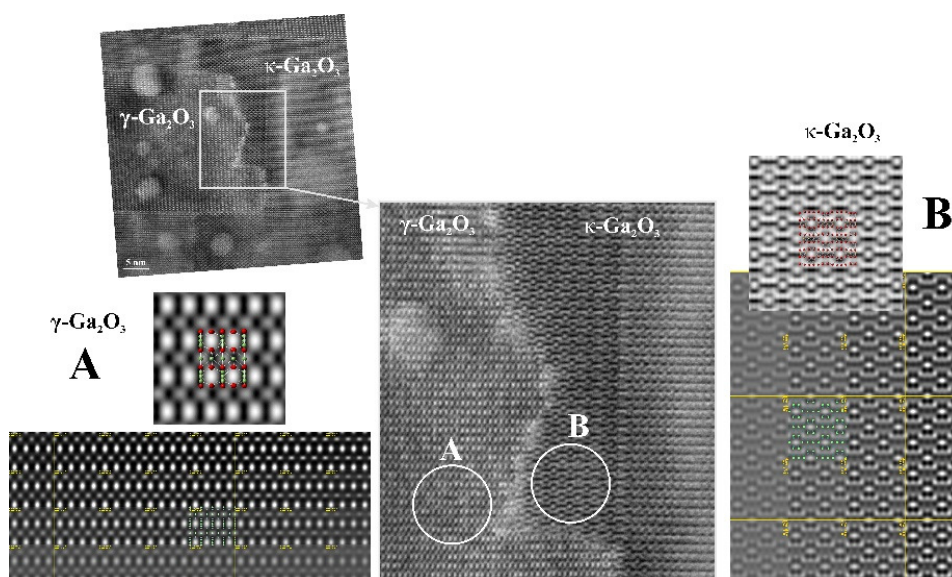


Figure 1: The interface of the transformation on HRTEM image in the middle. Left from the interface ('A') the symmetry averaged, filtered HRTEM image of  $\gamma$  phase with the simulated one for comparison. Right from the interface ('B') is the same but for the  $\kappa$ - $\text{Ga}_2\text{O}_3$ .

## Related publications

- [1] F. Mezzadri, G. Calestani, F. Boschi, D. Delmonte, M. Bosi and R. Fornari: *Crystal Structure and Ferroelectric Properties of  $\epsilon$ - $\text{Ga}_2\text{O}_3$  Films Grown on (0001)-Sapphire*, Inorg. Chem. **55**, 12079 (2016)
- [2] I. Cora, F. Mezzadri, F. Boschi, M. Bosi, M. Čaplovičová, G. Calestani, I. Dódonny, B. Pécz, R. Fornari: *The real structure of  $\epsilon$ - $\text{Ga}_2\text{O}_3$  and its relation to  $\kappa$ -phase*, CrystEngComm **19**:(11) 1509-1516 (2017)
- [3] R. Fornari, M. Pavesi, V. Montedoro, D. Klimm, F. Mezzadri, I. Cora, B. Pécz, F. Boschi, A. Parisini, A. Baraldi, C. Ferrari, E. Gombia, M. Bosi: *Thermal stability of  $\epsilon$ - $\text{Ga}_2\text{O}_3$  polymorph*, Acta Materialia **140**, 411-416 (2017)

# THE INFLUENCE OF BATH ADDITIVES ON THE THERMAL STABILITY OF NANOCRYSTALLINE Ni FILMS PROCESSED BY ELECTRODEPOSITION

T. Kolonits (MFA, ELTE, PhD student), L. Péter (Wigner), I. Bakonyi (Wigner), J. Gubicza (ELTE, supervisor) and Zs. Czigány (MFA, supervisor)

The effect of various organic additives (such as saccharin and trisodium-cytrate) on the microstructure (grain size, dislocation and twin densities), mechanical properties and thermal stability of electrodeposited Ni films was investigated by X-ray diffraction (XRD) line profile analysis and transmission electron microscopy (TEM). The main task of the project is to investigate the thermal stability of different initial microstructures which could be formed by solving organic additives in the original electrolyte.

The electrodeposited layers were deposited at room temperature at low current density onto copper substrate. The basic electrolyte mainly contained nickel-sulphate ( $\text{NiSO}_4 \cdot 7 \text{H}_2\text{O}$ ) and boric acid ( $\text{H}_3\text{BO}_3$ ). XRD and TEM grain size and phase analysis was carried out to determine the microstructure. Hardness tests were made to examine the mechanical properties. Heat treatment (at 400, 500, 600, 750 and 1000 K) was applied to investigate the stability of the micro and macro properties.

According to our former research [1] even a small amount of organic additives has a significant effect on the microstructure (grain size, defect density and texture) of nanocrystalline Ni films. In this work three different microstructures were formed: the organic additive free bath resulted a large grain size (90-130 nm), a low dislocation density ( $13 \times 10^{14} \text{ m}^{-2}$ ) and a (220) type texture. Trisodium citrate resulted a moderate grain size (60-80 nm) and dislocation density ( $30 \times 10^{14} \text{ m}^{-2}$ ) and the direction of the texture was changed into (200). The additive saccharin resulted in the smallest grain size (20-30 nm), the largest defect density ( $160 \times 10^{14} \text{ m}^{-2}$ ), the highest hardness and the texture was eliminated. The differences were caused by the presence of incorporating sulphur and sodium [1].

The changes of the hardness and the microstructure can be followed on Figure 1. It was found that the layer with additive saccharin which showed the highest hardness on room temperature has the worst thermal stability since the high defect density led to a large driving force for recrystallization; the recrystallization process occurred between 750-1000 K and took place in a few minutes. The best thermal stability was achieved in the layer processed with trisodium-cytrate as recrystallization has not been observed even after heating up to 1000 K.

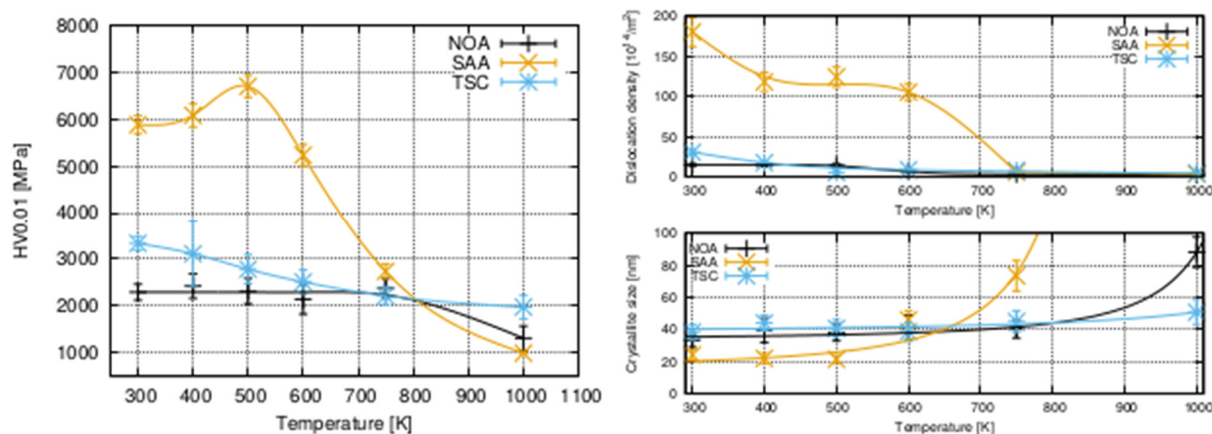


Figure 1: Hardness, dislocation density and crystallite size of heat treated electrodeposited nanocrystalline nickel layers

## Related publication

- [1] T. Kolonits, P. Jenei, L. Péter, I. Bakonyi, Z. Czigány and J. Gubicza: *Effect of bath additives on the microstructure, lattice defect density and hardness of electrodeposited nanocrystalline Ni films*, Surface and Coatings Technology, **349**: 611-621 (2018)

# STRUCTURE AND MECHANICAL PROPERTIES OF HARD AND TOUGH WBC LAYERS – POSSIBLE INDUSTRIAL APPLICATION

S. Mirzaei (Brno), M. Alishahi (Brno), P. Soucek (Brno), L. Zábbransky (Brno), V. Buršíková (Brno), M. Stupavská (Brno), V. Peřina (Rež), K. Balázsi (MFA), Zs. Czigány (MFA), P. Vašina (Brno)

A cooperation of Thin Film Physics Dpt. and Dpt. of Physical Electronics Masaryk University is running since 2016 in research of tungsten boron carbide (WBC) thin films. The main challenge in deposition of protective coatings to produce films, which simultaneously exhibit high hardness and enhanced fracture toughness. Nowadays, popular ceramic based protective coatings show difficulties to cope with these increased demands due to their inherent brittleness. Materials exhibiting such seemingly contradictory combination of mechanical properties - high hardness and moderate ductility - was already realized experimentally in  $\text{Mo}_2\text{BC}$  and recently predicted by ab-initio calculations in crystalline  $\text{X}_2\text{BC}$  system ( $\text{X} = \text{Ti}, \text{V}, \text{Zr}, \text{Nb}, \text{Mo}, \text{Hf}, \text{Ta}, \text{W}$ ). Our aim is to produce fracture tough WBC protective coatings and in the long run to produce the theoretically predicted  $\text{W}_2\text{BC}$  crystalline phase which was predicted to have the best mechanical properties in the  $\text{X}_2\text{BC}$  family. However, low enthalpy of formation of  $\text{W}_2\text{BC}$  phase and existence of WB and WC phases instead of  $\text{W}_2\text{BC}$  phase indicate difficulties of deposition of crystalline  $\text{W}_2\text{BC}$  phase. Our results were published in Surface and Coatings Technology [1,2]. In these two papers we have investigated the mechanical, bonding and structural properties of the film at fixed C content with variation of B/W ratio and constant B content with changing C/W ratio, especially in the vicinity of the composition range of  $\text{W}_2\text{BC}$ . WBC films were deposited by combination of DC magnetron sputtering of W and  $\text{B}_4\text{C}$  targets and pulsed DC sputtering for C in Ar at  $500^\circ\text{C}$ . The pulsed regime resulted in 2.5 times increase of ion flux at 350 kHz and 65% duty cycle compared with DC sputtering. Bonding structure and mechanical properties were investigated by XPS and nanoindentation, respectively. Structural properties were investigated by TEM (including HRTEM and SAED) using JEOL3010 equipment at MFA. It was determined, that the coatings far from the composition of  $\text{W}_2\text{BC}$  phase are amorphous, while those coatings close to  $\text{W}_2\text{BC}$  composition are nanocomposites containing nanocrystals with size of  $\sim 5\text{nm}$  embedded into an amorphous matrix (Figure 1). A certain level of short range ordering can be observed even in the amorphous films which is manifested in short, curved and irregular lattice fringes in the HRTEM images. All the layers exhibited high hardness ( $>20\text{GPa}$ ) so they all can be classified as hard coatings. The level of crystallinity played no crucial role in determining the hardness of the coating, while the effect of the coating structure and bonding was clear – the densest coating with the highest relative amount of W-B bonds exhibited the highest hardness of  $\sim 29\text{GPa}$  (Figure 2).

We are planning to continue the research with coatings deposited in industrial deposition chamber and other members of  $\text{X}_2\text{BC}$  family (e.g.  $\text{Mo}_2\text{BC}$ ).

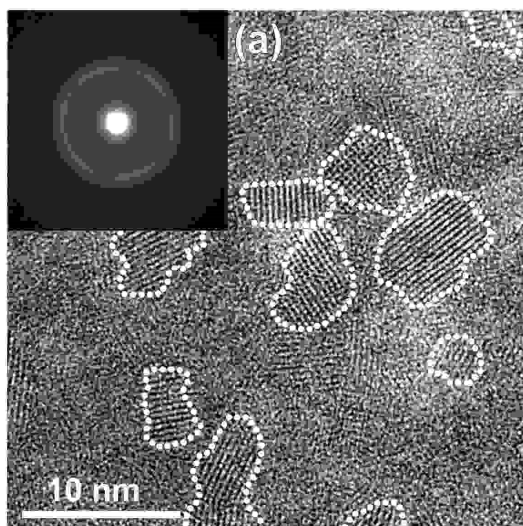


Figure 1: HRTEM image and SAED pattern of  $\text{W}_{53}\text{B}_{17}\text{C}_{30}$  film. The film has nanocomposite structure with nanocrystals embedded in the amorphous matrix.

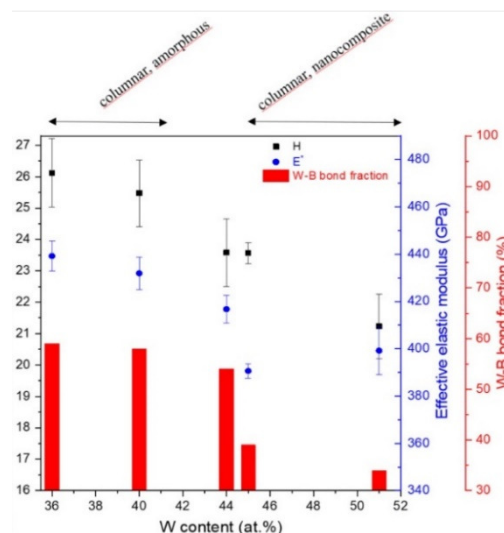


Figure 2: Hardness and Young's modulus correlates with fraction of stiff W-B bonds for sputter deposited  $\text{W}_x\text{B}_y\text{C}_z$  coatings

## Related publications

- [1] M. Alishahi, S. Mirzaei, P. Soucek, L. Zábbranský, V. Buršíková, M. Stupavská, V. Peřina, K. Balázsi, Zs. Czigány, P. Vašina: Evolution of structure and mechanical properties of hard yet fracture resistant W-B-C coatings with varying W and C content, Surface and Coatings Technology **340**, 103-111 (2018)
- [2] S. Mirzaei, M. Alishahi, P. Souček, L. Zábbranský, V. Buršíková, M. Stupavská, V. Peřina, K. Balázsi, Zs. Czigány and P. Vašina: On the origin of the hardness of fracture resistant W-B-C coatings with varying B/W ratio, Surface and Coatings Technology **358**, 843-849 (2019)

# NEW TYPE FUNCTIONAL ALLOY FILMS

(NN OTKA-112156)

F. Misják, K. Hajagos-Nagy, M. Čaplovičová (Slovak University of Technology in Bratislava)  
G. Radnóczy

## *Effect of growth temperature on the growth of CoCrFeNiCu high entropy alloy (HEA) films*

Five-component CoCrFeNiCu HEA films were deposited by DC magnetron sputtering using spark-melted targets at background pressure of  $6 \times 10^{-8}$  mbar with a deposition rate of  $\sim 10$  nm/min. The working pressure was  $3 \times 10^{-3}$  mbar by applying 99.9 % pure Argon as sputtering gas. Films were deposited onto thermally oxidized (100)-oriented Si wafers. The growth was carried out at room temperature, as well as, elevated temperature of 380 °C.

The nanostructure of the films was analyzed by transmission electron microscopy (TEM) in a Philips CM20 microscope at 200 kV accelerating voltage. HREM measurements were made in a 200 kV JEOL JEM ARM 200cF microscope. Samples for TEM investigation were produced in cross section views, embedding the films in Ti rings and grinded by mechanical polishing to about 50  $\mu$ m thickness. The thinning was then followed by Ar<sup>+</sup> ion milling at grazing incidence.

The structure of the films grown at room temperature is single-phase FCC and corresponds to zone T structure, with a well expressed <111> texture. Width of the columns is uniform about  $\sim 25$  nm and the growth competition region is about 50 nm thick in the 500 nm thick film. The columns are rather defective, the main defects are planar defects, stacking faults and twin lamellae. Their density is very high; it is around 2-3 faults/nm (Figure 1). As the film is grown in good vacuum conditions ( $p=6 \times 10^{-8}$  mbar) no impurity effects are expected to be present. The impingement rate of oxygen/metallic species is  $\sim 5 \times 10^{-3}$ . The five-constituent components are randomly distributed in the FCC structure; no ordering or separation of components is detected.

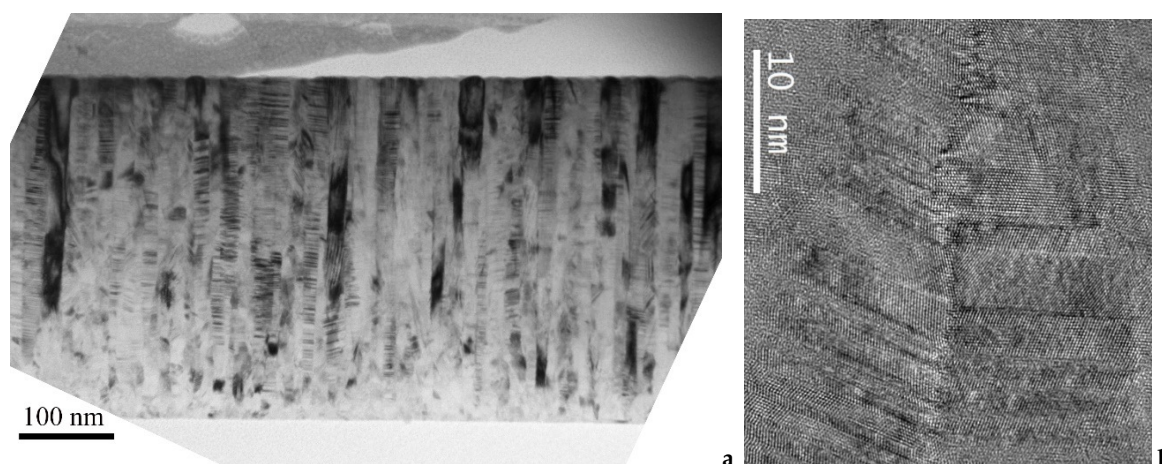


Figure 1: Overall (a) and high resolution (b) image of CrFeCoNiCu alloy film grown at 20°C substrate temperature and  $6 \times 10^{-8}$  mbar background pressure

The morphology of the film grown at 380 °C substrate temperature corresponds to the transition between zones II and III of the structure zone model and possesses dominant single phase FCC structure. Repeated nucleation is clearly observed (Figure 2a), meaning the formation of a covering or blocking layer during the growth of alloy crystallites.

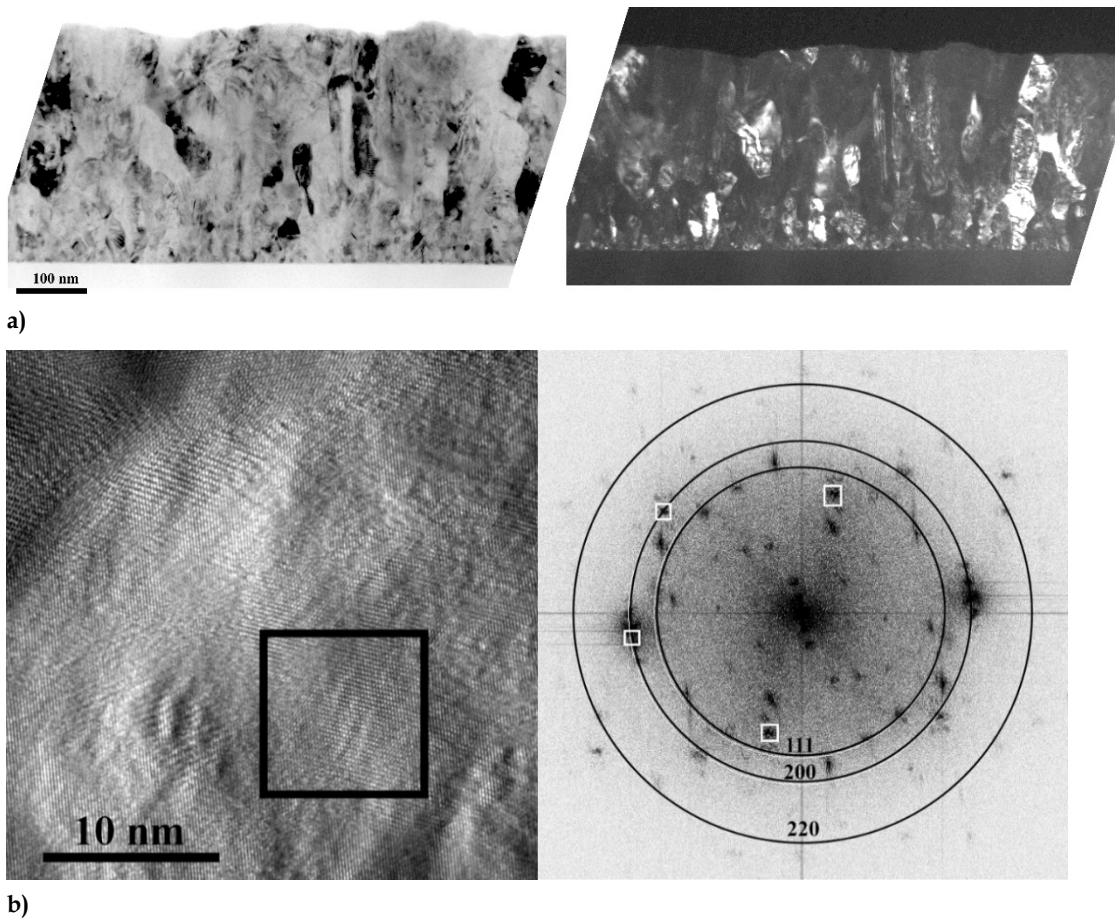


Figure 2: Overall bright field and dark field (a) and high resolution and FFT (b) images of CrFeCoNiCu alloy film grown at 380°C substrate temperature and  $4 \times 10^{-6}$  mbar background pressure

This is also supported by the random crystallographic orientation of the grains. The vacuum during growth was maintained at  $p=4 \times 10^{-6}$  mbar, resulting in an impingement ratio of impurity to metal species  $\sim 1 \times 10^{-1}$ .

This impingement ratio can result in the formation of a covering layer (either oxide or nitride or their mixture) leading to repeated nucleation. The FFT (Fast Fourier Transform) obtained from the high resolution image shows the presence of the FCC reflections (those falling on the rings in Figure 2b) but shows the presence of other reflections as well, indicating the formation of second crystalline phases in the film. Their quantity is however small, as they are not detectable in the overall diffraction patterns obtained from the film.

## TEM STUDY OF COPPER SILICIDES

*E. Dódony (PhD student), G. Z. Radnóczy (supervisor)*

Copper-silicides attracted considerable interest due to their wide range of applications.  $\text{Cu}_3\text{Si}$  is an important phase of the family (Figure 11). It is used in ultrapure silicon synthesis for photovoltaic and electric devices, as contact material in microelectronics and as catalyst for carbon nanowire and semiconductor production. Despite the importance of copper-silicides, their phase and structural relations are not entirely solved yet. Due to their importance, we are studying the formation of copper-silicides in thin amorphous silicon (a-Si) films. A 10 nm thick a-Si film was transferred to copper grid (Cu-grid) and heated in-situ in a Philips CM20 transmission electron microscope. During the heating the Cu-grid acted as an unlimited source for the diffusion of metal into the a-Si film. Silicide formation started at 500 °C (Figure 2). We observed the  $\eta$ - $\text{Cu}_3\text{Si}$ -phase and its modulations during our experiments.

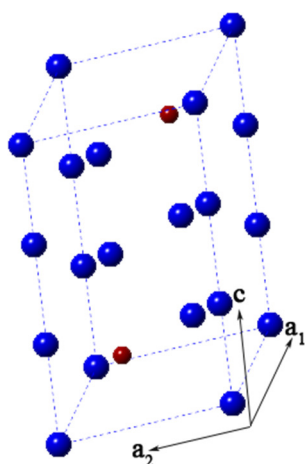


Figure 1: Structural model of  $\text{Cu}_3\text{Si}$ ; space group:  $P-3m1$ ,  $a_0$ : 4.06 Å,  $c_0$ : 7.33 Å

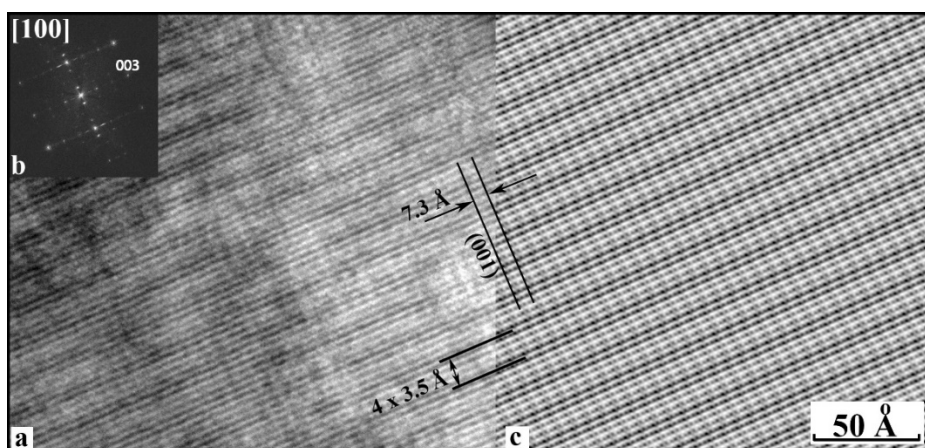


Figure 2: Raw [100] projected experimental HRTEM image of modulated  $\text{Cu}_3\text{Si}$  with four times of the (100) periodicity (= 14.0 Å) of the basic structure (a), its Fourier-transform (b) and the Fourier-filtered experimental image (c)

For the phase and structural measurements, we recorded high resolution (HRTEM) images and selected area electron diffraction (SAED) patterns, under Jeol3010 and Philips CM20 transmission electron microscopes, respectively. By analysing SAED patterns and HR images, we found that the  $\eta$ -phase's structural model does not fit our experimental data and that many modulations of the phase formed under the experimental conditions.

Through measurements, calculations and modelling we gave a new structural model for the  $\eta$ - $\text{Cu}_3\text{Si}$ -phase (Figure 1) and solved two of the many modulations formed by the different ordering of the Cu - Si atoms forming supercells. One is shown in Figure 2 with modulation in the  $a$  direction with four times periodicity of the basic  $\text{Cu}_3\text{Si}$  structure.

# THE INFLUENCE OF ARTIFICIAL AGING ON THE MICROSTRUCTURE OF AN AL-ZN-MG-ZR ALLOY PROCESSED BY EQUAL CHANNEL ANGULAR PRESSING

J. L. Lábár (MFA), J. Gubicza<sup>1</sup>, J. Lendvai<sup>1</sup> and N. Q. Chinh<sup>1</sup>

<sup>1</sup>Department of Materials Physics, Eötvös Loránd University

There is a large interest in age-hardenable Al-Zn-Mg alloys (7xxx series) due to their technological and practical importance, as these alloys can be treated to have a preferable combination of ductility and strength, as well as reasonable weldability and corrosion resistance. If a supersaturated Al-Zn-Mg alloy is aged under different conditions, various metastable and stable precipitates may form. Therefore, aging can be used for tailoring mechanical behaviour of these alloys. Although, the microstructure obtained by equal channel angular pressing (ECAP) has been extensively studied in the literature, the effect of artificial aging on the precipitation and the strength of SPD-processed supersaturated Al-Zn-Mg alloys has not been clarified so far.

In this paper, the effect of artificial aging on the microstructure and hardness of an ultrafine-grained (UFG) Al-4.8%Zn-1.2%Mg-0.14%Zr (wt.%) alloy was studied. The UFG microstructure with an average grain size of about 260 nm was obtained by severe plastic deformation (SPD) applying four passes of ECAP at room temperature. Then, artificial aging was performed on the ECAP-processed samples at 120 °C and 170 °C for 2 h.

The size and morphology of the matrix grains and the precipitates were characterized by transmission electron microscopy (TEM). Thin TEM-lamellae were prepared by Ar-ion milling with special care taken to avoid heating (and possible transformation) of the samples during preparation. TEM and energy-disperse X-ray spectroscopy (EDS) examinations were performed in a Titan Themis G2 200 STEM equipped with a four-segment Super-X EDS detector. The corrector for the spherical aberration (Cs) was applied at the imaging part, while no probe-correction was present. Image resolution limit is 0.08 nm in phase-contrast HRTEM mode, while resolution is 0.16 nm in STEM Z-contrast imaging mode (recorded with a Fishione high-angle annular dark-field (HAADF) detector). HRTEM images were recorded at 200 keV with a 4k × 4k CETA 16 CMOS camera. EDS data were recorded (together with the HAADF signal) in spectrum-image (SI) mode, where individual X-ray count data can later be post-processed pixel-by-pixel and elemental intensities (and quantified elemental concentrations) can be obtained from any post-selected regions. In that way, distribution of concentrations can be visualized along any lines or over any area.

In the ECAP-processed sample Guinier-Preston (GP) zones, MgZn<sub>2</sub> precipitates and a high dislocation density were observed (Figure 1). After aging at 120 °C, coarse MgZn<sub>2</sub> precipitates were formed in the grain boundaries, leading to softening, while the dislocation density did not decrease (Figure 2). Annealing at 170 °C yielded a growth of the matrix grains to ~530 nm with a significant decrease of the dislocation density (Figure 3). In addition, GP zones disappeared and MgZn<sub>2</sub> precipitates were formed in both the grain interiors and the boundaries. This overaging of the precipitate structure and the decrease of the dislocation density resulted in a lower hardness than after annealing at 120 °C. It was found that the hardness-reduction due to the change of the precipitate structure at 170 °C was higher than that caused by the decrease of the dislocation density.

This research was supported by the Hungarian-Russian Bilateral Research Program (TÉT) No. 2017-2.3.4-TÉT-RU-2017-00005 and by grant no. VEKOP-2.3.3-15-2016-00002 of the European Structural and Investment Funds.

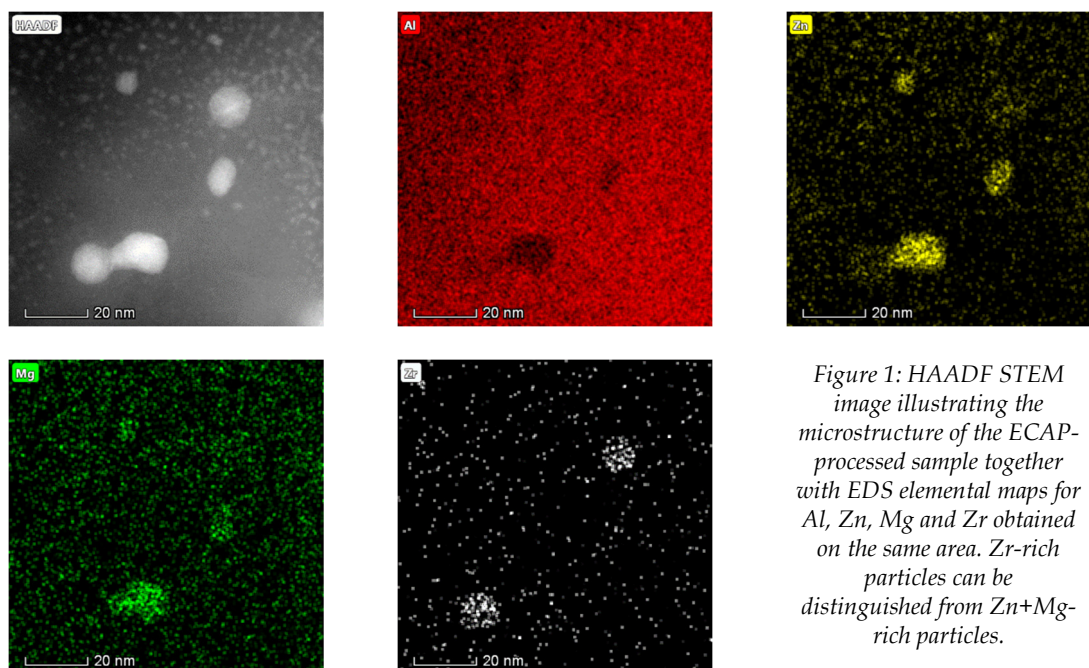


Figure 1: HAADF STEM image illustrating the microstructure of the ECAP-processed sample together with EDS elemental maps for Al, Zn, Mg and Zr obtained on the same area. Zr-rich particles can be distinguished from Zn+Mg-rich particles.

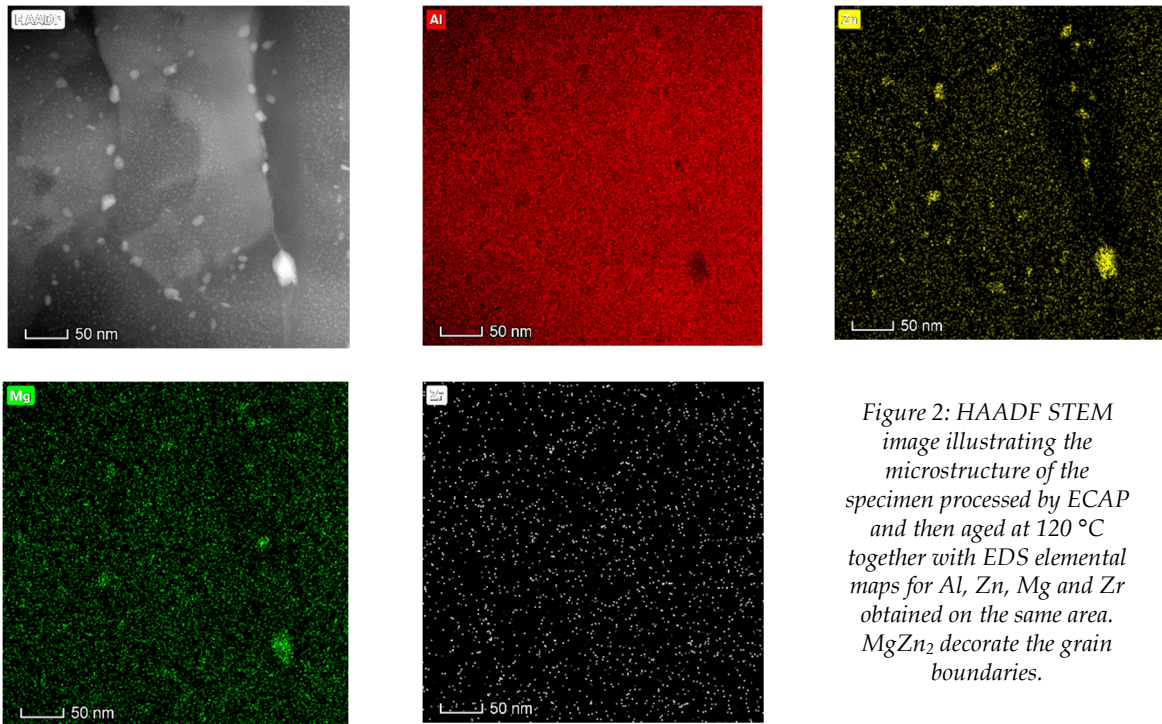


Figure 2: HAADF STEM image illustrating the microstructure of the specimen processed by ECAP and then aged at 120 °C together with EDS elemental maps for Al, Zn, Mg and Zr obtained on the same area.  $MgZn_2$  decorate the grain boundaries.

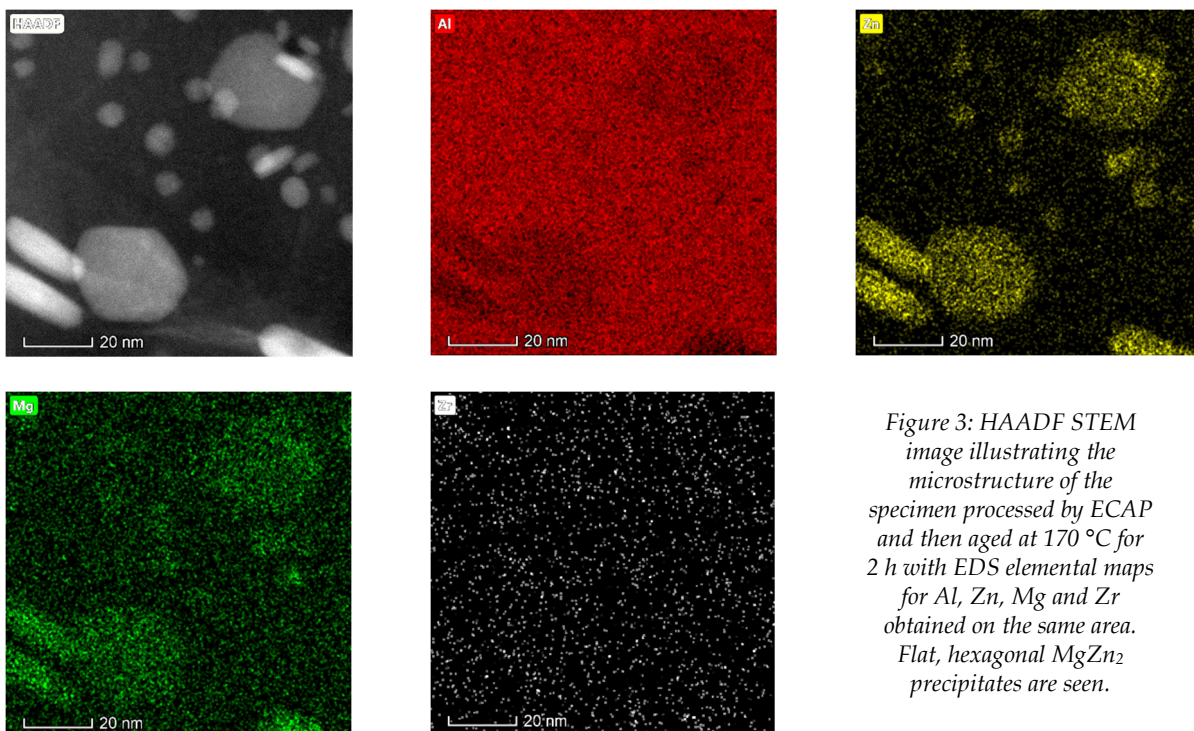


Figure 3: HAADF STEM image illustrating the microstructure of the specimen processed by ECAP and then aged at 170 °C for 2 h with EDS elemental maps for Al, Zn, Mg and Zr obtained on the same area. Flat, hexagonal  $MgZn_2$  precipitates are seen.

# WEAR MECHANISM OF SPARK PLASMA SINTERED MULTIWALL CARBON NANOTUBES REINFORCED ZIRCONIA COMPOSITES UNDER DRY SLIDING CONDITIONS

*S. Lamnini (PhD student), K. Balázsi (supervisor), C. Balázsi (supervisor)*

Multiwall carbon nanotubes (MWCNTs) reinforced ceramics matrix served not only as enhancing factor of the mechanical properties, but also enabled the formation of an intrinsic solid lubricant effect, thus affording low friction response and remarkable wear resistance. However, controversial results have been often reported with different concentrations. In this work, multiwall carbon nanotubes (MWCNTs) reinforced 8 mol. % yttria-stabilized zirconia (8YSZ) composites were synthesized using ball milling and spark plasma sintering (SPS, at 1400 °C) in different compositions (0, 1, 5, 10 wt. % MWCNTs). The aim of our investigation is to provide an explicit understanding of the wear mechanism features evaluated after friction-test against  $\text{Si}_3\text{N}_4$  balls used as a counterpart, which can contribute largely to avoid the easier mechanical failure. Furthermore, the effect of sliding speed namely at low ( $V_1=0.036$  m/s) and high ( $V_2=0.11$  m/s) was also highlighted (Figure 1). In fact, an outstanding wear improvement at low sliding speed ( $V_1$ ) was reported with the addition of 1 wt. % of MWCNTs. This was most likely attributed to two main reasons: 1) the formation of a perfectly continuous and uniform tribo-film. 2) the improved flexural strength, fracture toughness and density. Based on Scanning Electron Microscopy (SEM) and Energy Dispersive X-ray spectroscopy (EDS) results, we have concluded that the applied sliding speed, grain size / geometry, surface roughness, MWCNTs content and its dispersion into the matrix, altogether plays a vital role to beneficially or adversely influence the tribological performance of the composites.

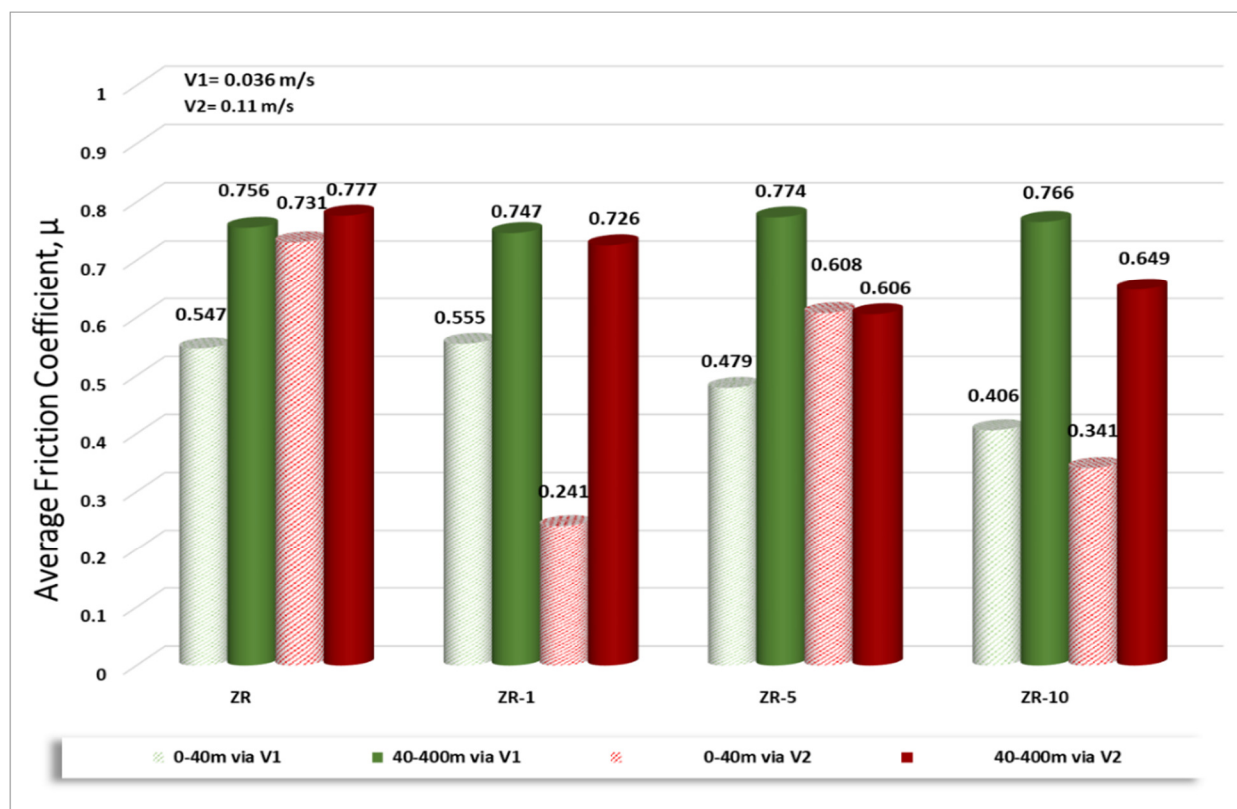


Figure 1: Comparative graph presenting the Average Friction Coefficient ( $\mu$ ) during transitory state (0-40m) and steady state (40-400m) for all the composites tested at fix normal load (5N) and different sliding rates ( $V_1=0.036$  m/s,  $V_2=0.11$  m/s)

# EXAMINATION OF MILLED HEXAGONAL BORON NITRIDE ADDITION ON SINTERED $\text{Si}_3\text{N}_4$ -h-BN CERAMIC COMPOSITES

(FLAG.ERA "Ceranea" NN127723)

K. Balázsi, M. Furkó, Zs. Fogarassy, C. Balázsi

Silicon nitride ( $\text{Si}_3\text{N}_4$ ) ceramics containing 1 and 5 wt.% of hexagonal boron nitride (h-BN) have been prepared by attrition milling and hot-isostatic pressing using three different milling conditions. Thorough morphological characterizations have been carried out to reveal the influence of the milling parameters on the size of the h-BN additives. The results confirmed significant decrease in h-BN particle size by increasing milling time. The transmission electron microscopy (TEM) observations revealed that the h-BN particles were evenly incorporated into the ceramic matrix (Figure 1). Moreover, the increase of the h-BN content decreased significantly the hardness of materials and the hardness values were higher when the size of h-BN was larger (Figure 2).

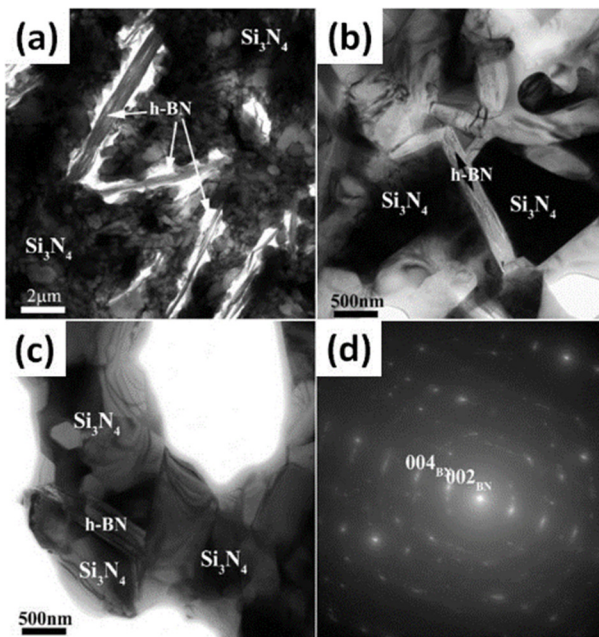


Figure 1: Bright-field (BF) TEM images of B1/5 (a) C2/1 (b) and D3/1 (c) samples as well as selected area electron diffraction (SAED) on one h-BN platelet within the B1/5 sample (d)

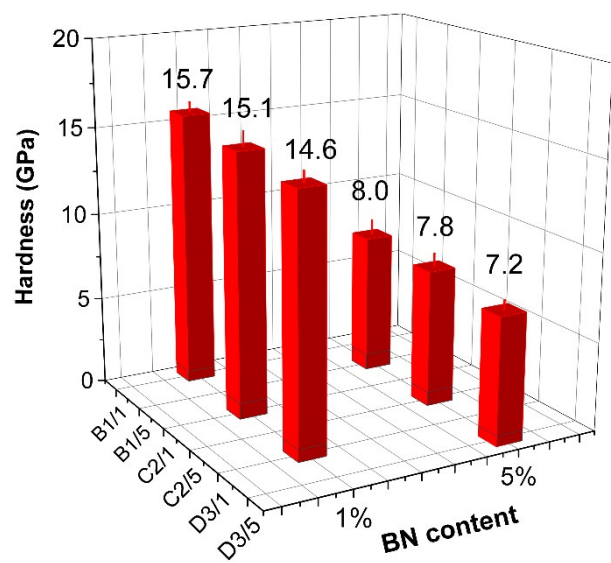


Figure 2: Hardness measurement on  $\text{Si}_3\text{N}_4$ /h-BN composite samples containing 1 and 5 wt.% h-BN additives prepared with different methods. B1/1 and B1/1 samples: h-BN added without pre-milling, C2/1 and C2/5 samples: h-BN added 30 minutes before the milling, D3/1 and D3/5 samples: h-BN added at the beginning of the milling

# CO<sub>2</sub> REFORMING OF METHANE BY Ni-In/SiO<sub>2</sub> CATALYST WITH NO COKE FORMATION

J. Károlyi, M. Németh, C. Evangelisti, G. Sáfrán (MFA), Z. Schay, A. Horváth, F. Somodi

The current opinion is that the reduction of carbon dioxide with methane (dry reforming of methane (DRM)  $\text{CO}_2 + \text{CH}_4 = 2\text{CO} + 2\text{H}_2$ ) would be a suitable reaction, since the product is synthesis gas, which is one of the most important feedstock of chemical industry [1-3]. Unfortunately, carbon deposits more readily form on nickel than on noble metal surfaces during the reaction leading to fast deactivation of the catalyst. Potential catalysts for CO<sub>2</sub> – methane dry reforming were tested in a cooperation of MTA EK Surface Chemistry and Catalysis Laboratory and CNR, Institute of Molecular Science and Technologies Milano [4]. It was shown that the presence of 2 wt% indium on the surface of a 3 wt%Ni/SiO<sub>2</sub> catalyst prevented coke formation during dry reforming of methane.

In efforts to understand the mechanism, TPR revealed that indium was unstable against sintering without nickel on the silica surface, however in the bimetallic catalyst it was in metallic state and mixed with nickel after reduction at 700 °C. The presence of indium profoundly changed the adsorption properties of nickel, as CO-TPD (Temperature Programmed Desorption) measurements suggested. XPS measurements showed changes in the electronic structure of nickel on the Ni-In/SiO<sub>2</sub> catalyst after reduction, moreover, they revealed the presence of bimetallic particles which surface composition found to be Ni<sub>2.2</sub>In, lower than the expected Ni<sub>3</sub>In, referring to indium enrichment on the surface.

Table 1: Hydrogen consumption during TPR and the average particle size and dispersion of nickel calculated based on the results of CO pulse chemisorption

	3 wt% Ni/SiO <sub>2</sub>			3 wt%Ni–2 wt%In/SiO <sub>2</sub>		
	1st	2nd	3rd	1st	2nd	3rd
H <sub>2</sub> (cm <sup>3</sup> /g) <sup>a</sup>	9.8	10.3	10.5	15.4	15.3	14.7
CO (cm <sup>3</sup> /g)	0.4	0.8	0.7	1.3	0.7	0.6
D (%) <sup>b</sup>	4.3	7.1	6.0	11.7	5.8	5.2
d (nm) <sup>b</sup>	23.4	14.3	16.9	8.6	17.5	19.5

<sup>a</sup>Values at standard temperature and pressure (22414 cm<sup>3</sup> /mol).

<sup>b</sup>Values calculated from the amount of chemisorbed CO.

Simultaneously, HRTEM analysis of the bimetallic catalyst showed the presence of NiIn and Ni<sub>2</sub>In alloy nanoparticles. TEM analysis of the spent catalysts after 24h time on stream showed that the average particle size of the bimetallic catalyst was slightly smaller than that of the monometallic catalyst.

Based on the present results, the higher catalytic activity and outstanding carbon tolerance of the bimetallic Ni-In/SiO<sub>2</sub> catalyst is the consequence of a structural and electronic effects of indium.

## Related publications

- [1] S. Wang, G.Q. (Max) Lu, G.J. Millar: *Carbon Dioxide Reforming of Methane to Produce Synthesis Gas over Metal-Supported Catalysts: State of the Art*, Energy Fuels **10**:(4), 896 (1996)
- [2] M.-S. Fan, A.Z. Abdullah, S. Bhatia: *Catalytic Technology for Carbon Dioxide Reforming of Methane to Synthesis Gas*, ChemCatChem **1**:(2), 192 (2009)
- [3] G. Centi, S. Perathoner: *Opportunities and prospects in the chemical recycling of carbon dioxide to fuels*, Catal. Today **148**:(3–4), 191 (2009)
- [4] J. Károlyi, M. Németh, C. Evangelisti, G. Sáfrán, Z. Schay, A. Horváth, F. Somodi: *Carbon dioxide reforming of methane over Ni-In/SiO<sub>2</sub> catalyst without coke formation*, Journal of Industrial and Engineering Chemistry **58**, 189–201 (2018)

# THINNING OF TEM SAMPLES (KNOW-HOW)

Gy. Sáfrán, N. Szász

## Introduction

Conventional preparation of TEM samples in MTA EK MFA is carried out by Ar-ion beam thinning so that the sample is mounted on the holder by carbon paste. Carbon contamination of samples is a severe problem when working with new generation  $C_s$ -corrected Transmission Electron Microscopes (TEM). High intensity beam in HRTEM and STEM modes may, unfortunately, deposit artefacts of cracking products from the migrating residue of the carbon paste. The deposited contamination raises difficulties or balks the TEM investigation. Fixing the sample with carbon paste is difficult and time consuming. Furthermore, it is risky, since during its removal the sample may be spoiled with the dissolved carbon paste. Consequently, using carbon paste is disadvantageous from the point of view of both preparation and TEM study of the samples! The installation of the  $C_s$ -corrected TEM "THEMIS" in the Thin Films Physics Laboratory arise the need to further develop our thinning technology and to skip carbon paste.

## New technology and sample holder design

In order to replace carbon paste used earlier for mounting the samples a new sample holder (Figure 1) has been constructed that implements mechanical fixing of the sample. In addition, with carbon-free technology in mind, we changed the composition of glue that embeds the slabs of samples into the Ti disk: instead of Araldite mixed with carbon powder we use Gatan G1 with alumina or Ti-powder (Figure 2).

## Results

The new mechanical construction, together with the new composition of embedding glue, was tested in our lab during daily TEM sample preparations over the year 2018. It showed, undoubtedly, that the new solution provides reliable, clean, mounting of samples, good heat conductance, small access angle of ion beam, backlight illumination- and centring possibility. Besides, it is simple and cheap, easy to manufacture, and compatible with all variations of sample holders from IV 3 till IV7.

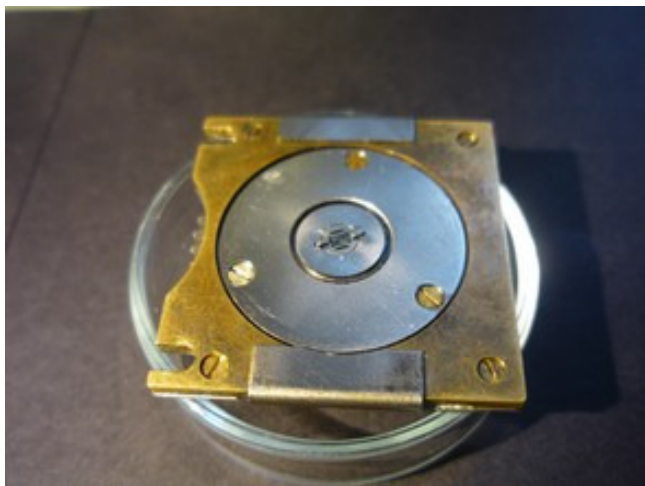


Figure 1: View of the newly designed holder for ion beam thinning of TEM samples. The sample is fixed mechanically with Ti clamps.

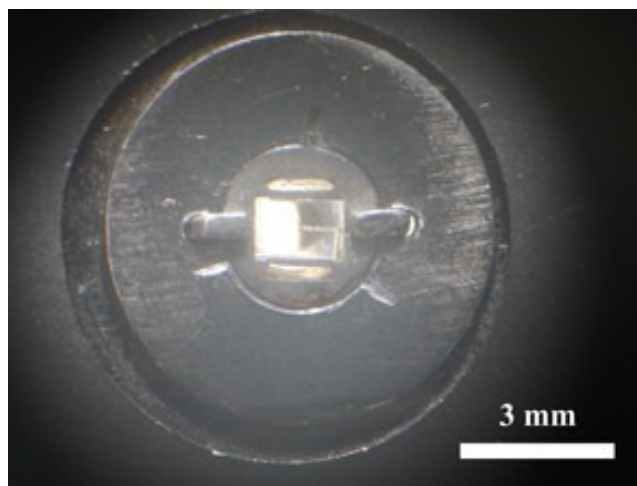


Figure 2: Seat plate with the sample and the fixing clamps. The offset position demonstrates that the construction permits sample centring.

## Exploitation of know how

Beside daily utilization in the Thin Films Physics Laboratory the know-how of the new construction has been sold for 3Mft to TECHNOORG LINDA, manufacturer of our ion beam thinning equipment's.

# MICRO-COMBINATORIAL ANALYSIS OF CONCENTRATION DEPENDENT PROPERTIES OF BINARY FILMS

G. Sáfrán, T. Lohner, B. Kalas, P. Petrik, Zs. Zolnai, M. Serényi, M. Fried, G. Dobrik, J. Gubicza (ELTE), N.Q. Chinh (ELTE)

A “one sample concept” combinatorial method has been worked out and patented for an efficient TEM study of concentration dependent properties of binary films [1,2]. The new technique called „ $\mu$ -combinatory” has been adapted to further analytical measurements e.g. AES, XRD, RBS, ellipsometry, nanoindentation. Contrary to traditional “multiple sample combinatorial techniques” we synthesize a single sample of suitable size that exhibits a concentration gradient and includes all compositions of a binary system. The  $\mu$ -combinatorial sample for TEM appears as a thin gradient film on a 3mm diameter TEM grid, while for other analytical measurements the gradient sample is deposited on a 25x10 mm<sup>2</sup> wafer. That permits a very efficient, even automated, analysis of the microstructure, physical and chemical properties and the collection of complete data libraries within a single measuring session. A major technical progress in 2018 was that the manual control has been replaced by a processor unit controlling both power of DC magnetrons and synchronized movement of the mechanics.

The efficiency of the method is demonstrated by achievements as below.

**AlMg system:** In a cooperation with N.Q. Chinh (ELTE) TEM and nano-hardness studies of the AlMg system were carried out in the technologically relevant range of 0-30 Mg%. Figure.1. shows the microstructure revealed by TEM and SAED of MgAl at 1%, 10% and 30% Mg content indicating that Mg addition radically decreases grain size. Pure Al layer shows fcc Al phase with large grains of typically 60-120nm. By adding 1w% Mg the grain size decreases to 30-100nm. Up to about 10% Mg the fcc Al(Mg) solid solution phase is present exhibiting 20-40nm grains. At 25% Mg and above (30%), however, a very fine grained Al<sub>3</sub>Mg<sub>2</sub> phase appears beside the still existing fcc Al(Mg) that shows 10-20 nm size grains (Figure 1).

Nanoindentation measurements pointed out that 1% Mg content increases hardness to 3-times of that of Al, followed by monotonous increase to a saturation of 4.5-times of Al at 20% Mg.

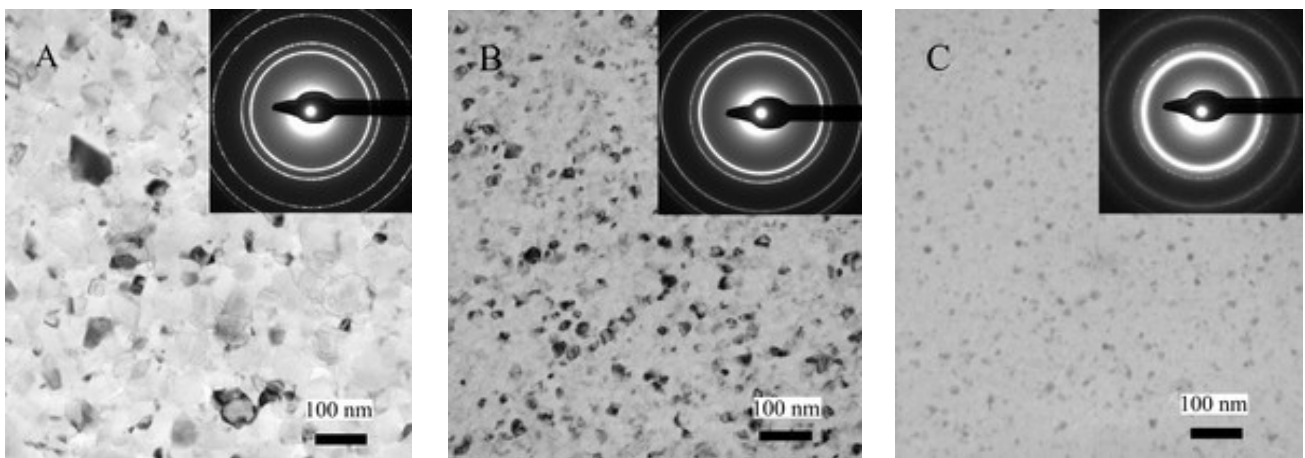


Figure 1: BF TEM and SAED of MgAl  $\mu$ -combinatorial sample measured at (a) 1%, (b) 10% and (c) 30% Mg content places revealed 30-100nm, 20-40nm and 10-20nm grain sizes, respectively: Mg addition decreases, remarkably, the grain size and, simultaneously, increases hardness.

**SiGe system:** TEM, RBS, and ellipsometry investigations were carried out, together with researchers of the Photonics Laboratory, on non-hydrogenated  $\mu$ -combinatorial SiGe samples. The concentration diagrams, depicted in Figure 2, measured by RBS and EDS along the length of the 25x10mm<sup>2</sup> size  $\mu$ -combinatorial sample show linear change with the position. The full range concentration dependence of refractive index  $n$  and absorption  $k$  of a-SiGe (Figure 3) was determined and plotted in a color-coded map by ellipsometry in the  $\lambda=400-1600$  nm wavelengths range [3,4]. The extracted diagrams show Vegard’s low-like, linear dependence of  $n$  and  $k$  on composition. Similarly, XRD measurements (by J. Gubicza, ELTE) of SiGe layers crystallized by annealing also showed Vegard’s low-like, linear dependence of lattice parameter on composition.

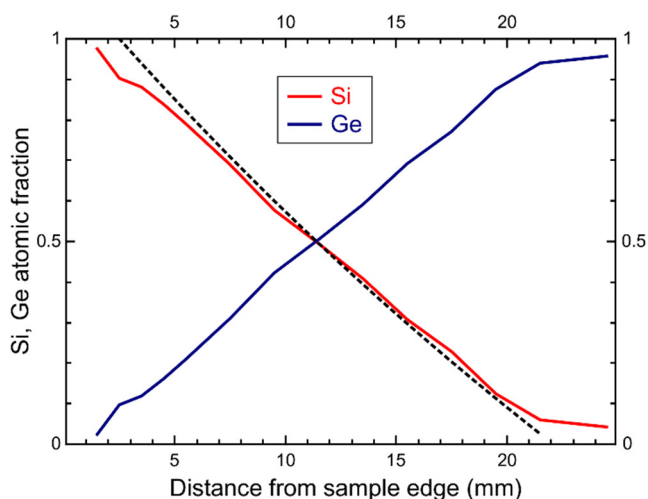


Figure 2: Concentration diagrams measured along the gradient of a  $\mu$ -combinatorial SiGe sample ( $25 \times 10 \text{ mm}^2$  size) by RBS (continuous) and EDS (---), respectively

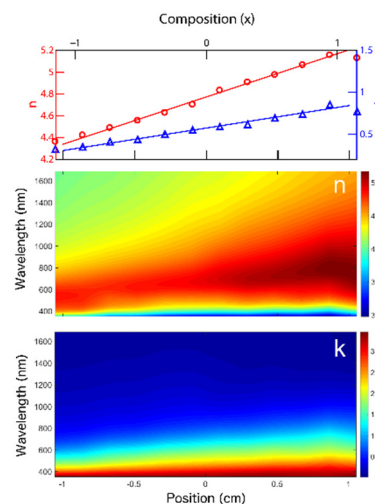


Figure 3: Color-coded maps of refractive index  $n$  and absorption  $k$  of  $a$ -SiGe as a function of composition at wavelengths of  $\lambda = 400\text{--}1600 \text{ nm}$ . Top: cleared diagrams of  $n$  and  $k$  at  $\lambda = 849.7 \text{ nm}$ . (Positions of  $-1, 0$  and  $1 \text{ cm}$  correspond to  $\text{Si}_x\text{Ge}_{1-x} = 1, 0.5$  and  $0$ , respectively.)

### Related publications

- [1] Sáfrán Gy.: Hung. Patent #P1500500.
- [2] Gy. Sáfrán: "One-sample concept" micro-combinatory for high throughput TEM of binary films, *Ultramicroscopy* **187**, 50–55 (2018)
- [3] T. Lohner, B. Kalas, P. Petrik, Zs. Zolnai, M. Serényi, G. Sáfrán: *Refractive Index Variation of Magnetron-Sputtered  $a$ -Si $_{1-x}$ Ge $_x$  by "One-Sample Concept" Combinatory*, *Appl. Sci.* **8(5)**, 826 (2018)
- [4] OTKA K129009 "Efficient, combinatorial synthesis and analysis of cutting edge functional materials"
- [5] Hungarian Development and Innovation Operative Program GINOP-2.1.7-15-2016-02073 The development of the  $\mu$ -combinatorial method and device is done in a co-operation of MTA EK MFA and Holocom

# DEVELOPMENT AND CHARACTERIZATION OF MULTI-ELEMENT DOPED HYDROXYAPATITE COATINGS ON METALLIC IMPLANT MATERIALS

*M. Furkó (PhD student), C. Balázs (supervisor)*

The aim of this research work is to develop coatings onto implant materials which possess both antimicrobial and biocompatible properties. Coatings were prepared by pulse current deposition technique. The pure hydroxyapatite (HAp) layer was doped and co-deposited with  $\text{Ag}^+$ ,  $\text{Zn}^{2+}$ ,  $\text{Mg}^{2+}$  and  $\text{Sr}^{2+}$  ions (Figure 1). The corrosion and biodegradable properties of layers were studied by carrying out electrochemical impedance spectroscopy measurements in simulated body fluid (SBF) using three-electrode open cell over a long time period. The biocompatible characteristics of layers were investigated by seeding osteoblast-like MG-63 cells onto the samples' surface. The most corrosion rate of coating increase with immersion time, which proves its biodegradable property (Figure 2).

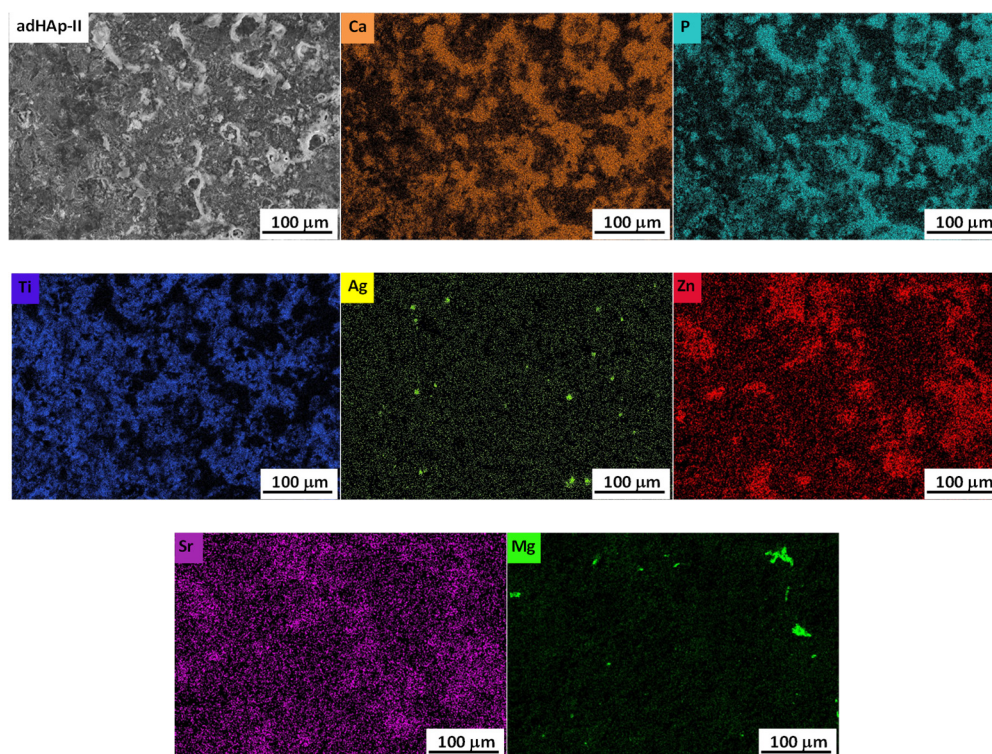


Figure 1: The elemental map of the composition of multi-element doped HAp (reference - silver, Ca - orange, P - blue, Ti - dark blue, Ag - yellow, Zn - red, Sr - purple, Mg - green)

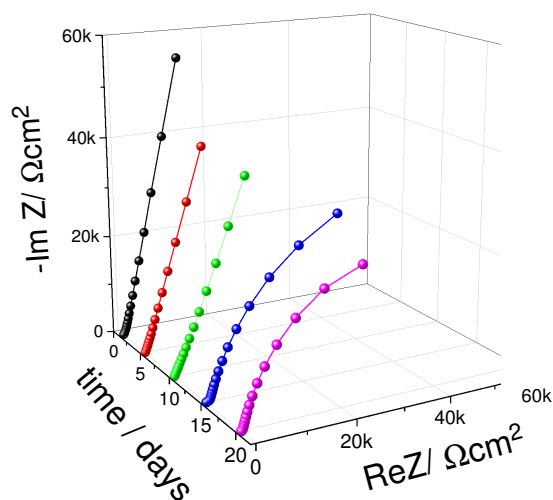


Figure 2: Nyquist diagrams of multi-element doped HAp coated Ti6Al4V alloy. The curves were recorded several times over a two-week period in SBF solution at 37 °C.

## CERAMIC DISPERSED AUSTENITIC STRENGTHENED STEELS

*H. R. Ben Zine (PhD student), F. Cinar Sahin (ITU Istanbul), Zs. Czigány, K. Balázs (supervisor), C. Balázs (supervisor)*

In this work, the 316L austenitic strengthened stainless steel based composites were developed by powder technology. Attrition milling and sintering were used for production of Ceramic Dispersed Austenitic Strengthened Steels (CDSS) with 0.33 wt% and 1 wt% nanosized SiC addition. The highly efficient attrition milling provided an efficient size reduction of the 316L steel grains and homogeneous distribution of the ceramic nanoparticles before sintering process. Spark plasma sintering (SPS) was used for fast compaction of milled powder mixtures. The density of composites decreased with increasing the amount of SiC due to its lower density. The SiC addition improved the hardness of the 316L, the 316L/1 wt% SiC shows lower hardness compared to the 316L/0.33 wt% SiC composite due to its lower density. A simultaneous transgranular and intergranular fracture behaviour (Figure 1) have been observed after the 3 points bending test of the 316L/1wt% SiC composite where an average bending strength high as 1127.4 MPa has been recorded at room temperature. In the case of the 316L/0.33wt% SiC the samples were just bended due to their higher ductility. Tribological properties of the sintered composites have been studied, and it was observed that the addition of the SiC improves the tribological properties of the 316L stainless steel. Friction coefficients of 0.962, 0.879 and 0.930 have been measured, respectively, for all of the sintered reference sample 316L, 316L/ 0.33 wt% SiC and the 316L/1wt% SiC composites. The investigation of the sintered composites by TEM confirmed the distribution of the ceramic particles to the grains boundaries (Figure 2).

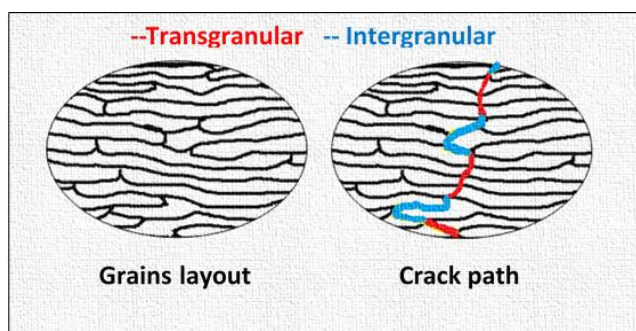


Figure 1: Schematic views of fracture propagation

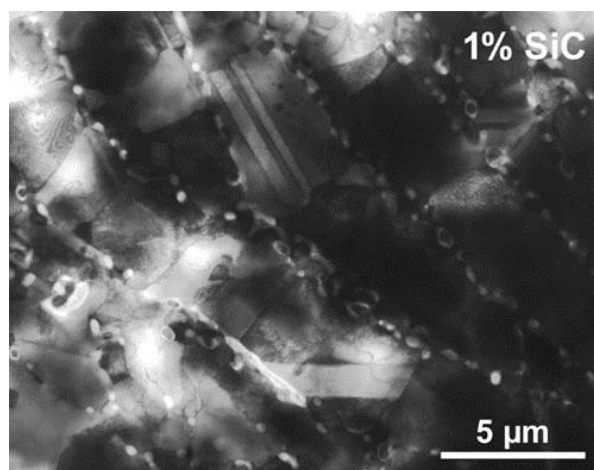


Figure 2: TEM image of CDSS with 1 wt% SiC addition

# NEW APPROACHES IN THE DEVELOPMENT OF HYPOALLERGENIC IMPLANT MATERIAL IN ORTHOPAEDICS: STEPS TO PERSONALISED MEDICINE

(EU FP7 "HypOrth")

K. Balázsi, Zs. Fogarassy, V. Varga, T. Zagyva, D. Delfonse (Mathys, Switzerland), C. Lohman (Magdeburg Un., Germany), J. Lorenzen (Teknologisk Institute, Denmark), C. Balázsi

Conventional materials of endoprostheses, such as Metal-on-Metal (MoM) are not suitable for all people, as some individuals develop adverse immune reactions to the constituents of metal alloys. The process, which leads to this adverse immune reaction and why some individuals react to the implanted materials whereas others do not, are not yet understood. The main aspect of our project was the development of the novel material combination for endoprostheses with excellent hypoallergenic and antibacterial properties. This new biomaterial was developed from raw waste biogenic materials as seashells using combination of the powder technology with novel electrodeposition method – electro spraying.

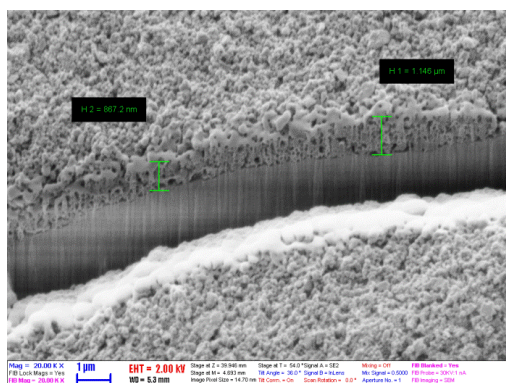


Figure 1: SEM image of electro sprayed hydroxyapatite film on TiAlV implant surface

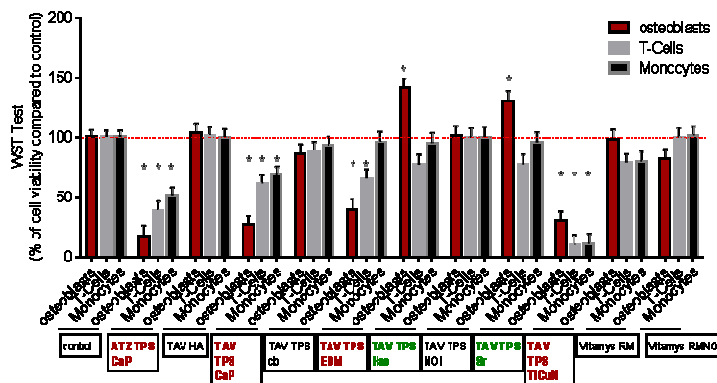


Figure 2: Test of implant material combinations (bioceramic and coating) for biocompatibility and osteointegration

Nanosized bioactive powder from seashells was prepared by highly efficient attritor milling. Electro spraying was used as a coating technology for the bioceramics film deposition (Figure 1). We confirmed that these coatings contained important trace elements as strontium or magnesium which increased the osteointegration activity. Moreover, the seashell derived coating (TAV TPS HAS (titanium-aluminium-vanadium/plasma-sprayed titanium/hydroxyapatite)) exhibited the highest biocompatibility among the examined coatings (Figure 2). We also confirmed that the properties of coatings after sterilization were similar from the point of view of structure, adhesion and biocompatibility to starting as-received bioactive coatings. The detailed steps of preparation and characterization are confidential. The project was successfully accomplished and the final report was accepted by EU Commission.

# GRAPHENE-CERAMIC COMPOSITES FOR TRIBOLOGICAL APPLICATION IN AQUEOUS ENVIRONMENTS

(OTKA M-ERANET "Grace")

C. Balázsi, Zs. Fogarassy, V. Varga, M. Knoch (FCT), J. Dusza (IMR SAS, Slovakia),  
A. Kailer (IMW Franhoufer, Germany), K. Balázsi

The M-ERANET „Grace” project was oriented to the development of advanced  $\text{Si}_3\text{N}_4$ / graphene and  $\text{SiC}$ /graphene ceramic composites. There is a strongly growing demand for highly wear resistant and reliable ceramic materials that may be widely used in industrial applications and energy production. Special attention is paid to components that are used under severe conditions and only lubricated by the surrounding media that are mainly aqueous. Reliability and efficiency of these components need to be improved by using high performance ceramics with superior tribological and mechanical properties.

Recent basic research of the project partners on the development of graphene containing ceramic composites showed that the realization of the nanocomposites with remarkably increased wear resistance and fracture toughness was possible. Multi-layered graphene (MLG) was prepared by attritor milling at 10 h intensive milling of few micrometre sized graphite powders. The large quantity, low cost and quick preparation process are main strengths of our MLG.  $\text{Si}_3\text{N}_4$ /MLG nanocomposites were prepared by attritor milling and sintered by hot pressing (HP). The  $\text{Si}_3\text{N}_4$  ceramics were produced with 1 wt%, 3 wt%, 5 wt% and 10 wt% content of MLG. The tribological behaviour of composites in aqueous environment was investigated (Figure 1). This study showed decrease of wear at increased MLG content (Figure 2).

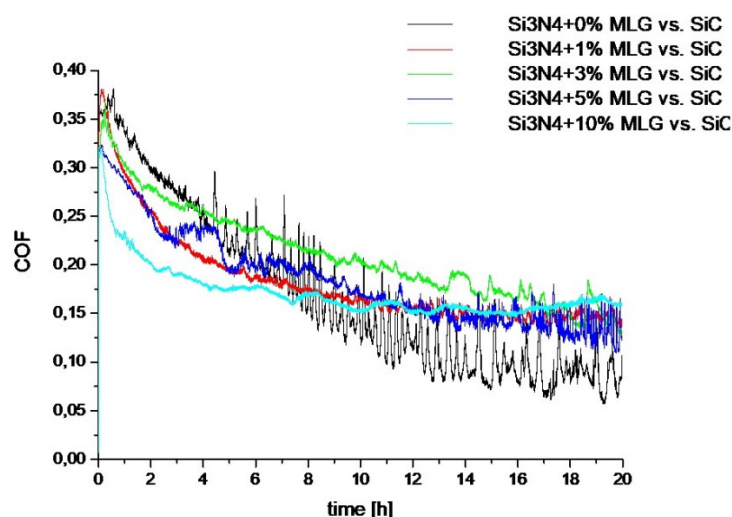


Figure 1: Friction property of  $\text{Si}_3\text{N}_4$  / MLG composites with different MLG content.

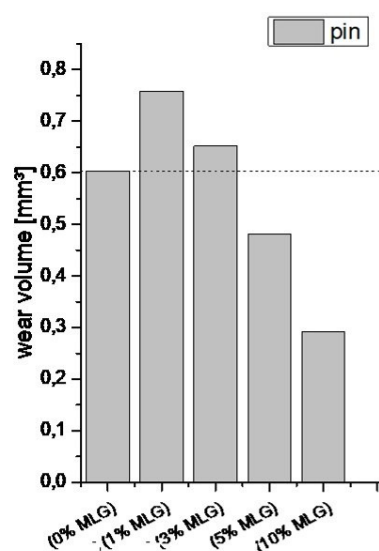


Figure 2: Wear of composites as function of MLG content.

Our current knowledge in the field of ceramic nanocomposites shows that is possible to make ceramic materials by incorporating graphene into the  $\text{Si}_3\text{N}_4$  and  $\text{SiC}$  structure. The new approach is very promising, since ceramic microstructures can be designed with high toughness and provide improved wear resistance at low friction.

## BACTERIA REPELLENT LAYER MADE OF FLAGELLIN

("Lendület" grant LP2012-26/2012 of HAS, ERC\_HU, BIONANO GINOP-2.3.2-15-2016-00017, OTKA grant NN117849)

B. Kovacs, D. Patko, A. Klein (University of Pannonia, Veszprém), B. Kakasi (University of Pannonia, Veszprém), A. Saftics, S. Kurunczi, F. Vonderviszt (University of Pannonia, Veszprém), R. Horvath

The development of bacteria repellent surface coatings is critical in various fields ranging from biosensing to health care, biotechnology and food production. In the present study we exploit that the protein flagellin rapidly forms a dense and oriented monolayer on hydrophobic surfaces upon adsorption from aqueous solution. This oriented layer mimics the surface of bacterial flagellar filaments and has excellent bacteria repellent properties. *In situ* OWLS (Optical Waveguide Lightmode Spectroscopy) measurements were used to monitor on-line both the formation of the protein layer on the silanized sensor surface and subsequent bacterial adhesion (see Fig. 1). The adhered cells were also visualized by fluorescent microscopy and the formed protein film was characterized by AFM (Atomic Force Microscopy). In parallel control experiments, the adherence of bacteria was measured on bare hydrophobic surfaces as well. Both OWLS and microscopy results well confirmed that the flagellin coating drastically reduced the adhesion of *E. coli* cells. Therefore, a novel type of bacteria repellent layer made of flagellin is demonstrated [1].

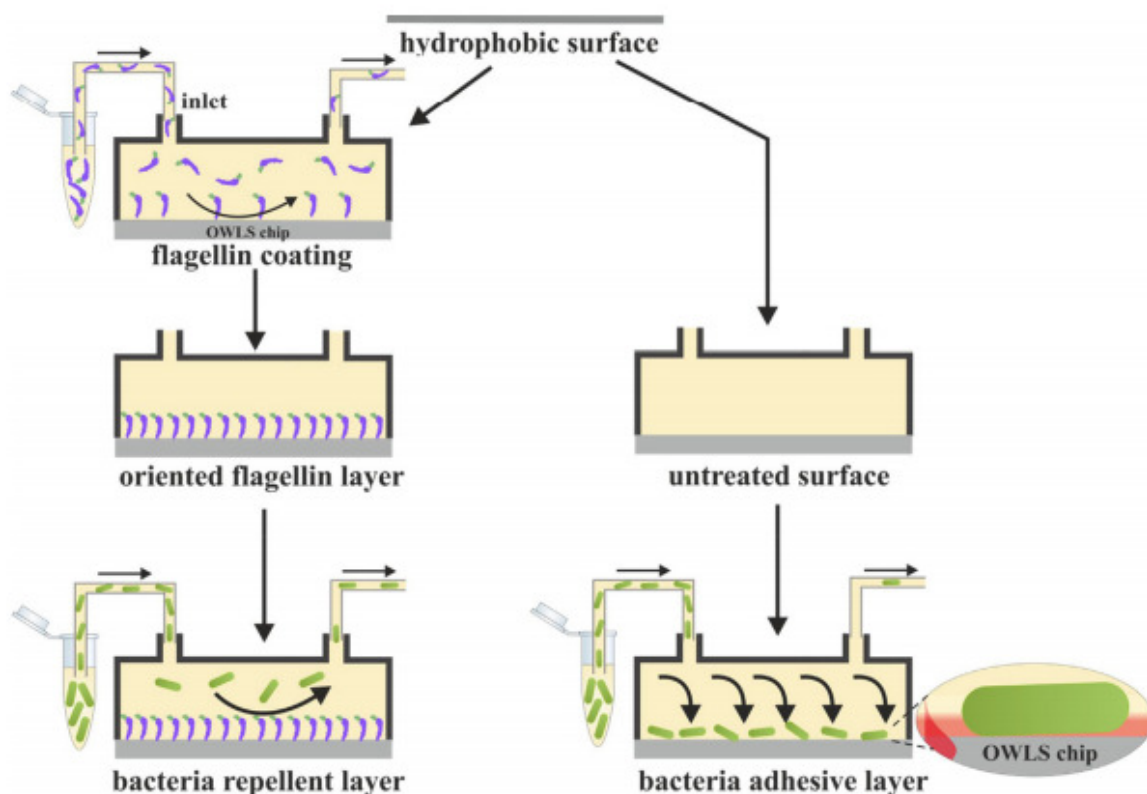


Figure 1: Schematic representation of the differences between the bacterial adhesion on the flagellin coated and on the uncoated hydrophobic surface

### Related publication

- [1] B. Kovacs, D. Patko, A. Klein, B. Kakasi, S. Kurunczi, F. Vonderviszt, R. Horvath: *Bacteria repellent layer made of flagellin*. Sens. Actuator B-Chem., **B. 257**, 839–845 (2018)

# KINETICS AND STRUCTURE OF SELF-ASSEMBLED FLAGELLIN MONOLAYERS ON HYDROPHOBIC SURFACES IN THE PRESENCE OF HOFMEISTER SALTS: EXPERIMENTAL MEASUREMENT OF THE PROTEIN INTERFACIAL TENSION AT THE NANOMETER SCALE

("Lendület" grant LP2012-26/2012 of HAS, ERC\_HU, KH-17, NKFI-6, K-124932, BIONANO\_GINOP-2.3.2-15-2016-00017, OTKA grant NN117849)

B. Kovacs, A. Saftics, A. Biro, S. Kurunczi, B. Szalontai (University of Pannonia, Veszprém), B. Kakasi (University of Pannonia, Veszprém), F. Vonderviszt (University of Pannonia, Veszprém), A. Der (MTA Biological Research Centre, Szeged), R. Horvath

Flagellins (building blocks of bacterial flagellar filaments) does not preferentially adsorb on hydrophilic substrates, but very rapidly forms an oriented, dense and stable monolayer on hydrophobic surfaces, where the hypervariable D3 domain (one of the four flagellin domains) is oriented toward the solution. It presents a repellent surface coating to bacteria or cancer cells, thus this property can be utilized in biosensors and biofunctionalized surfaces. In this work, we monitored the adsorption-desorption kinetics and adsorbed layer structure of the bacterial protein flagellin in the presence of Hofmeister salts by a surface sensitive label-free optical biosensor (optical waveguide lightmode spectroscopy, OWLS). The recorded OWLS data were analysed by a computer code using a set of coupled differential equations modelling the adsorption-desorption process. By supposing reversibly and irreversibly adsorbed protein states with different adsorption footprints, the kinetic data could be perfectly fitted. We revealed that the proteins adsorbing in the presence of kosmotropic salts had smaller footprints, leading to a more oriented and densely packed layer. Kosmotropic salts increased both the adsorption rate constant and the transition rate constants from the reversibly to the irreversibly adsorbed state (see Fig. 1). In contrast, chaotropic salts increased the desorption rate constant and led to decreased adsorbed mass and a more loosely packed film. Neither circular dichroism spectroscopy in bulk solutions or Fourier transform infrared spectroscopy of surface-adsorbed flagellins could reveal significant structural changes due to the presence of the Hofmeister salts, and supported our conclusions about the adsorption mechanism. On the basis of the measured kinetic and structural data (footprints of adsorbed proteins), we developed a model to calculate the protein-water-substrate interfacial tension in the presence of Hofmeister salts, and compared the experimentally obtained values with related literature data. The calculated values are consistent with previously published data of surface tension changes, and – to the best of our knowledge – represent the first experimental results for this quantity [1].

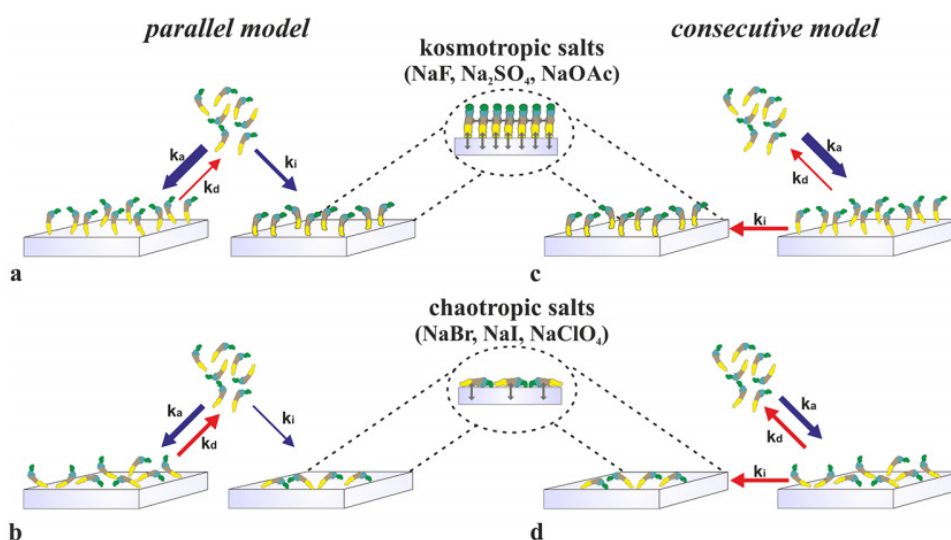


Figure 1: Schematic illustration of the adsorption kinetics of flagellin proteins on a hydrophobic surface

## Related publication

- [1] B. Kovacs, A. Saftics, A. Biro, S. Kurunczi, B. Szalontai, B. Kakasi, F. Vonderviszt, A. Der, R. Horvath: *Kinetics and Structure of Self-Assembled Flagellin Monolayers on Hydrophobic Surfaces in the Presence of Hofmeister Salts: Experimental Measurement of the Protein Interfacial Tension at the Nanometer Scale*. *J. Phys. Chem. C* **122**, 21375–21386 (2018)

# INTERACTION OF POSITIVELY CHARGED GOLD NANOPARTICLES WITH CANCER CELLS MONITORED BY AN IN SITU LABEL-FREE OPTICAL BIOSENSOR AND TRANSMISSION ELECTRON MICROSCOPY

(“Lendület” grant LP2012-26/2012 of HAS, ERC\_HU, KH-17, MedinProt)

B. Peter, I. Lagzi (BME, Budapest), S. Teraji (KIT, Kyoto, Japan), H. Nakanishi (KIT, Kyoto, Japan), L. Cervenak (Semmelweis University, Budapest), D. Zámbo, A. Deák, K. Molnár (Eötvös Lóránd University, Budapest), M. Truszka (Eötvös Lóránd University, Budapest), I. Szekacs, R. Horvath

Functionalized nanoparticles (NPs) can penetrate into living cells and vesicles, opening up an extensive range of novel directions. For example, NPs are intensively employed in targeted drug delivery and biomedical imaging. However, the real-time kinetics and dynamics of NP–living cell interactions remained uncovered. In this study, we in situ monitored the cellular uptake of gold NPs –functionalized with positively charged alkaline thiol– into surface-adhered cancer cells, by using a high-throughput label-free optical biosensor employing resonant waveguide gratings. The characteristic kinetic curves upon NP exposure of cell-coated biosensor surfaces were recorded and compared to the kinetics of NP adsorption onto bare sensor surfaces. We demonstrated that from the above kinetic information, one can conclude about the interactions between the living cells and the NPs (see Fig. 1). Real-time biosensor data suggested the cellular uptake of the functionalized NPs by an active process. It was found that positively charged particles penetrate into the cells more effectively than negatively charged control particles, and the optimal size for the cellular uptake of the positively charged particles is around 5 nm. These conclusions were obtained in a cost-effective, fast, and high-throughput manner. The fate of the NPs was further revealed by electron microscopy on NP-exposed and subsequently fixed cells, well confirming the results obtained by the biosensor. Moreover, an ultrastructural study demonstrated the involvement of the endosomal–lysosomal system in the uptake of functionalized NPs and suggested the type of the internalization pathway. NPs may act as model systems to imitate host cell–bacteria interactions and penetration in biosensor measurements. Furthermore, these measurement settings and results can be applied to study the uptake of NPs by bacteria as well [1].

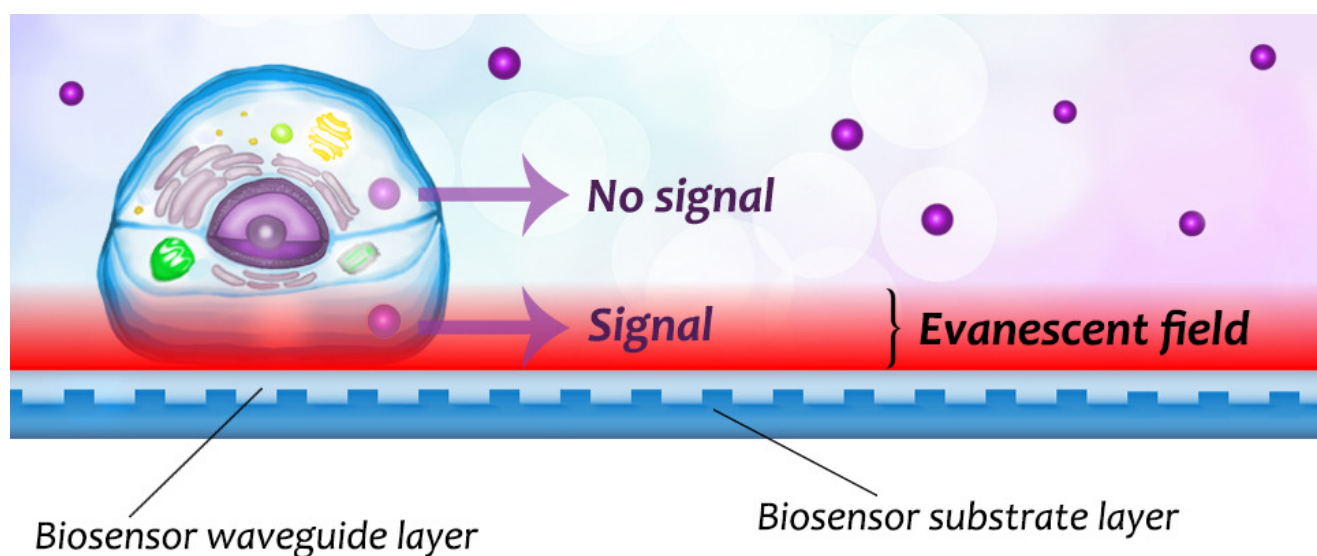


Figure 1: Schematic illustration of the concept of evanescent label-free biosensors in NP uptake detection

## Related publication

- [1] B. Peter, I. Lagzi, S. Teraji, H. Nakanishi, L. Cervenak, D. Zámbo, A. Deák, K. Molnár, M. Truszka, I. Szekacs, R. Horvath: *Interaction of Positively Charged Gold Nanoparticles with Cancer Cells Monitored by an in Situ Label-Free Optical Biosensor and Transmission Electron Microscopy*, ACS Appl. Mater. Interfaces **10**, 26841–26850 (2018)

# HIGH-RESOLUTION ADHESION KINETICS OF EGCG-EXPOSED TUMOR CELLS ON BIOMIMETIC INTERFACES: COMPARATIVE MONITORING OF CELL VIABILITY USING LABEL-FREE BIOSENSOR AND CLASSIC END-POINT ASSAYS

("Lendület" grant LP2012-26/2012 of HAS, ERC\_HU, KH-17, OTKA grant 104275)

B. Peter, R. Ungai-Salanki (Eötvös Lóránd University, Budapest), B. Szabó (Eötvös Lóránd University, Budapest), A. G. Nagy, I. Szekacs, Sz. Bósze (Eötvös Lóránd University, Budapest), R. Horvath

A high-throughput label-free resonant waveguide grating biosensor, the Epic BenchTop (Epic BT) was utilized to in situ monitor the adhesion process of cancer cells on Arg-Gly-Asp tripeptide (RGD) displaying biomimetic polymer surfaces. Using highly adherent human cervical adenocarcinoma (HeLa) cells as a model system, cell adhesion kinetic data with outstanding temporal resolution were obtained. We found that pre-exposing the cells to various concentrations of the main extract of green tea, the (-)-epigallocatechin gallate (EGCG), largely affected the temporal evolution of the adhesion process. For unexposed and low dosed cells, sigmoid shaped spreading kinetics was recorded. Higher dose of EGCG resulted in a complete absence of the sigmoidal character, and displayed adsorption-like kinetics. By using the first derivatives of the kinetic curves, a simple model was developed to quantify the sigmoidal character and the transition from sigmoidal to adsorption-like kinetics (see Fig. 1). The calculations showed that the transition happened at EGCG concentration of around 60  $\mu\text{g}/\text{mL}$ . Using the 3-(4,5-dimethylthiazol-2-yl)-2,5-diphenyltetrazolium bromide end-point assay, we concluded that EGCG is cytostatic but not cytotoxic. The effect of EGCG was also characterized by flow cytometry. We concluded that, using the introduced label-free methodology, the shape of the cell adhesion kinetic curves can be used to quantify in vitro cell viability in a fast, cost-effective, and highly sensitive manner [1]. This method probably can be used with bacterial cells as well to demonstrate the antibacterial effects of certain further natural compounds.

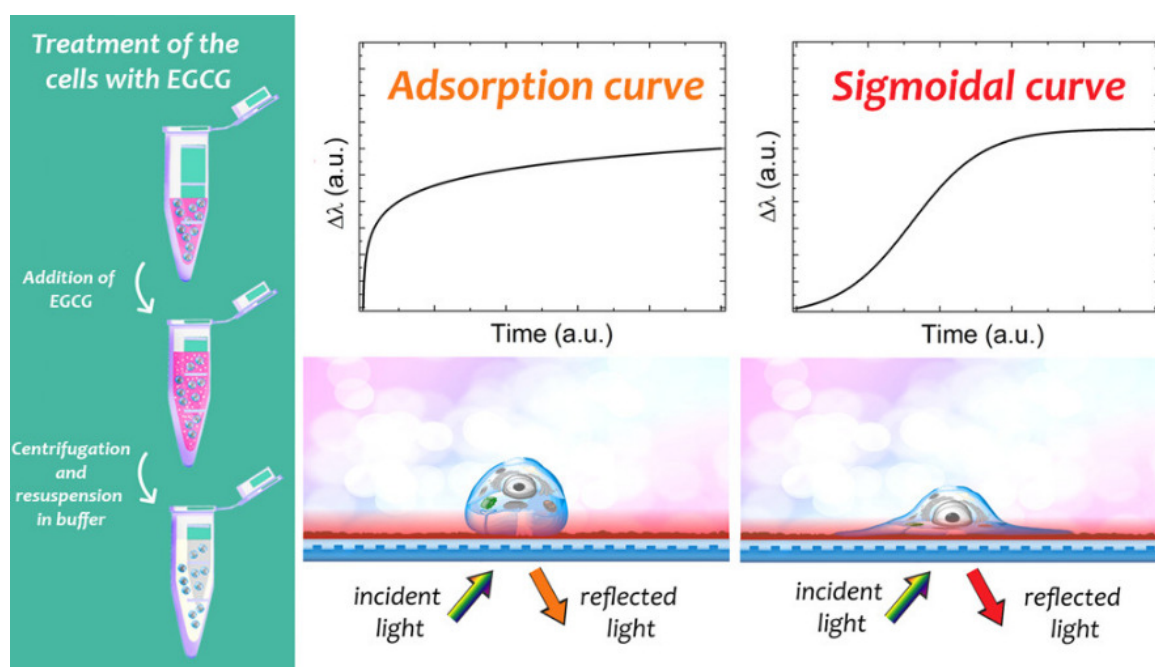


Figure 1: Schematic illustration of the working principle of the Epic BT biosensor and the steps of the measurement (left). In case of adsorption kinetic curve, the cell attaches but does not adhere onto the biosensor surface. This phenomenon indicates a nonliving, "dead" process. Note, it also occurs when proteins adsorb onto the surface. In case of sigmoidal kinetic curve, the cells adhere onto the biosensor surface. This phenomenon indicates a "living" process.

## Related publication

- [1] B. Peter, R. Ungai-Salanki, B. Szabó, A.G. Nagy, I. Szekacs, Sz. Bósze, R. Horvath: High-resolution adhesion kinetics of EGCG-Exposed tumor cells on biomimetic interfaces: Comparative monitoring of cell viability using label-free biosensor and classic end-point assays. ACS Omega **3**, 3882–3891 (2018)

# LABEL-FREE OPTICAL BIOSENSOR FOR REAL-TIME MONITORING THE CYTOTOXICITY OF XENOBIOTICS: A PROOF OF PRINCIPLE STUDY ON GLYPHOSATE

("Lendület" grant LP2012-26/2012 of HAS, ERC\_HU, OTKA grant K109865)

E. Farkas, A. Szekacs (Agro-Environmental Research Institute, Budapest), B. Kovacs, M. Olah (Agro-Environmental Research Institute, Budapest), R. Horvath, I. Szekacs

Rapid and inexpensive biosensor technologies allowing real-time analysis of biomolecular and cellular events have become the basis of next-generation cell-based screening techniques. Our work opens up novel opportunities in the application of the high-throughput label-free Epic BenchTop optical biosensor in cell toxicity studies. The Epic technology records integrated cellular responses about changes in cell morphology and dynamic mass redistribution of cellular contents at the 100–150 nm layer above the sensor surface. The aim of the present study was to apply this novel technology to identify the effect of the herbicide Roundup Classic, its co-formulant polyethoxylated tallow amine (POEA), and its active ingredient glyphosate, on MC3T3-E1 cells adhered on the biosensor surface (see Fig.1). The half maximal inhibitory concentrations of Roundup Classic, POEA and glyphosate upon 1 h of exposure were found to be 0.024%, 0.021% and 0.163% in serum-containing medium and 0.028%, 0.019% and 0.538% in serum-free conditions, respectively (at concentrations equivalent to the diluted Roundup solution). These results showed a good correlation with parallel end-point assays, demonstrating the outstanding utility of the Epic technique in cytotoxicity screening, allowing not only high-throughput, real-time detection, but also reduced assay run time and cytotoxicity assessment at end-points far before cell death would occur [1].

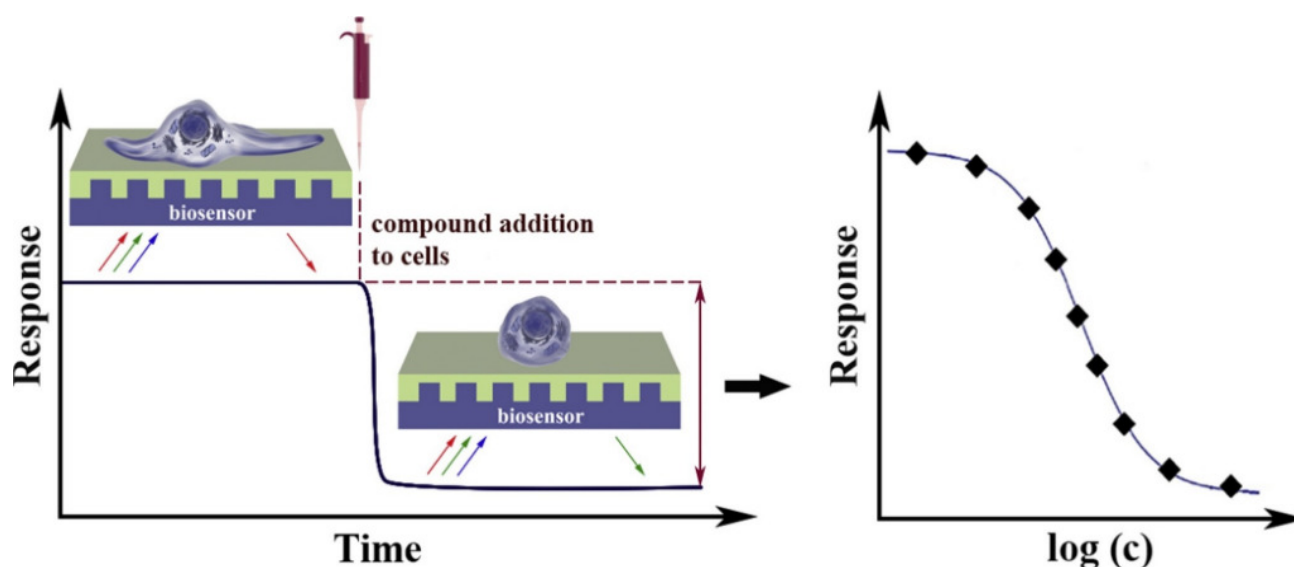


Figure 1: Schematic representation of the measurement and data evaluation methodology

## Related publication

- [1] E. Farkas, A. Szekacs, B. Kovacs, M. Olah, R. Horvath, I. Szekacs: *Label-free optical biosensor for real-time monitoring the cytotoxicity of xenobiotics: A proof of principle study on glyphosate*. J. Haz. Mat. **351**, 80-89 (2018)

# INTEGRIN TARGETING OF GLYPHOSATE AND ITS CELL ADHESION MODULATION EFFECTS ON OSTEOBLASTIC MC3T3-E1 CELLS REVEALED BY LABEL-FREE OPTICAL BIOSENSING

("Lendület" grant LP2012-26/2012 of HAS, ERC\_HU, KH-17, NVKP\_16-1-2016-0049, OTKA grant K109865)

I. Szekacs, E. Farkas, B.L. Gemes (Agro-Environmental Research Institute, Budapest), E. Takacs (Agro-Environmental Research Institute, Budapest), A. Szekacs (Agro-Environmental Research Institute, Budapest), R. Horvath

Cell adhesion is the crucial event in numerous physiological and pathophysiological processes. Foreign substances can affect cellular processes through receptors, ion channels, enzymes, binding proteins or the cytoskeleton. Biosensor techniques and their application in different areas, including cytotoxicology, is becoming of growing significance. Whole cell-based sensors gain utmost importance due to their capability to measure comprehensive and functional effects of different xenobiotics.

An evanescent field based surface-sensitive resonant waveguide grating (RWG) biosensor was applied for high-throughput label-free detection of impacts of the world leading herbicide active ingredient glyphosate on cell adhesion in real time and quantitative evaluation. In the present study we discovered and thoroughly examined a new, yet unidentified, properties of glyphosate as cell adhesion modulator. The RWG technique was employed for measuring kinetics of cell adhesion to glyphosate adsorbed on biosensor surfaces and by measuring the antagonistic action of glyphosate on cell binding to Arg-Gly-Asp (RGD)-displaying polymer surfaces (see Fig. 1). The results obtained demonstrate that living preosteoblastic cells can adhere to glyphosate adsorbed on the sensor surface, showing ligand-specific kinetics. Soluble glyphosate significantly reduces cell adhesion via blocking RGD-specific integrins in a concentration-dependent manner, as also validated by competitive binding assays to recombinant receptor  $\alpha v \beta 3$  in both enzyme-linked immunosorbent assay (ELISA) and biosensor formats. Using this novel methodology, the half maximal inhibitory concentration ( $IC_{50}$ ) for glyphosate in living osteoblastic cells was determined to be 20.6 mM. The affinity of glyphosate to cell adhesion receptors is also determined. The introduced methodology is fast, sensitive, and biological effects were revealed using intact, living cells [1].

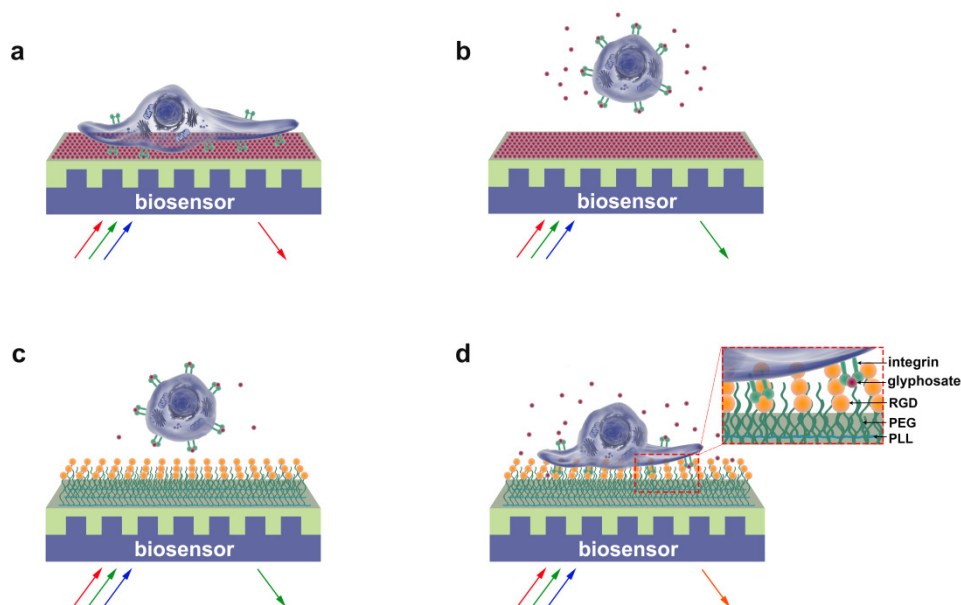


Figure 1: Schematic illustration of the working principle of the cell-based biosensor and the concentration-dependent effects of glyphosate on cell adhesion. (a) MC3T3-E1 cells spread on a sensor surface treated with 0.1% glyphosate solution. (b) Inhibition of cell adhesion by glyphosate at 0.2–1.7% concentration in the solution (with complete blockage achieved at 1.7%). (c) Prevention of cell adhesion onto PP:PPR surface by preincubation of the cells with glyphosate at 0.47% concentration in the solution. (d) Detaching MC3T3-E1 cells adhered to a surface modified with PP:PPR by glyphosate at 0.9% concentration in solution.

## Related publication

- [1] I. Szekacs, E. Farkas, B.L. Gemes, E. Takacs, A. Szekacs R. Horvath: *Integrin targeting of glyphosate and its cell adhesion modulation effects on osteoblastic MC3T3-E1 cells revealed by label-free optical biosensing*. *Sci. Rep.* **8**, 17401 (2018)

# IN SITU VISCOELASTIC PROPERTIES AND CHAIN CONFORMATIONS OF HEAVILY HYDRATED CARBOXYMETHYL DEXTRAN LAYERS: A COMPARATIVE STUDY USING OWLS AND QCM-I CHIPS COATED WITH WAVEGUIDE MATERIAL

("Lendület" grant LP2012-26/2012 of MTA, ERC\_HU, KH-17)

A. Saftics, Gy. A. Pr6sz, B. T6rk, B. Peter, S. Kurunczi, R. Horvath I. Szekacs, E. Farkas, B.L. Gemes (Agro-Environmental Research Institute, Budapest), E. Takacs (Agro-Environmental Res. Inst., Budapest), A. Szekacs (Agro-Environmental Res. Inst., Budapest), R. Horvath

Hydration, viscoelastic properties and dominant structure of thin polymer layers on the surface of waveguide material were evaluated using optical waveguide lightmode spectroscopy (OWLS) and quartz crystal microbalance (QCM) methods. The fundamentally different principles of the two applied label-free biosensors enable to examine analyte layers from complementary aspects, e.g. to determine the amount of bound water in hydrated layers. In this study, a new QCM instrument with impedance measurement (QCM-I) was introduced. Its specially designed sensor chips, covered by thin film of waveguide material ( $\text{SiO}_2\text{-TiO}_2$ ), supply identical surface as used in OWLS sensors, thus enabling to perform parallel measurements on the same type of surface. Viscoelastic analysis of the measured data was performed by our evaluation code developed in MATLAB environment, using the Voinova's Voigt-based model. *In situ* deposition experiments on the ultrathin films of poly(L-lysine)-graft-poly(ethylene glycol) (PLL-g-PEG) were conducted for instrumental and code validation. Additionally, a novel OWLS-QCM data evaluation methodology has been developed based on the concept of combining hydration and viscoelastic data with optical anisotropy results from OWLS measurements (see Fig. 1). This methodology provided insight into the time-dependent chain conformation of heavily hydrated nano-scaled layers, resulting in unprecedented structural, hydration and viscoelastic information on covalently grafted ultrathin carboxymethyl dextran (CMD) films, which are basically antifouling coatings that can be specifically conjugated by adhesive motifs in order to arrange cells and bacteria on biosensor surfaces. The measured mass values as well as hydration and viscoelastic properties were compared with the characteristics of PLL-g-PEG layers [1].

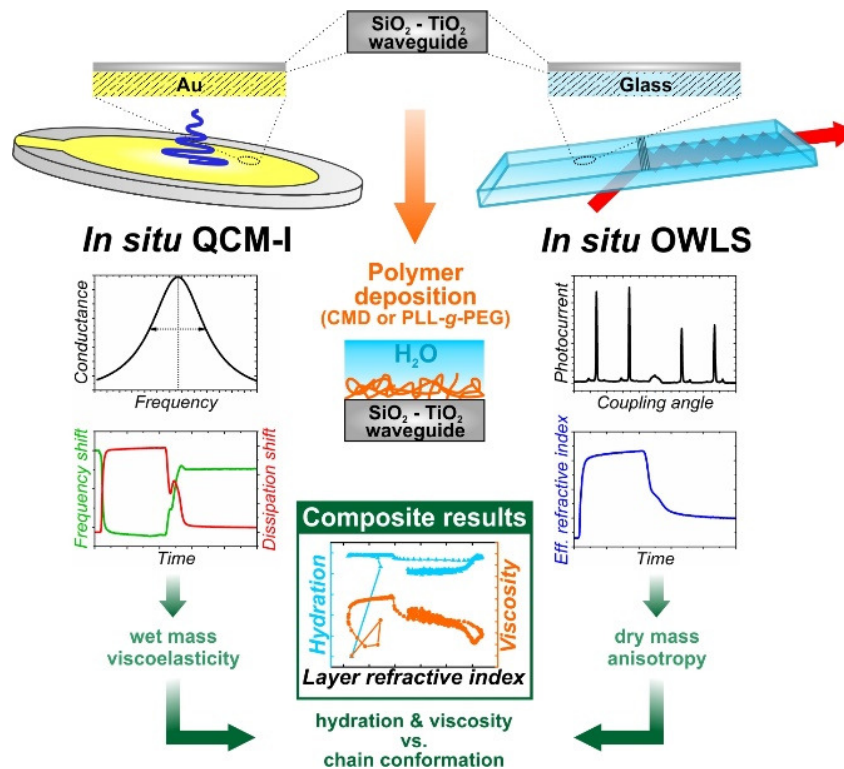


Figure 1: Schematic representation of the measurement and data evaluation methodology developed and applied in this work

## Related publication

- [1] A. Saftics, Gy. A. Pr6sz, B. T6rk, B. Peter, S. Kurunczi, R. Horvath: *In situ viscoelastic properties and chain conformations of heavily hydrated carboxymethyl dextran layers: a comparative study using OWLS and QCM-I chips coated with waveguide material*, Sci. Rep. **8**, 11840 (2018)

# COMPETITION AND PARTNERSHIP BETWEEN CONFORMITY AND PAYOFF-BASED IMITATIONS IN SOCIAL DILEMMAS

(OTKA K120785)

A. Szolnoki and X. Chen

Learning from a partner who collects a higher payoff is a frequently used working hypothesis in evolutionary game theory. One of the alternative dynamical rules is when the focal player prefers to follow the strategy choice of the majority in the local neighbourhood, which is often called a conformity-driven strategy update. In this work we assumed that both strategy learning methods are present and compete for space within the framework of a coevolutionary model.

We have shown that there are parameter regions, like strong snowdrift game situations at high temptation ( $T$ ) or high sucker's payoff ( $S$ ) values where the competition of different learning methods results in the unambiguous victor of payoff-driven strategy learning. Here the role separating cooperator-defector pairs provide so high collective payoff value that cannot be beaten by a homogeneous domain which would be a consequence of a conformity-driven learning method.

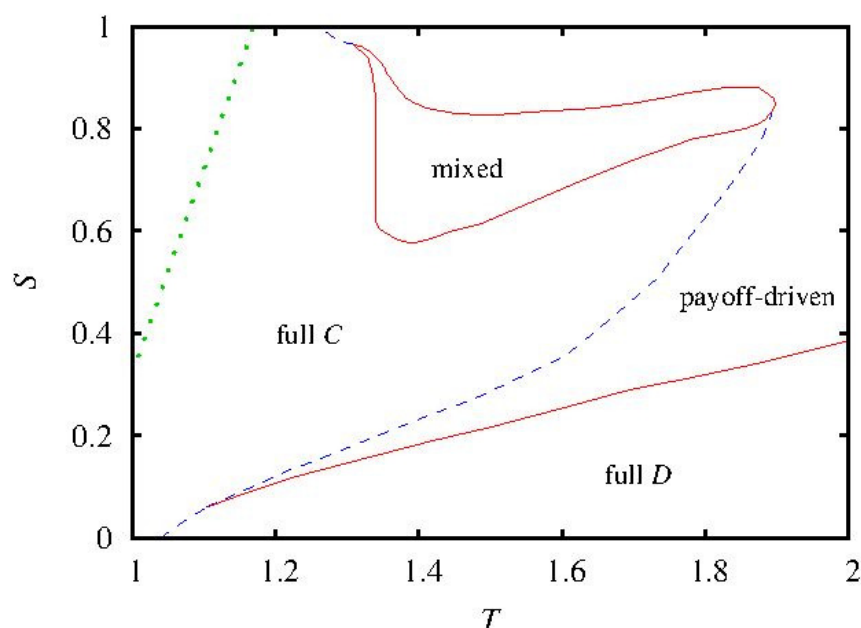


Figure 1: Phase diagram of snowdrift game where payoff-driven and conformity-driven strategy learning protocols are competing for space. Full C (full D) label marks the parameter regions where only co-operator (defector) strategies survive in the stationary state. 'Payoff-driven' label marks the region where payoff-driven strategy learning protocol pre-vails and related cooperator and defector players form a stable winning solution. The phase denoted by 'mixed' label shows where all learning protocols and all strategies coexist. For comparison, green dotted line marks the border of full cooperator state when only payoff-driven learning protocol is available for players in a uniform system.

Nevertheless, for less sharp snowdrift game regions at smaller  $T$  and  $S$  values the coevolution of different learning methods is useful to reach a full cooperative state that would not be reachable otherwise. In the latter case the homogeneous cooperator domains can invade the whole space by enjoying the advantage of conformity-driven learning method. Interestingly, in the stag-hunt game region the simultaneous presence of different learning methods reveals a novel way of collaboration that cannot be observed otherwise. Here conformity-driven cooperators can resist the invasion of payoff-driven defectors and neighbouring payoff-driven cooperators can attack conformity-driven defectors successfully. The expected symmetry is broken for defectors because conformity-driven ( $o_D$ ) and payoff-driven ( $p_D$ ) states cannot form similarly efficient alliance. In this way the active partnership of different types of cooperator players allows them to extend the full cooperator state to those parameter values which belonged to the sovereignty of defectors in the classic payoff-driven model.

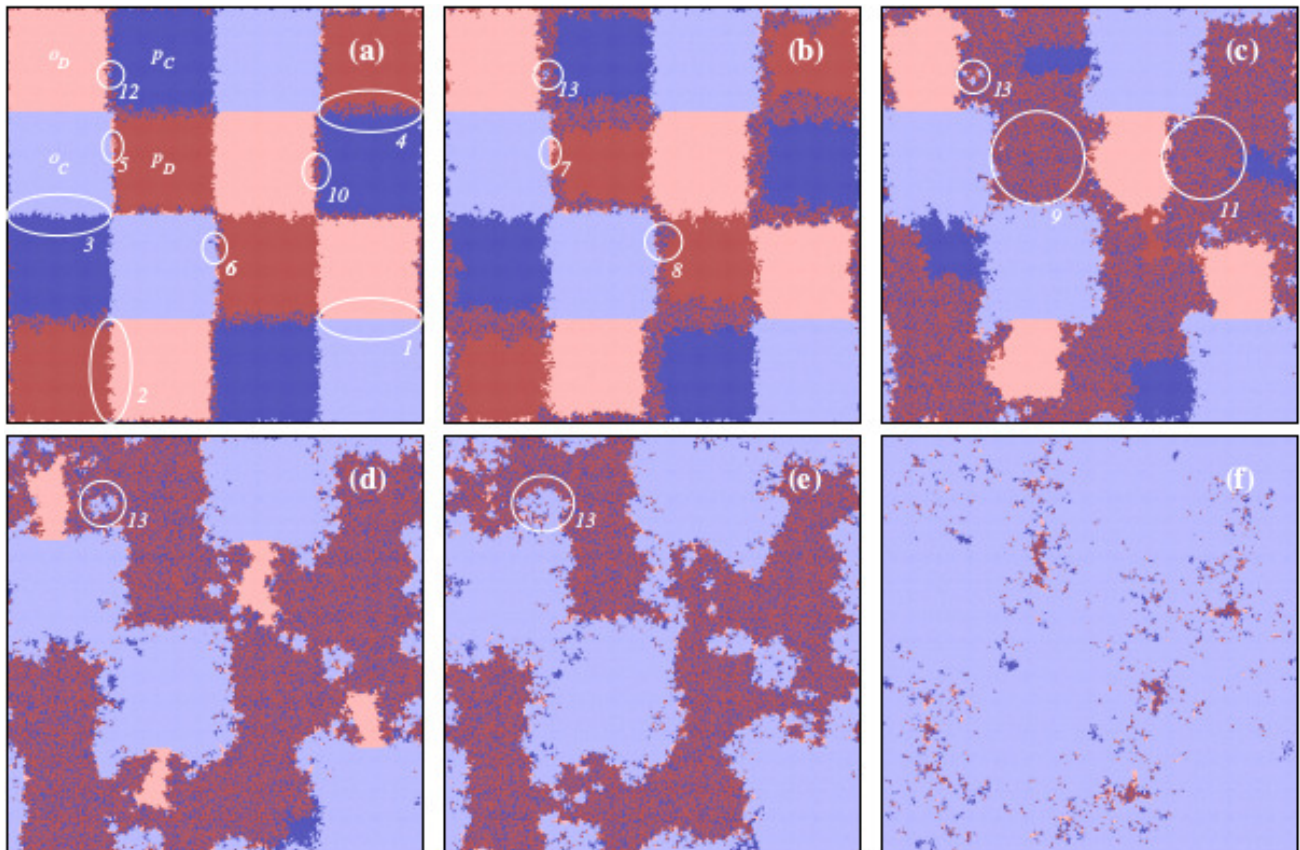


Figure 2: Spatial evolution of the four competing states in a  $400 \times 400$  system at  $T=1.4$  and  $S=0.4$  where the simulation is launched from a prepared patch-like initial state where all kind of interfaces between competing players can be found. In this way we can monitor all emerging pattern formations simultaneously via a single run. Here dark (light) blue denotes payoff-driven (conformity-driven) cooperators, while dark (light) red marks payoff-driven (conformity-driven) defectors, as it is marked by white labels in panel (a). This panel represents the early stage of evolutionary process after 20 MCSs. Further stages of the evolutionary process are shown at 50, 150, 250, 350, and 800 MCSs. Finally, the system evolves into a homogeneous oC state (not shown). The circles and ellipses highlight the specific invasion fronts between different types of domains.

### Related publication

- [1] A. Szolnoki and X. Chen: *Competition and partnership between conformity and payoff-based imitations in social dilemmas*, New J. Phys. **20**, 093008 (2018)

# GRIFFITHS PHASES IN INFINITE-DIMENSIONAL, NON-HIERARCHICAL MODULAR NETWORKS

(OTKA K109577)

Géza Ódor, Silvio Ferreira, Wesley Cota

Griffiths phases (GPs), generated by the heterogeneities on modular networks, have recently been suggested to provide a mechanism, rid of fine parameter tuning, to explain the critical behaviour of complex systems. One conjectured requirement for systems with modular structures was that the network of modules must be hierarchically organized and possess finite dimension. We investigate the dynamical behaviour of an activity spreading model, evolving on heterogeneous random networks with highly modular structure and organized non-hierarchically. We observe that loosely coupled modules act as effective rare-regions, slowing down the extinction of activation. As a consequence, we find extended control parameter regions with continuously changing dynamical exponents for single network realizations, preserved after finite size analyses, as in a real GP. The avalanche size distributions of spreading events exhibit robust power-law tails. Our findings relax the requirement of hierarchical organization of the modular structure, which can help to rationalize the criticality of modular systems in the framework of GPs.

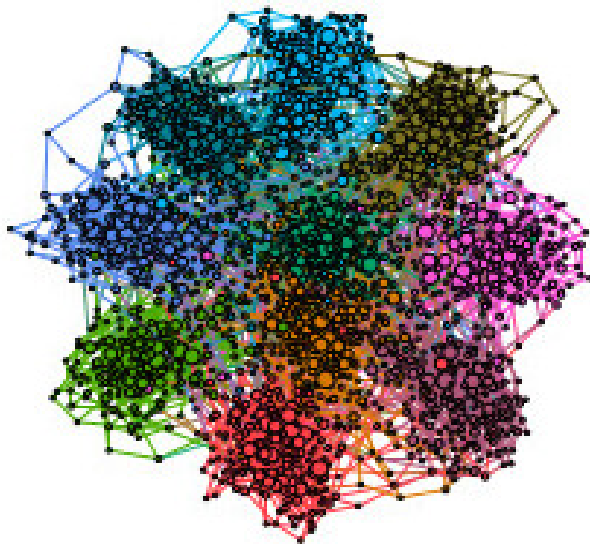


Figure 1: Example of a modular structure. Networks with 100 modules of same size of 200 nodes and number of inter-modular connections  $k = 10$ , representing loosely and densely connected modular graphs, respectively. The network degree distribution is given by  $P(k) \sim k^{-2.7}$ . Connected modular structures can clearly be observed.

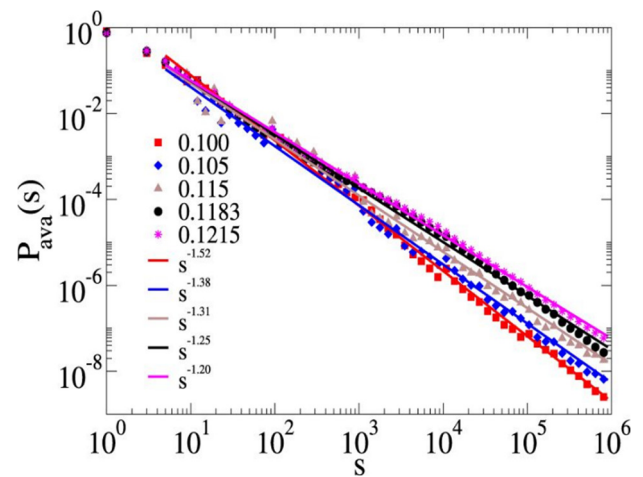


Figure 2: Avalanche size distributions of the Susceptible Infected Modular (SIS) spreading on a single Hierarchical Modular Network (HMN). Only topological disorder is considered and the number of modules is 103. Different values of  $\lambda$  are indicated by the legends. Simple PL tail fits are also shown.

## Related publication

- [1] W. Cota, G. Ódor & S. C. Ferreira: *Griffiths phases in infinite-dimensional, non-hierarchical modular networks*, Scientific Reports **8**, 9144 (2018)

# CORRELATION ANALYSIS OF JOINTLY PROPAGATING GENETIC AND MUSICAL CHARACTERISTICS OF MODERN AND ANCIENT POPULATIONS IN EURASIA AND AMERICA – A SIMULTANEOUS QUEST FOR ANCIENT HUMAN POPULATIONS AND THEIR MUSICAL PARENT LANGUAGES

Z. Juhász, H. Pamjav et al.

In this study, we aimed to illustrate the efficiency of correlation analysis of musical and genetic characteristics in research for certain common ethnic and ethno-musical roots of the mankind. The comparison of the results to archaeogenetic data shows that correlations of recent musical and genetic data may reveal past cultural and migration processes resulting in recent connections. (Accepted for publication in *Molecular Genetics and Genomics*.)

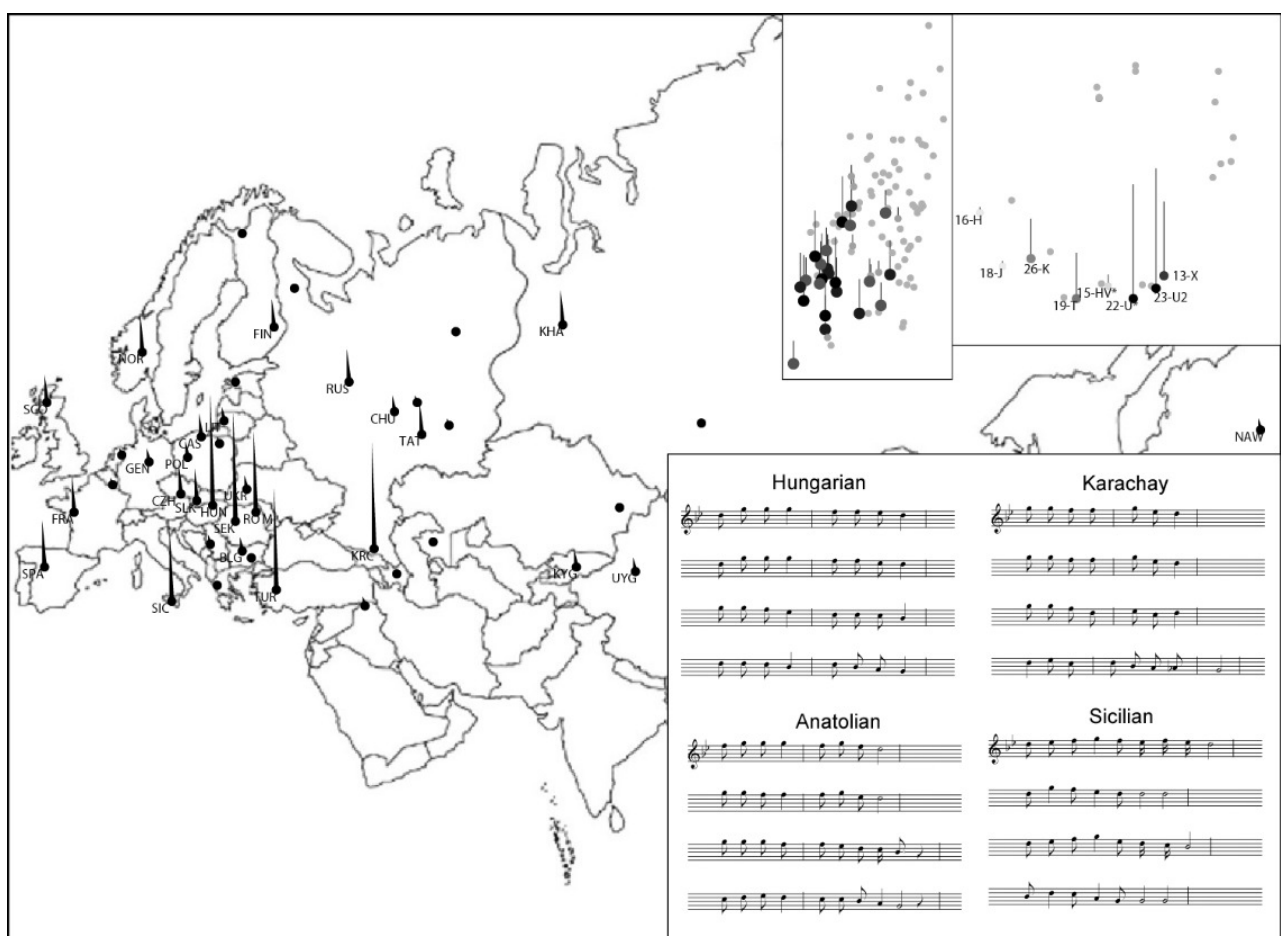


Figure 1: a) distribution of the common mean weight vectors derived from similar rank lists of the populations studied, belonging to the musical types and haplogroups indicated in the right upper part. The result refers to an association of haplogroups X, U\*, U2, HV\*, T, K, J and H, as well as melody types of descending melody contours and high ranges. The highest weights of this association of genetic and musical types are found in Anatolia, the Carpathian Basin, the Caucasus and Sicily. The given haplogroup association was compared to ancient archaeogenetic samples, and it was found to be dominant in Neolithic farmer populations in the Fertile Crescent, so the corresponding association of melody types may be attributed to one of the well-known Neolithic migrations. Four closely related melodies arising from Hungary, the Caucasus-area (Karachay), Anatolia and Sicily verify the existence of this hypothetical musical parent language.

## ABBREVIATIONS

1DPC	One-Dimensional Photonic Crystal
AEKI	Institute for Atomic Energy Research
AER	Atomic Energy Research
AES	Auger Electron Spectroscopy
AFM	Atomic Force Microscopy
ALD	Atomic Layer Deposition
ANS	American Nuclear Society
ANSI	American National Standards Institute
AOP	Advanced Oxidation Processes
ARDTM	Automatic Radioactive Material Detection
ALLEGRO	Experimental Helium Gas Cooled Fast Reactor Developed by the European V4G4
ATOMKI	MTA Institute for Nuclear Research
ATR IR	Attenuated Total Reflection Infrared Spectroscopy
BAGIRA	New Irradiation Device at the Budapest Research Reactor
BCC	Body Centred Cubic
BCF	Boda Claystone Formation
BCP	Land Border Crossing Place
BCS	Boron Coated Straw
BITS	Bin Type Statistical Simulation
BME	Budapest University of Technology and Economics
BNC	Budapest Neutron Centre
BrightnESS	EU Funded Project in Support of the European Spallation Source (ESS)
BRR	Budapest Research Reactor
BSW	Bloch Surface Wave
BZN	Bay Zoltán Nonprofit Ltd. for Applied Research
CAN bus	Controller Area Network
CATHARE	French Thermohydraulic Code
C-BORD	H-2020 EU Project, effective Container inspection at BORDER control points
CDSS	Ceramic Dispersed Austenitic Strengthened Steel
CERIC	Central European Research Infrastructure Consortium
CERN	Centre Européen pour la Recherche Nucléaire (French name of the European Organization for Nuclear Research)
CERTA	(OAH) Centre for Emergency Response
CFD	Computational Fluid Dynamics
CHANDA	EU Funded Project (CHALLENGES in Nuclear Data for the Safety of European Nuclear Facilities)
CIEMAT	Centre for Energy, Environment and Technology, Madrid
CNR-ISTM	Italian Istituto di Scienze e Tecnologie Molecolari
CNS	Cold Neutron Source
CMC	Carboxymethyl-Cellulose
CMD	Classical Molecular Dynamics, Carboxymethyl-dextran
CMOS	Complementary Metal-oxide Semiconductor
CODEX	Core Degradation Experiment
CONCERT	EU H2020 Project for the Integration of Radiation Protection Research
CONFIDENCE	Consortia of an European Joint Programme (COPing with uNcertainties For Improved modelling and DEcision making in Nuclear emergenCiEs)
CRP	IAEA Coordinated Research Project
CTC	Circulating Tumour Cell
CVD	Chemical Vapour Deposition
D&D	Decommissioning and Dismantling
D3S	Distributed Space Weather Sensor System

DFT	Density Functional Theory
DGA	Diglycol Amide
DHR	Decay Heat Removal
DICP	Dalian Institute of Chemical Physics, China
DLR	German Aerospace Centre
DLS	Dynamic Light Scattering
DNA	Deoxyribonucleic Acid
DPA	Displacement Per Atom
DRIE	Deep Reactive Ion Etching
DRIFTS	Diffuse Reflectance Fourier Transform Infrared Spectroscopy
DRM	Dry Reforming
DS	Dual Scattering
DSBs	Double Strand Breaks
DSC	Differential Scanning Calorimetry
ECAP	Equal Channel Angular Pressing
ECSS	European Cooperation for Space Standardization
EDM	Electrical Discharge Machining
EDS, EDX	Energy-dispersive X-ray Spectroscopy
EELS	Electron Energy Loss Spectroscopy
EEW	Electric Explosion of Wires
EGCg	Epigallocatechin Gallate
EIS	Electrochemical Impedance Spectroscopy
EMC	Electromagnetic Compatibility
EMR	Electron Magnetic Resonance
ELISA	Enzyme-Linked Immunosorbent Assay
ELTE	Eötvös Loránd University, Budapest
EM	Engineering Model
ENTSO	European Network of Transmission System Operators for Electricity
EPS	Environmental Protection Service
EQM	Engineering Qualification Model
ESA	European Space Agency
ESEO	European Student Earth Orbiter
ESI-MS	Electrospray Ionisation Mass Spectrometry
ESIS	European Structural Integrity Society
ESS	European Spallation Source, Lund
EURDEP	European Radiological Data Exchange Platform
EWE	Electric Wire Explosion
EXAFS	Extended X-ray Absorption Fine Structure
F2R	Flex to Rigid
FA	Fuel Assemblies
FCC	Face Centred Cubic
FEM	Finite Element Method
FESEM	Field Emission Scanning Electron Microscopy
FFT	Fast Fourier Transform
GC	Gas Chromatography
GFR	Gas-Cooled Fast Reactor
GP	Guinier-Preston
GPA	Geometrical Phase Analysis
GPU	Graphics Processing Unit
GPs	Griffiths Phases
GRS	„Gesellschaft für Anlagen- und ReaktorSicherheit“
GTN model	Gurson–Tvergaard–Needleman Material Model
GSTP	General Support Technology Programme
HAADF	High-angle Annular Dark-field Imaging

Hap	Hydroxyapatite
h-BN	Hexagonal Boron Nitride
HEA	High Entropy Alloy
HEC	Hydroxyethylcellulose
HEMT	High-electron-mobility Transistor
HER	Hydrogen Evolving Half-cell Reaction
HLW	High-level Radioactive Waste
HMN	Hierarchical Modular Network
HP	Hot Pressing or Hydrothermal Process
HPGe	High-purity Germanium
HPLWR	High Performance Light Water Reactor
HREM	High-resolution Electron Microscopy
HRTEM	Resolution Cross-sectional Transmission Electron Microscopy
HZE	High (H) atomic number (Z) and energy (E)
IAEA	International Atomic Energy Agency
IBM	Ion-beam Mixing
IBMP	Institute for Biomedical Problems, Moscow
IEE	Institute of Electrical Engineering
ICP-MS	Inductively Coupled Plasma Mass Spectrometry
ICP-OES	Inductively Coupled Plasma Optical Emission Spectrometry
ILL	Institut Laue-Langevin
INFN	Italian Frascati National Laboratories
IOD	In-Orbit Demonstration
IPE	International Plant-Analytical Exchange
IPERION CH	EU Funded Project (Integrated Platform for the European Research Infrastructure ON Cultural Heritage)
IRIX	International Radiological Information Exchange
ISE	International Soil-Analytical Exchange
ISO	International Organization for Standardization
ISS	International Space Station
ITO	Indium Tin Oxide
ITRAP	H-2020 EU Project, Illicit Trafficking Radiation Assessment Program
KAERI	Korea Atomic Energy Research Institute
KARATE	Reactor Physical Program Code System
KARATE-1200	Reactor Physical Program Code System for VVER-1200 Reactors
KDE	Kernel Density Estimates
keff	Effective Multiplication Factor
KFKI	Former Name of the Research Centre, Nowadays the Campus Name
KIKO3DMG	Nodal Reactor Physics Calculation Code Developed in the CER
KIT	Karlsruhe Institute of Technology
L3PSA	Level 3 Probabilistic Safety Assessment
LC	Liquid Chromatography
LET	Linear Energy Transfer
LIBS	Laser Induced Breakdown Spectroscopy
LLNL	Lawrence Livermore National Laboratory
LOC	Lab-on-a-Chip
LOCA	Loss of Coolant Accident
LP	Linear Programming
LSC	Liquid Scintillation Counting
LTO	Long Term Operation
LWR	Light Water Reactor
MAT	Magnetic Adaptive Testing
MATTER	EU FP7 Project (MATERial TESting and Rules)
MBA	Mercaptobenzoic Acid

MCNP	Monte Carlo N-Particle Transport Code
MELODI	EU Strategic Research Agenda for Low Dose Research
MEIS	Medium Energy Ion Scattering
MEMS	Microelectromechanical System
MEPHI	Moscow Engineering Physics Institute
MFA	Institute of Technical Physics and Materials Science (Hungarian acronym)
MILC	Metal Induced Lateral Crystallization
MIS	Minimally Invasive Robotic Surgery
MLG	Multi-layered Graphene
MoM	Metal-on-Metal
MOS	Metal-oxide Semiconductor
MOX	Mixed Oxide
MPH	Material Property Handbook
MS	Mass Spectrometry or Mössbauer Spectroscopy
MTA EK	Hungarian Academy of Sciences Centre for Energy Research (Hungarian acronym)
MTBs	Mirror Twin Boundaries
MZI	Mach-Zender Interferometer
MU	Mock-up
MULTICELL	Reactor Physical Transport Code
MVM	Hungarian Power Companies
MWCNT	Multiwall Carbon Nanotube
NAA	Neutron Activation Analysis
NAL	Nuclear Analysis and Radiography Department, MTA EK
ND	Neutron Diffraction
NDE	Non Destructive Evaluation
NEAAA	Neutron-based Element Analysis and Activation Assessment
NEMS	Nano Electromechanical System
NII	Non-Intrusive Inspection
NIPS	Neutron Induced Prompt Gamma-ray Spectroscopy
NKFIH	National Research, Development and Research Office (Hungarian acronym)
NLD	Nuclear Level Density
NMR	Nuclear Magnetic Resonance
NMX	Neutron Macromolecular Diffraction
NNK	National Public Health Centre
NNKP	National Nuclear Research Program
NOMAD	Non-destructive Evaluation System for the Inspection of Operation-Induced Material Degradation in Nuclear Power Plants (EU H2020 project)
NORM	Naturally-Occurring Radioactive Materials
NP	Nanoparticle
NPP	Nuclear Power Plant
NPs	Nanoparticles
NR	Neutron Radiography
NRC	Nuclear Regulatory Commission
NUBIKI	Nuclear Safety Research Institute
OAH	Hungarian Atomic Energy Authority (Hungarian acronym)
OECD	Organisation for Economic Co-operation and Development
OECD NEA	Organisation for Economic Co-operation and Development, Nuclear Energy Agency
OKSER	National Environmental Radiation Protection Control System (Hung. Acronym)
ORC	Organic Rankine Cycle
OSJER	National Environmental Radiation Protection Control System (Hung. Acronym)
OTKA	Hungarian Scientific Research Fund (Hungarian Acronym)
OWLS	Optical Waveguide Light Mode Spectroscopy

Paks NPP	Paks Nuclear Power Plant
PBW	Proton Beam Writing
PCB	Printed Circuit Board
PCMI	Pellet-Cladding Mechanical Interaction
PCT	Peak Cladding Temperature
PDMS	Polydimethylsiloxane
PGAA	Prompt-gamma Neutron Activation Analysis
PGAI	Prompt-gamma Activation Imaging
PIE	Post Irradiation Examination
PIPS	Passivated Implanted Planar Silicon
PIXE	Particle-induced X-ray Emission or Proton-induced X-ray Emission
PL	Photoluminescence Spectrometer
PLL-g-PEG	Random Graft Co-polymer with a Poly(L-lysine) Backbone and Poly(ethylene glycol) Side-chains
POEA	Polyethoxylated Tallow Amine
PRD	Personal Radiation Dosimeter
PSA	Probabilistic Safety Analysis
PSI	Paul Scherrer Institute, Villigen, Schweiz
PSF	Photon Strength Function
PXRD	Powder X-ray Diffractometry
pXRF	Portable XRF Spectrometer
PWR	Pressurized Water Reactor
QCM	Quartz Crystal Microbalance
QMS	Quadrupole Mass Spectrometer
QRPA	Quasiparticle Random-phase Approximation
RAD	Static/dynamic Thermal-neutron and X-ray Imaging Station at BNC
RADCUBE	A Joint Mission Name of the ESA
RadMag	Instrument for Measuring Space Radiation and Magnetic Field Parameters
RBE	Relative Biological Effectiveness
RBS	Rutherford Backscattering
RF	Radio-frequency
RGD	Arg-Gly-Asp (peptide sequence)
RHA	Radiation Hardness Assurance
RHE	Reversible Hydrogen Electrode
RID	Radionuclide Identification Device
RMC method	Reverse Monte Carlo Method
RPM	Radiation Portal Monitor
RPV	Reactor Pressure Vessel
ROS	Reactive Oxygen Species
RRAM	Resistive Random Access Memory
RWG	Resonant Waveguide Grating
SAA	Sulphanilamide
SAED	Selected Area Electron Diffraction
SAFEST	EU Funded Project: Severe Accident Facilities for European Safety Targets
SANS	Small Angle Neutron Scattering
SBF	Simulated Body Fluid
SBO	Station Blackout
SBR	Signal-to-Background Ratio
SCC	Stress-Corrosion Cracking
SCWR	Supercritical Water Cooled Reactor
SEM	Scanning Electron Microscopy
SERS	Surface Enhanced Raman Spectroscopy
SGD	Sulfaguanidine
SI	Structural Integrity

SINE2020	EU Funded Project: Science and Innovation with Neutrons in Europe in 2020
SINAC	Simulator Software for Interactive modelling of environmental consequences of Nuclear ACCidents
SIS	Susceptible Infected Modular
SLM	Stochastic Lung Model
SMAD	Solvated Metal Atom Deposition
SMD	Solvation Model Density
SMX	Sulfamethoxazole
SNMS	Secondary Neutral Mass Spectrometry
SOC	Spin Orbit Coupling
SOD	Superoxide Dismutase
SOI	Si-on-Insulator
SOL	Sol Immobilisation Method
SP	Safeguards Support Programme
SPD	Severe Plastic Deformation
SPENVIS	Space Environment Information System
SPR	Surface Plasmon Resonance
SPS	Spark Plasma Sintering
SR	Synchrotron Radiation
SRA	Strategic Research Agenda
SRPM	Spectroscopic Radiation Portal Monitor
SS	Stainless Steel or Single Scattering
SSA	Space Situational Awareness
SSD	Solid-state Drive
SSNTD	Solid State Nuclear Track Detector
SWE	Space Weather Service Network
SZIKKTI	Materials Research and Testing Laboratory for Silicate Industry Ltd., Budapest
SZTAKI	MTA Institute for Computer Science and Control
STEM	Scanning Transmission Electron Microscopy
STM	Scanning Tunnelling Microscopy
STZ	Sulfathiazole
SWV	Square Wave Voltammetry
TAV TPS HAS	Titanium-aluminium-vanadium/Plasma-sprayed titanium/Hydroxyapatite
TCD	Thermal Conductivity Detector
TEM	Transmission Electron Microscopy
TÉT	Bilateral Research Program (Hungarian acronym)
TFC	Trilateral Flash Cycle
TID	Total Ionizing Dose
TLD	Thermoluminescent Dosimeter
TMDC	Transition Metal Dichalcogenide
TNA	Technology Needs Assessment Project
TOAB	Tetraoctylammonium Bromide
TOF <sub>surf</sub>	Turnover Frequencies Related to Surface
TOF-ND	Time of Flight Neutron Diffraction
TPD	Temperature Programmed Desorption
TPO	Temperature Programmed Oxidation
TPR	Temperature Programmed Reduction
TRITEL	Three Dimensional Silicon Detector Telescope
TRL	Technology Readiness Level
TRT	Thermal Release Tape
T-VAC	Thermal-Vacuum Test
TXRF	Total-reflection X-ray Fluorescence
UFG	Ultrafine-grained
UOX	Uranium oxide

UTS	Ultimate Tensile Strength
UV	Ultraviolet
UV-VIS	Ultraviolet-Visible (Spectroscopy)
VERONA	Reactor Core Monitoring and the Reactivity Measurement System for VVER Type NPPs
VVER	Water-Cooled Water-Moderated Energetic Reactor, Russian acronym
VVER-SCP	VVER Supercritical Pressure
XAS	X-ray Absorption Spectrometry
XPS	X-ray Photoelectron Spectroscopy
XRD	X-ray Diffraction
XRF	X-ray Fluorescence Analysis
YAG	Yttrium-aluminium-garnet
YSZ	Ytria-stabilized Zirconia
WBC	Whole Body Counter or Tungsten Boron Carbide
WEPAL	Wageningen Evaluating Programs for Analytical Laboratories
WG	Work Group
WMDs	Weapons of Mass Destruction
zzMTBs	Zigzag Mirror Twin Boundaries

## **IMPRINT**

### **Editors**

*László Redler  
Attila R. Imre*

### **Lector**

*Ferenc Szlávik  
Jesse Weil*

### **Publisher**

*Ákos Horváth  
Tamás Belgya  
MTA Centre for Energy Research  
H-1121, Budapest, Konkoly-Thege Miklós út 29-33.  
Hungary*

### **Design**

*Éva Krebsz*

### **Picture credits**

*Centre for Energy Research,  
Hungarian Academy of Sciences*

### **Accessibility**

<http://www.energia.mta.hu/>

### **Contact**

*Centre for Energy Research, Hungarian Academy of Sciences  
**Location:** KFKI Campus 29-33 Konkoly-Thege Miklós street 1121 Budapest, Hungary  
**Mailing address:** 1525 Budapest 114., P.O. Box 49., Hungary  
**Phone:** (+36 1) 395 91 59 **Fax:** (+36 1) 395 92 93  
**E-mail addresses:** [info@energia.mta.hu](mailto:info@energia.mta.hu)*





Hungarian Academy of Sciences  
Centre for Energy Research  
Budapest 114, P.O.Box 49, H-1525 Hungary  
Phone: +36 1 395 9159, e-mail: [info@energia.mta.hu](mailto:info@energia.mta.hu)  
Homepage: [energia.mta.hu](http://energia.mta.hu)